A STUDY OF COMPLEMENTARY REACTIONS: SINGLE-PROTON KNOCKOUT AND SINGLE-PROTON PICKUP

by

Sean Michael McDaniel

A DISSERTATION

Submitted
to Michigan State University
in partial fulfillment of the requirements
for the degree of

DOCTOR OF PHILOSOPHY

PHYSICS

2011

ProQuest LLC.
789 East Eisenhower Parkway
P.O. Box 1346
Ann Arbor, MI 48106 - 1346

ABSTRACT

A STUDY OF COMPLEMENTARY REACTIONS: SINGLE-PROTON KNOCKOUT AND SINGLE-PROTON PICKUP

By

Sean Michael McDaniel

Knockout reactions using fast, exotic beams in inverse kinematics are an established tool for probing the ground state wave function of the incident projectile and studying the spectroscopy of the projectile-like knockout residue. In a knockout reaction, the removal of a nucleon from the projectile populates *single-hole states* in the residue. Measured partial cross sections and longitudinal momentum distributions to final states of the residue, as tagged by the detection of γ rays emitted in-flight and correlated event-by-event to the residue, are used to quantify the single-particle composition of the projectile wave function.

Recently, pickup reactions using fast, exotic beams in inverse kinematics have emerged as a complementary tool to single-nucleon knockout reactions by populating *single-particle* states in the residue. Recent analyeses have shown qualitative agreement between theoretical and measured strengths and population patterns to final states in the residue. This agreement suggests that pickup reactions can provide similar information about the ground state wavefunction of the projectile and the spectroscopy of the residue.

Two experiments were run at the NSCL that show the power and highlight the differences of these two complementary reactions. The one-proton knockout experiment ^{9}Be(^{54}Ti, ^{53}Sc + γ)X at 72 MeV/u was performed to probe the single-proton configurations of the $N = 32$ nuclei ^{54}Ti and ^{53}Sc and test the validity of the nuclear shell model and valance space in this interesting neutron-rich mass region. An unexpectedly large spectroscopic strength to excited states was observed. The magnitude of strength observed was

incompatible with shell model calculations using the fp model space only, and was therefore attributed to the knockout of deeply-bound sd-shell protons outside the calculation valance space. This interpretation was substantiated through a comparison to previous experimental work, the analogous ^{50}Ti(d,^{3}He)^{49}Sc transfer reaction and the two-proton knockout reaction ^{9}Be(^{54}Ti,^{52}Ca$+\gamma$)X, and through the comparison of the inclusive momentum distribution to a theoretical distribution that assumes sd-shell contributions. The results highlight the need for proton cross-shell interactions for the $sdpf$ valance space.

Three different one-proton pickup reactions on proton-rich nuclei centered around ^{50}Fe were studied on two different targets, ^{9}Be and ^{12}C: ^{9}Be(^{48}Cr,^{49}Mn$+\gamma$)X, ^{9}Be(^{49}Mn,^{50}Fe$+\gamma$)X, ^{9}Be(^{50}Fe,^{51}Co$+\gamma$)X, ^{12}C(^{48}Cr,^{49}Mn$+\gamma$)X, ^{12}C(^{49}Mn,^{50}Fe$+\gamma$)X, and ^{12}C(^{50}Fe,^{51}Co$+\gamma$)X. The investigation of these reactions, through the comparison of the experimentally measured and theoretically predicted partial cross sections and population pattern to final states in the pickup residue, was done with the goal of further developing pickup reactions as a spectroscopic tool. The theoretical partial cross sections were calculated using shell-model spectroscopic factors and single-particle cross sections calculated in a post-form Coupled Channels Born Approximation (CCBA) framework assuming two-body final states. The reaction mechanism was further probed by measured longitudinal momentum distributions whose comparison to calculated distributions that assume the two-body character of the final reaction product tests the direct nature of the reaction processes, and by the use of the two different targets, through which the importance of including only a subset of target final states can be judged. We report the results for the first fast beam, inverse-kinematics, proton pickup reactions in the fp-shell, and the first proton pickup reactions from a ^{12}C target.

To my parents, Mike and Jan McDaniel

ACKNOWLEDGMENTS

This acknowledgment is an attempt to inform you, the reader, that even though my name is on the cover, I was not alone. I received a tremendous amount of guidance, love, and friendship from a great number of people. Without their support, this thesis would not be possible. In their name, here is my *et al*..

My adviser, Alexandra Gade, guided me through my graduate career. Each stage of this long journey—experimental proposal, data analysis, and presentation of work—has benefited from her expertise and generous help. Her tireless editing has significantly improved the quality of thesis. Any errors or faults that remain are mine alone.

Thank you to all current and former members of my graduate committee for your guidance and encouragement: Alex Brown, Alexandra Gade, Thomas Glasmacher, William Hartmann, Wayne Repko, and Vladimir Zelevinsky. And thank you to the graduate secretary Debbie for her ability to handle all the bureaucratic frustrations I created and dropped upon her desk.

A big thanks to the gamma group, past and present. The graduate students—Travis Baugher, Chris Campbell, Johnathan Cook, Chris Lawrence, David "Floyd" Miller, Kyle Siwek, Ragnar Stroberg, Andrew Ratkiewitcz, Aimee Shore, Russ Terry, Phill Voss, and Kathy Walsh—the post-docs—Christian Diget, Geoff Grinyer, Alexander Obertelli, and Ryan Winkler—and our excellent staff physicist Dirk Weisshaar. There is a small poster by my desk that I have guarded for the last several years. It reads: "Mistakes: It could be that the purpose of your life is only to serve as a warning to others." I would like to dedicate a signed copy of that poster in everyone's honor.

Nuclear research is collaborative. As an experimentalist, I relied on the effort of the A1900 group, the S800 group (especially Daniel Bazin), and the cyclotron operators to create and deliver the appropriate rare-isotope, cocktail beam to the experimental vault. Dirk Weisshaar and the gamma group helped set up and maintain SeGA. Shifts were covered

by the members of the gamma group. Jeff Tostevin and Alex Brown did the theoretical calculations. Every person in the orchestration deserves praise and credit for a superb job.

I've met many good friends during my time at Michigan State who have kept me sane and reminded me of the honest importance of what lies within and beyond the walls of the lab. In particular, Ana Beccerril, Chris Farrow, Luke Granlund, and Tony Nettelton. They have been here throughout my graduate career, are lunch, drinking, and gaming buddies without peer, and I will miss them greatly. I will always have an open door to welcome them in.

I'm grateful I was able to spend the last part of my graduate career with a wonderful woman, Sonia. I hope that we'll continue to pickup, throw down, and push through all the bright and wonderful or dark and sad. With you, everything's better.

Lastly, I would like to thank my family. The nuclear crew (Dad, Mom, Devin, and Aaron), my extended family (Grandma Rene, Grandpa Vic, Grandma Fran, Uncle Bob, Peggy, Grandma Mary Ann, Uncle Jim, Aunt Terri, Ryan and Jamie), and the departed, whom I hope, through grace, are acknowledged (Grandpa Stan, Grandpa Bob, and Sadie). I love you all.

I've dedicated this thesis to my parents, Mike and Jan McDaniel. It's my small remembrance and immense gratitude for their unconditional love. As an experimentalist, I can't prove there's a better family. The reader will just have to accept it as an axiom of fact.

The good stuff follows.

TABLE OF CONTENTS

LIST OF TABLES

LIST OF FIGURES

Chapter 1

INTRODUCTION

1.1 Overview

This thesis is concerned with the experimental observation and theoretical description of the single-particle structure of a variety of exotic nuclei, accessed using two complementary nuclear reactions: the single-proton knockout reaction and the single-proton pickup reaction, specifically ^{9}Be(^{54}Ti, ^{53}Sc + γ)X, ^{9}Be(^{48}Cr, ^{49}Mn + γ)X, ^{9}Be(^{49}Mn, ^{50}Fe + γ)X, ^{9}Be(^{50}Fe, ^{51}Co + γ)X, ^{12}C(^{48}Cr, ^{49}Mn + γ)X, ^{12}C(^{49}Mn, ^{50}Fe + γ)X, and ^{12}C(^{50}Fe, ^{51}Co + γ)X[1]. Because this work joins a much larger narrative, the broad history of nuclear physics, an overview of the major discoveries in the path to modern nuclear structure physics is given in Appendix B.

The work is broken down into seven chapters. Chapter 1 provides an overview of the atomic nucleus. This introduction proceeds a detailed motivation (Chapter 2) for the original work contained in this thesis. Chapter 3 introduces the nuclear shell model and the single-proton pickup and single-nucleon knockout reactions. Shell model calculations and reaction theory (pickup or knockout) are combined to predict the experimentally observable inclusive and partial cross sections. The technical details of the experimental setup are covered in Chapter 4. This includes details of the production of exotic nuclei at the National Superconducting Cyclotron Laboratory (NSCL) Coupled Cyclotron Facility (CCF), a description of the major experimental devices used, the Segmented Germanium Array (SeGA) and the S800 magnetic spectrograph, and an overview of how the single-particle observables, γ ray transition energies and cross sections, are calculated using data

[1] The nomenclature of these reactions are explained in Section 3.3

collected from these devices.

Chapters 5 and 6 cover the original experimental work, whose data was collected in two separate experiments. Chapter 5 covers the single-proton knockout reaction ^{9}Be(^{54}Ti, ^{53}Sc + γ)X. Chapter 6 covers the single-proton pickup reactions ^{9}Be(^{48}Cr, ^{49}Mn + γ)X, ^{9}Be(^{49}Mn, ^{50}Fe + γ)X, ^{9}Be(^{50}Fe, ^{51}Co + γ)X, ^{12}C(^{48}Cr, ^{49}Mn + γ)X, ^{12}C(^{49}Mn, ^{50}Fe + γ)X, and ^{12}C(^{50}Fe, ^{51}Co + γ)X. A final summary is found in Chapter 7.

1.2 The Atomic Nucleus

1.2.1 What is a nucleus?

The nucleus is a femtometer scale, quantum, mesoscopic collection of protons and neutrons bound together by the residual strong force and interacting through three of the four fundamental forces of nature: the strong, weak, and electromagnetic forces. The nucleus contains nearly all the mass of the nucleus ($\approx 99.9\%$) but has negligible size in comparison to the diameter of the atom. Atomic radii are on the order of 10^{-10} m; nuclear sizes are on the order of 10^{-15} m.

Protons and neutrons are not fundamental (indivisible) particles. They belong to a class of composite particles called hadrons composed of fundamental particles called quarks. More specifically, protons and neutrons are composed of three quarks, either two up quarks and one down quark (proton, uud) or one up quark and two down quarks (neutron, udd). Although the term "strong force" was originally applied to the force between protons and neutrons, so named because the force had to be stronger than the Coulomb force to bind the positively charged protons within the nucleus (see Table 1.1 for a comparison of the coupling constants of the four forces), the name now applies to the more fundamental interaction between quarks. This force, similar to all other fundamental forces, is modeled through the exchange of particles. For quarks the force carriers are massless gluons.

Force	**Relative strength** (ratio to strong)	**Range** (m)
Strong	1	10^{-15}
Electromagnetic	1/137	∞
Weak	10^{-6}	10^{-18}
Gravity	6×10^{-39}	∞

Table 1.1: Coupling strength and interaction range of the four fundamental forces relative to the strong force.

A bit of the strong force leaks out from the strongly bound triplet of quarks. This residual force, a remaining polarization analogous to the relationship between the Coulomb and Van der Waals force, binds protons and nucleons together. This residuum is either referred to as the "residual strong force" or the "nuclear force" (see Figure 1.1) and the relative strength of the strong force allows the pertubative effects of the Coulomb and the weak force[2] to be ignored when searching for the basic framework that describes the interaction and motion of nucleons within the nucleus.

1.2.2 The Nuclear Force

Despite the complexity of the nuclear force, the non-central tensor components (the force between nucleons is not parallel to the radial position vector between them), the dependence on the momentum and position of the nucleons, the presence of many-body forces, and so forth, it is worth reviewing its broad phenomenological features. We only consider only the two-body component. Because of high-quality nucleon-nucleon scattering data, the two-body nucleon-nucleon (NN) force is well described (see Refs. [2–4] for the modern Argonne V18, the Nijm1, Nijm2, Nijm93, and Reid93 nucleon-nucleon

[2]The mechanism of flavor changing whereby a up quark changes to a down quark or a down quark to an up quark through the emission of an intermediate heavy W^- boson. For example, the weak interaction drives the processes called β-decay, whereby a neutron changes to a proton through the emission of an electron and an electron antineutrino (β^- decay: $n \to p + e^- + \bar{\nu}_e$) or a proton changes to a neutron through the emission of a positron and an electron neutrino (β^+ decay: $p \to n + \nu_e$).

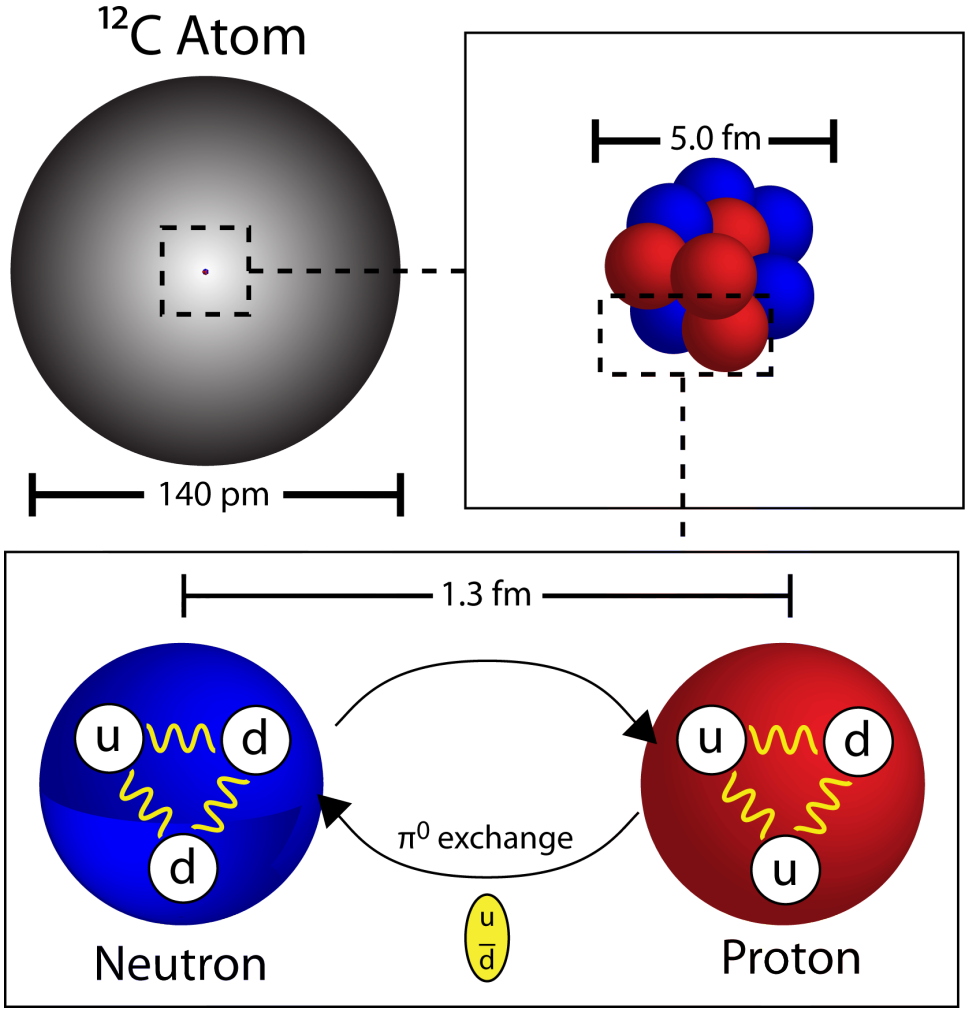

Figure 1.1: Approximate sizes of the constituents of a ^{12}C atom. At medium ($d \approx 1-2\,\text{fm}$) and large distances ($\gtrsim 2\,\text{fm}$), the nuclear force can be modeled as the exchange of light mesons (π, ρ, and ω), as first proposed by Hideki Yukawa in 1934 [1]. *For interpretation of the references to color in this and all other figures, the reader is referred to the electronic version of this dissertation.*

potentials, and the CD-Bonn potential). Modifications to the bare NN potential to account for the nuclear medium and three-body forces, although important, preserve the two-body phenomenological features reviewed below.

The complete force can be decomposed into a central, two-body spin-orbit interaction, and a tensor component [5]. The nuclear force is both charge symmetric and charge independent, i.e. the force that describes all nucleon-nucleon interactions is identical. Because the nuclear Hamiltonian is invariant under a change of nucleon type, which can

be experimentally observed through the similar spectra of mirror nuclei, pairs of nuclei with identical A but with switched numbers of protons Z and neutrons N[3], a conserved quantum number is introduced to reflect the symmetry. This quantum number is called *isospin*. Isospin symmetry is broken by the electromagnetic interaction which effects protons but not neutrons.

The dependence of the interaction on the position, spin, isospin can be written as

$$V(1,2) = V(\boldsymbol{r}_1, \sigma_1, \tau_1; \boldsymbol{r}_2, \sigma_2, \tau_2), \tag{1.1}$$

and its decomposition gives

$$V(1,2) = V_c(1,2) + V_{LS}(1,2) + V_T(1,2). \tag{1.2}$$

The central interaction depends on the relative distance between the nucleons. We have,

$$V_C(1,2) = V_0(r) + V_\sigma(r)\,\sigma_1 \cdot \sigma_2 + V_\tau(r)\,\tau_1 \cdot \tau_2 + V_{\sigma\tau}(r)\,(\sigma_1 \cdot \sigma_2)\,(\tau_1 \cdot \tau_2). \tag{1.3}$$

and for the two-body spin-orbit interaction,

$$V_{LS} = \left(V_{LS}^{is}(r) + V_{LS}^{iv}(r)\,\tau_1 \cdot \tau_2\right) \boldsymbol{L} \cdot \boldsymbol{S} \tag{1.4}$$

where $\boldsymbol{L}$ is the relative orbital momentum between the two interacting nucleons and $\boldsymbol{S}$ is the intrinsic spin $\boldsymbol{S} = 1/2(\sigma_1 + \sigma_2)$. The labels *is* and *iv* indicate isoscaler (isospin singlet, $\boldsymbol{T} = \tau_1 + \tau_2 = \boldsymbol{0}$) and isovector (isospin triplet, $\boldsymbol{T} = \tau_1 + \tau_2 = \boldsymbol{1}$) components. The tensor component is

$$V_T(1,2) = \left(V_T^{is}(r) + V_T^{iv}(r)\tau_1 \cdot \tau_2\right) \hat{S}_{12}(r) \tag{1.5}$$

where

$$S_{12}(r) = \frac{3}{r^2}(\sigma_1 \cdot \boldsymbol{r})(\sigma_2 \cdot \boldsymbol{r}) - \sigma_1 \cdot \sigma_2 \tag{1.6}$$

In all cases $r = |\boldsymbol{r}_1 - \boldsymbol{r}_2|$, τ_1 and τ_2 are the respective isospin vectors of nucleon 1 and 2, and σ_2 and σ_2 are their spin matrices.

[3]Examples include $^{11}\mathrm{B} \leftrightarrow {}^{11}\mathrm{C}$ and $^{21}\mathrm{Na} \leftrightarrow {}^{21}\mathrm{Ne}$.

The radial part of the nuclear force can be divided into three distinct ranges. At very short distances ($d \lesssim 0.5\,\text{fm}$) the force is extremely repulsive (nearly infinite). At medium range ($0.5\,\text{fm} \lesssim d \lesssim 2\,\text{fm}$) it is strongly attractive, and at long range ($d \gtrsim 2\,\text{fm}$), only a small, attractive exponential tail remains. Beyond 2.5 fm, the Coulomb force dominates. The radial part of the nuclear force illustrated in Figure 1.2. At medium and long distances, the nuclear force can be modeled by the exchange of light mesons (π, ρ and ω), as proposed by Yukawa in 1934 [1] and experimentally seen in 1947 by Cecil Powell, Giuseppe Occhialini and César Lattes [6, 7]. As will be described in Section 1.2.4, the single-pion exchange is a very good approximation because on average nucleons only feel the very tails of the nuclear force. The average nucleon-nucleon distance of $d \sim 2.4\,\text{fm}$ is much larger than the point ($\sim 0.7\,\text{fm}$) at which the nucleon-nucleon binding potential is strongest.

Recent efforts have begun to derive the nuclear force from quark degrees of freedom. Lattice quantum chromodynamics QCD calculations [8] show broad phenomenological agreement with the central component of the nuclear force (repulsive core, attraction at medium range, long-range tails consistent with pion exchange) but these efforts are computationally extremely demanding and have only been done for a limited selection of two nucleon states (e.g. $^1s_0$ and $^3s_1$). The derivation of nuclear properties from fundamental QCD calculations remains a long-term goal. For calculations of multi-nucleon systems, as studied in this work, we start with the nucleon as the basic degree of freedom. There are several ways to label these systems by total atomic number A, nuclear charge Z, and number of neutrons N, but in this work will adopt the conventions of only using A (total mass) and Z (atomic number), for example ^{53}Sc ($A = 53$ and $Z = 21$ for Scandium) and ^{48}Cr ($A = 48$ and $Z = 24$ for Chromium).

1.2.3 The Nuclear Landscape

Nuclear physicists organize the wide spectrum of nuclei according to their nuclear charge and number of neutrons in a similar way that chemists organize the elements by their

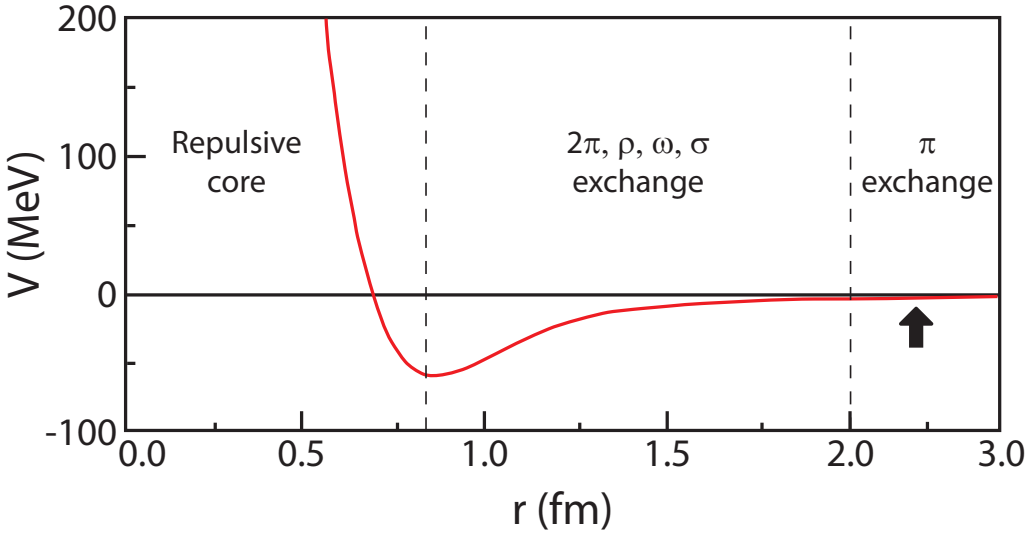

Figure 1.2: Central projection of the nucleon-nucleon (NN) potential showing general features: the hard repulsion at short range, a minimum just below 1 fm, and a limited ($\approx$ 2.5 fm) NN interaction range. The average nucleon-nucleon distance of $d \approx 2.4$ fm, located well outside the minimum, is indicated by a black arrow.

nuclear charge and group. This chart, seen in Figure 1.3, is called a nuclear or Sergè chart. A nuclear chart has a few important features:

The black squares in Figure 1.3 indicate stable elements. The entire collection of stable elements is called the "valley of stability". This valley ranges from the light isotopes, starting with Hydrogen (^{1}H) where $N = Z$ and $N/Z = 1$, all the way up through Bismuth (^{209}Bi), where $N > Z$ and $N/Z = 1.5$, i.e. there are 52% more neutrons than protons. Past Bismuth at $Z = 83$, all isotopes are unstable. Elements heavier than Bismuth that exist in the Earth's crust, for example ^{238}U and ^{232}Th have half-lives on the order of the age of our solar system ($\tau_{1/2}(^{238}\mathrm{U}) = 4.468(3) \times 10^{9}$ y, $\tau_{1/2}(^{232}\mathrm{Th}) = 1.41(1) \times 10^{10}$ y) or they lie in the decay chains of one of these very long-lived isotopes. This increasing neutron-proton asymmetry with respect to proton number is caused by the interplay between the short-range nuclear force, which favors the very strong proton-neutron combination, and the repulsive Coulomb force which decreases the binding energy of nucleons within the nucleus. The nuclear contribution to the binding energy increases linearly with A (a

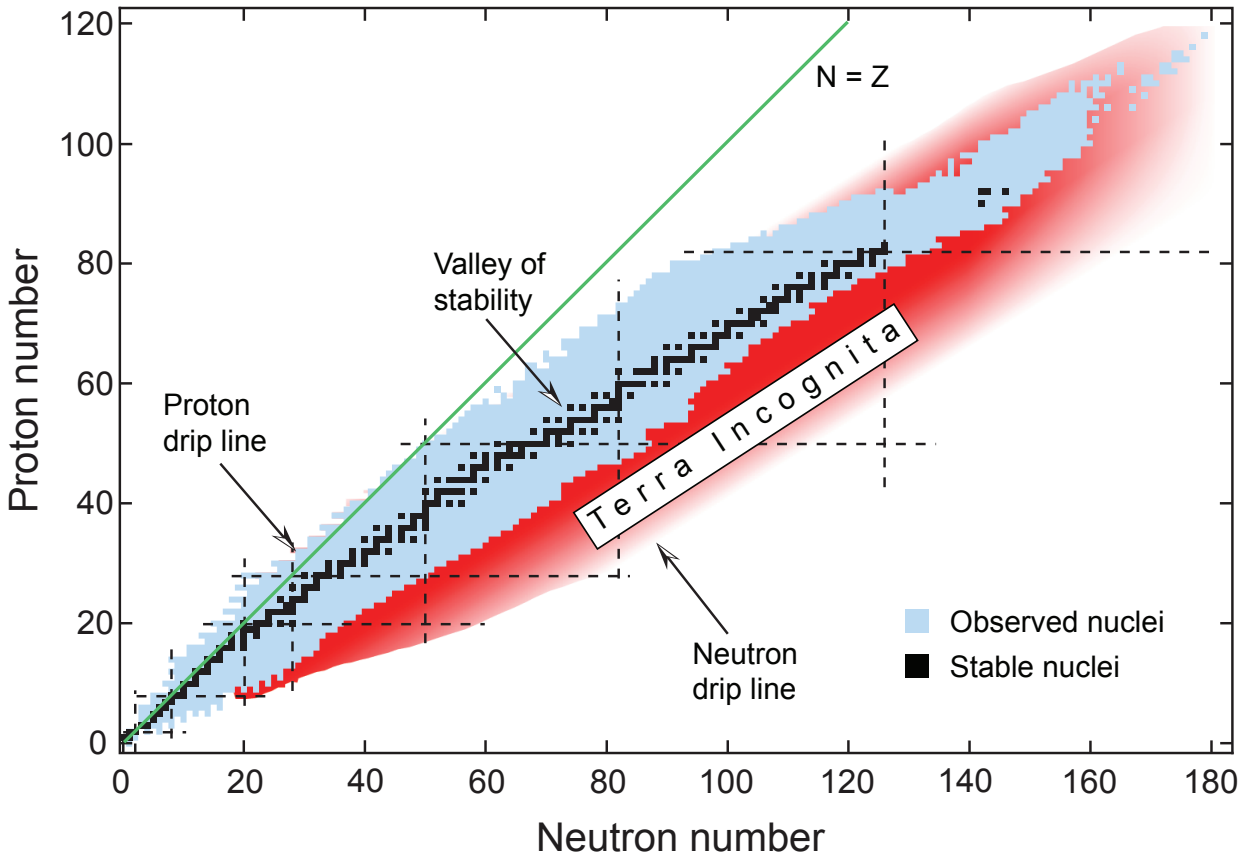

Figure 1.3: The nuclear chart is used for organizing the nuclear isotopes. Stable elements (valley of stability) are shown in black. The dotted lines indicate the magic numbers at N,Z = 2, 8,20, 50, 82 and 126. The figure is adapted from Figure 2.1 of Ref. [9]

nucleon is only affected by its nearest neighbors), and the binding energy per nucleon, once we move beyond the very strong shell effects at low mass and reach nuclear saturation, is an approximate $B(N,Z)/A|_{A>12} \approx -8.5$ MeV/u (see Ref [10, page 2]). The Coulomb contribution to the total binding energy increases quadratically with A (each proton feels all other protons). The interplay of proton-neutron pairing, Coulomb effects, and the contribution of the strong force to nuclear binding is shown in the semi-empirical mass formula of Bethe and Weizäcker [10–12].

$$B(N,Z) = a_V A + a_S A^{2/3} + a_C \frac{Z^2}{A^{1/3}} + a_p \frac{(N-Z)^2}{A} - \delta(A), \tag{1.7}$$

where the nuclear binding (volume) constant a_V, surface constant a_S[4], Coulomb constant a_C, paring constant a_p, and odd-even term $\delta(A)$ can be found through fits of measured masses. The constants depend upon the fit method and included masses. Fit values and further detail are found is Refs. [13–15]. A sample is listed below:

$$a_V = -15.68\,\text{MeV}, \qquad a_s = 18.56\,\text{MeV}, \qquad a_c = 0.717\,\text{MeV}, \quad a_p = 28.1\,\text{MeV} \tag{1.8}$$

$$\delta A = \begin{cases} 34\,A^{-3/4}, & \text{for even-even} \\ 0 & \text{for even-odd} \\ -34\,A^{-3/4} & \text{for odd-odd} \end{cases}$$

Nuclei off the valley of stability are not stable against β-decay, α-decay, or spontaneous fission. Neutron-rich nuclei to the right of the valley of stability move towards stability through β^- decay (${}^{Z}_{N}A \rightarrow {}^{Z+1}_{N-1}A$), nuclei to the left of the valley of stability (proton-rich for lighter nuclei) head towards stability through electron capture or β^+-decay (${}^{Z}_{N}A \rightarrow {}^{Z-1}_{N+1}A$). β^- decay, electron capture, and β^+ decay involve the weak process. For additional information, see Refs. [16, 17]. Heavy elements, such as those beyond ^{209}Pb, typically emit α particles (${}^{Z}_{N}A \rightarrow {}^{Z-2}_{N-2}(A-4)$), until they can β-decay to a stable isotope. The N, Z boundary at which nuclei become particle-unbound, i.e $S_n > 0$ or $S_p > 0$, are called drip-lines and are indicated in Figure 1.3.

Of the $\sim$ 6000 isotopes predicted to exist [18], approximately 3000 have been made with particle accelerators or nuclear reactors. 270 are stable. The unexplored areas, labeled "terra incognita" in Figure 1.3, contain a wealth of physics important for nuclear structure, astrophysics, and reaction theory. Newly discovered isotopes offer a test for the predictive power of nuclear models. Nuclei far from stability can exhibit novel properties such as nuclear halos, shape coexistence, inversion of traditional single-particle levels, new collective behavior, and so forth. These novel properties are often sensitive to different aspects of the nuclear force that are broadly noticeable in the study of stable nuclei, and

[4]Nucleons near the surface of the nucleus contribute less to the total binding energy

fully folding these new properties with the existing theoretical framework leads to a better understanding of the complete nuclear many-body system. Furthermore, many important astrophysical processes, like the reaction pathways for the *r* and *rp*-processes [19, 20], lie in areas currently unexplored and inaccessible by experiment.

The production yields of these extremely exotic nuclei are presently too low to scientifically explore, but new, second generation facilities for the production of exotic nuclei, like Système de Production d'Ions in Ligne, Génération 2[5] (SPIRAL2) at Grand Accélérateur National d'Ions Lourds (GANIL)[6], Facility for Antiproton and Ion Research (FAIR) at Gesellschaft für Schwerionenforschung[7] (GSI), RIBF at Rikagaku Kenkyūsho (RIKEN), and the Facility for Rare-Isotope Beams (FRIB) at Michigan State University (MSU), will provide the beams of exotic nuclei necessary to start such research.

1.2.4 Magic Numbers

Magic numbers begin with the concept of nucleons as independent particles moving on discrete orbits. Like electrons, nucleons have an intrinsic spin of 1/2 and are Fermions: they obey the Pauli exclusion principle. Thus, protons and neutrons (separately) cannot share the same quantum numbers. The Pauli principle and a nearly infinite repulsive core (see Figure 1.2), lead to a diffuse nucleus where nucleons on average feel the tails of the nuclear force[8]. These two effects allow us to treat the particles individually, and it forces nucleons, as they are added to a nucleus, to occupy consecutively higher-energy orbitals in exactly the same manner that electrons fill the orbitals in atoms.

[5] English translation: system of ion-production online

[6] English translation: large heavy-ion accelerator

[7] English translation: Society for Heavy-Ion Research

[8] The ratio of the minimal volume possible (maximal packing fraction) of nucleons in a nucleus to the measured volume is 1:100, $V_{\text{min}}/V_{\text{meas}} = (c/2r_0)^3 \approx 1/100$. See [10, Page 36, Ch. 2] and [21, Section 2.5]

There is a crucial difference between electrons and nucleons. All electrons move in a central potential well generated by the positively charged nucleus. Nucleons, however, are not bound by an external potential. Because the nuclear force is short range, as inferred by the saturation of binding energy per nucleon, the nuclear potential is a common average over nearest neighbors. The homogeneity of the potential associated with saturation allows us to define a nuclear *mean field*, an average nuclear potential. Describing a uniform and similar potential for all nucleons allows us to decouple the many-body problem and consider each nucleon individually. This framework of independent particle motion where each nucleon only feels the average potential generated by all other particles is called the Independent Particle Model (IPM), and its final formulation was done by Brueckner in 1954 [22, 23].

As in atomic physics, there are certain orbitals (the valance orbitals) that when fully occupied lead to an especially nonreactive atom. Nuclear physics, similarly, has very stable nuclei (experimental signatures are seen below) when certain orbits are fully filled. The energies of the proton and neutron orbitals are not uniformly distributed. Instead they are grouped into shells with wide energy gaps between each shell (see Figure 1.4). When all the orbitals in a shell are full and there is a large gap in energy between the outermost filled orbital and the next unfilled orbital, we call the nucleus *magic*. Nuclei where either the protons or neutrons are in magic configurations are called *semi-magic* and nuclei where both the proton and neutron shells fulfill the magicity condition are called *doubly magic*. The total number of protons and neutrons necessary to fulfill this condition are called *magic numbers* and they occur, for example, at $N, Z = 2, 8, 20, 50, 82,$ and 126. Examples of doubly magic nuclei are ^{4}He, ^{16}O, ^{40}Ca, ^{48}Ca, ^{56}Ni, and ^{208}Pb.

These magic numbers manifest experimentally in numerous ways. A few signatures:

1. *High binding energies:* Semi-magic and doubly magic nuclei have higher binding energies, which can be seen in their deviation from the Weiszäcker empirical mass formula.

2. *Nucleon pickup cross section:* The neutron or proton pickup cross section is two orders lower in magnitude for nuclei with a magic number of neutrons or protons.

3. *High excitation energy:* The energy of the first excited states is higher than corresponding states in neighboring nuclei.

4. *Two-nucleon removal energies:* The two-neutron S_{2n} and two-proton S_{2p} separation energies are higher for magic nuclei. The two-nucleon, rather than single nucleon (S_p and S_n) separation energies are used to eliminate the effects of the pairing force which binds even numbers of protons and neutrons more tightly.

5. *Zero electrical quadrupole moment:* Indicates that magic nuclei are nearly spherical in shape.

The location and spread of the single particle orbitals was first described in nearly simultaneous papers in 1949 by Mayer [24] and Haxel, Jensen, and Suess [25]. Mayer and Jensen combined the harmonic oscillator potential with a spin-orbit term[9]. This spin-orbit term breaks the degeneracy within the harmonic oscillator shells, and causes the descent of levels with higher angular momentum ℓ into the major oscillator shell below, explaining the origin of the magic numbers above 20[10]. This split in degeneracy is seen in Figure 1.4. Orbitals are defined by three quantum numbers: the principal quantum number N (major oscillator shell), the orbital angular momentum ℓ, and the total angular momentum j. The orbital angular momentum is given in spectroscopic notation where $\ell = s, p, d, f, g, h \cdots$ (**s**harp, **p**rincipal, **d**iffuse, and **f**undamental) and is equivalent to $\ell = 0, 1, 2, 3, 4, 5, \cdots$. Past g the numbers increment in alphabetic order. N is usually replaced by n the number of radial nodes in the wave function, leading to the quantum numbers $n\ell j$, written as

[9]The addition of the spin-orbit term causes the agreement. Both the base harmonic oscillator or a base realistic potential (e.g. finite square well with rounded edges) give a similar level structure.

[10]We label the magic numbers created by the major oscillator quantum number, *HO magic numbers*, and those created by the spin-orbit force, *LS magic numbers*.

$n\ell_j$. This number either starts at either 0 or 1 depending if the radial node at the origin is counted. Under the convention that the first radial node is counted, the first several orbitals are labeled $1s_{1/2}$ (s-shell), $1p_{3/2}$, $1p_{1/2}$ (p-shell), $1d_{5/2}$, $2s_{1/2}$, $1d_{3/2}$ (sd-shell), and $1f_{7/2}$.

For several decades, the location and origin of these magic numbers, seen uniformly through the valley of stability, was a convenient dogma. New facilities like the NSCL CCF facility, however, have allowed experiments to be conducted with radioactive beams. Starting in the 1970s, experimentalists noticed that the $N = 20$ shell gap did not necessarily persist in Na, Ne, and Mg isotopes [26–28] and they concluded that the canonical shell gaps did not hold in regions of extreme proton-neutron asymmetry. The natural question arises: what drives these evolutions in shell structure? This question, as seen in Chapter 2 can be addressed experimentally through probing a nucleus's single-particle structure, and is one of the major motivations of the experimental work contained in this thesis.

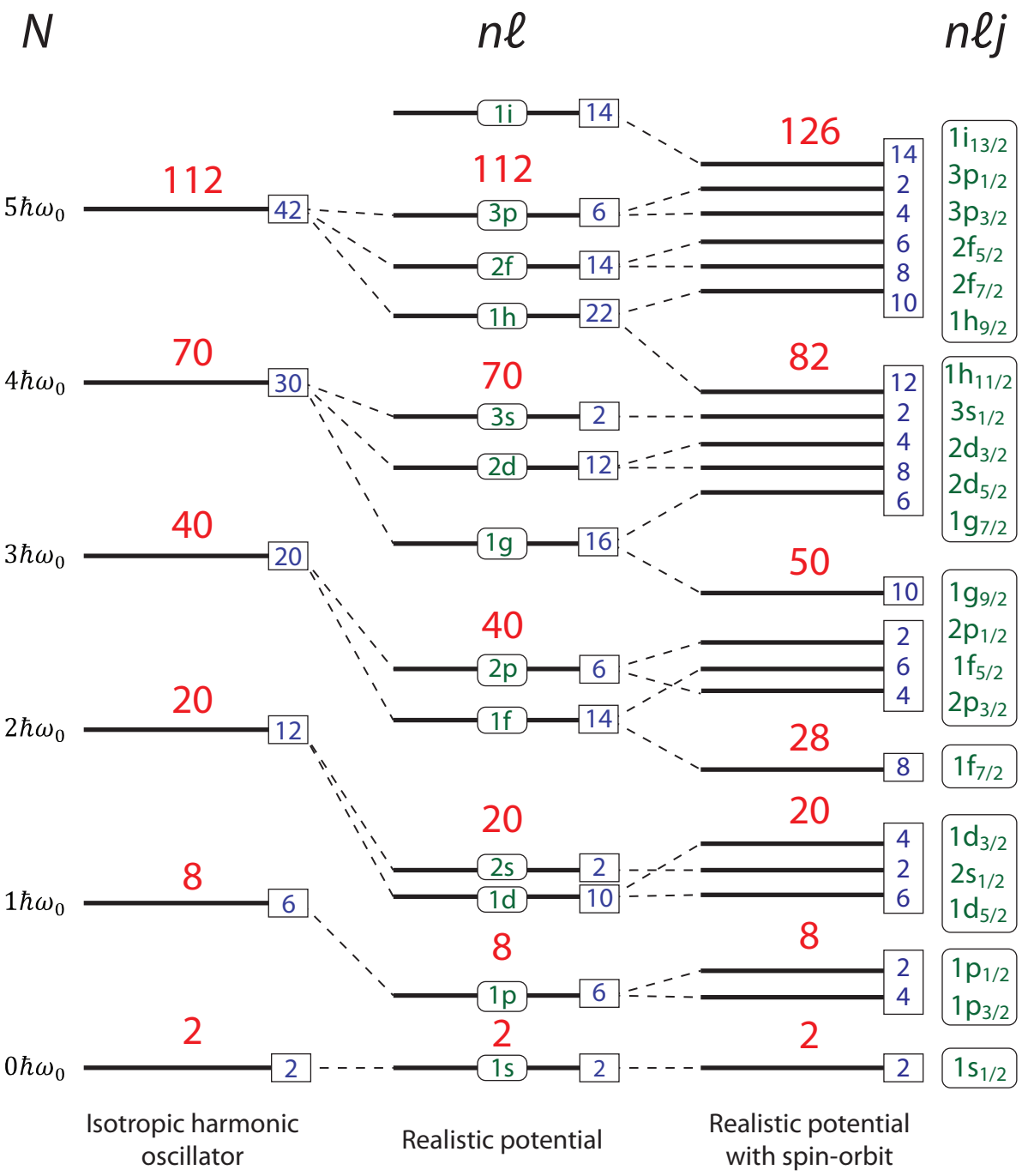

Figure 1.4: Single particle orbitals under consequentially more complicated nuclear potentials: pure isotropic harmonic oscillator, isotropic harmonic oscillator with angular momentum effects (labeled "releastic potential"), and the harmonic oscillator with spin-orbit splitting. The harmonic oscillator with the spin-orbit terms reproduces the magic numbers (red font text) seen in nuclei near stability. The quantum numbers (green font text) and occupancies (blue font text) for each level are given. N for the harmonic oscillator potential, $n\ell$ for the realistic potential, and $n\ell j$ for the realistic potential with a spin-orbit term.

Chapter 2

MOTIVATION

2.1 Single-particle Structure and Nuclei far from Stability

The atomic nucleus can exhibit a wide range of phenomena, like collectivity, shape co-existence, pronounced single-particle character, and magic numbers, and as a result of the diversity of nuclear behavior, a corresponding diversity of experimental techniques have been developed to probe specific aspects of the nucleus. For example, we can probe the existence of a nucleus (drip-line location), its life-time (β-decay, α-decay), nuclear mass, nuclear shape (prolate, oblate, triaxial), proton and neutron density distributions, and single-particle structure (the location and occupancy of orbitals). These unique nuclear attributes, in tandem with theoretical models, allow physicists to address some of the major and fundamental goals of nuclear science. What is the nature of the nuclear force? What are the limits of nuclear existence? What is the origin of the heavy elements in the Universe? And what are the basic explanations for the emergence of simple patterns in complex nuclei like shell gaps, collective motion, deformation, and so forth? [29]

This thesis approaches the nucleus with two specific reactions, single-nucleon knockout and single-nucleon pickup, that provide information on the single-particle degree of freedom. Tracking the location and occupation of single-particle orbitals have several important applications.

First, we can track the migration of the shells to aid in the quest of unraveling the driving forces behind shell evolution. Starting in the 1970's with with $N = 20$ nuclei ^{31}Na [27] and ^{32}Mg [26, 28], as experimenters gained access to beams of unstable nuclei, it became clear that the canonical harmonic oscillator and spin-orbit shell gaps at 8,

20, 28, 50, 28 and 126, softened or even disappeared for nuclei that shared similar magic numbers but were located off the valley of β-stability. The disappearance of magic numbers and migration of orbitals were and are viewed as critical for the wider problem of understanding the nucleon-nucleon interaction in the nucleus (see Section 3.2 for an overview and Equation 3.7 for the definition of the two-body matrix elements that are the foundation of modern shell-model calculations).

Following the fall of the ephemeral $N = 20$, other shell gaps were found to disappear as experimenters moved from the valley of stability to the proton or neutron drip line. For example, $N = 8$ for ^{11}Li and ^{12}Be [30, 31] and $N = 28$ for ^{42,40}Si [32–35] and ^{44}S [36]. Shell migration can also lead to the emergence of new energy gaps, for example $N = 14$ for ^{22}O, $N = 16$ for ^{24}O [37, 38], and $N = 32$ for Calcium (^{52}Ca) through Chromium (^{56}Cr) isotones [39–46] (See Section 5.2 for additional information). For a comprehensive review of these and other shell closures and appearances, see Refs. [5, 47] and citations therein.

Second, tracking the migration of orbitals can reveal the role and strength of specific matrix elements of the nuclear Hamiltonian in driving shell evolution. Analyzing the occupancies and relative energy difference of the $1d_{3/2}$ and $2s_{1/2}$ orbitals for the $Z = 19$ nucleus Potassium, with one hole in the $\pi 1d_{3/2}$ orbital, between $N = 20$ ($^{39}_{19}$K) and $N = 28$ ($^{47}_{19}$K) using $(d, ^3\mathrm{He})$ and $(e, e'p)$ reactions, revealed a decrease in energy and eventual crossing between the two orbitals as neutrons were added to the $\nu f_{7/2}$ orbital. This change in the energy spacing of the $\pi d_{3/2}$ and $\pi(2s_{1/2})^1$ orbital, measured by calculating the energy difference between the first $E(3/2^-_1)$ and $E(1/2^-_1)$ states, with respect to neutron occupancy of the $\nu f_{7/2}$ orbital, revealed the role of the monopole forces $V_{\sigma\tau}(d_{3/2}f_{7/2})$ and $V_{\sigma\tau}(s_{1/2}f_{7/2})$ in driving the proton shell evolution [48–50]. Similar analysis was performed for the Chlorine chain, with one proton in the $\pi d_{3/2}$ orbital in Ref. [51] through the spectroscopy of ^{43}Cl and ^{45}Cl, and a comparable evolution of the $\pi d_{3/2}$ and $\pi(2s_{1/2})$ orbitals was seen.

[1] The radial quantum number n is only included to avoid confusion with $1s_{1/2}$ orbital.

The dominance of these matrix element reflects a few underlying properties of the nuclear interaction that should be pointed out. First, the $\pi\nu$ NN iteraction is strongest when the proton and neutron wavefunctions strongly overlap—this occurs when the proton and neutron share the same radial quantum number n and the same orbital angular momentum ℓ—and second when their spins are opposite. The spin-flip $\Delta\ell = 0$ and $\Delta\ell = 1$ $\pi\nu$ monopole interactions tend to drive the evolution of the single particle-orbitals near shell gaps. The strongest negative interaction occurs between $j_< = \ell - 1/2$ and $j_> = \ell + 1/2$, $\Delta\ell = 0$, spin-flip partners. See Ref. [5] for a comprehensive review. Shell gaps modified by this interaction include $N = 8$ ($\pi p_{3/2} - \nu p_{1/2}$), $N = 20$ ($\pi d_{5/2} - \nu d_{3/2}$), $N = 28$ ($\pi f_{7/2} - \nu f_{5/2}$), $N = 50$ ($\pi g_{9/2} - \nu g_{7/2}$), and $N = 82$ ($\pi h_{1/2} - \nu h_{9/2}$). The spin-flip $\Delta\ell = 1$ is important for shell evolution in ${}_{19}$K isotopes ($\pi d_{3/2} - \nu f_{7/2}$), ${}_{29}$Cu isotones ($\pi f_{5/2} - \nu g_{9/2}$), and ${}_{51}$Sb isotones ($\pi g_{7/2} - \nu h_{11/2}$) [5]. The force that drives the collapse of the $N = 28$ shell gap is also partially responsible for the creation of the $N = 32$ shell gap, a point that will be further addressed in the discussion of the one proton knockout reaction ^{9}Be(^{54}Ti, ^{53}Sc + γ)X (see Section 5.2).

Third, as we continue enumerating the advantages of probing single-particle structure, often outwardly macroscopic properties, like deformation can be understood or explained through single-particle behavior. Two classic examples, ^{32}Mg and ^{31}Na ($N = 20$) were studied soon after rare-isotope beams became available. They belong to a cluster of nuclei with similar deformations called the "island of inversion".

As the neutron $d_{3/2}$ and $f_{7/2}$ orbitals move closer, driven by changes to the $\pi d_{5/2} - \nu d_{3/2}$ spin-flip monopole interaction as the $\pi d_{5/2}$ and $\nu d_{3/2}$ orbitals are occupied, cross shell excitations develop, i.e. neutrons are promoted from the lower energy $\nu d_{3/2}$ orbital to one of the higher energy *fp*-shell orbitals across the $N = 20$ shell gap, predominately the $\nu f_{7/2}$ orbital. Because the $N = 20$ shell gap is a harmonic-oscillator shell gap, the orbitals above and below the gap have opposite parity. Parity is conserved in the strong interaction, and therefore only even-n particle-hole excitations are allowed, of which the two-particle –

two-hole ($2p2h$) are the most probable. The two promoted neutrons have the full set of $f_{7/2}$ quantum states available, and they can therefore arrange themselves in the lowest energy configuration. The system gains quadrupole correlation energy through the preferential arrangement of the neutron orbitals that is greater than the energy of the energy difference between the orbitals. This neutron configuration leads to pronounced deformation [52]. A single-neutron knockout experiment ^{9}Be(^{32}Mg, ^{31}Mg + γ)X, showing the power of the knockout reaction process to probe the ground state wavefunction of nuclei[2], quantified the presence of neutrons in the negative parity fp-shell. Because of this inversion between the standard normal-order configuration, because of the observed difference in occupancy between the $d_{3/2}$ and the higher energy $f_{7/2}$ orbitals, and because similar inversions are seen in a limited selection of neighboring nuclei roughly centered on $20 \leq N \leq 22$ and $10 \leq Z \leq 12$ [52], this area of the nuclear landscape is called the "island of inversion."

Forth, the description of phenomena through a single particle perspective can reveal the limitations of the valance space used in nuclear shell model calculations. Original efforts to study the properties of ^{32}Mg using the Universal SD (USD) effective interaction [53] failed. The anomalous properties of "island of inversion" nuclei are caused by the promotion of neutrons to the fp-shell orbits, which lie outside of the sd model space[3] used in the USD effective interaction. Through the inclusion of the fp-shell in the SDPF-M effective interaction, Refs. [54, 55] found broad agreement between the measured and calculated spectroscopic factors for the ground-state wavefunction of ^{32}Mg.

The fifth and last point: experimental energies are essential in the determination of the two-body matrix elements (TMBEs), used to represent the residual interaction between nuclei, and the single-particle energies (SPEs) used in shell-model effective Hamiltonians[4]. The 195 TMBEs and 4 SPEs in the GXPF1 effective interaction for the fp-shell

[2]See Section 3.4 for experimental and theoretical details on knockout reactions.

[3]See Section 3.2.4 for a definition of model spaces the associated effective interactions

[4]See Section 3.2.3 for a more through definition of TMBEs and SPEs. Section 3.2 covers

$(1f_{7/2}2p_{3/2}1f_{5/2}2p_{1/2})$ were calculated by fitting 70 linear combinations of TMBEs to 699 energy levels in the mass range 47 – 66 [56]. Judicious experimental measurements of the location of specific orbitals can lead to the select modifications of matrix elements corresponding to the interaction between pairs of orbitals for specific quantum numbers. For example, the $N = 34$ shell gap predicted by the GXPF1 effective interaction was not seen in the $E(2_1^+)$ of ^{56}Ti [43, 44, 57]. When the experiment did not observe the predicted shell gap, five $T = 1$ matrix elements were modified[5] resulting in the GXPF1A effective interaction [58] which has higher predictive power in the mass region for nuclei with $N \geq 32$. The GXPF1 effective interaction was used to calculate the level structure and spectroscopic factors for the ^{9}Be(^{54}Ti, ^{53}Sc + γ)X reaction; the GXPF1A effective interaction provided similar information for the six different proton-pickup proton-pickup reactions.

Theory and experiment evolve simultaneously. Often experiment reveals the limitations of shell-model theory, like the need to include the intruder states in the valance space of ^{32}Mg. The observation of new phenomena, outside the traditional model space, drives this change in scope. With this last point, we recap the applications and advantages of tracking single-particle structure. Through tracking single-particle structure one can:

1. Work towards a microscopic explanation for the migration of orbitals and the changes in shell spacing. This includes the disappearance of traditional shell gaps and the emergence of new shell gaps.

2. Decompose the nucleon-nucleon, in-medium nuclear interaction into its individual multipole components.

3. Analyze and explain macroscopic properties, like deformation, through the location and occupation of orbitals.

---

the nuclear shell model.

[5]Defining V as $V(2j_a2j_b2j_c2j_d;JT)$, the five altered matrix elements are $V(7777;01)$, $V(5511;01)$, $V(1111;01)$, $V(5151;21)$, and $V(5151;31)$. See Honma et al. [58] for additional details.

4. Expose limitations of the current valence spaces through the observation of new phenomena that cannot be explained by shell-model calculations in a restricted model space.

5. Provide data and constraints for the determination of TMBEs and SPEs.

2.2 Techniques

It is clear that looking at the nucleus through the lens of single-particle structure can undress hidden components of the nuclear interaction and explain a variety of observed phenomena. The best way to extract this information is through a nuclear reaction that can probe the single-particle degree-of-freedom. Because of the symmetry between particles and holes in a nucleus, it is clear we can take two different routes. We can track particles or we can track holes.

Knockout reactions, the removal of a single nucleon in a direct process from a nucleus in the fast, projectile beam, are an established technique for tracking single-particle states in exotic nuclei. These reactions are covered in Section 3.4 and in review articles by Hansen and Tostevin [59] and Gade and Glasmacher [47]. Through the removal of a nucleon in the initial projectile with mass A, *hole-like states* in the $A-1$ residue are populated, providing information on the ground-state wavefunction of the mass A projectile. Recently, single nucleon pickup reactions, in inverse kinematics with fast, exotic beams have emerged as a possible new tool for probing single-hole structure [60, 61]. Because the heavy A projectile picks up a nucleon from the target, *particle-like states* are populated in the mass $A+1$ residue. Thus, the information provided by the pickup reaction is complementary: knockout reactions populate single-hole states and pickup reactions populate single-particle states.

2.3 Summary of specific motivations

This thesis approaches both the use and development of knockout and pickup reactions for the determination of single-particle structure. The specific motivations:

1. Through the ^{9}Be(^{54}Ti, ^{53}Sc + γ)X reaction, probe the single-particle proton configurations of the $N = 32$ nuclei ^{54}Ti and ^{53}Sc, and test the validity of the shell model and valance space in this neutron rich-region.

2. Continue the development of pickup reactions as qualitative spectroscopic tool by: (1) Comparing measured partial and inclusive cross sections for three different proton-rich reactions centered around ^{50}Fe to theoretical predictions that combine CCBA reaction calculations and shell model theory; (2) Varying the experimental conditions through the use of two different targets, ^{9}Be and ^{12}C; and by (3) Comparing measured longitudinal momentum distributions to theoretical distributions that assume a direct reaction process. The six different reactions studied, ^{9}Be(^{48}Cr, ^{49}Mn + γ)X, ^{9}Be(^{49}Mn, ^{50}Fe + γ)X, ^{9}Be(^{50}Fe, ^{51}Co + γ)X, ^{12}C(^{48}Cr, ^{49}Mn + γ)X, ^{12}C(^{49}Mn, ^{50}Fe + γ)X, and ^{12}C(^{50}Fe, ^{51}Co + γ)X, are on the proton-rich side of the valley of stability, have a conveniently limited number of excited states, and lie in a region of the nuclear landscape with well understood shell structure.

Chapter 3

NUCLEAR SHELL MODEL AND REACTION THEORY

3.1 Reactions and Structure

The size of the nucleus presents a difficult problem. How does one obtain information on the individual constituents of a system when the total system size is femtometer scale? The method, as will be outlined in Section 3.3, is to use a nuclear reaction. The combination of an experimental probe and a theoretical framework in which to interpret results, allows scientists to make powerful statements about the properties of a nucleus and its nucleons. The choice of the nuclear reaction is critical. To probe the wavefunction of a nucleus, one should ideally use reactions that excite only the single-particle degree of freedom. The direct one-nucleon pickup and knockout reactions, which will be outlined in this Chapter in Sections 3.4 and 3.5, provide such a selectivity.

For this work, nuclear reaction theory is combined with shell model calculations to provide theoretical estimates for experimentally observable quantities like partial and inclusive cross sections. The goal of the nuclear shell model is a fully microscopic description of the atomic nucleus. Information on the nuclear shell model follows.

3.2 The Nuclear Shell Model

3.2.1 Overview

The nuclear shell model describes the nucleus from a microscopic basis under the assumptions that the nucleus is a quantum mechanical, many body system, relativistic effects can be ignored, and the interaction between nucleons is dominantly two-body in character. The core components of the nuclear potential were finally resolved by Mayer [24] and Haxel, Jensen, and Suess [25] in 1949 through the addition of a strong a spin-orbit term to the existing, central, harmonic oscillator (HO) potential. The result was an improved agreement with the experimentally measured single-particle levels for stable nuclei including the first correct description of all experimentally observed magic numbers (see Figure 1.4). The combination of the extremely repulsive core in the nuclear potential (see Figure 1.2) and Pauli blocking leads to a dilute system of Fermions that in zeroth order, can be approximated as completely independent. The many body system where each nucleon interacts with its closest neighbors is replaced by a collection of one-body equations where each particle interacts with a mean field generated by the averaged potential of all nucleons. This framework is called the independent particle model (IPM) [22, 23].

The IPM had immediate successes. Because nucleons usually pair to $J = 0$, the IPM accurately described the spins and parities of many odd-A nuclei in terms of the last unpaired nucleon, and as mentioned above, it also described the existence and location of magic numbers observed in stable nuclei (see Figure 1.3). Unfortunately, there were also clear failures that indicated the need to include effects beyond the simple IPM mean-field model. The IPM could not describe the rotational and vibrational behavior of nuclei, including signature rotational and vibrational bands [10, 17].

Aa. Bohr, Rainwater, Mottelson, and Nilsson tried to merge these separate phenomena into one model in two ways: the deformed shell model where the individual nucleons move in a deformed potential caused by the true physical deformation of the nucleus

and the particle plus rotor model where a few valence nucleons are coupled to a rotor representing the internal behavior of the remaining nucleons. These "unified models" of a particle moving in a deformed mean field are an extension of the IPM. The effect of these deformed potentials can be seen in Nilsson diagrams [62] which plot the energies of the single-particle levels with respect to the deformation of the nucleus.

The unified model shares one critical similarity with the IPM. The nucleons still move in a mean field. There are no two-body interactions or higher order terms (three-body, etc.). The desire to include these experimentally observed components of the nuclear interaction led theorists to develop the modern Configuration-Interaction Shell Model (CI), henceforth simply called 'shell model'. The shell model is predicated on the idea that calculations using a purely microscopic, two-body interaction can predict the full range of nuclear phenomena, including collective behavior. An example of this connection was shown in 1958 by Elliot who outlined the microscopic origin of rotational motion in Refs. [63, 64].

Although the concept is simple, the problem is difficult in practice [65]. The shell model has the following characteristics:

1. *Many-body problem*. In a nucleus composed A nucleons, each nucleon can interact with $A-1$ partners. This interaction can occur between neutrons ($\nu\nu$), protons ($\pi\pi$), or between a proton and a neutron ($\pi\nu$), in principle for all available orbitals.

2. *The nuclear interaction is very complicated*. See Section 1.2.2 for an overview of the bare nucleon-nucleon force. Higher-order aspects of the force are still unknown.

3. *The system is mesoscopic*. The nucleon number is too small to use statistical or thermodynamical approximations but too large to be completely computationally tractable. Approximation methods must be used.

4. *The interaction is both microscopic and effective*. On microscopic: we begin with the individual proton and neutron degrees of freedom, as opposed to a collective

aggregate model. On effective: each nucleon interacts within the medium of the nuclear matter, which modifies the bare nucleon-nucleon (NN) interaction. Effective interactions are largely derived from fits to experimental data.

The introduction of the residual (remaining two-body interaction after the subtraction of the dominant mean-field strength) two-body interaction creates correlations between different proton and neutron orbitals (off-diagonal interaction matrix elements) and causes the mixing of Slater determinants associated with different possible configurations of protons and neutrons within the model space. The result are occupation numbers for a single nucleon that vary between 0 and 1. Through this *configuration mixing*, effects that are outside of the traditional naive IPM, like deformation and other collective behavior, are describable. CI codes include NuShell and NuShellX [66], ANTOINE [67], MSHELL [68], REDSTICK [69], and OXBASH [70]. A review of the basic steps in a shell model calculation follow. For a more thorough coverage see one of the many reviews on the subject [65, 71–74].

3.2.2 Basic Shell-Model Procedure

Nuclear shell model codes, through the solution of the time-independent Schrödinger equation (TISE), provide the energies and wavefunctions (used to calculate other observables) of the low-lying states in nuclei. Calculations usually involve the following choices:

1. *Choice of a model space*: It is currently computationally impossible to calculate the properties of medium to large mass nuclei ($A \gtrsim 12$) from the *ab initio*, nucleon degree of freedom[1]. A decision must be made: which proton and neutron orbitals are important to describe the observed experimental phenomena. The selected truncated set of orbitals forms the *valance space* (the core and valance space form the complete

[1]Success up to $A = 12$, starting with the bare NN interaction, has been achieved with Green's Function Monte Carlo (GFMC) [75–77] and *ab initio* no core [78, 79] shell model calculations using accurate NN potentials [2–4].

model space). For both the pickup and knockout experiments, covered in Chapters 5 and 6, an fp-shell ($1f_{7/2}$, $2p_{3/2}$, $1f_{5/2}$ and $2p_{1/2}$ orbitals) valance space with ^{48}Ca and ^{40}Ca cores was used. See the indicated chapters for specific details.

2. *Choice of an effective interaction*: The effective interaction, in the form of single-particle energies and two-body matrix elements (see Section 3.2.3), define the interactions between the particles and holes within a particular model space. Matrix elements for or of effective interactions appropriate for the same model space, e.g. GXPF1A and KB3G, will differ, and the choice of an effective interaction may depend on the particular mass region and physical phenomena one is interested in describing.

3. *Choice of a shell model code*: Shell model codes execute the complex matrix algebra (diagonalization of matrices of up to 10^{11} elements) and the configuration mixing associated with the solution of the many-body Schrödinger equation. There are many shell model codes available. OXBASH and NuShellX were used for the calculation of energies and spectroscopic factors for the pickup and knockout experiments, respectively. There are notable differences between codes, including the choice of a coupling scheme. To form states with good total angular momenta, J, and projection, M, quantum numbers, the angular momentum j_i and projection m_i of the active protons and neutrons within the model space must be coupled. There are several methods of doing so: the M-scheme [67–69], J coupled scheme, and the JT coupled scheme [66, 70].

4. *Comparison to experiment*: Calculated level energies can be directly compared to experiment, and the wavefunctions, using renormalized operators (operators renormalized to the model space), can be used to calculate other nuclear properties, like electromagnetic transition rates and spectroscopic factors.

3.2.3 Nuclear Hamiltonian

The solution of the nuclear many-body problem begins with the time-independent Schrödinger equation

$$\hat{H}\Psi = E\Psi \longrightarrow (\hat{T} + \hat{V})\Psi = E\Psi \tag{3.1}$$

where

$$\hat{H} = \sum_{i=1}^{A} \frac{\boldsymbol{p}_i^2}{2m} + \sum_{i\neq k}^{A} V_{ik}(|\boldsymbol{r}_i - \boldsymbol{r}_k|) \tag{3.2}$$

Starting with Equation 3.2, we can separate the potential into a principal single-particle term (independent motion in a mean-field) and a residual two-body term[2]

$$\hat{H} = \sum_{i=1}^{A}\left[\frac{\boldsymbol{p}_i^2}{2m} + U(|\boldsymbol{r}_i|)\right] + \left[\sum_{i\neq k}^{A} V_{ik}(|\boldsymbol{r}_i - \boldsymbol{r}_k|) - \sum_{i=1}^{A} U(|\boldsymbol{r}_i|)\right] = \hat{H}_0 + \hat{V}_{\text{residual}} \tag{3.3}$$

Under the IPM approximation, the residual interaction $\hat{V}_{\text{residual}}$ is zero $\hat{H}_{\text{IPM}} \approx \hat{H}_0$, and the full wave function is the product of the wave functions of the individual nucleons ϕ_i. A harmonic oscillator (HO) basis is chosen for the nucleon wave functions for several reasons: they have an analytic form (i.e. $\phi(\boldsymbol{r_k}) = [\psi_{n\ell}^{\text{H.O.}}(r_k) \otimes Y_{\ell m}(\theta_k, \phi_k)]_j$); HO wave functions are the natural framework for annihilation and creation operators and the Fock-space basis (basis with occupational number representation); and they permit the many-body Hamiltonian of Equation 3.3 to be be cleanly separated into intrinsic and center-of-mass terms [65, 80].

For an A nucleon system,

$$\Psi_{1,2,\cdots,A}^{\text{sym}} = \prod_{k=1}^{A} \phi_k(\boldsymbol{r}_k), \tag{3.4}$$

where the index k indicates occupancy of the nucleon in any of the N available orbitals in the valence space and ϕ_k is appropriate the single-particle wave function. Because nucleons are Fermions, the wave function must be properly anti-symmetrized. This is

[2]Although this method is used by B.A. Brown and Rae in their shell model codes, an alternative method of multipole decomposition exists, see Refs. [65, 72, 73] for details.

represented by a single Slater determinant

$$\Psi^{\text{asym}}_{1,2,\cdots,A} = \begin{vmatrix} \phi_1(\boldsymbol{r}_1) & \phi_1(\boldsymbol{r}_2) & \cdots & \phi_1(\boldsymbol{r}_A) \\ \phi_2(\boldsymbol{r}_1) & \phi_2(\boldsymbol{r}_2) & \cdots & \phi_2(\boldsymbol{r}_A) \\ \vdots & \vdots & \ddots & \vdots \\ \phi_A(\boldsymbol{r}_1) & \phi_A(\boldsymbol{r}_2) & \cdots & \phi_A(\boldsymbol{r}_A) \end{vmatrix} \tag{3.5}$$

The presence of the residual interaction $\hat{V}_{\text{resid.}}$ causes mixing of the different Slater determinants, a process called *configuration mixing*, and as a result, single-nucleon occupancies will vary between 0 and 1 (or for a complete orbital, occupancies will range between 0 and $2J+1$). The final wave function with the residual interaction included is

$$\Psi^{\text{assym}}_{1,2,\cdots,A} = \sum_j C_j \Psi^{\text{assym}}_j(1,2,\cdots,A,\cdots,N). \tag{3.6}$$

The sum is over all possible configurations of nucleons that preserve the conserved quantities as given by the coupling scheme. The goal of a CI code is to determine this complete wavefunction, with coefficients C_j, and the associated energies.

The use of a harmonic oscillator basis introduces a center-of-mass (COM) energy that gives the system a non-zero energy. These states are called *spurious states* and must be removed, usually by adding a center of mass Hamiltonian [81]. With the subtraction of the COM motion, the Hamiltonian of Equation 3.3, this time in the notation of second quantization (particle creation and annihilation operators), can be written as

$$\hat{H} = \sum_j \epsilon_j a^\dagger_j a_j + \sum_{j_1 j_2 j_1' j_2'} \langle j_1' j_2' | \hat{V}_{\text{resid.}} | j_1 j_2 \rangle_{JT} a^\dagger_{j_1}, a^\dagger_{j_2}, a_{j_1} a_{j_2}, \tag{3.7}$$

where total angular momentum J and isospin T are good quantum numbers. Pairs of nucleons are created on orbitals j_1' and j_2' and annihilated on orbits j_1 and j_2.

The parameter ϵ_j of Equation 3.7 is the *single particle energy* (SPE) of the state j. It represents the total energy of the proton or neutron in a mean field. SPEs can be experimentally estimated from the difference in binding energies between A and $A \pm 1$ nuclei.

The second term $V_{j_1' j_2' j_1 j_2} \equiv \langle j_1' j_2' | \hat{V}_{\text{resid.}} | j_1 j_2 \rangle_{JT}$ is the *two-body matrix element* (TBME). The TBME represents the residual attraction between the nucleons. An effective interaction is completely determined by its SPEs and TBMEs. Popular effective interactions such as USD [53], GXPF1 [56], and KB3G [73], have slightly different SPEs and TBMEs depending upon the valence space and the experimental data from which the matrix elements are derived.

3.2.4 Model Space and Truncation

The size of the matrices associated with mass $A \geq 12$ nuclei becomes computationally intractable when we consider the combination of each nucleon interacting with every other nucleon. The size of the matrices grows exponentially with the inclusion of new orbitals in the shell model valance space up to the modern limit of $\sim 10^{11}$ [82]. If we are interested in low-lying states, particle or hole states near the Fermi surface may be sufficient to describe a nucleus' low-lying properties. This allows us to treat the other nucleons as an inert core and fold in the core effects (e.g. the binding energy between the active nucleons and the core) into the Hamiltonian of the valence nucleons. By ignoring the interaction of the nucleons in the core with the valence nucleons included the valence space, the Hamiltonian must be modified. This process of adjusting the Hamiltonian to the valence space is called *renormalization*.

The choice of a model space is important and there are trade-offs to consider. With more terms, in general, one gets more complete results, including effects that do not manifest within a more limiting valence space. See, for example, the intruder states of ^{32}Mg and neighboring nuclei [26, 28, 52, 55, 83]. Large valence spaces, unfortunately, dramatically increase the computational complexity and the complexity of the effective interaction. The largest basis, the M-scheme, explodes exponentially as

$$D_T = \binom{D_\pi}{n_\pi} \cdot \binom{D_\nu}{n_\nu}. \tag{3.8}$$

$D_{\pi,\nu}$ is the total occupancy of the orbitals in the valence space, and $n_{\pi,\nu}$ are the number

of nucleons filling those orbitals for protons, π, and neutrons, ν, respectively. Maximum matrix size occurs when $n_{\pi,\nu} = \frac{1}{2}D_{\nu\pi}$. For the p-shell, which includes the $1p_{3/2}$ and $1p_{1/2}$ orbitals and has 6 holes available for both the protons and neutrons, the maximum matrix size is 400 (e.g. ^{10}B). For the sd shell with the $1d_{5/2}$, $2s_{1/2}$, and $1d_{3/2}$ orbitals, the maximum matrix size is approaching 1 million (853776). For the fp shell with the $1f_{7/2}$, $2p_{3/2}$, $1f_{5/2}$ and $2p_{1/2}$ orbitals, the maximum matrix size is 3.4×10^6. Given the exposition of matrix sizes with the inclusion of additional orbitals, it is evident why a full ab initio calculation that includes all orbitals up through the fp space is impossible.

The large spacing between orbitals that occur at the magic numbers make $N, Z =$ 2, 8, 20, 28, 50, 82, and 126 natural places for model space truncation. The large shell gaps minimize the off-diagonal matrix elements. The strongest correlations occur when the wave functions strongly overlap, i.e. when the orbitals are close in energy and share certain quantum numbers. Other effects, as mentioned above, that originate from nucleons outside the model space, can be folded into the valence-space nucleon-nucleon interactions. Consider, for example ^{53}Sc. ^{53}Sc has 21 protons and 32 neutrons and thus ^{48}Ca with $N = 28$ and $Z = 20$ is a natural choice for an inert core. An OXBASH calculation [81] using the GXPF1 [56] effective interaction, was used to calculate the level scheme (for ^{53}Sc) and spectroscopic factors for the ^{9}Be(^{54}Ti, ^{53}Sc + γ)X reaction (see Section5.4). Calculations used an fp model space and an inert ^{48}Ca core. For the neutron rich isotopes, ^{48}Cr, ^{49}Mn, and ^{50}Fe, and their associated reactions[3],the spectroscopic factors and energies were calculated using the GXPF1A effective interaction [58] and a ^{40}Ca core. See Figure 3.1 for a cartoon representation of the ^{53}Sc model space and Figure 3.2 for the dimension of several model spaces with respect to the nuclear chart.

[3] ^{9}Be(^{48}Cr, ^{49}Mn + γ)X, ^{12}C(^{48}Cr, ^{49}Mn + γ)X, ^{9}Be(^{49}Mn, ^{50}Fe + γ)X, ^{12}C(^{49}Mn, ^{50}Fe + γ)X, ^{9}Be(^{50}Fe, ^{51}Co + γ)X, and ^{12}C(^{50}Fe, ^{51}Co + γ)X

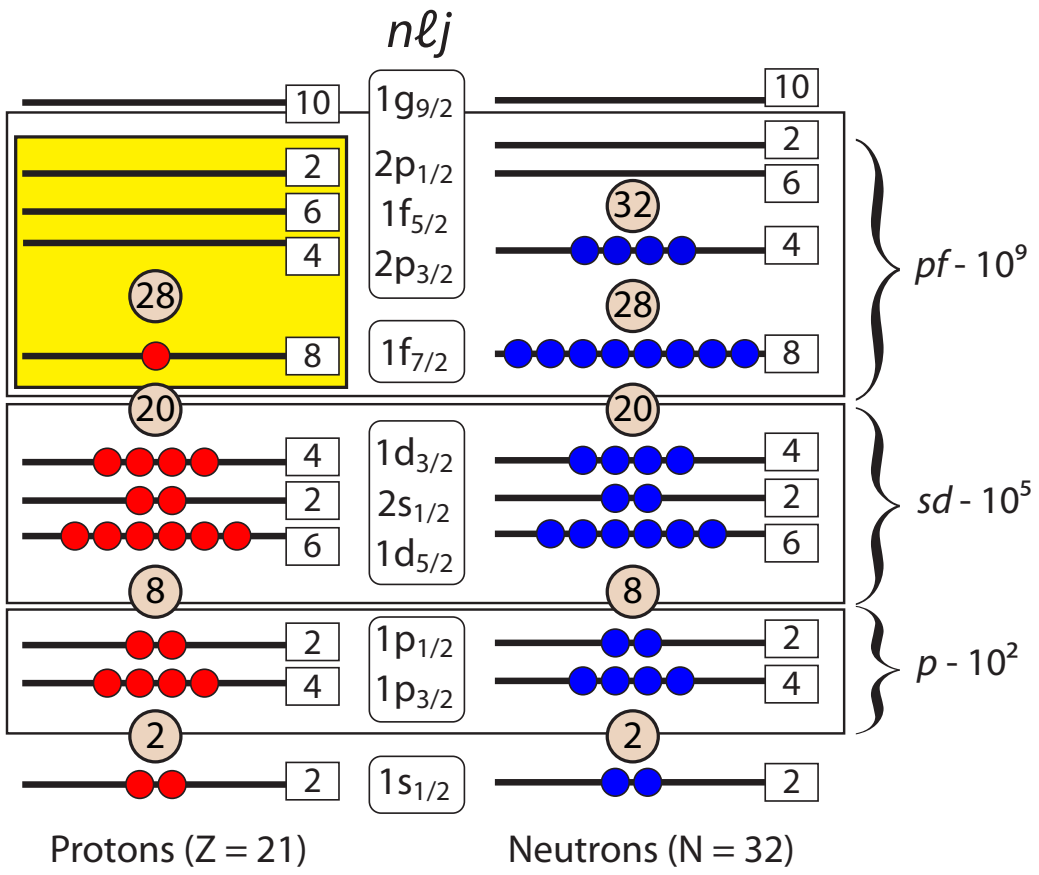

Figure 3.1: Valence space (yellow highlight) used in the calculation of ^{53}Sc excited states and spectroscopic factors for the ^{9}Be(^{54}Ti, ^{53}Sc + γ)X reaction. The matrix dimensions and names for common valence spaces are shown. Magic numbers for the neutrons and protons (including the emergent $N = 32$ shell gap) are independently listed (tan circles). The orbitals in the $pf_{5/2}g_{9/2}$ valence space are not shown (see also Figure 3.2).

3.2.5 Model Space Limitations

A given model space can only handle phenomena associated with the configuration of nucleons within that model space. Occasionally, behavior emerges that is caused by processes that involve the promotion of nucleons into or out of the model space. These states are called *intruder states* and they are usually occur at energies close to the excitation energy of the first excited state in a closed shell [71]. For example in ^{53}Sc such intruder states may occur near the energy of the 2^+_1 state in ^{48}Ca (E_x = 3382 keV). Sometimes, however, a weakening shell gap and increase in NN correlations can lead to cases where

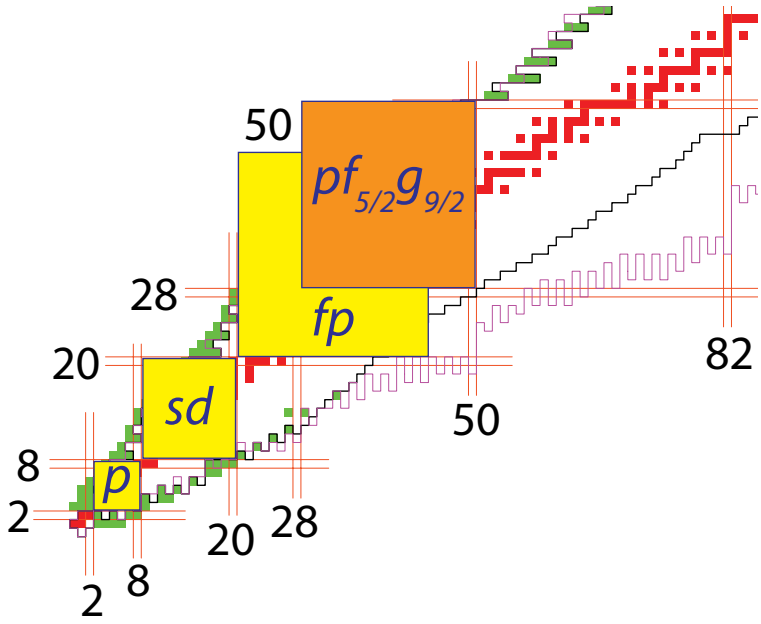

Figure 3.2: Nuclear chart showing the size and applicable mass range of valance spaces used in shell model calculations: the p, sd, fp and new $pf_{5/2}g_{9/2}$ valance spaces are shown.

these intruder states can occur at lower energies [71]. The $1/2^-$ state at 110 keV in ^{19}F or the $1/2^+$ state in ^{11}Be are intruder states. Intruder states can only be handled by increasing the model space and their identification can indicate the limitations of a model space and a need for cross shell interactions. Chapter 5 covers the observation of positive-parity intruder states in the low-lying spectrum of ^{53}Sc and the implications of their discovery on the choice of valance spaces and cross shell interactions.

3.2.6 Shell Model Spectroscopic Factors

Using their calculated wavefunctions, shell model codes can provide spectroscopic factors. For the single-nucleon pickup or knockout reactions, these spectroscopic factors are defined as

$$S_j^{\text{knock.}} = \frac{1}{2J_i+1}|\langle\Phi_i^A|a_k^\dagger|\Phi_f^{A-1}\rangle|^2 \tag{3.9}$$

$$S_j^{\text{pick.}} = \frac{1}{2J_i+1}|\langle\Phi_{\text{i}}^A|a_k|\Phi_{\text{f}}^{A+1}\rangle|^2, \tag{3.10}$$

where by convention the factor $2J_i + 1$ is associated with the mass A projectile. Φ_i is the internal wave function of the projectile. Φ_f is the internal wavefunction of the projectile-like residue after the addition or removal of a nucleon, depending upon the reaction. $\hat{a}_k^\dagger$ and $\hat{a}_k$ are the creation and annihilation operators for the creation or removal of a nucleon with quantum numbers $k \equiv (nj\ell m)$. Spectroscopic factors provide the parentage of the initial ground state with respect to a specific final state and thus provide information about the occupation of orbitals in the A projectile ground state.

The cross section for the removal of a nucleon $\sigma_{\text{knock.}}$ emerges from the reduced matrix element

$$\begin{aligned}
\sigma_{\text{knock.}} &\propto \frac{1}{2J_i+1} \sum_{M_f, M_i, m} |\langle \Phi_i^A | a_k^\dagger | \Phi_f^{A-1} \rangle|^2 \\
&= \sum_{M_i, M_f, m} \begin{pmatrix} J_f & j & J_i \\ -M_f & m & M_i \end{pmatrix} \begin{pmatrix} J_f & J & J_i \\ -M_f & m & M_i \end{pmatrix} |\langle \Phi_i^A | a_k^\dagger | \Phi_f^{A-1} \rangle|^2 \qquad (3.11) \\
&= \frac{1}{2J_i+1} |\langle \Phi_i^A | a_k^\dagger | \Phi_f^{A-1} \rangle|^2 = S_{\text{knock.}}
\end{aligned}$$

The proportionality factor between the spectroscopic factor S and the knockout cross section σ_{knock} is the single-particle cross section, the reaction probability assuming $S = 1$ (see Equation 3.17). Notice the explicit sum over final states M_f and average over initial states M_i. The cross section for the pickup reaction $\sigma_{\text{pick.}}$ follows similar algebra.

A specific example may be more illustrative. Consider the ^{9}Be(^{54}Ti, ^{53}Sc$+\gamma$)X reaction, where a proton is removed from the ^{54}Ti ground state leaving the ^{53}Sc heavy residue in one of many states, including the ground state. The final states populated depend on the quantum numbers (the orbital) of the removed proton. If a proton is removed from the ^{54}Ti $\pi(1f_{7/2})$ orbital we expect, in the absence of fragmentation of strength from the $f_{7/2}$ orbital, to populate the ^{53}Sc $7/2^-_{\text{g.s.}}$ ground state. The magnitude of the overlap scales with occupancy. If there are two protons in the proton $f_{7/2}$ orbital for the ^{54}Ti ground state, we expect a large spectroscopic factor of nearly 2 to the ^{53}Sc ground state. If there are no protons in the $\pi(1f_{7/2})$ orbital, we expect a negligible overlap with

the ^{53}Sc ground state and a $\pi f_{7/2}$ spectroscopic factor of nearly zero. Because isospin is a conserved quantum number, and because, as a vector, it has similar couping algebra as angular momentum, spectroscopic factors are usually provided with the appropriate Clebsch-Gordan isospin-coupling coefficient as C^2S.

The number of available particle-like and hole-like states for an orbital with quantum numbers $k \equiv (n\ell j)$ is clearly related to the orbital's maximum occupancy $2j+1$. Because knockout and pickup reactions probe particle-like and hole-like states, the relationship between particles, holes, and occupancy for orbital k is observed in their spectroscopic factors. This relationship is called a *sum rule*, and it takes the following form:

$$\sum_{m-} S_{\text{knock}} + \sum_{m+} (2J_f + 1) S_{\text{pick}} = 2j + 1 \tag{3.12}$$

The sums are over all states in the $A-1$ nucleus ($m-$) and the $A+1$ nucleus ($m+$). The additional $2J_f+1$ factor in front of the pickup spectroscopic factor S_{pick} accounts for the difference in M state averaging.

If spectroscopic factors are calculated using a harmonic oscillator basis (wave functions) moving relative to a fixed point rather than the with respect to the center-of-mass (COM) motion of the A nucleons rather than the $A-1$ (knockout) or $A+1$ (pickup) nucleons, a center-of-mass (COM) correction [84] is required. These corrections $\mathcal{C}_{\text{knock.}}$ and $\mathcal{C}_{\text{pick.}}$ take the form

$$\mathcal{C}_{\text{knock.}} = \left(\frac{A}{A-1}\right)^N \qquad \mathcal{C}_{\text{strip.}} = \left(\frac{A}{A+1}\right)^N, \tag{3.13}$$

where N is the major oscillator quantum number ($N = n + \ell$ where n by convention, starts at 0). This correction was necessary for both OXBASH (knockout) and NuShellX (pickup) calculations.

With configuration mixing, the wavefunction is the combination of several Slater determinants rather than one, and therefore the occupancy of orbitals is usually never a discrete integer. So besides providing information on the occupancy of orbitals, spectroscopic factors provide a measure of the purity of the single particle state. Experimental

observables that relate to spectroscopic factors (e.g. partial cross sections) are some of the most fundamental tests of shell-model wave functions. Over the last decade, single nucleon knockout reactions have been proven as an effective method for quantifying spectroscopic strength in exotic nuclei [85], and more recent work by Gade et al. [60, 61], showed single-nucleon pickup reactions can also provide similar qualitative information.

3.3 Reaction Theory

In a nuclear reaction a nucleus is subjected to an external field (electromagnetic or nuclear) created by another nucleus, and the response of the nucleus to the external field provides information on both the nucleus's constituent protons and neutrons (shell structure) and the interaction between the nucleus and its interaction partner (reaction theory). Reaction theory and shell model calculations can be combined in a straight-forward way to predict directly observable experimental quantities: partial and inclusive cross sections.

To gain information about the single-particle structure, a small wavelength probe must be used. Long-wavelength, low-energy probes only tell us about the strength of the interaction. Short-wavelength, high-energy probes are needed to provide a detailed map of the region of interaction. Ideally, the interaction should only involve the single-particle states (nucleons) we want to probe. A class of reactions called *direct reactions* satisfies these restraints. Direct reactions are characterized by short time-scales ($\tau \sim 10^{-22}$ sec) and single-step transitions from initial to final states. In inverse-kinematics these constraints are typically satisfied by intermediate (or higher) energy projectiles and grazing reactions. Both single nucleon knockout (Figure 3.3) and proton pickup reactions (Figure 3.4) are direct reactions.

Pickup and knockout reactions reactions access single-particle structure either through the population of single hole-states through the removal of a nucleon from the projectile (knockout reactions) or through the population of single-particle states through the addition of a nucleon to the projectile (pickup reactions). Knockout reactions allow a

determination of partial cross sections (which are connected to spectroscopic factors and thus occupation numbers) [85, 86], and recent evidence suggests that single nucleon pickup reactions may provide similar information, so far on a more qualitative basis [60, 61].

There are two possible notations used to describe a nuclear reaction depending on the reaction kinematics. A reaction in *regular kinematics* uses a target made from the isotope of interest and the beam is used to probe the target. These reactions are written in the form

$$P_i(T_i, T_f)P_f \tag{3.14}$$

where $P_{i,f}$ and $T_{i,f}$ are the initial and final states of the target and projectile.

The first nuclear reactions were in regular kinematics (see Appendix B) and today, established single-nucleon transfer techniques using light beams (e.g. deuteron d, tritium t, or ^{3}He beams) are used for obtaining spectroscopic information on stable target nuclei. In regular-kinematics transfer, a nucleon is transfered from the light projectile to the target, and based on the differential cross sections, angular distribution and energy of the light reaction residue, information on the occupancy, orbital angular momentum, and energy of states in the target nuclei are obtained. For example, in the $d(^{50}\mathrm{Ti}, ^{49}\mathrm{Sc})^3\mathrm{He}$ reaction of Ref. [87], a deuteron, d, accelerated to 52 MeV, impinged on a ^{50}Ti target. The deuteron picked up a proton, leaving the target nucleus one proton lighter as ^{49}Sc. Through the measurement of the cross section, energy, and angular distribution of the ^{3}He nuclei, information is inferred about the occupancy of states in ^{50}Ti.

In contrast, in an *inverse kinematics* reaction, the projectile is the species of interest and the target is used as a probe. Such reactions are written in the form

$$T_i(P_i, P_f)T_f, \tag{3.15}$$

e.g. $^9\mathrm{Be}(^{54}\mathrm{Ti}, ^{53}\mathrm{Sc} + \gamma)\mathrm{X}$ and $^9\mathrm{Be}(^{48}\mathrm{Cr}, ^{49}\mathrm{Mn} + \gamma)\mathrm{X}$. In an inverse-kinematics knockout or pickup reaction (see Figures 3.3 and 3.4), a short-lived nucleus, moving at velocity of about $v \sim 0.3\,\mathrm{c}$ interacts with a light target, typically ^{9}Be. The more exotic the isotope,

as judged by its neutron-proton asymmetry, the shorter its half-life. It is impossible to make targets out of species with half-lives shorter than a few days, but inverse kinematics reactions allow one to study nuclei with short half-lives. Facilities, such as the NSCL, that can produce beams of nuclei with short half-lives, have only emerged within the last few decades. This work concentrates on the modern inverse-kinematics nucleon removal and addition reactions with fast beams. Henceforth, unless qualified, *knockout* and *pickup* will refer to the inverse-kinematics techniques.

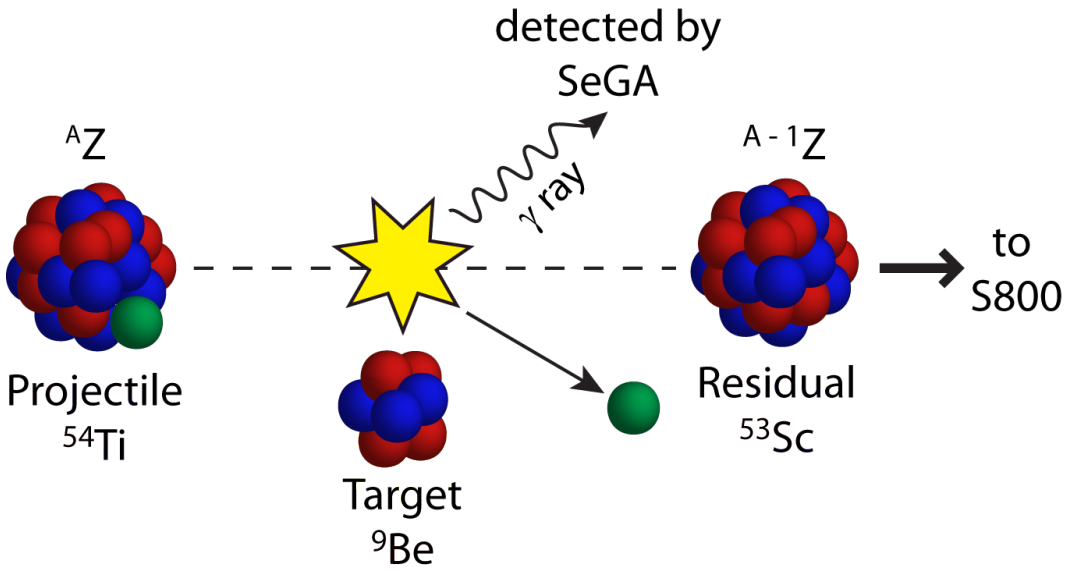

Figure 3.3: Knockout reaction schematic for the example of the ^{9}Be(^{54}Ti, ^{53}Sc + γ)X reaction. A nucleon from the incoming projectile of mass A (^{A}Z) is removed (green) creating a final heavy projectile (residue) of mass $A-1$ ($^{A-1}$Z or $^{A-1}$(Z-1)). The removed nucleon is either absorbed by the target (stripping) or, as seen in the figure, continues with the same velocity as the incoming beam (diffraction). Both the residue and its de-excitation γ rays are detected. The final state is a three-body system.

The knockout and pickup reactions discussed here were developed for the specific experimental constraints of the National Superconducting Cyclotron Facility (NSCL) Coupled Cyclotron Facility (CCF) [88, 89]. Nuclei are short lived: we use fast beams in inverse kinematics. It is much easier to detect the "spectator", the mass $A-1$ residue left after the addition or subtraction of a particle: we relate the properties of the residual nucleus to the properties of the transfered nucleon. The high beam velocity compresses the angular

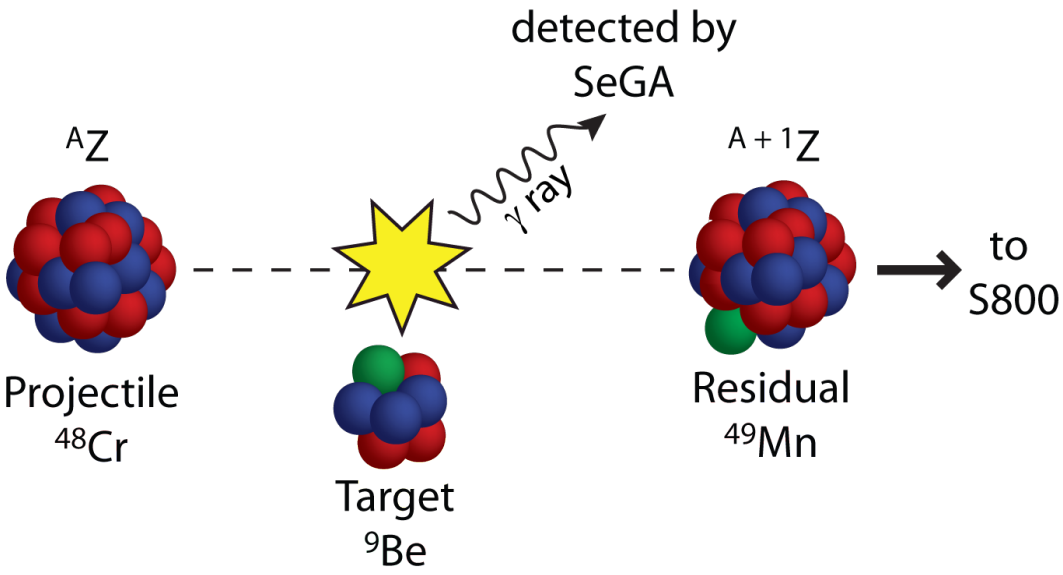

Figure 3.4: Pickup reaction schematic for the example of the ^{9}Be(^{48}Cr, ^{49}Mn+γ)X reaction. An incoming projectile of mass A (^{A}Z) picks up a nucleon from the target, creating a final heavy projectile with mass A ($^{A+1}$Z or $^{A+1}$(Z+1)). The final projectile and its de-excitation γ rays are detected. The final state is a two-body system.

distribution of the reaction products and the γ rays emitted in flight in a forward cone: we use a magnetic spectrograph that typically accepts the full momentum width of the residue and a γ ray spectrometer (see Section 4.4) that measures both the energy and the angle of the emitted γ ray in the lab frame. The γ ray spectrometer, through the measurement of the angle of γ ray emission by the excited residue, reconstructs the energy of the γ ray energy to the projectile's rest frame.

Despite the switch from regular to inverse kinematics, knockout and pickup reactions can provide similar information to classic transfer reactions. Through the detection of γ rays emitted by the residue in flight and the identification of the corresponding transitions in the Doppler-reconstructed, residue rest-frame spectrum, final states in the residue are identified. From the measurement of partial cross sections to the populated states in the residue, experimental spectroscopic factors can be extracted in comparison to reaction theory, and for knockout reactions, the shape of the parallel momentum distribution of the residues offers information on the orbital angular momentum of the removed nucleon.

3.4 Knockout reactions

The kinematics of a knockout reaction can be rewritten in a slightly modified form of Equation 3.15 to explicitly highlight the critical components of the reaction

$$P\,(=c_i+x)+T_i \longrightarrow c_f+T_f \tag{3.16}$$

The incoming projectile $P=c_i+x$, written in terms of a spectator core c and participating nucleon x, loses its nucleon x in a direct, single-step interaction with the target T (stripping or diffraction). The core c is left in a particular final state c_f. The removed nucleon x is not detected. The incoming projectiles, assumed to be in its ground state, are identified event-by-event through a time-of-flight difference. The orbital angular momentum ℓ of the removed nucleon is inferred from the measured longitudinal momentum distribution of the ensemble of projectile-like one-nucleon knockout residues. The final state of the projectile-like residue is determined through γ ray spectroscopy. Knockout reactions are a proven and established technique for tracking single-particle structure and probing nuclear phenomena [59, 90]. Two representative examples follow.

Knockout reactions probed the radial extent and wave function of "halo nuclei," nuclei where one or more neutrons (e.g. in ^{11}Be, ^{11}Li, or ^{6}He) or protons (e.g. in ^{8}B or ^{17}B) tunnel through the nuclear potential formed by a well-defined core to form an extended, diffuse matter distribution [91, 92]. The large spatial extent of the "halo" nucleus ^{11}Be was qualified by the narrow momentum distribution of the ^{10}Be core following the removal of the valance nucleon from ^{11}Be in a knockout reaction [93]. The ^{11}Be ground state wavefunction was quantified in a knockout reaction, i.e. ^{9}Be(^{11}Be, ^{10}Be + γ)X, through the additional tagging and identification of final states using γ ray spectroscopy with a position-sensitive NaI array [94].

Knockout reactions helped delineate the island of inversion. The composition of the ground state wavefunctions of ^{32}Mg, ^{30}Mg, and ^{28}Ne was quantified through the knockout reactions ^{9}Be(^{32}Mg, ^{31}Mg + γ)X, ^{9}Be(^{30}Mg, ^{29}Mg + γ)X [95], and ^{9}Be(^{28}Ne, ^{27}Ne + γ)X

[55]. A gradual onset of the intruder ground-state configurations was shown, further expanding the early predicted boundary of $10 \leq Z \leq 12$ and $20 \leq N \leq 22$ [52]. For further successes of knockout reactions, including the quantification of the effect of correlations, both short- and long-range, and the resultant quenching of spectroscopic strength, see Refs. [47, 59, 90, 96]

3.4.1 Theoretical Cross Sections

As first shown in Section 3.2.6 in the discussion of spectroscopic factors, one can break down the total cross section into two separate parts: a component that describes the reaction theory (single-particle cross section) and a component that describes the nuclear structure (spectroscopic factor) [47, 96]. The single-particle cross section quantifies the probability that the removal of a single nucleon (spectroscopic factor of $S = 1$) from a specific orbital in the initial mass A projectile will lead to a particular final state in the mass $A-1$ residue. The total cross section, because it has to scale with the occupancy of the orbital, includes multiplication by a spectroscopic factor. The final form is written as [59, 90, 97, 98]

$$\sigma(I^\pi) = \sum_j C^2S(j, I^\pi)\, \sigma_{\text{sp}}\left(j, S_{\nu,\pi} + E_x(I^\pi)\right). \tag{3.17}$$

Whenever the spectroscopic factors are calculated using Harmonic oscillator wave functions about a fixed center, as was true for both the OXBASH and NuShellX codes used to calculate the spectroscopic factors for the knockout and pickup analyses of Chapters 5 and 6, the COM correction of Equation 3.13 must be applied. Equation 3.17, with the addition of the COM correction, is written as

$$\sigma(I^\pi) = \sum_j \left(\frac{A}{A-1}\right)^N C^2S(j, I^\pi)\, \sigma_{\text{sp}}\left(j, S_{\nu,\pi} + E_x(I^\pi)\right) \tag{3.18}$$

The sum in Equations 3.17 and 3.18 is over all angular momenta j of the removed nucleon that can couple the spin and parity I^π of the residue to the spin and parity of the incident projectile J^π. E_x is the excitation energy of the residue and S_π and S_ν are the proton and

neutron separation energies of the incident projectile[4]. If a proton is removed $S_{\pi,\nu} \equiv S_\pi$ and if a neutron is removed $S_{\pi,\nu} \equiv S_\nu$. N is the major harmonic oscillator quantum number.

For an even-even incident projectile with a 0^+ ground state, the angular momentum coupling is especially simple. The total angular momentum and parity I^π of the residue has the same total angular momentum and parity j^π of the removed nucleon. The relationship between the population of specific states with quantum numbers I^π and the removal of a nucleon with quantum numbers j^π is the fundamental spectroscopic background of knockout reactions (see Figure 3.5). If the complete strength (summed partial cross sections) from the ground state in the projectile is accounted for—particularly for cases where the spectroscopic strength is spread over several final states in the residue, a phenomena called *fragmentation*—experimental spectroscopic factors can be extracted with the aid of reaction theory (single-particle cross sections)[5] (see Equation 3.18).

3.4.2 Single Particle Cross Sections

Single-particle cross sections are broken down into three components

$$\sigma_{\text{sp}} = \sigma_{\text{strip}} + \sigma_{\text{diff}} + \sigma_{\text{Coul}}. \tag{3.19}$$

The Coulomb component is negligible for light, low-Z targets like ^{9}Be[6] and the reaction cross section can be reliably calculated from just the stripping and diffractive components. In stripping, the removed nucleon interacts at most inelastically with the target, exciting

[4]The separation energies are written as S_π and S_ν instead of the more traditional S_n and S_p to avoid confusion with the nucleon and core scattering matrices $\mathcal{S}_n$ and $\mathcal{S}_c$

[5]Spectroscopic factors cannot be directly extracted from experiment; only inclusive and partial cross sections can.

[6]Using a light, ^{9}Be target has several advantages: the coulomb component is negligible, and the highly-absorptive residue-target interaction (^{9}Be has no bound excited states), combined with the experimental observation of the residue (the residue must survive), ensures a peripheral collision [59].

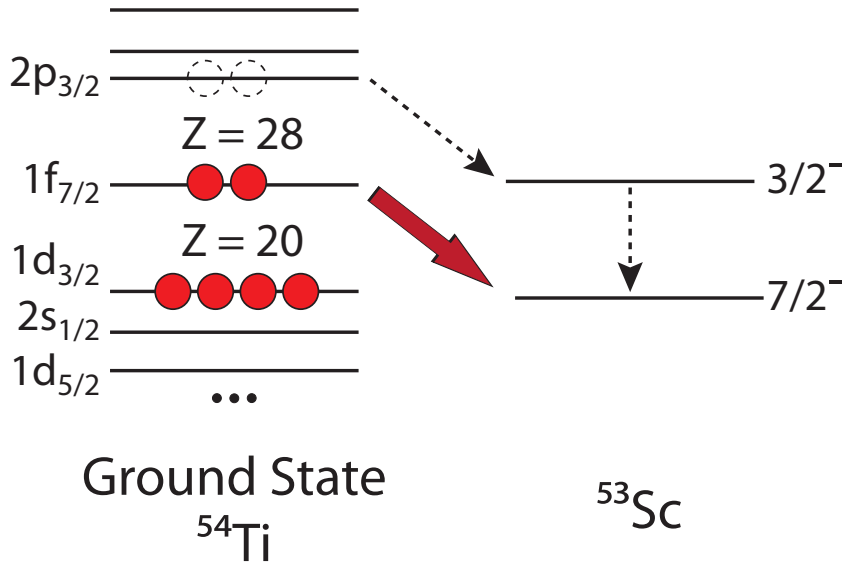

Figure 3.5: Population of final states in the example ^{9}Be(^{54}Ti, ^{53}Sc+γ)X knockout reaction. For even-even nuclei with zero total angular momentum $I = 0$ (the ground state) the removal of a nucleon with quantum numbers j^{π} populates final states with the same total angular momentum I^{π}. For example, the removal of a $\pi(f_{7/2})$ proton from the ground state in ^{54}Ti populates the $7/2^{-}_{\text{g.s.}}$ ground and possibly higher-lying $f_{7/2}$ fragments in ^{53}Sc. The removal of a $p_{3/2}$ proton may populate one or many $3/2^{-}$ states in ^{52}Sc. If the strength to the $7/2^{-}$ and $3/2^{-}$ states can be quantified through the measurement of their partial cross sections, information about the wavefunction of ^{54}Ti can be extracted. In the case above, comparatively large partial cross section to the ground state of ^{53}Sc in comparison to the partial cross section to the population of the first $3/2^{-}$ state (assuming minimal fragmentation), reveals that the two valence protons are predominately in the $\pi(f_{7/2})$ orbital. See the analysis of the ^{9}Be(^{54}Ti, ^{53}Sc + γ)X reaction in Chapter 5.

the target, and is absorbed. Its contribution to σ_{sp} is [99]

$$\sigma(\text{strip}) = \frac{1}{2I+1}\int d\mathbf{b} \sum_{M} \langle \phi^{c}_{IM} | (1 - |\mathcal{S}_{xT}|^2) | \mathcal{S}_{cT}|^2 | \phi^{c}_{IM} \rangle. \tag{3.20}$$

The total stripping reaction probability is the product of the probability of elastically scattering the core $|\mathcal{S}_{cT}|^2$ and the probability of inelastic absorption of the nucleon by the target $(1 - |\mathcal{S}_{xT}|^2)$ integrated over all impact parameters $\mathbf{b}$ and averaged over all M substates. The quantum numbers I and M refer to final states of the core. ϕ^{c}_{IM} is the single-particle, relative motion wave function of the removed nucleon and the projectile-like core (residue) in the final state (see Section 3.4.3). Note that the norm of the scattering

matrices for the nucleon-target and core-target systems, $\mathcal{S}_{xT}$ and $\mathcal{S}_{cT}$, are the transmission probabilities, e.g. $T_{cT} = |\mathcal{S}_{cT}|^2$ is the probability the core survives (emerges) in the elastic channel and $T_{xT} = |\mathcal{S}_{xT}|^2$ is the probability that the nucleon emerges in the elastic channel. $1 - |\mathcal{S}_{xT}|^2$ is the probability that a nucleon is removed.

The contribution of the diffractive or elastic component, where the removed nucleon interacts elastically with the target and is dissociated from the residue, is more complicated. It includes a summation over continuum relative-motion states [90]

$$\sigma(\text{diff}) = \frac{1}{2I+1} \sum_{\sigma,M} \int d\mathbf{k} \int d\mathbf{b} \, |\langle \phi_{\mathbf{k}\sigma} | (1 - \mathcal{S}_{xT}\mathcal{S}_{xT}) | \phi_{IM} \rangle|^2, \tag{3.21}$$

but because the spectator-core approximation allows us to assume that $\phi_{\vec{k}\sigma}$ is an eigenstate of the same bound Hamiltonian whose eigenvector gives ϕ_{jm}[7], we can rewrite Equation 3.21 without the integration over the continuum as

$$\sigma(\text{diff}) = \frac{1}{2I+1} \int d\mathbf{b} \left(\sum_{M} \langle \phi^c_{IM} \| 1 - \mathcal{S}_{cT}\mathcal{S}_{xT}|^2 | \phi^c_{IM} \rangle - \sum_{MM'} |\langle \phi^c_{IM} | (1 - \mathcal{S}_{cT}\mathcal{S}_{xT}) | \phi^c_{IM'} \rangle|^2 \right). \tag{3.22}$$

This is the form used in the calculation of the single-particle cross sections. A similar integration over all impact parameters and average over all M substates occurs. The removed nucleon is either absorbed or diffracted according to the processes (stripping or diffraction).

The effects of the interaction of the nucleon and the core with the target including absorption are seen through phase shifts included in $\mathcal{S}_{xT}$ and $\mathcal{S}_{cT}$. The approximations used in the derivation of Equations 3.20 and 3.22—spectator-core, Glauber (eikonal), and static density approximations—are covered in the subsequent sections.

[7] We have assumed that the two-body Hamiltonian has only one excited state. Additional bound states, assumed to have a small contribution at intermediate energies, will slightly decrease the diffractive contribution.

3.4.2.1 Spectator Core Approximation

The momentum distribution of the projectile-like fragment, measured at small grazing angles (given the absorptive core-target interaction, the reaction is assumed to be peripheral), peaks near the momentum of the projectile. Given this observation, a *spectator-core* approximation is used: the interaction between the projectile and the target can be approximated by the interaction between the participating nucleon and the target. The core is treated as a spectator, i.e. it is only allowed to elastically scatter. The influence of the target on the incoming projectile and outgoing residue is only reflected in their optical wavefunctions. These wavefunctions are calculated using the eikonal Glauber approximation.

3.4.2.2 Glauber approximation

The Glauber approximation is rooted in physical optics. It assumes the incident projectile will continue in a straight path (eikonal approximation) as it interacts with the target; it ignores the negligibly small contribution to the integral in the calculation of the wavefunction that come from components that deviate from the incoming projectile wave vector $\vec{k}$. Thus the multi-nucleon projectile can be broken down into a series of one-dimensional problems at frozen impact parameters. The entire interaction is reflected in a phase [100] whose imaginary component represents the strong absorption of the projectile, core, or nucleon by the target. This formalism greatly decreases the dependence on the entrance and exit channel optical model potentials used as in DWBA calculations for classic transfer reactions [47, 101].

There are two conditions that must be satisfied: the energy, E, of the incident particle must be greater than the magnitude of the potential, V, and the wavelength of the particle must be much shorter than the size of the potential. The first statement, written as $V/E \ll 1$ is equivalent to the statement that $V(x)$ changes slowly within a particle wavelength. This places kinetic energy restrictions on the incident projectile, and the Glauber approximation is only used for incident projectile energies around 50 MeV/u or greater. The projectile

beam energy for the knockout data analysis contained in Chapter 5 was 72 MeV/u.

The Glauber phase ξ_i for the projectile-target, core-target, and nucleon-target interaction can be written as

$$\xi_i(b_i) = \frac{1}{\hbar v} \int_{-\infty}^{z_b} \Delta k_i \, dz. \tag{3.23}$$

and represents the amount of Born-approximation phase-shift accumulated along the straight trajectory defined by the beam axis. Δk is defined as

$$\Delta k_i \equiv \frac{k}{2E} V_i(z,b) = \frac{k_i}{2E_i}(U_i(r) + iW_i(r)), \tag{3.24}$$

where W is the imaginary component of the strongly-absorptive nuclear potential and E is the energy of the projectile.

The Glauber S-matrices for elastic scattering $\mathcal{S}_{pT}$ and $\mathcal{S}_{xT}$ naturally emerge as

$$\mathcal{S}_{xT} = e^{2i\delta_{xT}(b)} \tag{3.25}$$

$$\mathcal{S}_{pT} = e^{2i\delta_{pT}(b)} \tag{3.26}$$

where the total phase shift accumulated $\delta_i(b)$ is

$$\delta_i(b) = \int_{-\infty}^{z} dz' \, \frac{ik}{2E} W(z', b). \tag{3.27}$$

3.4.2.3 Static Density Approximation to the Scattering Matrices

The strong nuclear absorption W contained in the S-matrices phase shifts is represented by double-folding the projectile nuclear density and the target nuclear density with the NN nuclear interaction. The general result for Eqns. 3.25 and 3.26 is

$$\mathcal{S}_i(b) = \exp\left[-\frac{f_{NN}}{2} \int d^2\mathbf{x} \, \rho_i^{(z)}(|\mathbf{x}|) \, \rho_T^{(z)}(|\mathbf{b}_j - \mathbf{x}|)\right] \tag{3.28}$$

where $i = cT, xT$ (core-target and nucleon-target), b_j is the impact parameter, ρ_P and ρ_T are the ground state densities of the projectile and the target, and f_{NN} is the empirical, free, isospin-weighted, nucleon-nucleon, forward scattering amplitude evaluated at the

incident projectile energy [102], as parametrized by L. Ray [103], and includes the ratio of the real to imaginary parts of the forward scattering amplitude to account for incomplete absorption [103–106]). $\mathcal{S}_j(b_j)$ is integrated over the plane ($d^2\boldsymbol{x}$) perpendicular to $\boldsymbol{b}$. The superscript (z) indicates the projection of the density distribution onto the unit vector $\hat{z}$ (parallel to $\boldsymbol{b}$) that defines the beam axis, e.g.

$$\rho_i^{(z)}(b) = \int_{-\infty}^{\infty} dz\, \rho_i(|\mathbf{b}+\mathbf{z}|) \tag{3.29}$$

Gaussian matter distributions have been assumed for the core ρ_c and target ρ_T density distributions before 2003, but for more recent calculations, as done in this thesis, matter distributions were taken from Hartree-Fock calculations using the SkX Skyrme force [81].

For the core-target integration, the S-matrix (Equation 3.28) becomes

$$\mathcal{S}_{cT}(b_j) = \exp\left[-\frac{f_{NN}}{2}\int d^2\mathbf{x}\rho_P^{(z)}(|\mathbf{x}|)\rho_T^{(z)}(|\mathbf{b}-\mathbf{x}|)\right] \tag{3.30}$$

and for the core-nucleon S-matrix, where density distribution for a single nucleon reduces to a delta function, we have

$$\mathcal{S}_{xT}(b_j) = \exp\left[-\frac{f_{NN}}{2}\rho_T^{(z)}(b_j)\right]. \tag{3.31}$$

These scattering matrices are calculated for a specific impact parameter (Glauber approximation). Equations 3.30 and 3.31 are the final forms used in Equations 3.22 and 3.20.

3.4.3 Projectile Wave Functions

The projectile wave functions ϕ_{IM}^c of the nucleon-core system, as seen in Equation 3.20 and Equation 3.22, are constructed from the bound states (eigenvalues) of a two-body interaction approximated by a Woods-Saxon potential

$$V = \frac{V_0}{1+\exp\left(\frac{r-R}{a}\right)}. \tag{3.32}$$

The potential strength V_0 is fixed to the core / valence-nucleon separation energy in the final state, i.e. the addition of the proton or neutron separation energy (S_π or S_ν) and the excitation energy of the $A-1$ residual, $E = S_{\pi,\nu} + E_x(I^\pi)$. Originally, Woods-Saxon radii $R = r_0 A^{1/3}$ were calculated using $r_0 = 1.25\,\text{fm}$ and the mass of the core [47, 59]. For current calculations, the root-mean-square (RMS) separation R was taken from a self-consistent Hartree-Fock (HF) calculation using the SkX Skyrme interaction [47, 81] at a fixed diffuseness $a = 0.7\,\text{fm}$. Gade et al. [107] tested the sensitivity of the single-particle cross sections, for the one-neutron knockout reaction from three $N = 16$ isotones (^{32}S, ^{33}Cl, and ^{34}Ar), to the radius R and diffuseness parameters a through finite difference calculations. They found that the single-particle cross sections were insensitive to the choice of diffuseness parameter a[8], but a 0.1 fm error of the RMS radius R translated to a 13 % relative error. Ref. [107] also noted the accuracy of the HF calculations: calculated charge radii were accurate to within 0.02 fm of existing experimental data. Thus, through the HF calculation of the relative core-nucleon RMS radius R, the uncertainty of the single-particle cross section on input parameters that depend on nuclear sizes was reduced.

3.4.4 Momentum Distributions

As defined in the introduction, the *longitudinal* momentum distributions of the heavy residues were first used to determine the radial extent of the nuclear halos [91]. Further theoretical and experimental development allowed the extraction of the orbital angular momentum ℓ of the removed nucleon from the experimental *longitudinal* momentum distribution. The longitudinal momentum distribution is less sensitive to Coulomb effects and is easier to calculate than the transverse parallel momentum distribution.

Longitudinal momentum distributions were calculated using the code MOMDIS [106]. MOMDIS uses the same eikonal framework (e.g. elastic scattering matrices $\mathcal{S}_c$ and $\mathcal{S}_n$) used

[8] The full partial derivative evaluated by Ref. [107] through finite difference calculations was $\delta\sigma_{\text{sp}}/\sigma_{\text{sp}} = (1.286\,\text{fm}^{-1})\,\delta R + (0.181\,\text{fm}^{-1})\,\delta a$.

to calculate the single-particle cross sections whose stripping and diffractive components were shown in Equations 3.20 and 3.22. The shape of the momentum distributions of the diffractive dissociation and stripping components, as shown by Ref. [108], have similar shapes, and thus MOMDIS only calculates the stripping component. The full form of the longitudinal momentum distribution in cylindrical coordinates (where k_z is the longitudinal component of the momentum of the core $\boldsymbol{k}_c$, and $\boldsymbol{r} \equiv (\rho, z, \phi) = \boldsymbol{r}_x - \boldsymbol{r}_c$), as taken from Ref. [106], is

$$\frac{d\sigma_{\text{str.}}}{dk_z} = \frac{1}{(2\pi)^2}\frac{1}{2\ell+1}\sum_m \int_0^\infty d^2b_x \left[1 - |\mathcal{S}_{xT}(b_x)|^2\right] \times \int_0^\infty d^2\rho\, |\mathcal{S}_{cT}(b_c)|^2 \left| \int_{-\infty}^{\infty} dz \exp[-ik_z z] \phi^c_{IM}(\boldsymbol{r}) \right|^2 \quad (3.33)$$

where $\mathcal{S}_{xT}$ and $\mathcal{S}_{cT}$ are the nucleon-target and core-target eikonal S-matrices of Equations 3.31 and 3.30, $b_{x,c} = |\boldsymbol{\rho} - \boldsymbol{b}_{x,c}|$, and ϕ^c_{IM} is the single-particle, bound-state wave function of the core-nucleon $(c + x)$ system.

Sample theoretical momentum distributions, calculated in the center of mass of the projectile, are shown in Figure 3.6.

3.4.5 Accuracy

The single particle cross sections and momentum distributions have been verified against other approximations, including solution of the full time-dependent Schrödinger equation [109], semi-classical transfer to continuum including isolated an overlapping resonances [110], and continuum-discretized coupled channels calculations [111, 112]. The current formalism incorporating the Glauber approximation, gives adequate single-particle cross sections, and thus allows an accurate comparison to experimental spectroscopic strength.

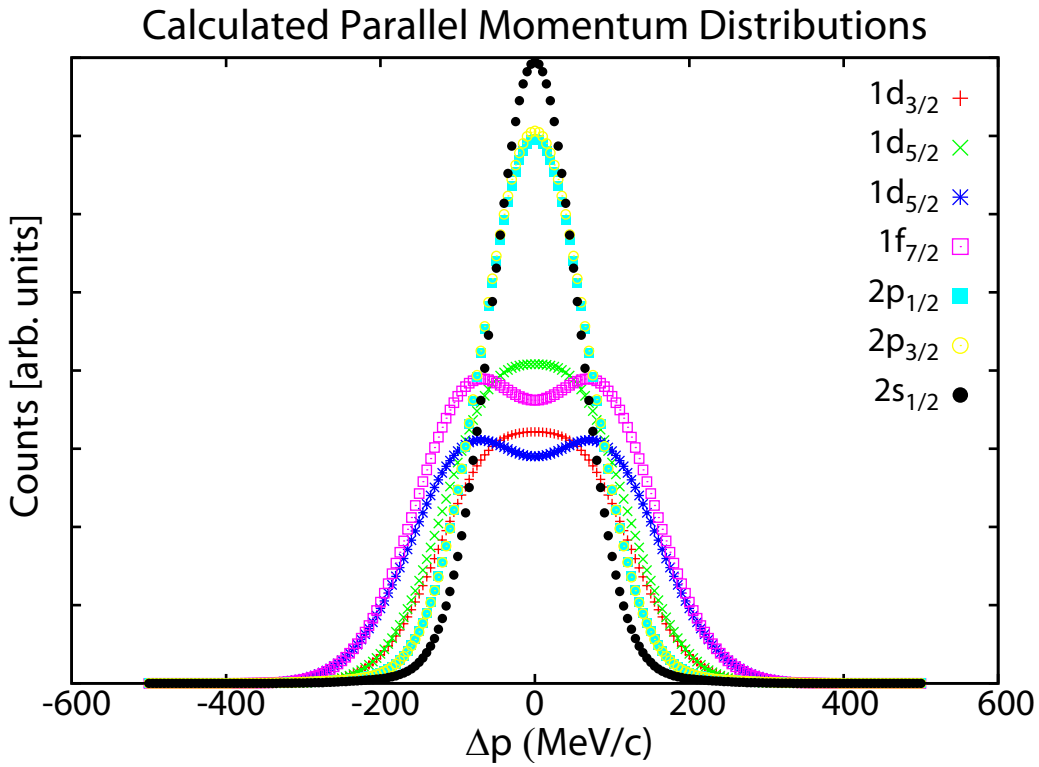

Figure 3.6: Theoretical momentum distributions of ^{53}Sc in the ^{9}Be(^{54}Ti,^{53}Sc+γ)X reaction for the removal of a proton from the indicated orbital from ^{54}Ti. There are clear shape differences between the removal of a nucleon with s, d, p, and f (ℓ = 0,1,2 and 3) orbital angular momentum. Additional steps are necessary before comparing these distributions to theory. These steps are covered in Section 4.5.3.

3.5 Single Nucleon Pickup Reactions

3.5.1 General Features

In knockout reactions, a particle is removed from the mass A projectile leaving a mass $A-1$ residue. By removing a nucleon, knockout reactions selectively populate *hole-state* configurations relative to the projectile. In pickup reactions, by contrast, a particle is added to the projectile, selectively populating *particle-state* configurations in the residue. This suggests that knockout and pickup reactions will populate a different set of final states and therefore serve as complementary spectroscopic tools.

In pickup reactions, momentum matching is important [113–115]. The maximum Fermi momentum p_F can be calculated from the number density of infinite nuclear matter

$\rho = 0.17\,\mathrm{fm}^{-3}$ through $p_F = \hbar(2\pi\rho_i)^{1/3}$. This gives an approximate Fermi momentum of $p_F \approx 250\,\mathrm{MeV/c}$. The Fermi momentum is related to the mean-square momentum through $p_F^2 = 5/3\langle \boldsymbol{P} \rangle^2$. Measurements of the Fermi momentum for the light target nuclei ^{9}Be and ^{12}C used in this thesis have found results consistent with this estimation (e.g. for ^{12}C, Ref. [116] measured a Fermi momentum of 221 MeV/c). The measured Fermi momentum, p_F, however, is still much smaller than the translational momenta of nucleons in a nucleus accelerated to intermediate energy (≥ 50 MeV/u), such as the beams delivered by the NSCL CCF facility. For example, ^{48}Cr, at a projectile kinetic energy of 70 MeV/u, has a translational momentum of 17.6 GeV/c or a momentum per nucleon of 367 MeV/c. Fortunately, the high binding energy of nucleons in light nuclei, like ^{9}Be ($S_\pi = 16.9\,\mathrm{MeV}$) and ^{12}C ($S_\pi = 16.0\,\mathrm{MeV}$), and the nucleons' small spatial confinement with the tightly bound nucleus, lead to wide momentum distributions with high momentum components that overlap with the momentum of the incoming projectile. These advantages lead to experimentally reasonable cross sections of ~ 1 mb when a deeply bound proton from ^{9}Be or ^{12}C is picked up [60]. Momentum matching also implies a sensitivity to the higher j single-particle orbitals with fast beams are used [117]. Such sensitivity may be useful for mapping the descent of higher j orbitals into a lower oscillator shell, for example mapping high momentum intruder states, like the $\ell = 3$ neutron intruder states in the island of inversion around $N = 20$ [60].

There is an important difference between knockout and pickup reactions. In pickup reactions, no information on the orbital angular momentum of the picked-up nucleon can be extracted from the parallel momentum distribution of the residue. The theoretical width is equal to the momentum distribution of the incoming beam convoluted with the differential momentum loss in the target. There is little broadening from the reaction process. This insensitivity comes from the two-body final state (target, mass $A+1$ residue) in contrast to the three-body final state (target, mass $A-1$ residue, removed nucleon) in knockout reactions, where the removed nucleon is related through momentum coupling

to the $A-1$ residue. This can be seen mathematically. The differential momentum distribution of the reaction ($d\sigma_{\text{reac}}/dp_{\parallel}$) can be related to the differential momentum seen in the laboratory frame ($d\sigma/d\Omega_L$) through [60]

$$\frac{d\sigma_{\text{reac}}}{dp_{\parallel}} = \frac{2\pi}{p_R}\left(\frac{m_R}{m_R+m_T}\frac{p_P}{p_R}\cos\theta_L - 1\right)\frac{d\sigma}{d\Omega_L}. \tag{3.34}$$

p_P and p_R are the momenta of the incoming projectile and outgoing residue and θ_L is the angle of the heavy residue as seen in the laboratory frame. With high (≥ 50 MeV/u) energies and a peripheral reaction process, the lab angles are small and the momentum transfer is negligible, e.g. $p_R \approx P_P(A-1)/A$. The broadening due to the reaction process is overwhelmed by the experimental contributions to the momentum width (e.g. target thickness).

Even though the parallel momentum distribution cannot provide spectroscopic information about the projectile wave function, deviation from the predicted distribution can reveal the presence of reaction channels (coupled-channels effects, continuum, etc.) beyond the enumerated two-body states.

3.5.2 Early Work: The ^{9}Be(^{20}Ne, ^{21}Na + γ)X reaction

The investigation of fast-beam pickup reactions in inverse kinematics began with experiments at RIKEN by Shimoura [118] and Michimasa et al. [119] on ^{23}F. Because of the high momentum components associated with tightly bound nuclei, Shimoura and Michimasa et al. used ^{4}He as a target. ^{4}He has a proton separation energy of nearly 20 MeV ($S_\pi = 19.8$ MeV). The cocktail beam on target offered four reaction paths to ^{23}F: the proton transfer (pickup) $\alpha(^{22}\text{O}, ^{23}\text{F}+\gamma)$, inelastic scattering $\alpha(^{23}\text{F}, ^{23}\text{F}+\gamma)$, two-nucleon removal $\alpha(^{25}\text{Ne}, ^{23}\text{F}+\gamma)$, and one neutron knockout $\alpha(^{24}\text{F}, ^{23}\text{F}+\gamma)$. The pickup reaction from ^{22}O to ^{23}F populated states in ^{23}F with a cross section of approximately 1 mb.

Based on the success of the RIKEN experiments, Gade et al. [60] considered the pickup reaction ^{9}Be(^{20}Ne, ^{21}Na + γ)X off a much less experimentally complicated ^{9}Be target.

Doppler reconstructed γ rays were observed in coincidence with ^{21}Na at 330(3) keV, 1832(4) keV, and 2420 keV and attributed to the decay of the $5/2^+_1$ state to the $3/2^+_{\text{g.s}}$ ground state, the decay of the first $7/2^+$ to the $5/2^+$ state at 330 keV, and the decay of the first $1/2^+$ state to the ground state. 86(6)% of the total reaction strength populated the $3/2^+$ state. A residue rest-frame γ ray transition at 981 keV was observed and was attributed to the decay of the 1^+ state to the ground state in the target residue $^9\text{Be} - 1p \rightarrow {}^8\text{Li}(1^+)$.

The states and population strengths of ^{21}Na were compared to the direct (d,n) and $(^3\text{Ne},d)$ reactions, that is $^{20}\text{He}(d,n)^{21}\text{Na}$ and $^{20}\text{Ne}(^3\text{He},d)^{21}\text{Na}$ [120]. These transfer reactions showed quantitative information on agreement with the inverse kinematics results, as seen in Figure 3.7. Because transfer reactions are a well known spectroscopic tool for providing quantitative single-particle structure, the similar qualitative population of excited states for the proton pickup reaction implied similar potential as a spectroscopic tool.

3.5.3 Pickup Reaction Theory

Pickup reactions are treated as direct, two-body reactions. The couplings to intermediate states are small at high beam energies and are assumed to be zero for the present case. Therefore, for the $^9\text{Be}(^{48}\text{Cr}, {}^{49}\text{Mn}+\gamma)\text{X}$, $^{12}\text{C}(^{48}\text{Cr}, {}^{49}\text{Mn}+\gamma)\text{X}$, $^9\text{Be}(^{49}\text{Mn}, {}^{50}\text{Fe}+\gamma)\text{X}$, $^{12}\text{C}(^{49}\text{Mn}, {}^{50}\text{Fe}+\gamma)\text{X}$, $^9\text{Be}(^{50}\text{Fe}, {}^{51}\text{Co}+\gamma)\text{X}$, and $^{12}\text{C}(^{50}\text{Fe}, {}^{51}\text{Co}+\gamma)\text{X}$ reactions, the single-particle cross sections were calculated in post-form Coupled Channels Born Approximation (CCBA) (see Figure 3.8) using the reaction code FRESCO [121]. The initial state is three-body and the final state is two-body. The final state includes treatment of both the residue and the target. For example, in the $^9\text{Be}(^{48}\text{Cr}, {}^{49}\text{Mn}+\gamma)\text{X}$ reaction, rewritten as $^9\text{Be}(^{48}\text{Cr}, {}^{49}\text{Mn}(j^\pi))^8\text{Li}(I^+)$, the $I^\pi = 2^+$ (g.s.), 1^+ (981 keV), and 3^+ states in ^{8}Li, formed from ^{9}Be after the removal of a proton, are explicitly included. For the ^{12}C target, the $I^\pi = 3/2^-$ (g.s.), $1/2^+$ (2125 keV), $5/2^-$ (4445 keV) states in ^{11}B are included. Breakup effects, associated with the slow relative motion compared to the center-of-mass motion of

the participating nucleon target core, are ignored because of the high binding energy of the nucleons in ^{9}Be and ^{12}C.

The DWBA reaction process is given by the form

$$b + A \rightarrow B + a. \tag{3.35}$$

Using the post-form formalism, the ^{9}Be(^{48}Cr, ^{49}Mn + γ)X reaction components b (target, final state), A (projectile, final state), B (target, initial state), and a (projectile, initial state) are combined as $A(^{49}\mathrm{Mn}) = a(^{48}\mathrm{Cr}) + x$ and $B(^{9}\mathrm{Be}) = b(^{8}\mathrm{Li}) + x$ where x is the transfered nucleon. The exit channel potential is

$$V_{aB} = V_{ax} + U_{ab}, \tag{3.36}$$

and the transition matrix, in bracket form, is

$$T = \langle \chi_{\beta} \phi_{a} \phi_{B} | (V_{av} + U_{ab} - U_{aB}) | \chi_{\alpha} \phi_{A} \phi_{b} \rangle \tag{3.37}$$

The potential includes the binding potential V_{av} of the removed nucleon^{8}Li(I^{+}) to the core, and the optical potentials of ^{48}Cr on ^{8}Li (U_{ab}) and ^{49}Mn on ^{8}Li (U_{aB}). The absorptive part of the ^{49}Mn + ^{8}Li component in Equation 3.37 can be calculated, as in knockout reactions by double folding the neutron and proton densities of ^{49}Mn (from Hartree-Fock calculations) with the density of ^{8}Li and an effective NN interaction. See Equations 3.28, 3.30, and 3.31. χ_{β} and χ_{α} are the entrance and exit channel distorted wave functions.

The nucleon-core relative motion wavefunctions $\phi_{B}(^{9}\mathrm{Be})$ and $\phi_{A}(^{49}\mathrm{Mn})$ are created through the coupling of an excited core to the removed nucleon. In the most basic single-particle form, these are written as $\phi_{B}(^{9}\mathrm{Be}) = [^{8}\mathrm{Li} \otimes \phi_{j}]_{3/2^{-}}$ or $\phi_{B}(^{49}\mathrm{Mn}) = [^{48}\mathrm{Cr} \otimes \phi_{j}]_{j}$. The ^{49}Mn states were calculated using a Woods-Saxon potential with a spin orbit term of 6 MeV using the standard radius and diffuseness parameters of r_{0} = 1.25 fm and a = 0.7 fm. The separation energies are adjusted to the binding energy of the proton in the target and the excitation energy of the pickup residue. See Section 6.4.2 for further theoretical details and the full reaction calculations.

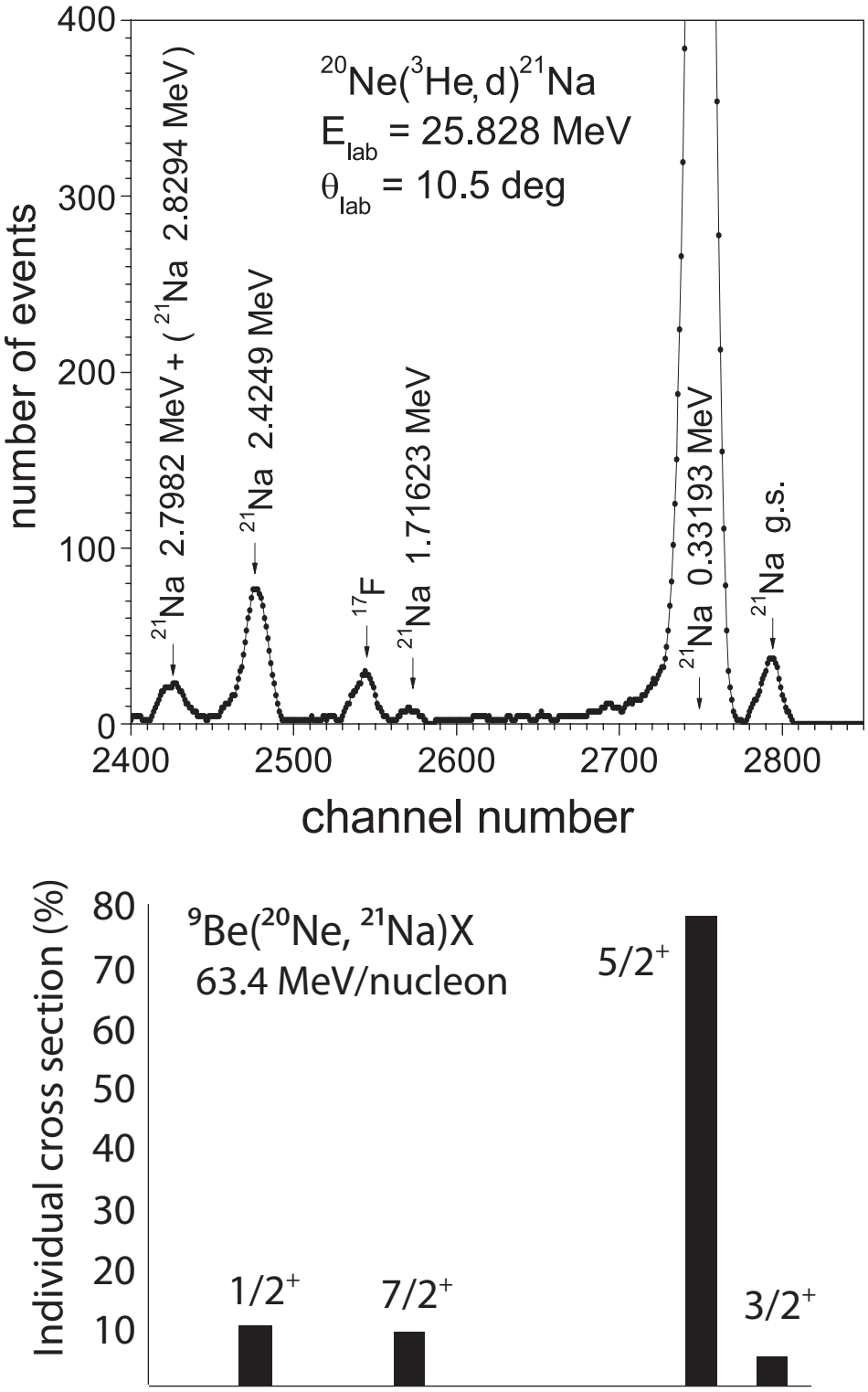

Figure 3.7: Comparison of the energies and population pattern of excited states in the transfer reaction ^{20}Ne(^{3}He, d)^{21}Na and the pickup reaction ^{9}Be(^{20}Ne, ^{21}Na + γ)X. The top half of the figure was extracted from Mukhamedzhanov et al. [120].

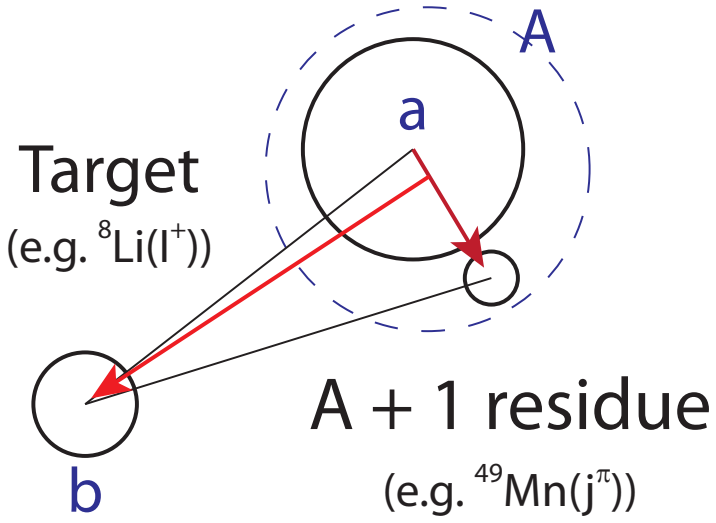

Figure 3.8: Post-form DWBA reaction schematic.

Chapter 4

EXPERIMENTAL SETUP AND ANALYSIS TECHNIQUES

4.1 Overview

The spectrum of experimental requirements for the study of exotic nuclei using single-nucleon pickup and knockout reactions include the production of a rare-isotope beam, particle identification of the mass A projectile, particle identification and momentum measurement of the mass $A-1$ or mass $A+1$ residue, and γ ray spectroscopy of the residue to tag the final state. The National Superconducting Cyclotron Laboratory (NSCL) Coupled Cyclotron Facility (CCF) [88], Segmented Germanium Array (SeGA) [122, 123], and the S800 magnetic spectrograph [124] provide the means. A schematic of the NSCL CCF facility is shown in Figure 4.1. Further information on the S800 and SeGA are found in Sections 4.3 and 4.4. Chapter 4 also covers the analysis techniques used in in the extraction of partial and inclusive cross sections and longitudinal momentum distributions common to the analysis of the ^{9}Be(^{54}Ti, ^{53}Sc + γ)X knockout reaction of Chapter 5 and the six pickup reactions[1] of Chapter 6.

[1] ^{19}Be(^{48}Cr, ^{49}Mn + γ)X, ^{9}Be(^{49}Mn, ^{50}Fe + γ)X, ^{9}Be(^{50}Fe, ^{51}Co + γ)X, ^{12}C(^{48}Cr, ^{49}Mn + γ)X, ^{12}C(^{49}Mn, ^{50}Fe + γ)X, and ^{12}C(^{50}Fe, ^{51}Co + γ)X

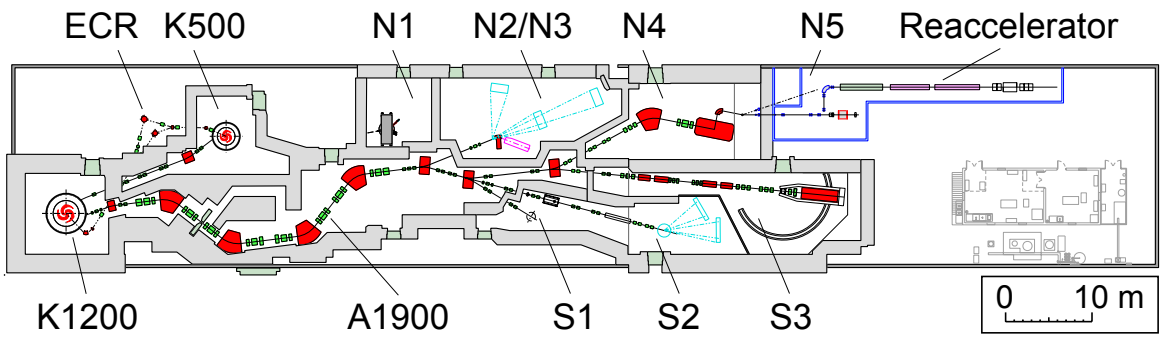

Figure 4.1: NSCL Coupled Cyclotron Facility showing both the location of beam production (ECR, K500, K1200, and A1900) and the experimental vaults that receive and study the nuclei in the secondary beam using a wide array of equipment. Both the knockout and pickup experiments were run in the S3 vault.

4.2 Beam Production

4.2.1 Production of Exotic Nuclei

Because of their short decay half-lives, the radioactive ions studied at the NSCL do not exist in nature. They must be produced as beams of short-lived nuclei. Beams at the NSCL are produced by *projectile fragmentation* at 80 – 150 MeV/u. A stable, primary beam, accelerated to velocities nearly half the speed of light, impinges on a thick production target of ^{9}Be (target thickness are several 100 mg/cm^2). Nuclei in the stable beam, as they pass through the production target, may fragment into residues of smaller mass and different ratios of N/Z with respect to the initial projectile. Because of the high beam energy, the fragmentation products exit the back of the target with nearly beam velocity. Typically the farther the N/Z ratio is from the isobaric ratio defined by the valley of stability, that is the more proton or neutron asymmetric the fragmentation products are, the smaller the production cross section and the more exotic the fragmentation product is.

From the remainder of the primary beam and the vast number of fragmentation products, one or a few specific isotopes must be selected using a highly selective filter called a *fragment separator*. Fragment separators offer purification of up to 10^{12}, e.g. an

exotic nuclear species, produced at a rate of 1 pps in the fragmentation processes, can be selected from a total primary beam rate of 10^{12} pps (see Figure 4.2 for a schematic of the A1900 fragment separator). In summary, in-flight separated, rare-isotope beam production can be broken down into three main parts: primary beam production, fragmentation, and selection of the isotope of intent.

To accelerate an originally charge-neutral atom in the intense electric fields of the cyclotron, it must be stripped of its electrons. The acceleration process begins in one of two Electron Cyclotron Resonance (ECR) ion sources, the Advanced TEMperatures Ion Source (ARTEMIS) [125] or the Superconducting Source for Ions (SuSI) [126]. ARTEMIS and SuSI ionize the stable ions, confined by a strong magnetic field within a small volume of plasma called a magnetic bottle, through repeated collisions with thermal electrons. A single charge state of the now ionized plasma of atoms is extracted from the ion source and injected into the K500 cyclotron, the first of the two coupled cyclotrons at the NSCL. In the cyclotrons, the charged nuclei are confined to a plane by a magnetic field and are accelerated in an outward spiral by an oscillating electric field. The frequency is tuned to exert a consistent force on the bunches of ions. In the K500 and K1200, the electric field is produced by three fan-shaped poles, called dees, charged to high voltages at radio frequencies ($\sim 100\,\mathrm{kV}$ and $\sim 24\,\mathrm{MHz}$ for the K1200). The high magnetic fields that confine the ion bunches to a plane are created by high-current, superconducting magnets. The ions are injected into the center of the K500, and, as they are accelerated, spiral out to the edge of the accelerating plane, where they are extracted by electrostatic deflectors.

The K500 accelerates the injected ions to about $v \sim 0.15\,\mathrm{c}$ (15% the speed of light). The maximum possible energy provided by either device is given by the name. The K in K500 or K1200 come from the relation,

$$\left(\frac{E}{A}\right) = k\left(\frac{q}{A}\right)^2 \tag{4.1}$$

where E/A is in $\mathrm{MeV/u}^2$.

[2]In practice, the energies of the nucleons leaving the K1200 are under one-half of this

The nuclei extracted from the K500 are injected into a second, even more powerful cyclotron, the K1200. A carbon stripper foil located 30 cm from the center of the K1200 removes additional electrons. The stripper foil leaves medium mass, primary beam nuclei, such as those used in this thesis, fully stripped. The maximally stripped nuclei are accelerated to an energy between 45 MeV/u for ^{238}U and 170 MeV/u for ^{24}Mg, depending on the mass and charge of the nuclei accelerated. These energies correspond to a highly relativistic velocity of up to $v \sim 0.5\,c$. Average beam currents are around 50 pnA where 1 pnA is 6.25×10^9 pps (particles per second). The stable, high intensity beam is extracted from the K1200 and is delivered onto on a thick Beryllium production target located in front of the A1900 fragment separator.

4.2.2 A1900 Fragment Separator

To select a nuclear species from the fragmentation products created from the interaction of the primary beam with the production target, the high-velocity nuclei are filtered through the high momentum ($\Delta p/p = 5\,\%$) and angular ($\Delta\Omega = 5$ msr) acceptance A1900 fragment separator. The entire 35 m long device is composed of 24 quadrupole magnets (3 per cryostat) used to focus the beam, and four 45° dipole magnets used to disperse the beam. The A1900 selects fragments based on their magnetic rigidity $B\rho$, the product of a dipole magnet's field strength and the trajectory curvature of the fragment through the dipole, and based upon their atomic charge Z. $B\rho$ is related to the properties of the fragment through the following relation,

$$B\rho = \frac{p}{q} \tag{4.2}$$

where p is the relativistic momentum $p = \gamma mv$, and q is the observed charge (equal to the atomic number Z for fully stripped nuclei).

---

value

Experiment	Primary Beam	Prod. Target Thickness (mg/cm^2)	Beam Energy (MeV/u)	*Al* Wedge Thickness (mg/cm^2)	Momentum Acceptance (%)
Knockout	^{76}Ge	423	130	300	1
Pickup	^{58}Ni	893	160	300	1

Table 4.1: The primary beam, ^{9}Be production target thickness, beam energy, aluminum wedge thickness, and momentum acceptance of the A1900 used in the production of the secondary beam.

The optics of the A1900 can be divided into two parts. The first half, up to the Image 2 position seen in Figure 4.2, selects particles based upon their magnetic rigidity. The fragments, dispersed in momentum by the first dipole magnet, pass through a collimating slit that selects a narrow range of magnetic rigidities. A single cut based on rigidity, however, does not uniquely define a nuclear specifies. Several fragmentation products may have similar ratios of p/q. Therefore, an achromatic wedge, placed at the Image 2 position of the A1900, is typically inserted to slow nuclei according to their atomic number Z. Nuclei with the same rigidity but different atomic charge experience a different differential momentum loss in the wedge [127], and thus nuclei with a common magnetic rigidity before the wedge, have different rigidities after the wedge. The second half of the magnetic separator, composed of a matching set of dipoles, quadrupoles, further purifies the beam through momentum dispersion and collimation.

Although the A1900 is highly selective, the final secondary beam often consists of several species and, in such cases, is called a *cocktail beam*. The primary beam, production target thickness, beam energy, aluminum wedge thickness, and momentum acceptance of the A1900 spectrograph for the knockout and pickup experiments are shown in Table 4.1. The secondary and primary beam characteristics of the cocktail beams used in this thesis—the primary beam, secondary beam component (the primary three constituents of the cocktail beam are listed), approximate rate at the S800 target position, and the energy of the beam before the reaction target located at the S800 pivot point, the reaction target

position, of the S800—are listed in Table 4.2.

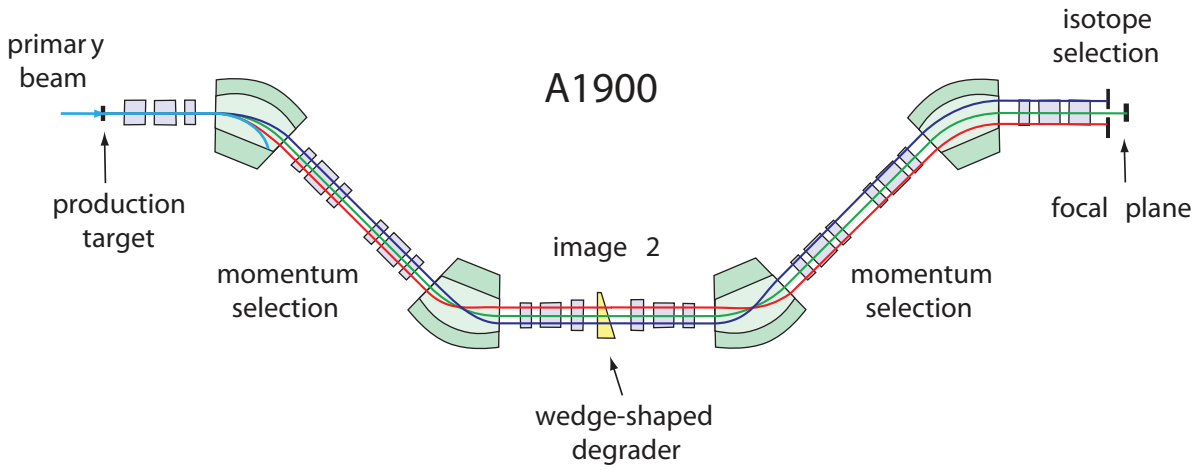

Figure 4.2: Schematic of the A1900 fragment separator. The location of the production target and wedge are shown. The bream direction is from left to right. The red, blue, and green lines show, for a fragment the A1900 is fully tuned to accept, the dispersion and focus of the beam in the dipole and quadrupole elements.

4.3 S800 Magnetic Spectrograph

From the focal plane of the A1900, the exotic cocktail beam is delivered to a reaction target at the pivot point of the S800 spectrograph. In the reactions of interest in this thesis, a nucleon is removed (knockout) or added (pickup) to the incoming projectile ${}^{A}Z$, leaving either a residue ${}^{A-1}_{N-1}Z$ or ${}^{A-1}_{N}(Z-1)$ (knockout reaction) or ${}^{A+1}_{N+1}Z$ or ${}^{A+1}_{N}(Z+1)$ (pickup reaction) that continues with approximately the same translational momentum per nucleon as the incoming beam (spectator-core and eikonal approximations). The target is surrounded by SeGA, a highly-segmented, high-purity germanium detector (HPGe) array, which detects and measures the de-excitation γ rays emitted in-flight by the residue.

The S800 is divided into two parts, the analysis beam line and the spectrograph (see Figure 4.3). The analysis beam line, leading up to the target position, is used for beam diagnostics and tuning the optics mode of the spectrograph. The constituents of the cocktail beam are identified through their difference in velocity, which appears as a

Primary beam	Secondary beam	Approximate rate (pps)	Purity (%)	Energy (MeV)
^{76}Ge	^{54}Ti	103	37	84
	^{55}V	85	30	89
	^{57}Cr	77	27	90
^{58}Ni	^{48}Cr	2.5×10^{3}	39	61
	^{49}Mn	2.0×10^{3}	40	63
	^{50}Fe	0.5×10^{3}	11	66

Table 4.2: Secondary and primary beam characteristics of the cocktail beams used in this thesis: the primary beam, secondary beam component (the primary three constituents of the cocktail beam are listed), approximate rate of the cocktail component on target, and the energy of the beam before the target. The target refers to the reaction target positioned at the pivot point of the S800 spectrograph and not the production target located before the A1900 fragment separator. All rates are quoted at 1 % A1900 momentum acceptance and include transmission losses in the beam lines.

difference in TOF between two thin plastic scintillators (127 µm thick) located at the end of the A1900 fragment separator (XFP scintillator) and in the object box of the S800 analysis line (OBJ scintillator). The spatial and angular profile of the beam can be detected by two Parallel Plate Avalanche Counters (PPACs) inserted at the intermediate image of the analysis line. Although the PPACs were inserted for both experiments, they were not used in the analysis.

The analysis line is operated in one of two modes: focused mode or dispersion-matched mode. In dispersion-matched mode, the beam is dispersed at the target and focused in the S800 focal plane, i.e. the focal plane is achromatic[3]. The dispersion at the target is 10 cm/% momentum. With a 2 in (5 cm) target, the dispersion matched mode limits the momentum profile of the projectile beam to an effective ±0.25 % or 0.5 % total momentum width. The increased momentum resolution at the S800 focal plane is gained at the expense of a momentum cut and thus the rate on target.

[3]From optics, an *chromatic* lens separates light into its constituent wavelengths, and an *achromatic* lens transmits light without separating it into its constituent wavelengths. In beam optics, achromatic and chromatic refer to the dispersion of momentum.

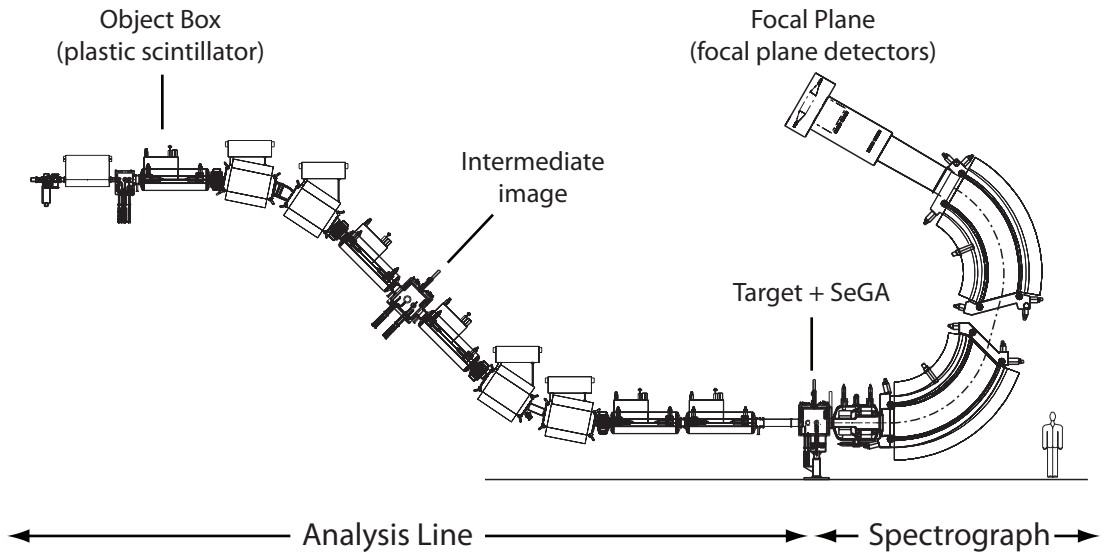

Figure 4.3: Side view of the S800 magnetic spectrograph. The secondary cocktail beam enters from the left and is guided to the target by the analysis line. The reaction residue of interest is selected by the magnetic rigidity of the S800 spectrograph and is identified in the S800 focal plane. A plastic scintillator (OBJ scintillator) located in the object box is used to provide a TOF difference relative to a timing scintillator located at the end of the A1900 (XFP scintillator) and a 3 mm scintillator located in the S800 focal plane (E1 scintillator)

.

Because knockout and pickup reactions are often run at very low beam rates down to a few particles per second, a consequence of the low yield of the exotic nuclei studied, the analysis line was tuned to focused mode. The beam was focused at the target, but dispersed at the focal plane (achromatic at the target and chromatic at the focal plane). The momentum width of the beam is directly folded into the momentum width observed in the focal plane of the S800. In focused mode, the full acceptance of the analysis line can be used to deliver a full ±2 % momentum spread to the spectrograph. The advantage of running in focused mode is increased rate that can be accepted on target. The target size does not restrict the momentum since the beam is focused on the target. A list of the acceptances and measured resolutions for the two optics mode is shown in Table 4.3.

The S800 spectrograph is located downstream of the target and consists of two dipoles, a quadrupole triplet, and a focal plane containing several detector systems (see Figure 4.4). The spectrograph is used for particle identification, and momentum and angle measure-

Property	Value
Spectrograph momentum acceptance	Both modes: ±3.0 % with greatly reduced acceptance near the edges [128]. In dispersion matched mode, a small target will restrict the momentum spread of the beam, much like the collimating slits in the A1900, e.g. a typical 2 in target restricts the beam momentum to ±0.25 %. In focused mode, the target does not restrict the momentum width.
Angular acceptance	Ω = 20 msr. The angular acceptance is elliptical: ±3.5° in the dispersive plane and ±5° in the non-dispersive plane.
Energy resolution	Intrinsic resolution: $\Delta E/E$ = 1/10 000. The measured momentum resolution depends on the beam tune and the S800 spectrograph mode. In dispersion matched mode, a typical resolution is $\Delta E/E \approx 1/2000$. In focused mode, the energy resolution is dominated by the intrinsic differential energy width of the beam.
Momentum resolution	Intrinsic resolution: $\Delta p/p$ = 1/20 000. The measured resolution, like the energy resolution, depends upon the beam tune and the optics mode. A typical value for dispersion matched mode is $\Delta p/p$ = 1/4000. In focused mode, the measured momentum widths reflect the momentum width of the beam ($\Delta E/E \approx 1/100$ for this work).
Angular resolution	$\Delta\Omega$ = 2 mrad.
Position resolution	0.5 mm in the dispersive and non-dispersive directions (position resolution of CRDC1 and CRDC2).
Dispersion (focal plane)	9.5 cm/% at CRDC1.

Table 4.3: Properties of the S800 Magnetic Spectrograph.

ments of the reaction residues. These measurements occur in the compact array of devices in the focal plane: two Cathode Readout Drift Chambers (CRDCs) for positions x, y and angles $\theta_{\text{disp.}}$, $\theta_{\text{non-disp.}}$ (dispersive and non-dispersive), a segmented ion chamber (IC) for energy loss ΔE, and a series of thick plastic scintillators TOF information.

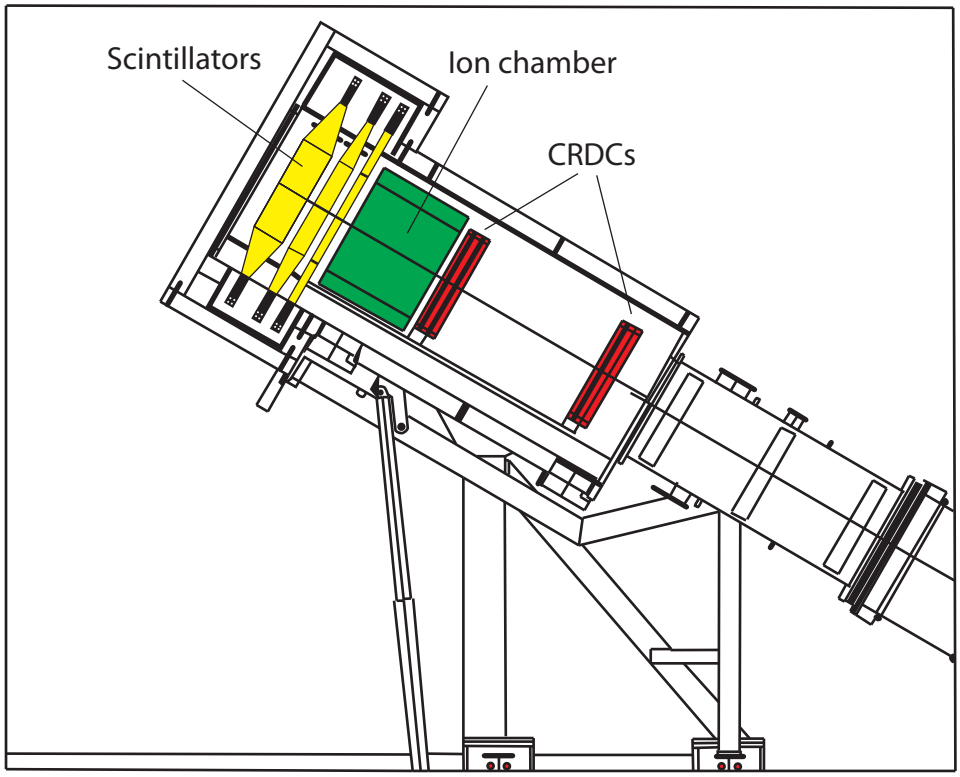

Figure 4.4: S800 focal plane showing the CRDCs (red), ion chamber (green), and scintillators (yellow). In the present work, the CRDCs were used for position and angle information, the ion chamber was used for energy loss, and the signal from the first (3 mm) scintillator was is used by the trigger logic to issue the master trigger.

The two CRDCs, separated by 1 m inside the focal plane, are position sensitive and are therefore responsible for the position and angle information of the heavy residue. Because of the momentum dispersion of the S800, the x-position is connected to the longitudinal momentum of the residue after the target. The active area of the CRDCs is ±28 cm (dispersive) and ±13 cm (non-dispersive). In the dispersive x direction, the position is determined by a fit of induced charges on 224 cathode pads. The non-dispersive y direction is determined via drift time of the ionization electrons (see Ref. [129] for

additional details). Both the dispersive and non-dispersive directions yield a position resolution of $r \sim 0.5$ mm. The drift time depends on the gas mixture, and it may may shift over the course of the experiment as the properties of the gas mixture change (80% CF_4 and 20% isobutane C_4H_4 at a pressure of 50 Torr). To ensure proper calibration, masks with a known pattern were placed in front of both CRDCs. Based on the known position of the mask holes and the measured position in the CRDCs, linear calibration parameters were applied to the raw values. The CRDCs limit the rate in the focal plane to 6×10^3 pps. At higher rates, rapid aging of the anode wire and performance degradation is typically observed.

The ion chamber (IC), collects ionization charge produced when an ion passes through its gas (P10 mixture of 90% Ar and 10% methane CH_4 at 140 Torr), and gives a ΔE measurement proportional to Z^2. Because any medium Z projectile will create ionization charge in the IC, the IC is assumed to be 100% efficient. Therefore the ion chamber serves as the reference to which the efficiency of all other particle detectors upstream are measured.

Three scintillators are located behind the ion chamber of thickness 3 mm, 5 cm, and 10 cm. The signal from the first 3 mm scintillator was used by the trigger module, for the S800 singles or particle-γ (p-γ) coincidence settings, to issue the master trigger (for pγ coincidences, a secondary trigger signal from the SeGA array was also required).

4.4 The Segmented Germanium Array (SeGA)

4.4.1 Detector Overview

The energy of an excited state of the residue is determined by the detection of its de-excitation γ rays emitted in flight. For the present work, γ rays were detected with a high-resolution germanium array position around the reaction target, the Segmented Germanium Array (SeGA) [122, 123], as seen in Figure 4.5 and Figure 4.7. SeGA, in its

so-called "classic" configuration, consists of 17 mounted detectors in two rings located at 37° and 90° relative to the beam axis. The detection volume is a n-type, High Purity germanium (HPGe) (single) crystal, 7 cm in diameter, and 8 cm long, and in a closed-axial configuration. Each single crystal is electrically segmented into 32 segments, formed from 8 slices and 4 quadrants (see Figure 4.6). Details on the role and necessity of this segmentation is found in Section 4.4.2. The central core, seen in Figure 4.6, provides the signal for timing and energy. A set of preamplifiers (33 total; one for the central contact signal and 32 for the segment signals) are included close to the crystal, and the entire crystal assembly is cooled down to liquid nitrogen temperatures in a cryostat ($T \sim 100\,\mathrm{K}$) that includes a large liquid nitrogen Dewar.

4.4.2 Segmentation and Doppler Reconstruction

The γ rays of energy E_{rest}, emitted in-flight by the reaction residues traveling at $v \sim 0.3\,c$, are subject to a Doppler shift into the laboratory frame to an energy $E^{\gamma}_{\mathrm{lab}}$[4]

$$E^{\gamma}_{\mathrm{lab}}(E^{\gamma}_{\mathrm{rest}}) = \frac{E^{\gamma}_{\mathrm{rest}}}{\gamma(1-\beta\cos\theta_{\mathrm{lab}})}, \tag{4.3}$$

or with rearrangement

$$E^{\gamma}_{\mathrm{rest}}(E^{\gamma}_{\mathrm{lab}}) = E^{\gamma}_{\mathrm{lab}}\gamma(1-\beta\cos\theta_{\mathrm{lab}}), \tag{4.4}$$

where θ_{lab} is the angle of the emitted γ ray relative to the direction of the beam in the laboratory frame, and $\beta = v/c$ is the average residue velocity at the point of γ ray emission. The Doppler shift has important experimental consequences. Because we are interested in measuring the energies emitted by the nucleus in its rest frame, according to Eqn. 4.3 we need the angle of emitted γ ray and the velocity of the moving nucleus β to reconstruct E_{rest}. Any uncertainties of the emission angle of the γ ray or of the beam velocity will

[4]A notation distinction is made for the energy of a γ ray emitted by the residue in its rest frame ($E^{\gamma}_{\mathrm{rest}}$), the energy of the emitted γ ray boosted into the laboratory frame through Eqn. 4.3 ($E^{\gamma}_{\mathrm{rest}}$), and any arbitrary γ ray detected by SeGA (E_{γ}) (e.g. γ rays emitted by a source or the environment).

directly affect the energy resolution of the observed transition ($\Delta E^{\gamma}_{\rm rest}/E^{\gamma}_{\rm rest}$). To greatly improve the energy resolution of the residue rest-frame spectrum, reconstructed from the lab-frame spectra through Eqn. 4.3, each crystal is electronically segmented into 32 segments and the energy deposited within each crystal segment was recorded for each event. In the case of multiple interaction points, as seen in Figure 4.8, the first interaction point is taken from the segmented with the highest energy deposition. With segmentation, the angular resolution of SeGA is approximately $\Delta\theta_{\rm lab} \approx 50\,$mrad (FWHM).

Because of the thickness of the target and the unknown or variable reaction point within the target, the pickup or knockout reaction occurs over a spread of energy and momentum. The spread in velocity, $\Delta\beta$, associated with the momentum width of the beam, together with the uncertainty in opening angle, $\Delta\theta_{\rm lab}$, taken from the 1 cm crystal segmentation and the distance from the target position to the crystal ($\approx 20\,$cm to the crystal edge and 24 cm to the crystal center), contribute to the total energy resolution through

$$\left(\frac{\Delta E^{\gamma}_{\rm rest}}{E^{\gamma}_{\rm rest}}\right)^2 = \left(\frac{\beta \sin\theta_{\rm lab}}{1-\beta\cos\theta_{\rm lab}}\right)^2 (\Delta\beta)^2 + \left(\frac{\cos\theta_{\rm lab}-\beta}{(1-\beta^2)(1-\beta\cos\theta_{\rm lab})}\right)^2 (\Delta\theta_{\rm lab})^2 . \qquad (4.5)$$

Typical values for the FWHM energy uncertainty $\Delta E^{\gamma}_{\rm rest}/E^{\gamma}_{\rm rest}$ at beam velocities of $\beta = 0.3$ range between 2% to 4%. The relative contribution of $\Delta\theta$ and $\Delta\beta$ depend on the angle of emission of the γ ray. This dependency of $(\Delta E^{\gamma}_{\rm rest}/E^{\gamma}_{\rm rest})$ with respect to $\theta_{\rm lab}$ is shown in Figure 4.9. The two rings of detectors, located at 37° and 90° are, positioned near the minimum of $\Delta E_{\rm r}/E_{\rm r}$. The contributions to the resolution from $\Delta\beta$ and $\Delta\theta_{\rm lab}$ dominate the intrinsic resolution of SeGA, as determined, for example, from the measurements using standard sources. The intrinsic resolution is approximately 2.5 keV for a 1 MeV γ ray.

The angle of Eqn. 4.3 is defined with respect to an assumed target position located in the center of the SeGA array at the pivot point of the S800 spectrograph. The exact target position, however, is not precisely known. Typically uncertainties are of the order of a few millimeters. The uncertainty in target position affects the angle $\theta_{\rm lab}$ used to reconstruct the residue rest-frame γ spectrum. To compensate, one can adjust the $z_{\rm tar}$ position in

software so that known energies (only transitions with short half-lives of order $\tau_{1/2} \sim 1\,\text{ps}$ are considered) are reconstructed satisfactory. The β value was chosen to align the energy of a γ ray transition in both the 37° and 90° rings. The β value is sensitive to the lifetime of the state due to the location of the decaying nucleus and should be determined separately for each observed transition (the optimal value of $\beta = 0.371$ for the 2.1 MeV transition in ^{53}Sc is close to the mid-target β value calculated using the magnetic rigidity of the analysis line). β and z_{tar} are independent for small changes about their optimal values and therefore they can both be independently optimized without worrying about simultaneous minimization on a grid of possible β and z_{tar} values. Details for the knockout and pickup reactions are found in Sections 5.6.2, 6.4.4 and 6.5.4.

4.4.3 Energy Calibration

Neither the energy response of SeGA nor the electronics is perfectly linear. Calibration parameters, mapping raw to true energies, must be calculated per detector for both the energies of the central contact (CCE) and the energies of the segments. For the central contact, a 2nd order polynomial fit between the measured transitions and known transitions of a calibration source (^{226}Ra or ^{152}Eu) provides the relationship between channel and energy. The fitting procedure for the 32 segments was automated in the analysis code SpecTcl [130] and is based upon Ref. [131]. The energies used for the ^{226}Ra or ^{152}Eu calibration procedure are listed in Table 4.4.

4.4.4 SeGA Efficiency

For SeGA we are interested in the *full-energy-peak* efficiency, the probability that a photon will both be detected and the photon will deposit its full energy in a SeGA crystal. There are three main ways that a γ ray interacts with matter: photoelectric absorption, Compton scattering, and pair production. Photoelectric absorption is the full absorption of a photon by an atom. The photon's energy is completely converted into a free electron whose energy

^{226}Ra (keV)	^{152}Eu (keV)
186.2	244.70
240.2	344.30
295.90	778.90
609.3	964.00
1120.3	1408.00
1764.5	
2447.8	

Table 4.4: Source energies used for SeGA energy calibration.

is equal to the photon energy minus the binding energy of the electron. Compton scattering is the scattering of a γ ray off a bound electron. The electron carries away part of the photon's energy, leaving the photon to Compton scatter again or deposit its energy through one of the other two processes. Frequently, a γ ray will deposit a portion of its energy in a SeGA crystal through a Compton scatter event, and then leave the crystal without depositing its full energy. Lastly, pair production is the creation of an electron-positron pair in the intense field of the proton. The positron immediately annihilates, creating two 511 keV γ rays which may or may not be detected within the crystal volume.

These three processes dominate within unique energy ranges. For germanium, complete absorption through the photoelectric effect dominates for energies lower than 140 keV. Between 140 keV and 10 MeV (approximate range), Compton scattering dominates. Pair production only becomes possible if the γ ray energy is equal to or exceeds the rest mass of the created electron and positron, i.e. above 1.022 MeV. Pair production becomes increasingly important as the energy of the incident γ ray increases and begins to approach the probability of Compton scattering around 10 MeV. These processes are not exclusive. The most likely scenario for the energies observed in this work is multiple Compton scattering followed by a single photoelectric event. Further details of these interactions can be found in Knoll [132], Chapters 10 and 12.

The efficiency of SeGA was measured using standard calibration sources, e.g. ^{226}Ra,

^{152}Eu, or ^{56}Co. The efficiencies for the measured transitions were fit by a curve, extrapolating the efficiency for any incident energy. The fit curve is empirical and is of the form

$$\epsilon^{R}_{S\acute{e}GA}(E_\gamma) = \frac{a}{(E_\gamma - b + e^{-0.269E_\gamma})^c}. \tag{4.6}$$

The efficiency is calculated per ring R (e.g. $\epsilon^{37^\circ}_{S\acute{e}GA}$ and $\epsilon^{90^\circ}_{S\acute{e}GA}$), instead of for the entire SeGA array, because the angle-dependent Lorentz transformations necessary to adjust the efficiency curve for a source at rest to a source moving at a typical beam velocity of $v \sim 0.3\,c$ depends upon the angle of the detector. We have, for each ring, the following experimental definition of efficiency $\epsilon^{\gamma}_{S\acute{e}GA}$ at energy E^i_γ:

$$\epsilon^{R}_{S\acute{e}GA}(E^i_\gamma) = \frac{\sum_d I_d(E_\gamma)}{\ell\, b(E^i_\gamma) R\, t}. \tag{4.7}$$

The summed number of counts in the photopeak for the ring, measured in time t, is the summed number of counts for all properly-calibrated detectors $\sum_d I_d(E^i_\gamma)$. ℓ is the live-time fraction of the data acquisition, and $b(E^i_\gamma)$ is the source branching ratio for the given transition i, i.e. the fractional number of γ rays expected per source decay (a given excited state may decay through more than one "branch", and each decay route has an associated probability). The source intensity, R, is calculated from the initial source activity R_0 and the time from source creation $t_>$ (standard radioactive decay law) as $R = R_0 e^{-t_>/\tau}$. See Section 5.5.2 and Section 6.3.3 for the experimental calibration curves for the knockout and pickup experiments.

A γ ray emitted in the residue rest frame will be seen as a distribution of energies in each detector, from $E^{\gamma,\mathrm{low}}_{\mathrm{lab}}$ to $E^{\gamma,\mathrm{high}}_{\mathrm{lab}}$, where the prime indicates the lab boosted energies, because each detector covers an angular range and the Lorentz boost is angle dependent (see Eqn. 4.3). The efficiency $\epsilon_{S\acute{e}GA}$, averaged over the angle covered by each crystal, for a residue rest-frame energy E_γ and a ring R is

$$\bar{\epsilon}^{R}_{S\acute{e}GA}(E^\gamma_{\mathrm{rest}}) = \frac{1}{E^{\gamma,\mathrm{high}}_{\mathrm{lab}}(E^\gamma_{\mathrm{rest}}) - E^{\gamma,\mathrm{low}}_{\mathrm{lab}}(E^\gamma_{\mathrm{rest}})} \int_{E^{\gamma,\mathrm{low}}_{\mathrm{lab}}(E^\gamma_{\mathrm{rest}})}^{E^{\gamma,\mathrm{high}}_{\mathrm{lab}}(E^\gamma_{\mathrm{rest}})} dE'\, \epsilon^{R}_{S\acute{e}GA}(E'), \tag{4.8}$$

^{152}Eu			^{226}Ra			^{56}Co		
E_γ (keV)	γ per Bq	d(g) (%)	E_γ (keV)	γ per Bq	d(g) (%)	E_γ (keV)	γ per Bq	d(g) (%)
121.8	0.28370	0.46	186.2	0.03560	0.60	846.8	0.99933	0.01
244.7	0.07530	0.53	242.0	0.07240	0.40	977.5	0.01619	6.27
344.3	0.26570	0.41	295.2	0.18370	0.40	1037.9	0.14130	0.35
367.8	0.00874	1.05	351.9	0.35590	0.40	1175.1	0.02239	0.49
411.1	0.02238	0.47	609.3	0.45570	0.40	1238.3	0.66070	0.29
444.0	0.03125	0.45	768.4	0.04870	0.50	1360.2	0.04256	0.35
488.7	0.00414	1.24	934.1	0.03093	0.50	1771.4	0.15490	0.32
678.6	0.00479	1.29	1120.3	0.14920	0.40	1810.8	0.01299	46.17
688.7	0.00859	1.06	1238.1	0.05860	0.50	1963.9	0.01099	18.22
778.9	0.12970	0.46	1377.7	0.03972	0.50	2015.2	0.03029	0.43
867.4	0.04214	0.59	1509.2	0.02113	1.30	2034.8	0.07771	0.35
964.0	0.14630	0.41	1729.6	0.02839	0.60	2113.0	0.00400	25.02
1005.1	0.00744	2.01	1764.5	0.15290	0.40	2214.5	0.00400	25.02
1085.8	0.10130	0.49	1847.4	0.02031	0.80	2598.5	0.16960	0.35
1089.7	0.01731	0.52	2118.5	0.01156	0.80	3010.1	0.00799	37.52
1112.1	0.13540	0.44	2204.1	0.04900	0.60	3202.0	0.03130	2.90
1212.9	0.01412	0.51	2447.7	0.01553	0.70	3253.8	0.07620	3.15
1299.1	0.01626	0.68				3273.0	0.01780	3.37
1408.0	0.20850	0.43				3451.2	0.00930	4.30
						3548.3	0.00178	5.06

Table 4.5: Energies E_γ, number of emitted γ rays per decay, and the uncertainty on the number of emitted γ rays per decay for the three sources used in energy calibration. Data was taken from Refs.[133, 134]. See the appropriate experimental sections, Section 5.5.2 or Section 6.3.3, for additional details.

ϵ^R_{rest} is the fit efficiency curve (Eqn. 4.6 with defined coefficients) for ring R. The Lorentz-boosted laboratory frame energies, $E^{\gamma,\text{low}}_{\text{lab}}$ and $E^{\gamma,\text{high}}_{\text{lab}}$, are evaluated at a residue rest frame energy E^{γ}_{rest} through Eqn. 4.3, and at the polar angles θ^R_{low} and θ^R_{high}. These angles are the lower and upper bounds of the polar angle covered by each germanium crystal, and thus are naturally ring dependent. Per ring, the angles are defined as $\theta^{37^\circ}_{\text{low,high}} = 37.0^\circ \pm 9.5^\circ$ and $\theta^{90^\circ}_{\text{low,high}} = 90.0^\circ \pm 9.5^\circ$.

One additional Lorentz transformation must be included. Although we make the assumption that the emitted γ rays are emitted in an isotropic distribution in the residue rest frame, they are not observed as an isotropic distribution in the lab frame. The

angular distribution is boosted in the forward direction. To take the boost into account the efficiencies are modified in the following way:

$$\varepsilon^{R}_{S\text{e}GA}(E^{\gamma}_{\text{rest}}) = \frac{\int_{\theta_{\text{low}}}^{\theta_{\text{high}}} d\theta_{\text{lab}} \sin\theta_{\text{lab}} W_{\text{lab}}(\theta_{\text{lab}}) / \int_{0}^{\pi} d\theta_{\text{lab}} \sin\theta_{\text{lab}} W_{\text{lab}}(\theta_{\text{lab}})}{2\pi \int_{\theta_{\text{low}}}^{\theta_{\text{high}}} d\theta_{\text{lab}} \sin\theta_{\text{lab}} / 4\pi} \cdot \bar{\epsilon}^{R}_{S\text{e}GA}(E^{\gamma}_{\text{rest}}) \tag{4.9}$$

where the use of $\varepsilon_{S\text{e}GA}$ rather than $\bar{\epsilon}_{S\text{e}GA}$ indicates the energy-averaged and boosted efficiency. W_{lab} is defined as

$$W_{\text{lab}}(\theta_{\text{rest}}) = \frac{\left(\sin^2\theta_{\text{rest}} + \gamma(\cos\theta_{\text{rest}} + \beta)^2\right)^{3/2}}{\gamma(1 + \beta\cos\theta_{\text{rest}})} \tag{4.10}$$

where

$$\theta_{\text{rest}} = \tan^{-1}\frac{\sin\theta_{\text{lab}}}{\gamma(\cos\theta_{\text{lab}} - \beta)}. \tag{4.11}$$

The array efficiency, for the detection of a residue rest frame energy E, is the summation of the fully averaged and boosted efficiencies for both rings, e.g.

$$\varepsilon^{\text{total}}_{S\text{e}GA}(E^{\gamma}_{\text{rest}}) = \varepsilon^{37^\circ}_{S\text{e}GA}(E^{\gamma}_{\text{rest}}) + \varepsilon^{90^\circ}_{S\text{e}GA}(E^{\gamma}_{\text{rest}}) \tag{4.12}$$

4.5 Analysis Techniques

4.5.1 Particle Identification

Nuclei in the focal plane are identified through TOF and energy loss ($\Delta t - \Delta$E). For example, see the particle identification (PID) spectrum for the ^{54}Ti reaction products, including ^{53}Sc, in Figure 4.10. Energy loss and TOF, as mentioned earlier, are determined by the ion chamber (IC) and the TOF between the scintillator in the object box and the first plastic scintillator in the focal plane (E1). The TOF depends on the nuclei's mass to charge ratio A/q, and the energy loss depends on the nuclei's atomic charge Z^2.

Additional TOF corrections had to be made for the variations in the nuclei's flight path through the spectrograph. These corrections depend on the scattering angle and the

momentum (approximated, because of the dispersion of the beam in the focal plane, by the position in the first CRDC, x_{CRDC1}) as

$$\mathrm{t} = \mathrm{t}_{\mathrm{OBJ}} + a \cdot \theta_{\mathrm{AFP}} + b \cdot x_{\mathrm{CRDC1}}. \tag{4.13}$$

Larger angles about the central trajectory lead to a longer flight path as do lower momenta projectiles. The parameters a and b were experimentally adjusted by optimizing a matrix of the angle in the focal plane (AFP) versus the TOF to provide the best resolution for particle identification.

Spectra, such as the PID of Figure 4.10, combine the signals from several detectors. The total particle detection efficiency folds in the efficiencies of all included detectors. In general, these efficiencies depend on the beam rate, beam energy, atomic charge, and mass of the nuclei identified. The product of the efficiencies, the efficiency of particle identification in the focal plane, is

$$\epsilon_{\mathrm{det}} = \epsilon(\mathrm{OBJ} \cdot \mathrm{XFP}) \cdot \epsilon(\mathrm{CRDC1} \cdot \mathrm{CRDC2}) \tag{4.14}$$

To provide accurate cross sections, the total efficiency must be measured. Efficiencies are determined relative to the IC which is assumed to be 100 % efficient. A software gate on the IC is applied to a spectrum that folds in the efficiencies of all detectors, a two-dimensional matrix of the time of flight difference between the XFP and OBJ scintillators versus the angle in the focal plane (the angle requires a valid CRDC1 and CRDC2 position). A ratio of the counts in an ion chamber gate to the total number of counts in the two-dimensional matrix with the IC gate applied gives the efficiency. The combined efficiencies for the detectors during the knockout data runs was near 0.99, and for the knockout data runs the detector efficiencies ranged between 0.97 and 0.99.

4.5.2 Inclusive Cross Sections

The inclusive cross section includes a sum over all reaction channels leading to bound states and can be measured solely by counting the number of knockout or pickup residues

detected in the S800 focal plane. The basic formula for the determination of the inclusive cross section from experiment is

$$\sigma_{\text{inc}} = \frac{1}{N_T}\frac{N_r}{N_p}. \tag{4.15}$$

N_r is the *total* number of reaction products (residues) of the specific reaction channel and N_p is the total number of incident A projectiles. The measured numbers of incident projectiles and reaction products are tempered by the angular and momentum acceptance limitations and efficiencies of the detectors and these effects must be folded into Eqn. 4.15. The cross section is the probability of the reaction occurring N_f/N_b, per total number of scattering centers seen by the projectile per unit area, N_T, in the target. N_T is defined in terms of the target thickness, given in the traditional units of mg/cm^2 and the mass density, the number of atoms per unit mass, as $N_T = nx$. x is the target thickness in mg/cm^2 and n is the target number density, the total number of atoms per cm^2. The value of n can be calculated from the atomic mass/mol and Avagadro's constant of $6.0221415 \times 10^{23}\,\text{mol}^{-1}$, the total number of atoms per mol.

Usually, the spectrograph cannot accept both the projectile beam and all reaction components created through the interaction of the incident beam with the target. This limitation has two causes. First, the momentum acceptance of the S800 is limited. Only a portion of the beam can be seen for a chosen $B\rho$ and usually it is not possible to simultaneously observe the unreacted beam and the desired fragmentation product. Second, the detectors in the focal plane are rate limited. The CRDCs can only handle a total rate of 6 kHz. Because of small reaction probabilities, the rate limitation does not affect the reaction products, but it does affect the measurement of the beam rate incident on target.

These limitations force separate measurements of the incoming rate and the rate of the reaction products. To measure the incoming rate, the $B\rho$ of the spectrograph is set to center the momentum distribution of the unreacted projectile passing through the target into the focal plane. The spectrograph, when tuned in this manner, is said to be in an *unreacted setting*. Because the reaction probabilities are so small, the presence of the target does

not affect the number of detected unreacted projectiles in a statistically significant way. For example, for a ^{9}Be 188 mg/cm^2 target, a 1 mb cross section corresponds to a reaction from one out of every ~ 80 thousand incident nuclei. All summed reaction channels, of a maximum order of a few hundred mb, affect the cross section at a statistically insignificant level.

The number of detected nuclei includes experimental detector efficiencies (see Eqn. 4.14). The total number of detected fragments (N_r or N_p), for either the unreacted or reacted run is

$$N_i = \frac{N^i_{\text{obs}} D_i}{N^i_{\text{norm}} \ell_i \epsilon^i_{\text{det}} A_i}. \tag{4.16}$$

where $i = r, p$ for the reaction residue (r) or incident projectile (p). N_{obs} is the number of observed (detected) fragments of interest, N_{norm} is the normalization of N_{obs} to the beam rate, and D is the downscaler (DS). Because separate runs were used to measure the total number of reaction residues and incoming projectiles, N_f and N_b (see Eqn. 4.15) were normalized to the beam rate through the average of the OBJ and XFP scalers.

To minimize deadtime in unreacted settings or conversely maximize the livetime of the data acquisition system, a downscaling factor D_i can be chosen, where 1 out of every N particles is used to trigger the system. The DS factor was 1 for both experiments. Deadtime is the fractional time that the DAQ is not able or ready to accept events. ℓ is the percentage livetime of the system and is the probabilistic reciprocal of the deadtime. $\ell = 1 - d_{\text{DT}}$. The livetime can either be taken from the number of total triggers (events) to the number of processed triggers (`live.trigger/raw.trigger`), or from a free running clock (oscillator) and clock that is gated by the DAQ not-busy (`clock.live/clock.raw`), where the total number of clock output by both clocks are counted by separate scalars which are not part of the DAQ system and thus are not impacted by the dead time. For both experiments, the two methods gave statistically similar results.

The last unknown component in Eqn. 4.15 is the acceptance A. The spectrograph is physically limited to a given momentum and angle acceptance, and for many reasons the

	Knockout	Pickup	
Target type	^{9}Be	^{9}Be	^{12}C
Thickness (mg/cm^2)	376(4)	188(4)	73(1)
Target density (g/cm^3)	1.85	1.85	1.87(4)

Table 4.6: Targets used in the knockout and pickup reactions

properties of the beam exceed these limitations: the momentum width of the reaction residues caused by the reaction, the location of the momentum distribution relative to the center momentum of the spectrograph, the tune of the analysis line, the momentum width of the incoming beam, and so forth. Usually these losses occur in the dispersive direction. The direct nature of the pickup and knockout reactions are reflected in a narrow reaction residue momentum distribution, and therefore only minimal acceptance corrections of order $\sim 5\,\%$ were necessary. These losses were estimated by simple parametric fits to the momentum and angle distributions reconstructed at the target from position and angle measurements at the focal plane.

With the full assortment of experimental adjustments, the inclusive cross section is

$$\sigma_{\text{inc}} = \frac{1}{nx}\left[\left(\frac{D_r}{\ell_r \epsilon^r_{\text{det}} A_r}\frac{N^r_{\text{obs}}}{\frac{1}{2}\left(N_r(\text{OBJ}) + N_r(\text{XFP})\right)}\right)\Big/\left(\frac{D_p}{\ell^p \epsilon^p_{\text{det}} A_p}\frac{N^p_{\text{obs}}}{\frac{1}{2}\left(N_p(\text{OBJ}) + N_p(\text{XFP})\right)}\right)\right] \quad (4.17)$$

The XFP and OBJ scalars and the number of observed residues or projectiles in the focal plane are given by the labels $N_i(\text{OBJ})$, $N_i(\text{XFP})$, and N^i_{obs} for $i \equiv r, p$. D_i is the DS factor, ℓ is the live time, ϵ_{det} is the combined detector efficiency, and A is the acceptance of the spectrograph. Uncertainties from the target thickness, statistical uncertainties, and systematic uncertainties all contribute to the final uncertainty budget.

Three different targets were used in the two experiments. Their properties are seen in Table. 4.6. For the beryllium target, the target thickness and uncertainty was provided by the manufacturer. For the carbon target, the thickness and density were calculated using a measured target area of $46.5(5)\,\text{cm}^2$, thickness of $390(5)\,\mu\text{m}$, and a weight of $3.38\,\text{g}$.

4.5.3 Longitudinal Momentum Distributions

The CRDCs measure the position and angle of the fragments entering the focal plane of the spectrograph. As in the A1900 fragment separator, the momentum dispersion of the spectrograph maps projectiles with different magnetic rigidities ($B\rho = p/q$) to different positions. In the A1900, the dispersion was used to select the secondary beam from the multitude of different reaction products. In the S800, the dispersion allows a position measurement to substitute for a momentum measurement. Using an optics map for S800 spectrograph, the position and angles of the nuclei in the focal plane, measured with the two CRDCs, can be mapped back to angle, position, and momentum of the nuclei at the target. The inverse matrix map used to relate vectors in the focal plane to vectors at the target was calculated using the optics code COSY infinity [124, 135]. Details on the comparison of the measured and theoretical longitudinal momentum distributions for the knockout and pickup reaction follow.

4.5.3.1 Single-nucleon Knockout Reaction

Additional concerns, like the focused mode of the S800 analysis line, which folds in the momentum spread of the incoming beam to the resolution in the focal plane require additional treatment. Rather than try to subtract these effects through de-convolutions of the experimental longitudinal momentum distribution, it is far easier to apply to the effects to the theoretical longitudinal momentum distributions (for details on the calculation of the theoretical distributions for single-nucleon knockout reactions, see Section 3.4.4). After the theoretical distribution includes similar momentum-broadening effects via folding, it can be compared to the experimental distribution. The similarities between the distributions, an example of which is shown in Figure 5.10 are used to make orbital angular momentum assignments to the removed nucleon.

A list of steps in this process follow:

1. Use the inverse map to map the measured positions and angles in the focal plane to a differential kinetic energy at the target position.

2. Convert the lab differential energy at the target d_t to differential momentum. The ratio between the two quantities is

$$\frac{\Delta p}{p} = \frac{\gamma}{\gamma + 1}\left(\frac{\Delta E}{E}\right) \tag{4.18}$$

which can be found from the differential of relativistic kinetic energy $E = (\gamma - 1)\, m_{\mathrm{A}} c^2$ to relativistic momentum $p = \gamma\, m_{\mathrm{A}} v$ with respect to beam velocity $\beta = v/c$.

3. Convert the theoretical distribution, typically calculated in the residue rest frame, to the lab frame. The lab frame and rest frame parallel momentum are related through

$$p^{\parallel}_{\mathrm{lab}} = \gamma p^{\parallel}_{\mathrm{rest}} \tag{4.19}$$

4. Because the spectrograph was operated in focused mode, the theoretical parallel momentum distribution, now converted from the rest frame to the lab frame (see Figure 3.6 for sample rest frame distributions), must be folded with the experimental resolution of the incoming beam. The experimental distribution intrinsically includes this folding. An analytical function[5] was fit to the unreacted beam and the result of the fit was convoluted with the theoretical momentum distribution. A typical width for the incoming momentum spread of the unreacted beam is 1 %. This value is determined by the momentum acceptance of the A1900 and is broadened by energy losses in the detectors and the target.

5. Finally, the theoretical distribution, converted to the lab frame and folded with the momentum resolution of the incoming beam, must account for the differential momentum loss in the target caused by the difference in reaction location in the target. Consider the case of the one proton knockout ^{9}Be(^{54}Ti, ^{53}Sc + γ)X. Because

[5] See the experimental Sections 5.7.3, 6.4.6, and 6.5.6 for the reaction specific details.

energy loss in a target is roughly proportional to Z^2, ^{54}Ti will lose more energy as it moves through the target than will ^{53}Sc. Thus, if the reaction takes place at the front of the target, the projectile will have more momentum relative to a reaction occurring at the center of the target (the average), and if the reaction takes place at the back of the target the projectile will have less momentum relative to the average. Because energy loss is roughly linear over the target thickness, the effect on momentum resolution due to the thickness of the target can be approximated by a top-hat function. This top-hat function is convoluted with modified theoretical distribution of step 4. The differential momentum losses were calculated using the computer program `Lise++` [136].

After the theoretical distributions are converted to the lab frame, and folded with all the experimental resolutions, they can be directly overlaid. The inclusive parallel momentum distribution for ^{53}Sc is shown in Figure 5.10 (page 118).

4.5.3.2 Single-nucleon pickup reactions

For single-nucleon pickup reactions, because the final state is two-body (as addressed in Section 3.5.1), there should be no broadening from the reaction processes. Thus, experimentally measured longitudinal momentum distributions are overlaid with a calculated distribution that convolutes the momentum broadening in the target with the momentum width of the incident beam.

4.5.4 Partial Cross Sections

Through the total number of detected γ rays emitted at the transition energy (see Figure 4.11), one can extract the partial cross section for the reaction channel. The experimental partial cross sections, in combination with the theoretical single-particle cross sections, are used to calculate the experimental spectroscopic factors for knockout reactions (see

Eqn. 3.18). Although the single-particle cross sections for single-nucleon pickup reactions have not yet been shown to provide quantitatively accurate spectroscopic factors, the extraction of partial cross sections can be used to both test reaction theory and provide qualitative estimates of relative orbital occupation. See Chapter 6 for experimental details and discussion on the set of proton pickup reactions ^{9}Be(^{48}Cr, ^{49}Mn+γ)X, ^{12}C(^{48}Cr, ^{49}Mn + γ)X, ^{9}Be(^{49}Mn, ^{50}Fe + γ)X, ^{12}C(^{49}Mn, ^{50}Fe + γ)X, ^{9}Be(^{50}Fe, ^{51}Co + γ)X, and ^{12}C(^{50}Fe, ^{51}Co + γ)X.

The partial cross section for the population of a final state in the residue are calculated from the total number of γ rays in the photopeak corresponding to the decay of the populated state. The math is similar to the calculation of the inclusive cross section in Eqn. 4.15, i.e.

$$\sigma_{\text{part.}}(E, J^{\pi}) = \frac{1}{N_{\text{T}}} \frac{N_{\gamma}}{N_b b_{\gamma}}, \tag{4.20}$$

with appropriate corrections for feeding and the branching ratio b_{γ} of the populated state. E and J^{π} are the energy and associated quantum numbers of the final state, E_{γ} is the measured energy of the observed transition. The decay of a state with energy E may populate several lower energy states, the fractional number of γ rays emitted from the decay of the initial state to possibly one of many final states i is the branching ratio b^{i}_{γ}. The state E may also be fed through the decay of higher lying transitions. This feeding strength must be subtracted. Thus,

$$\sigma_{\text{part.}} = \sigma_{\text{pop.}} - \sum_{j} \sigma^{j}_{\text{feed.}}. \tag{4.21}$$

where σ_{pop} is the total population cross section of Eqn. 4.21 (i.e. no feeding subtraction). The effects of feeding and branching can be visualized through the creation of a *level diagram* which places the transitions in the proper hierarchical ordering. Level ordering and assignment are assisted by intensity balancing, angular momentum assignments extracted from the parallel momentum distributions, and if needed, comparisons to shell model.

Although we can proceed in a similar way as Eqn. 4.16 through defining all efficiencies and quantities in N_γ and N_p, e.g.

$$N_\gamma(E^\gamma_{\text{rest}}) = \frac{N^\gamma_{\text{obs}} D_\gamma}{N_{\text{norm}} \varepsilon^{\text{total}}_{\text{SeGA}}(E^\gamma_{\text{rest}})\, \epsilon^r_{\text{det}} \ell_\gamma A_\gamma b^i_\gamma(E^\gamma_{\text{rest}})} \tag{4.22}$$

$$N_b = \frac{N^p_{\text{obs.}} D_p}{N^p_{\text{norm}} \varepsilon^p_{\text{det}} \ell_p A_p,} \tag{4.23}$$

N^γ_{obs} and N^b_{obs} are the number of observed γ rays and beam projectiles. These quantities must measured in separate runs because of the limitations of the spectrograph. As in Section 4.5.2, this forces separate normalizations relative to the XFP and OBJ scalars (N^γ_{norm} and N^p_{norm}), measurements of particle identification detector efficiency ($\epsilon^\gamma_{\text{det}}$ and ϵ^p_{det}), live time (ℓ_γ and ℓ_p), and spectrograph acceptance (A_γ and A_p).

Fortunately, we can make use of the S800-SeGA coincidence condition to simplify the math. When SeGA and the S800 spectrograph are run in coincidence mode, γ rays are only recorded when there is a detected residue in the focal plane. Under this condition, we can calculate a partial cross section as

$$\sigma_{\text{partial}} = \sigma_{\text{inc}} \frac{N^\gamma_{\text{obs.}}}{N^p_{\text{obs.}} b_\gamma(E_\gamma) \varepsilon^{\text{total}}_{\text{SeGA}}(E_\gamma)} - \sigma_{\text{feed}} \tag{4.24}$$

The quantities ϵ_{det}, ℓ and A cancel in the ratio and N_{norm} are not needed. $\epsilon_{\text{SeGA}}(E_\gamma)$ is the Lorentz-boosted SeGA efficiency for energy E_γ, evaluated at the residue rest-frame energy E_γ of the transition. The partial cross section to the ground state is

$$\sigma_{\text{g.s.}} = \sum_{\text{inc}} - \sum_i \sigma^i_{\text{part}} \tag{4.25}$$

assuming all feeding has been accounted for in the sum $\sum_i \sigma^i_{\text{part}}$.

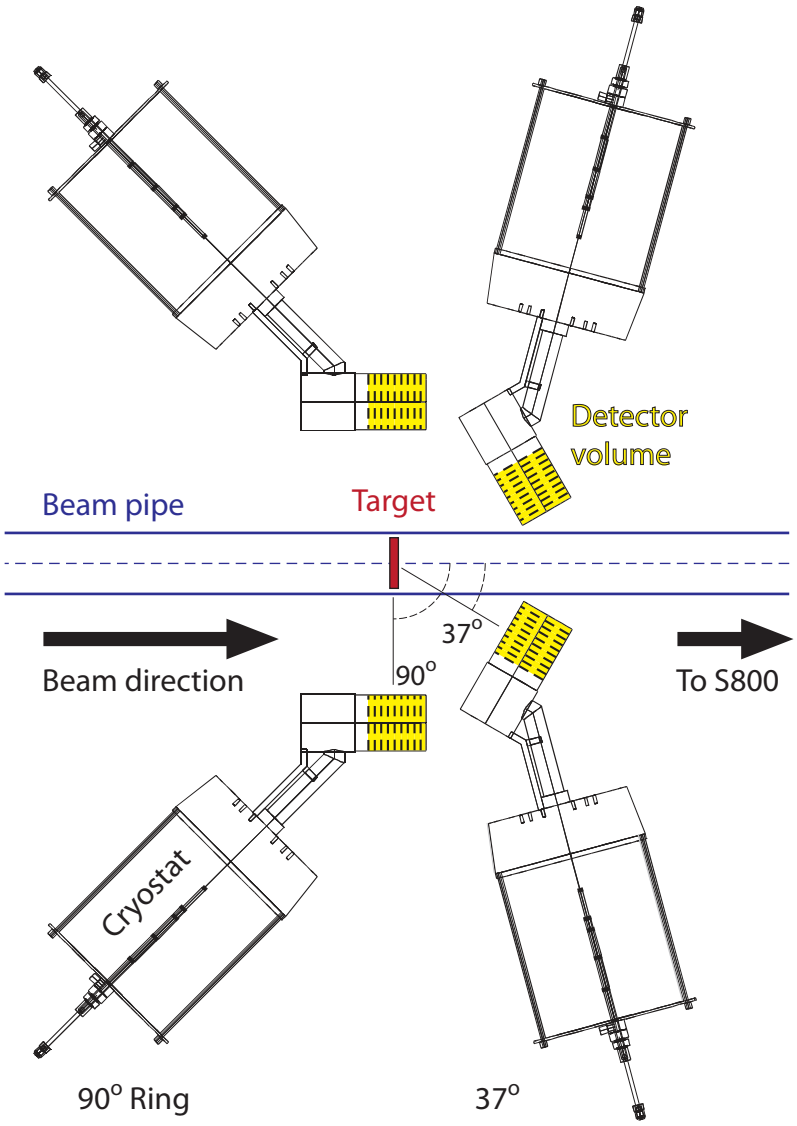

Figure 4.5: Schematic view schematic of the SeGA detector array with a cut along the mid-plane and through the beam axis. The two rings of detectors are arranged 37° and 90° with respect to the target position. The active detector volume is in yellow. The target is position equidistant from the crystals, at a distance of $d \approx 24\,\text{cm}$. The remainder of the detector hardware includes the cryostat (composed of the Dewar and crystal housing assembly), electronics and the appropriate housing for both.

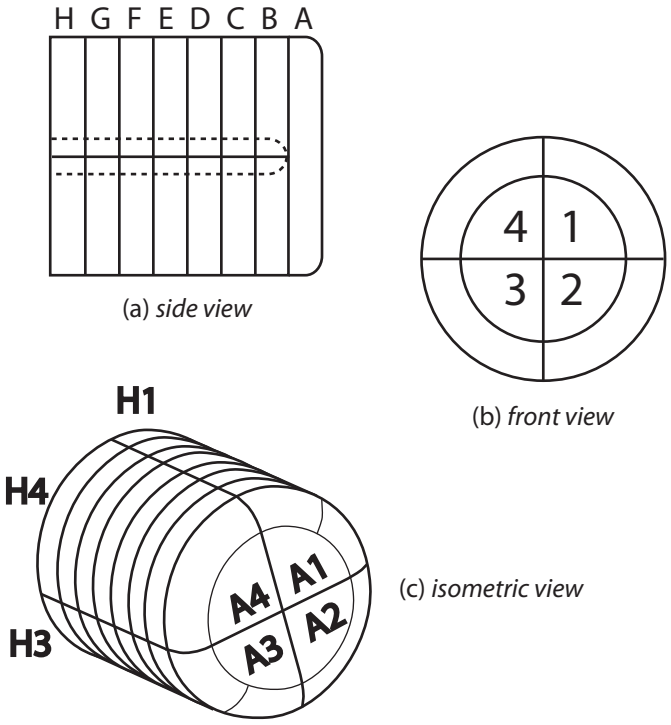

Figure 4.6: Segmentation of the SeGA crystal. The side view (a) shows the eight slices and the location of the central core. The signal from the central core is used for timing and total energy deposition. The front view (b) shows the four quadrants. And the isometric view (c) shows the complete detector volume.

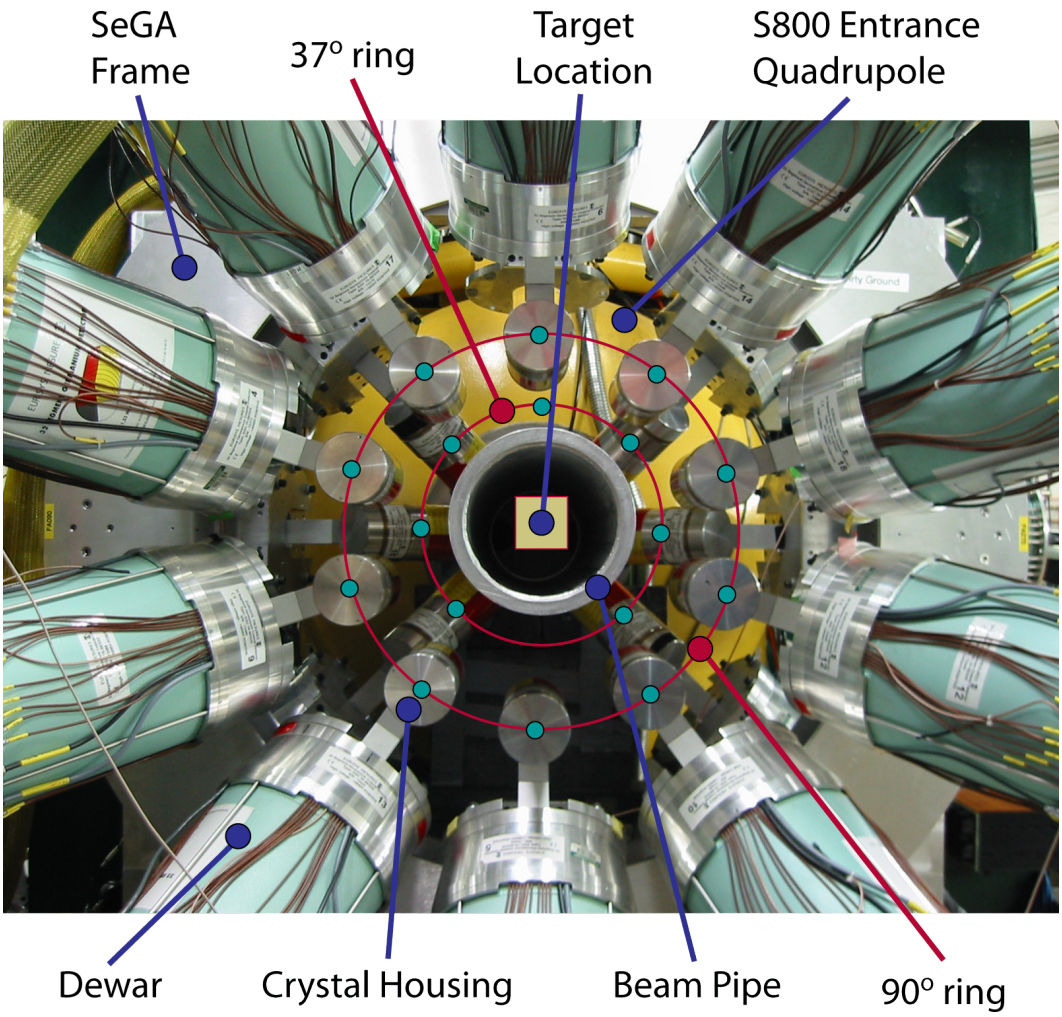

Figure 4.7: Photograph of the SeGA array in its "classic" configuration from a viewpoint upstream of the target position. Key components are labeled: the dewar and crystal housing for a single SeGA detector, the mounting ring, the 37° (7 detectors) and 90° rings (10 detectors), target location, 6 in diameter beam pipe, and the yellow entrance quadrupole to the S800 spectrograph. In the photograph one detector is missing from the forward ring (the only aqua circle that does not tag a crystal housing). This detector was present for both experiments run in this thesis.

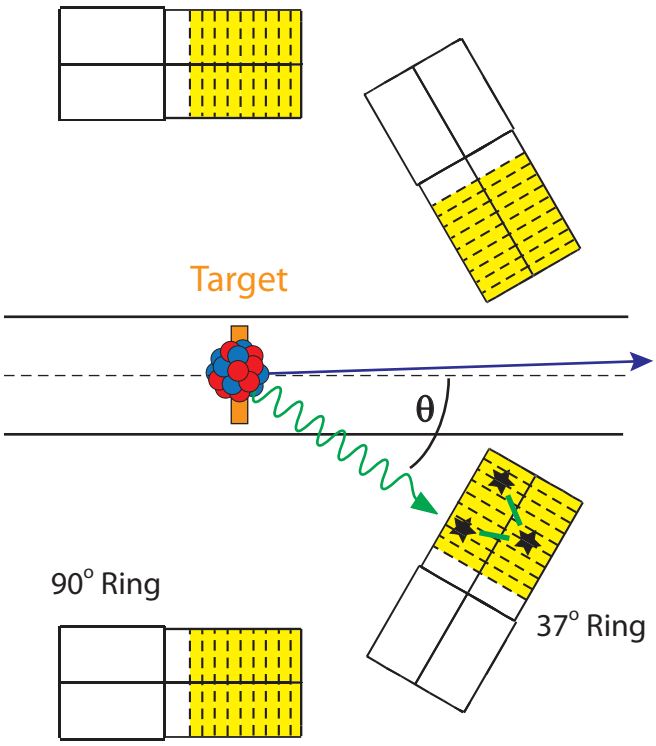

Figure 4.8: Side view of SeGA showing features important for the Doppler reconstruction of the γ ray emitted by a relativistic projectile. The two rings of detectors are arranged at angles of 37° and 90° with respect to the beam axis. The γ ray emitted in-flight by the residue following a nuclear reaction in the target is detected in one of the SeGA germanium crystals. The interaction point is determined by the segment with the highest energy deposition. The measured angles were not corrected for the different trajectories (angles) of the residues.

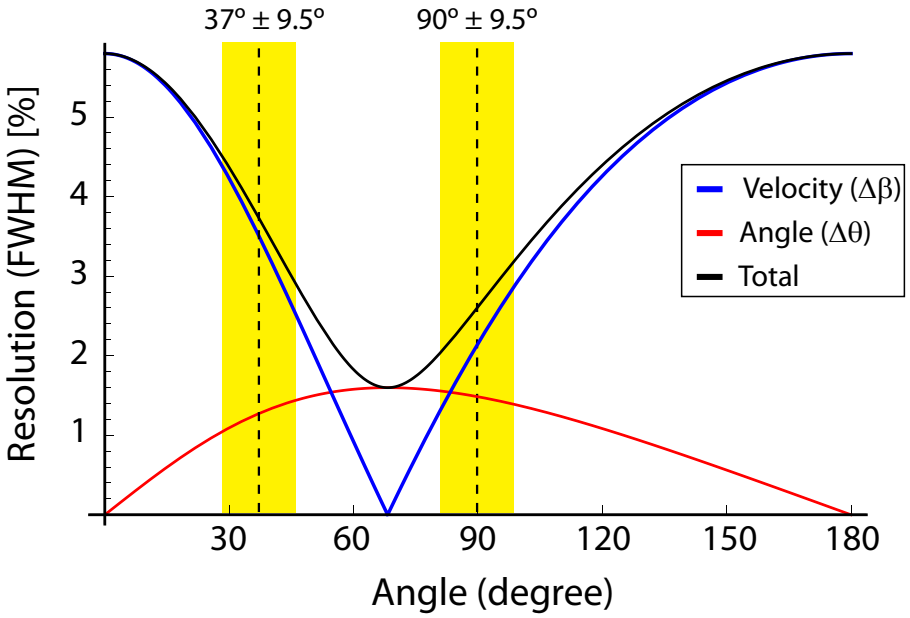

Figure 4.9: Contributions of the angular and velocity uncertainty to the total energy resolution of SeGA for $\beta = 0.371$, angular uncertainty of $\Delta\theta_{\text{lab}} = 0.04$ (from crystal segmentation size) and velocity uncertainty of $\Delta\beta = 0.05$ (from target energy loss). The polar angular coverage of each ring of detectors (37° and 90°) is shown in yellow.

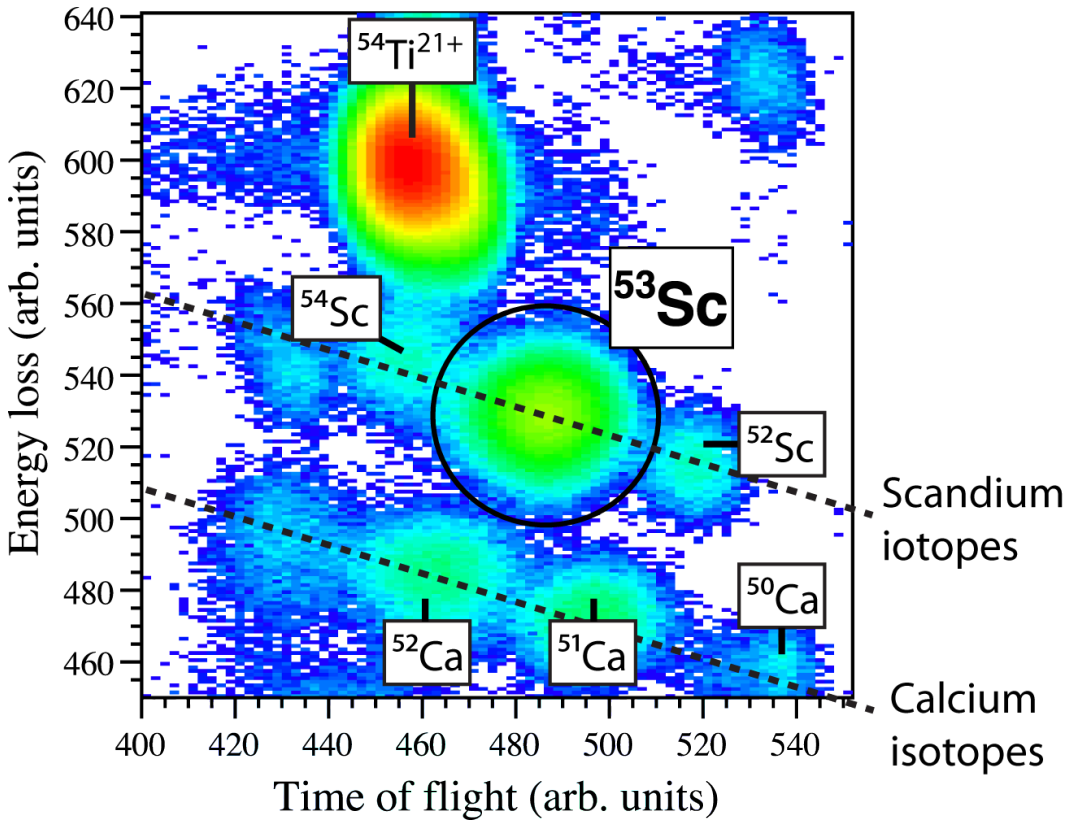

Figure 4.10: PID for the ^{9}Be(^{54}Ti, ^{53}Sc + γ)X reaction. ^{53}Sc, the one proton knockout residue from the incoming ^{54}Ti beam, is labeled, along with other reaction products. Isotopic lines are indicated for scandium and calcium to show how PID spectra are interpreted. Each reaction product is separated and has a definite loci. The colors, from blue to red, indicate intensity on a logarithmic scale. The high intensity loci to the upper left of ^{53}Sc is the $q = 21$ charge state of ^{54}Ti.

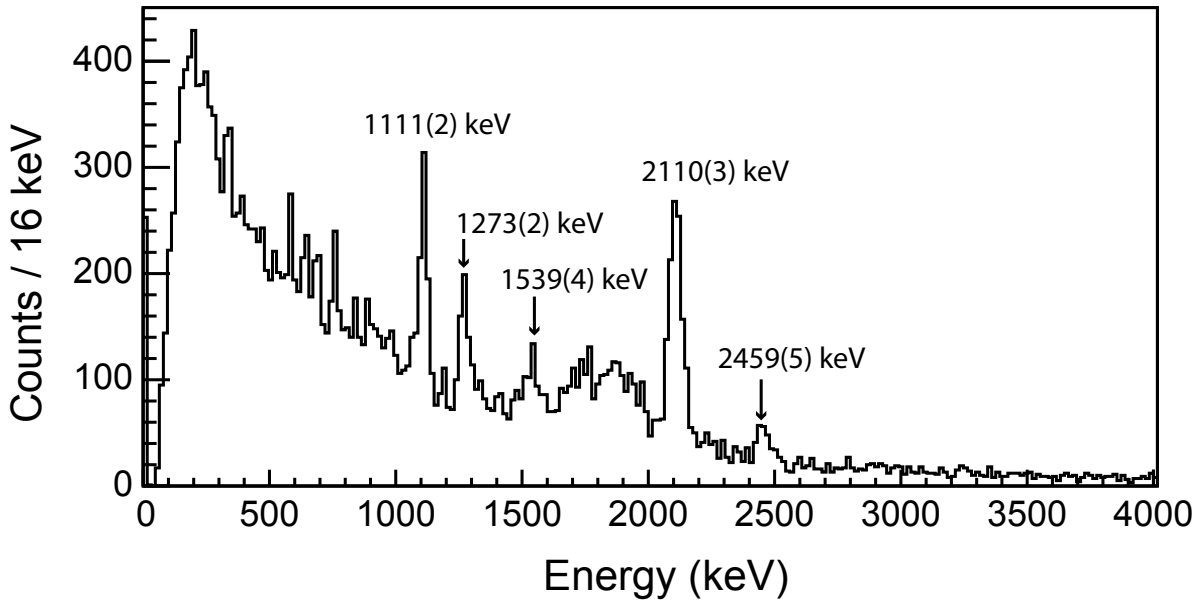

Figure 4.11: Doppler-reconstructed γ spectra in coincidence with the ^{53}Sc residues in the ^{9}Be(^{54}Ti, ^{53}Sc + γ)X reaction. A few transitions are labeled, including several newly reported transitions at 1111(2), 1273(2), 1539(4), and 2459(5) keV. For interpretation and further experimental details, see Section 5.6.2 (page 108).

Chapter 5

ONE PROTON KNOCKOUT FROM ^{54}TI TO ^{53}SC

5.1 Introduction and Motivation

The first experiment, whose analysis, results, and summary are contained in this chapter, focused on probing the single-proton structure of the $N = 32$ nuclei ^{54}Ti and ^{53}Sc with the goal of testing the validity of the nuclear shell model and valance space in this neutron rich region. The region around $N = 32$ from ^{52}Ca to ^{56}Cr has attracted considerable attention in recent years [40, 41, 43–46, 57, 137–143] as theorists and experimentalists (using a variety of experimental probes), have delineated the extent of the sub-shell gap and explicated its emergence in terms of fundamental components of the nuclear force.

Given the stated goals, knockout reactions provided the appropriate means. Knockout reactions, through the measurement of partial cross sections and longitudinal momentum distributions to final states in the knockout residue, can disentangle the ground-state nuclear wavefunction of the projectile and provide spectroscopic details of excited states in the residue (for example, the orbital angular momentum). For the ^{9}Be(^{54}Ti, ^{53}Sc $+\gamma$)X reaction, the experimentally extracted partial cross sections were starkly different than those calculated using a combination of shell model calculations (GXPF1 effective interaction and fp-shell model space) and single-particle cross sections, calculated in the eikonal framework reviewed in Section 3.4. Far more strength to excited states was measured (10.9(17) mb) than predicted (0.7 mb) (see Table 5.3). The investigation and resolution of this difference in strength, attributed to the knockout of deeply bound sd-

shell protons that lie outside the fp-shell model space, is addressed in this chapter. Before continuing with the details of the observed and predicted single-particle strength, it is worth reviewing the physics and background of the nuclear landscape around ^{54}Ti and ^{53}Sc, i.e. the $N = 32$ sub-shell gap. See Figure 5.1 for the location of the ^{9}Be(^{54}Ti, ^{53}Sc $+ \gamma$)X reaction within the nuclear landscape.

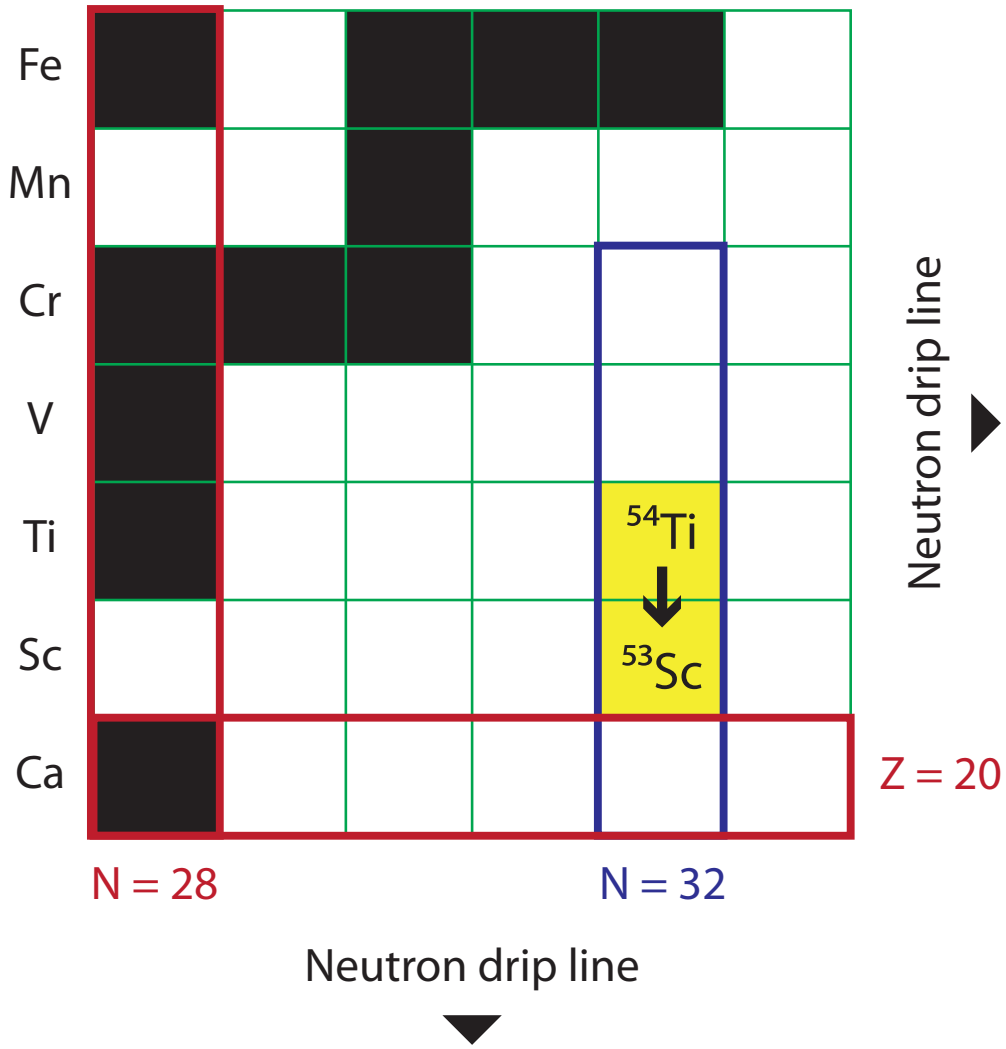

Figure 5.1: Nuclear landscape near the ^{9}Be(^{54}Ti, ^{53}Sc $+ \gamma$)X reaction, showing the stable isotopes in the valley of stability (filled black squares), the canonical $N = 28$ and $Z = 20$ shell gaps (red rectangles), and the emergent $N = 32$ sub-shell gap (blue rectangle), predicted and observed to occur between ^{52}Ca and ^{56}Cr. The gap disappears in ^{58}Fe because of the strength of the $V_{\sigma\tau}(\pi f_{7/2}, \nu f_{5/2})$ monopole force has sufficiently lowered the $\nu f_{5/2}$ orbital. The proton knockout reaction reaction from ^{54}Ti, in yellow, leads to the even more neutron-rich isotope ^{53}Sc.

5.2 The $N = 32$ shell gap

The $N = 32$ shell gap was first proposed by Tondeur [144] in 1981 from a self-consistent energy-density calculation. Following his prediction, a trove of experimental evidence has emerged confirming and delimiting the shell gap between the isotones ^{52}Ca and ^{56}Cr. The evidence includes mass measurements [39, 145], high $E(2_1^+)$ energies [40, 44, 138, 140], low electromagnetic transition probabilities $B(E2; 0^+ \rightarrow 2_1^+)$, and spacing of higher-spin structures [140, 143]. Two complementary mechanisms driving the change in shell structure were proposed [142]: a large gap between the neutron spin-orbit partners $\nu(2p_{3/2})$ and $\nu(2p_{1/2})$, and the reduction in strength of the strong $V_{\sigma\tau}(\pi f_{7/2}, \nu f_{5/2})$ monopole interaction between the $\pi(f_{7/2})$ and $\nu(f_{5/2})$ orbitals as protons are removed from the $f_{7/2}$ orbital. The reduction of the attractive force pushes the $\nu(f_{5/2})$ orbital to higher energy. As mentioned in Section 2.1, the spin-flip, $\pi\nu$ interactions, especially between $J_< = \ell - 1/2$ and $J_> = \ell + 1/2$ partners, are specially strong. $V(j_<^\pi, j_>^\nu)$ or $V(j_>^\pi, j_<^\nu)$ are proposed as the driving force behind the erosion of several major shells. The effect of the large spin-orbit splitting and reduction in the $V_{\sigma\tau}(f_{7/2}, f_{5/2})$ monopole interaction on the emergence of the $N = 32$ sub-shell gap for ^{53}Sc is shown in Figure 5.2.

A brief summary of the work on the $N = 32$ shell gap, per constituent isotope ^{52}Ca, ^{53}Sc, ^{54}Ti, ^{55}V, and ^{56}Cr, follows. Early β-decay work by Huck et al. [39] first identified the high 2_1^+ energy of ^{52}Ca at 2.56 MeV. They attributed the high energy of the 2_1^+ state to a subshell closure at $N = 32$. The energy of the 2_1^+ state was later verified through γ ray spectroscopy following the ^{9}Be(^{54}Ti, ^{52}Ca$+\gamma$)X reaction by Gade et al. [40]. The measured longitudinal momentum distributions of the ^{52}Ca residues were consistent with removal of two $f_{7/2}$ protons outside a ^{52}Ca core.

^{53}Sc, with one proton in the $1f_{7/2}$ orbital, had the least amount of spectroscopic information available. The first $3/2_1^-$ state was reported in Ref. [138] and its high excitation energy of 2109 keV was consistent with the existence of a $N = 32$ sub-shell gap. For additional details on ^{53}Sc, see Section 5.3.

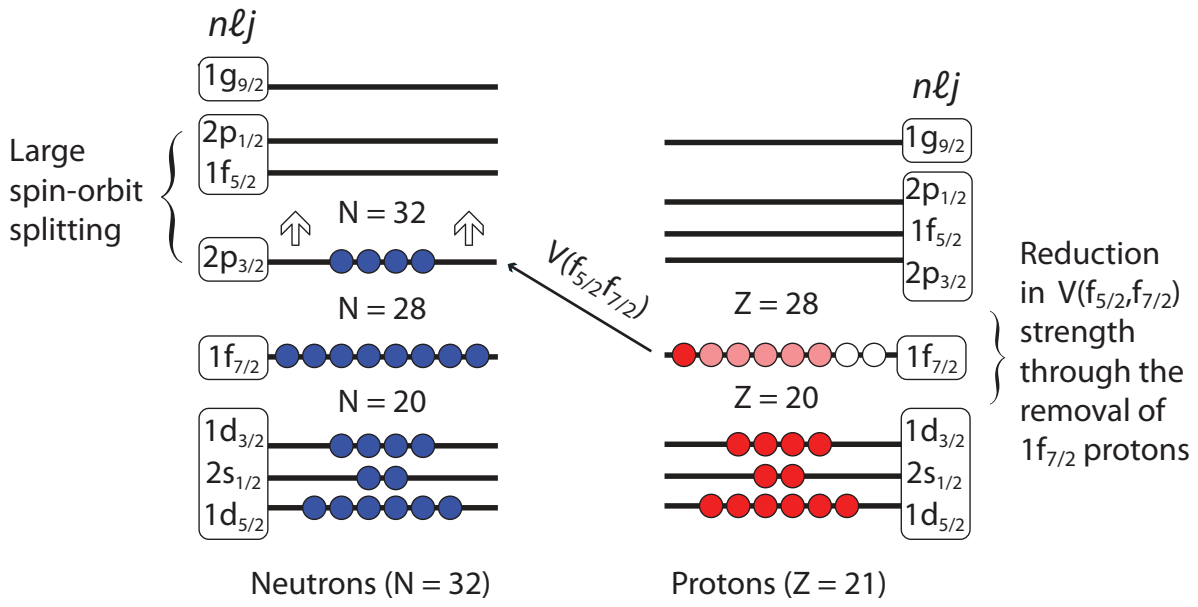

Figure 5.2: Physics of the $N = 32$ shell gap. Two effects are responsible: the large splitting between the spin-orbit partners $\nu(2p_{3/2})$ and $\nu(2p_{1/2})$, and the decrease in the strength of the strong, attractive $V_{\sigma\tau}(f_{7/2}, f_{5/2})$ monopole force as protons are removed from the $\pi 1f_{7/2}$ orbital. There are six protons shown in the $\pi f_{7/2}$ orbital. The first proton, shown as a red circle (●), represents ^{53}Sc. The addition of five more protons, shown as pink circles (●), to ^{53}Sc, creates ^{56}Cr, the upper limit of the $N = 32$ shell gap.

The spectroscopy of ^{54}Ti, by Janssens et al. [140], whom combined the spectroscopic results of two reactions, β-decay ($^{54}\text{Sc} \rightarrow {}^{54}\text{Ti}$) and deep-inelastic ($^{48}\text{Ca} + {}^{208}\text{Pb}$), provided evidence for the existence of a $N = 32$ sub-shell gap in ^{54}Ti through the measurement of the energy of the $E(2_1^+)$ state and though the measurement of the spacing and energies of the higher-spin states ($I \geq 8$). First, the measurement of the $E(2_1^+)$ energy for ^{54}Ti extended the systematics of the $E(2_1^+)$ states for even-even Titanium isotopes to ^{50,52,54}Ti, and the energy staggering, ending in a high $E(2_1^+)$ energy in ^{54}Ti of 1495 keV, mirrored similar staggering in ^{48,50,52}Ca and ^{52,54,56}Cr [142], nuclei previously shown to have a closed-shell character at $N = 32$.

Second, Ref. [140] noted the higher-energy spin states in ^{54}Ti, $J^\pi = 7^+ - 10^+$, involve neutron particle-hole excitations out of the closed-shell ^{52}Ca core. The 7^+ and 8^+ states are dominated by a $[\pi(f_{7/2})^2]_{J_p=6} \otimes [\nu(f_{7/2})^8(p_{3/2})^3(p_{1/2})^1]_{J_n=2}$ configuration, and the 9^+ and

10^+ states are dominated by a $[\pi(f_{7/2})^2]_{J_p=6} \otimes [\nu(f_{7/2})^8(p_{3/2})^3(f_{5/2})^1]_{J_n=3,4}$ configuration. The large spacing between the $J^\pi = 0^+_{\text{g.s.}}, 2^+_1, 4^+_1, 6^+$ orbitals, formed through the coupling of two $\pi f(f_{7/2})$ protons to the magic, $N = 32$ core, e.g. $[\pi(f_{7/2})^2]_{J_p} \otimes [\nu(f_{7/2})^8(p_{3/2})^4]_{J_n}$, and the higher-spin 8^+_1, 9^+_1, and 10^+_1 orbitals, created by the promotion of neutrons above the $N = 32$ sub-shell gap, reflects the high energy necessary to overcome the sub-shell gap. The spacing among the higher spin-states also reflects the relative spacing of the $\nu p_{1/2}$ and $\nu f_{5/2}$ orbitals and suggests, in reference to shell model calculations, the possible presence of a $N = 34$ shell gap.

This conjecture was later experimentally tested through the spectroscopy of ^{56}Ti by Fornal et al. [44] following heavy-ion, deep-inelastic collisions, and by Liddick et al. [57] in the β-decay of $^{56}\text{Sc} \rightarrow {}^{56}\text{Ti}$. Both experiments observed a $E(2^+_1)$ energy of 1128 keV that was not consistent with the presence of a $N = 34$ shell gap. Lastly, the work by Dinca et al. [43], confirmed the existence of the $N = 32$ shell gap through a simultaneous measurement of the energy of the $E(2^+_1)$ state and the reduced matrix element $B(E2; 0^+ \rightarrow 2^+_1)$ by the Coulomb excitation of ^{56}Ti. They did not find evidence for the $N = 34$ gap in ^{56}Ti.

The excitation spectra of ^{55}V and ^{55}Ti show similar evidence for a $N = 32$ shell gap [143]. The lower-spin $7/2^-_{\text{g.s.}}$, $11/2^-_1$, and $15/2^-_1$ states of ^{55}V (ground state, 1433 keV and 2508 keV respectively) are dominated by excitations in the proton $\pi f_{7/2}$ orbital, i.e. they have a dominate $[\pi(f_{7/2})^3]_{J_p} \otimes [\nu(f_{7/2})^8(p_{3/2})^4]_{J_n}$ configuration. The higher-lying spin states are dominated by neutron particle-hole excitations—for example, the $19/2^-_1$ state at 4696 keV has a dominate $[\pi(f_{7/2})^3] \otimes [\nu[(f_{7/2})^8(p_{3/2})^3(f_{5/2})^1]$ configuration—and the high excitation necessary to break the neutron configuration is evidence of the shell gap. Analysis of the spectrum of ^{55}Ti, in comparison to shell model calculations, showed similar jumps in energy in the excitation spectrum caused by a break in the neutron core. Thus, as reported in Ref. [143], ^{55}V and ^{55}Ti can be treated as a single proton and neutron outside of a semi-magic ^{54}Ti core.

As seen in Figure 5.1, ^{56}Cr marks the upper limit for the observed $N = 32$ shell gap.

The first work was done by Prisciandaro et al. [142], who completed the systematics of the even-even $N = 32$ isotones by measuring the energy of the first 2_1^+ state in ^{58}Cr through the β-decay of ^{58}K. A peak in excitation energy of the 2_1^+ state of ^{56}Cr in the chain of even-even Cr isotones suggested the presence of a shell gap. Additional spectroscopy was performed on the high-spin states following the heavy-ion, fusion-evaporation reaction $^{48}\mathrm{Ca}(^{11}\mathrm{B}, pxn)^{58-x}\mathrm{Cr}$ [46]. Both the energy of the $E(2_1^+)$ state and the ratio $E(4_1^+)/E(2_1^+)$, which approaches the vibrational limit, were good indicators of the $N = 32$ shell gap in ^{56}Cr. The complementary $B(E2; 0^+ \rightarrow 2_1^+)$ values for ^{54,56,58}Cr were measured by Bürger et al. [137], who observed a low $B(E2; \uparrow)$. The combination of high excitation energy of the 2_1^+ state and low electromagnetic transition probability are characteristic of shell gaps (see Section 1.2.4). The minimal $B(E2; \uparrow)$ values in the observed Chromium staggering occurred at $N = 28$ and $N = 32$. Finally, mass measurements of ^{56,57}Cr confirmed the increase of binding for ^{56}Cr through the difference between the measured two-neutron separation energy $S_{2n}(^{56}\mathrm{Cr})$ and a linear extrapolation based on $S_{2n}(^{54}\mathrm{Cr})$ and $S_{2n}(^{52}\mathrm{Cr})$.

5.3 Previous Studies of ^{53}Sc

Compared to its even mass neighbors ^{52}Ca and ^{54}Ti, less information was known about ^{53}Sc. A lower limit on the β-decay half-life of $\tau_{1/2}(^{53}\mathrm{Sc}) > 3\,\mathrm{s}$ was established by Sorlin et al. [146] during studies of the neutron-rich nuclei $^{53-55}$Sc and $^{56-69}$V. No decays were observed in the γ-ray spectrum following β decay within the 3.3 s observation window. Additional information was provided by Crawford et al. [138] through the β decay $^{53}_{20}\mathrm{Ca}_{33} \rightarrow {}^{53}_{21}\mathrm{Sc}_{32}$. A high energy of the $3/2_1^-$ state of 2110 keV was measured. The $3/2_1^-$ state was placed within a quintet of states from $3/2^-$ to $11/2^-$ formed by the coupling of the $\pi(1f_{7/2})$ orbital to the excited ^{52}Ca core: $[^{52}\mathrm{Ca}(2^+)] \otimes [\pi(f_{7/2})]_{J_p=7/2}$. Additional states in this quintet were measured at GANIL using deep-inelastic, multi-nucleon transfer reactions [147]. Of the measured transitions of 345(7), 2283(18), and 2617(20) keV, the two highest energy transitions were ascribed to the $9/2_1^-$ and $11/2_1^-$ yrast states.

5.4 Expectation and Prediction of Spectroscopic Strength in the *fp*-Shell Model Space

We can make a naive prediction for the strength of population of final states in ^{53}Sc, following the proton knockout reaction ^{9}Be(^{54}Ti, ^{53}Sc + γ)X, based upon a model of ^{54}Ti with two protons outside a doubly magic ^{52}Ca core. The removal of a proton from the $\pi(1f_{7/2})$ orbital in ^{54}Ti should strongly populate the $7/2^-_{\text{g.s.}}$ ground state of ^{53}Sc (see Figure 3.5), i.e. knockout to the ground state of ^{53}Sc should nearly exhaust the complete spectroscopic strength of 2 ($\pi f_{7/2}$ occupation number).

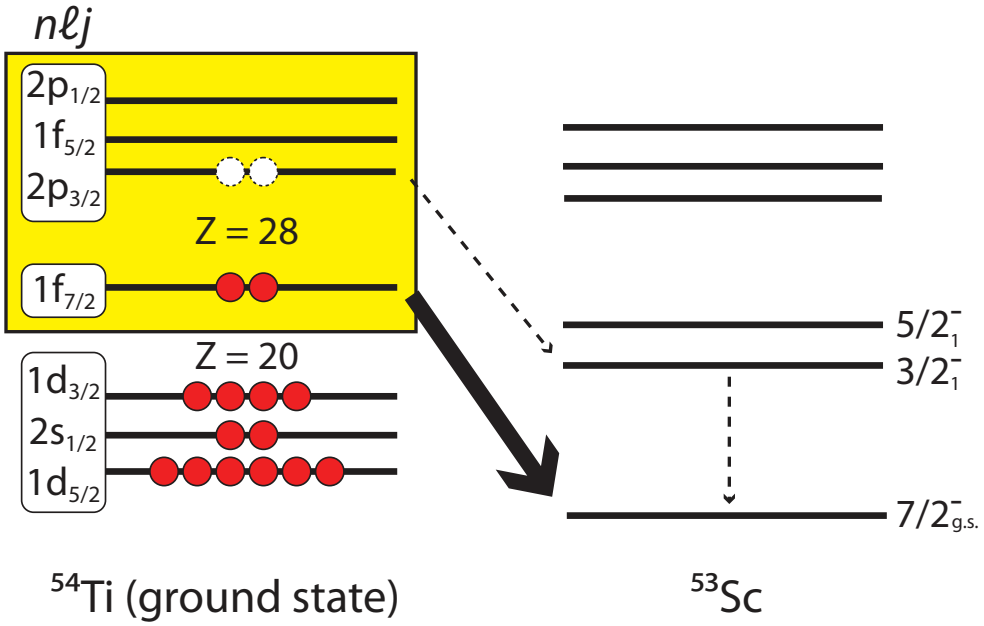

Figure 5.3: Naive model for the population of states in ^{53}Sc following the knockout of a proton from ^{54}Ti in the fp model space. With $Z = 22$, ^{54}Ti has two protons in the fp-model space that reside nearly exclusively, because of the canonical $Z = 28$ shell gap, in the $\pi(1f_{7/2})$ orbital. The removal of one of the $\pi(f_{7/2})$ protons will populate the ^{53}Sc $7/2^-_{\text{g.s.}}$ ground state (see Table 5.1). This strength is indicated by the large black arrow. There is a small probability of one or more protons occupying a higher orbital, e.g. the $\pi(2p_{3/2})$ orbital. The low occupancy is marked by dashed circles. The removal of a proton from the $\pi(2p_{3/2})$ orbital will predominately populate the $3/2^-_1$ state in ^{53}Sc, which will decay through γ ray emission. Note that by confining shell model calculations to the fp model space, strength from more deeply bound protons (e.g. sd shell) is not accounted for.

This basic prediction can be compared to shell-model calculations using the GXPF1 or

J^π	E_x (MeV)	C^2S
$7/2^-$	0 (g.s.)	1.85
$3/2^-$	2.194	0.062
$1/2^-$	3.231	0.012
$7/2^-$	2.246	0.008
$5/2^-$	3.361	0.005
$5/2^-$	5.294	0.005
$5/2^-$	5.513	0.004
$7/2^-$	3.486	0.003
$7/2^-$	5.154	0.002
$3/2^-$	5.178	0.002
$7/2^-$	5.582	0.001

Table 5.1: Theoretical energies and spectroscopic factors to final states in ^{53}Sc following the ^{9}Be(^{54}Ti, ^{53}Sc$+\gamma$)X reaction, listed in order of decreasing spectroscopic strength. Only values with $C^2S \geq 0.001$ are listed. Calculations were performed in OXBASH using the GXPF1 effective interaction and a fp model space. The spectroscopic strength to the ground state dominates, i.e. the removal of a proton from ^{54}Ti should almost exclusively populate the $7/2^-$ ground state of ^{53}Sc.

GXPF1A effective interaction [56, 58]. The GXPF1 effective interaction has been effective in predicting the spectroscopy of several isotopic chains through $N = 32$. That predictive power was experimentally shown to break down at $N = 34$. The GXPF1 effective interaction predicted a $N = 34$ shell gap in titanium that was not observed by Refs. [43, 44, 57], leading to the modification of five matrix elements mostly involving the $T = 1$ $f_{5/2}$ and $p_{1/2}$ orbitals. Shell model calculations using the GXPF1 and GXPF1A effective interactions gave similar excitation spectra (for ^{53}Sc) and spectroscopic factors for the ^{9}Be(^{54}Ti, ^{53}Sc $+\gamma$)X reaction. The results for the GXPF1 interaction are shown in Table 5.1. Note that there are no positive-parity states. These states, resulting from $1\hbar\omega$ particle-hole excitations from the *sd*-shell, are outside the model space. The *fp* model space used, $\pi(f_{7/2}p_{3/2}f_{5/2}p_{1/2})$ and $\nu(p_{3/2}f_{5/2}p_{1/2})$ (^{48}Ca core), excluded lower harmonic-oscillator shells.

The shell-model spectroscopic factors can be combined with calculated single-particle cross sections to provide theoretical partial cross sections that can be directly compared to experimental data (see Eqn. 3.18). Single-particle cross sections were calculated using

E_x (MeV)	$n\ell_j$	$S_p + E_x$ (MeV)	V_0 (MeV)	r_0 (fm)	a (fm)	σ_{strip} (mb)	σ_{diff} (mb)	σ_{total} (mb)
0.00	$1f_{7/2}$	15.26	64.2	1.29	0.7	6.57	1.68	8.25
2.11	$2p_{3/2}$	17.37	81.0	1.19	0.7	6.17	1.67	7.85
3.22	$1f_{5/2}$	18.48	72.0	1.31	0.7	5.44	1.32	6.76
3.38	$2p_{1/2}$	18.64	82.1	1.22	0.7	6.13	1.64	7.77

Table 5.2: Input parameters and results for the calculation of single-particle cross sections for the ^{9}Be(^{54}Ti, ^{53}Sc + γ)X reaction for *fp*-orbital knockout. The input parameters include the energy of the final state in ^{53}Sc (E_x), the orbital of the knockout nucleon in ^{54}Ti ($n\ell_j$), and the Woods-Saxon parameters used to calculate the wavefunction of the nucleon-core system (V_0, r_0, and a). The results of the calculation are broken down into stripping (σ_{strip}) and diffractive components (σ_{diff}). The total single-particle cross section is the sum of both.

the method outlined in Section 3.4.2. A Hartree-Fock calculation using the SkX Skyrme interaction [81] provided the density profile of the core. The density profile of the target was approximated as a Gaussian with a width σ of 2.36 fm. The core-nucleon wavefunction was calculated from the bound state of a Woods-Saxon Hamiltonian with a set diffuseness of $a = 0.7$ fm, and a orbital RMS separation radius of of $R_{sp} = r_0 A^{1/3}$. r_0 was adjusted so that R_{sp} matched the separation radius R_{sp}^{HF} predicted by the core Skyrme Hartree-Fock calculation. The potential depth V_0 was adjusted to reflect the physical separation of the nucleon from the core, i.e. $E_{\text{sep}} = S_p(^{54}\text{Ti}) + E_x(^{53}\text{Sc})$. The proton separation energy of ^{54}Ti is $S_p = 15.26$ MeV (systematic estimation, see Ref. [148]).

Combining the theoretical spectroscopic factors in Tables 5.1 and 5.2 with the center-of-mass correction of Section 3.2.6 and the single-particle cross sections, gives the theoretical partial cross sections for the population of final states in ^{53}Sc. These results are seen in Table. 5.3. The theoretical predictions, reflect our naive assumption. Nearly all the strength of the ^{9}Be(^{54}Ti, ^{53}Sc + γ)X reaction should populate the ground state of ^{53}Sc. The ^{53}Sc γ ray spectrum should be principally background, reflecting the negligible population of excited states of ^{53}Sc in the ^{9}Be(^{54}Ti, ^{53}Sc + γ)X reaction.

E_x (keV)	$n\ell j$	C^2S	σ_{sp} (mb)	σ_{th} (mb)
0	$1f_{7/2}$	1.85	8.25	16.2
2110	$2p_{3/2}$	0.06	7.85	0.5
2331	$1f_{5/2}$	0.01	6.76	0.1
3383	$2p_{1/2}$	0.01	7.77	0.1

Table 5.3: Theoretical spectroscopic factors (C^2S), single-particle cross sections (σ_{sp}), and theoretical partial-cross sections to final states in ^{53}Sc (σ_{th}). Only states with spectroscopic factors $C^2S \geq 0.01$ are shown (see Table 5.1).

5.5 Experimental Setup

5.5.1 Secondary-Beam Production

A ^{76}Ge primary beam, accelerated to 130 MeV/u and directed onto a 423 mg/cm^2 production target, produced a wide range of fragmentation products. The A1900 fragment separator, with a 300 mg/cm^2 Al wedge reduced the fragmentation products to a cocktail beam with three primary constituents: ^{54}Ti, ^{55}V and ^{57}Cr (see Figure 5.4 and Table 5.4). The cocktail beam was delivered to a 376 mg/cm^2 ^{9}Be target located at the pivot point of the S800 magnetic spectrograph. This secondary target was surrounded by SeGA in its classic configuration (see Section 4.4) consisting of 17 detectors arranged in two rings 37° and 90° with respect to the beam direction. The reaction residues produced in the reaction of the reaction beam with the secondary target were detected by the S800 spectrograph. The S800 detector systems were operated in coincidence with SeGA and therefore the heavy residuals detected in the spectrograph's focal plane could be correlated event-by-event to their de-excitation γ rays.

5.5.2 SeGA Efficiency Calibrations

As outlined in Section 4.4.3, the efficiency of SeGA is energy and threshold dependent and must be calculated on a per-experiment basis. Two sources were used to calibrate

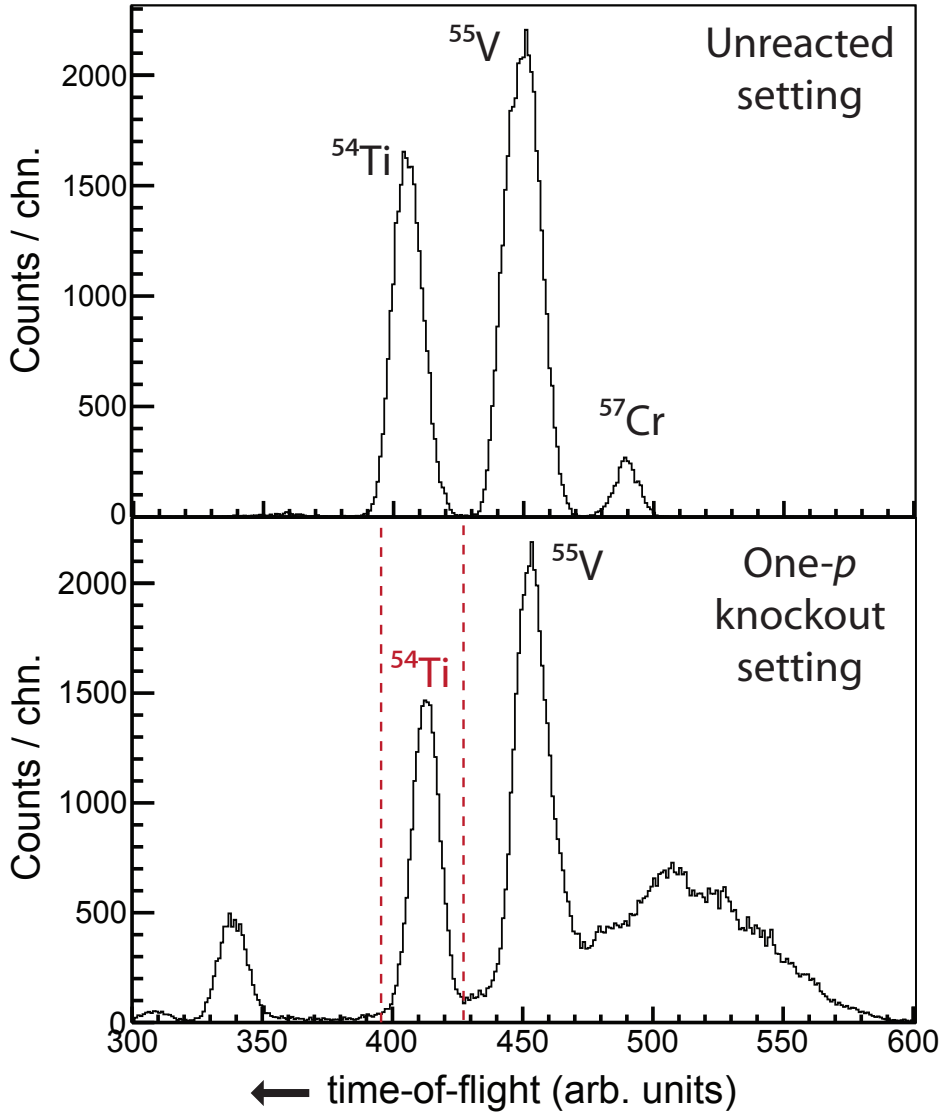

Figure 5.4: Time-of-flight spectrum for a unreacted run (top panel; projectiles centered in the S800 focal plane) and a reacted run (bottom panel; desired reaction channel centered in the focal plane) with ^{52}Ca centered in the focal plane. See text for more details. The TOF for the unreacted beam clearly shows the three cocktail components, ^{54}Ti, ^{55}V, and ^{57}Cr, listed in order of A/Q and therefore time-of-flight. The magnetic rigidity of the reacted run, set to center ^{52}Ca in the focal plane, also allows fragments created in the A1900 wedge with similar rigidity to enter the S800 focal plane. The fragmentation products produced in the wedge appear as broad hump at higher channels. Fortunately, a clean TOF gate can be placed around ^{54}Ti (red dotted line). The fragmentation products coincident with only incoming ^{54}Ti nuclei are shown in the PID plot of Figure 5.6.

Primary beam	^{76}Ge at 130 MeV/u and 25 pnA
Wedge	300 mg/cm^2 Al (achromatic)
A1900 momentum acceptance	Restricted 1 % momentum for the ^{53}Sc-centered and ^{54}Ti-centered runs used for the calculation of the inclusive and partial cross sections. No momentum restriction for γ-ray spectroscopy data collection runs (two-proton knockout residue ^{52}Ca centered in the S800 focal plane).
Typical intensity	^{54}Ti at 103 pps, ^{55}V at 85 pps, ^{57}V at 77 pps (1 % momentum acceptance)
S800 optics mode	Focus mode

Table 5.4: Secondary beam production for the ^{9}Be(^{54}Ti, ^{53}Sc + γ)X reaction.

the stationary-source efficiency of SeGA over a wide energy range, ^{152}Eu and ^{56}Co. The calibrations were done consecutively in two separate runs. The photopeak areas of nine peaks in the ^{152}Eu spectrum were extracted for energies between 121.8 keV to 1408.0 keV and the photopeak areas of eleven peaks from the ^{56}Co spectrum were extracted for energies between 846.8 keV to 3548.2 keV. The source calibration energies, listed in Table. 5.5, are a subset of the transitions listed in Table 4.5. The range of energies covered by the two calibration sources, 121.8 keV to 3451.2 keV, covered the full range of Doppler-boosted energies emitted by the fast-moving residue (see Eqn. 4.3). The highest energy transition seen in the residue's rest frame for ^{53}Sc, 2.4 MeV, was boosted to $\approx$ 3.0 MeV in the 37° ring.

The photopeak areas were then used to calculate the efficiency of SeGA for the specific source energies according to Eqn. 4.7. See Section 4.4.4 for further details. Given the high source activity, e.g. 313 100 Bq for ^{152}Eu, the DAQ livetime was low, below 20 %. The half-life of ^{152}Eu is $\tau_{1/2}(^{152}\text{Eu}) = 13.543\,\text{y}$; that of ^{56}Co, $\tau_{1/2}(^{56}\text{Co}) = 77.31\,\text{d}$. The ^{56}Co source was not absolutely calibrated and therefore the fit efficiency curve was scaled relative to the calibrated ^{152}Eu efficiency. Despite the lack of an absolute calibration, the ^{56}Co source was essential for providing calibration data for high-energy γ rays. The final

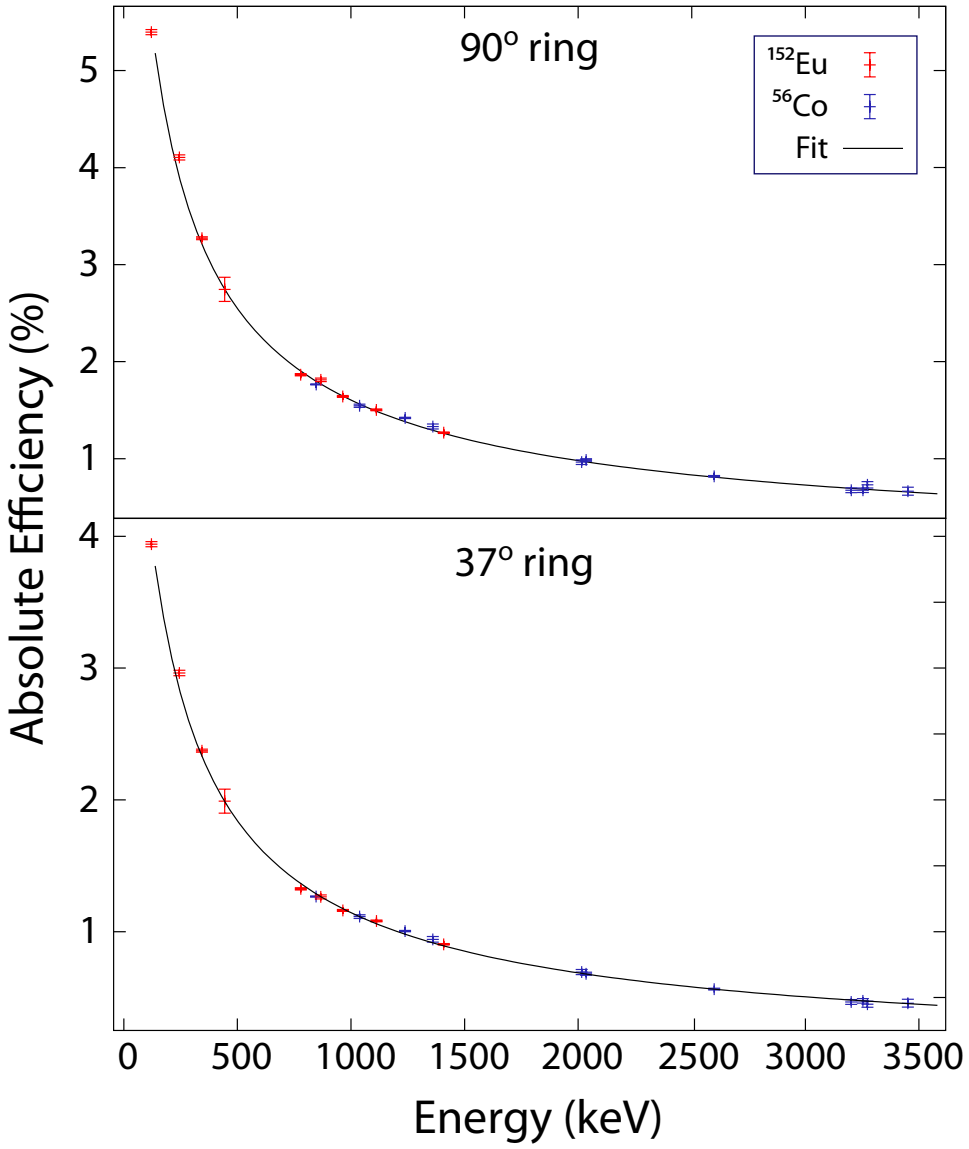

Figure 5.5: SeGA source efficiency curves for the 37° and 90° rings. The ^{56}Co source calibration was normalized to the calibrated ^{152}Eu source. The number of detectors in the 90° ring is greater than the number of detectors in the 37° ring (10 versus 7). This difference accounts for the increased efficiency of the 90° ring.

^{152}Eu (keV)	^{56}Co (keV)
121.8	846.8
244.7	1037.9
344.3	1238.3
444.0	1360.2
778.9	2105.2
867.4	2034.8
964.0	2598.5
1112.1	3202.0
1408.0	3253.4
	3273.0
	3451.2

Table 5.5: ^{152}Eu and ^{56}Co energies used in SeGA efficiency calibrations for the 37° and 90° rings.

	a	b	c
37°	2.943	0.792	-106.5
90°	3.259	0.759	-99.51

Table 5.6: Efficiency fit results for the ^{152}Eu and normalized ^{56}Co sources. The fit function is a slight rewrite of Eqn. 4.6: $f(E_\gamma) = a\exp(-b\log(E_\gamma - c + \exp(0.269E_\gamma)))$.

efficiency curves for the 37° and 90° ring are shown in Figure 5.5, and the fit parameters a, b, and c, are listed in Table 5.6.

The efficiency for a source at rest must be transformed to the efficiency for a residue rest-frame transition boosted into the lab frame. The method of calculating the efficiency for a measured residue rest-frame energy is covered in Section 4.4.4. The boosted efficiency for the two highest-intensity transitions observed in the γ ray spectrum of ^{53}Sc, 2.11 MeV and 1.76 MeV, are 2.8(1)% and 1.76(5)%.

5.5.3 Particle Identification

The complete reaction process requires the identification of three components: the incoming projectile species, the projectile-like residue, and the γ rays coincident with the

reaction residue. As covered in Section 4.3, the incoming projectile is identified through its time-of-flight between two thin plastic scintillators located at the end of the A1900 fragment separator and at the object position of the S800 analysis beam line (XFP and OBJ scintillators). The associated spectra are shown in Figure 5.4 for a reacted run (upper panel) where the magnetic rigidity of the S800 spectrograph was changed (decreased relative to ^{54}Ti) to center ^{52}Ca in the focal plane, and an unreacted run (lower panel) where the magnetic rigidity of the S800 was tuned to center the incoming cocktail beam in the focal plane. The detection of a residue by the E1 scintillator is used by the S800 trigger module, along with input from a secondary detector depending on the trigger logic (S800 singles or S800-SeGA coincidences) to issue a master trigger. Because a projectile must survive to the focal plane to issue a trigger, the observed spectra for the OBJ or XFP scintillators depends on the rigidity of the spectrograph. Thus the difference in the two TOF spectra of Figure 5.4.

By applying the slice gate seen in the lower panel of Figure 5.4 to the reaction products detected in the S800 focal plane, only the reaction products of ^{54}Ti are selected. A particle-identification (PID) matrix of TOF versus energy loss in the ion chamber, gated on incoming ^{54}Ti projectiles, provides an identification of the reaction residues event-by-event. The PID for ^{54}Ti, corrected in the manner shown in Section 4.5.1, is shown in Figure 5.6.

5.6 Results

5.6.1 Inclusive Cross Section

A multitude of different fragmentation products, including the proton knockout reaction channel ^{9}Be(^{54}Ti, ^{53}Sc + γ)X, were detected in the focal plane[1]. Through the application of a TOF gate on the incident projectile ^{54}Ti (see Figure 5.6) and a contour gate on the

[1]The ^{9}Be(^{54}Ti, ^{53}Sc + γ)X knockout data was taken from a larger data set devoted to the two-proton knockout reaction ^{9}Be(^{54}Ti, ^{52}Ca + γ)X [40].

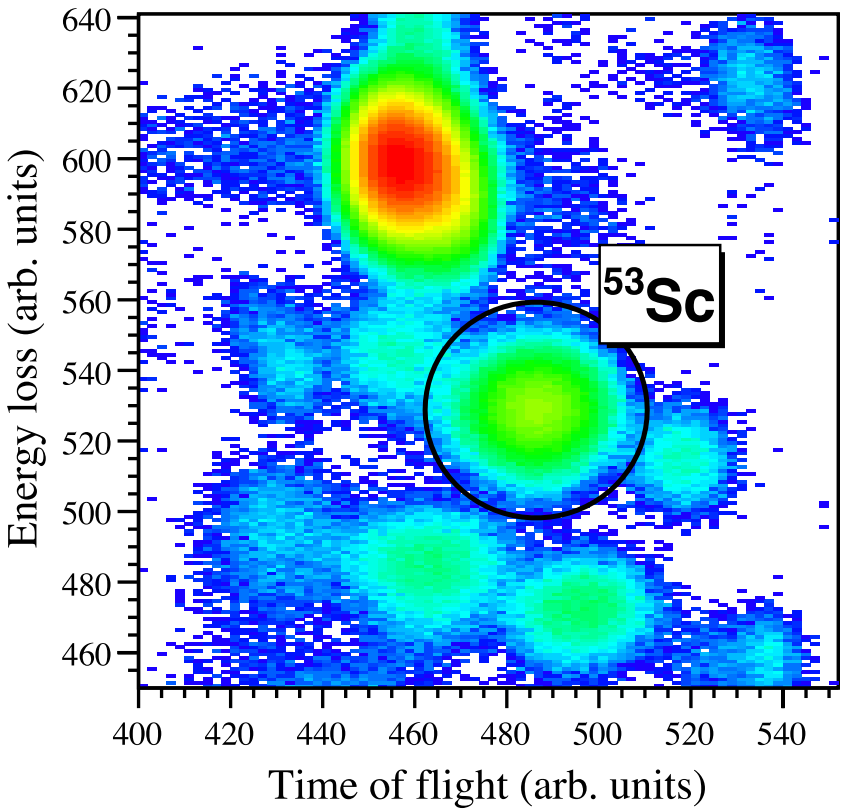

Figure 5.6: Particle identification plot for the ^{9}Be(^{54}Ti, ^{53}Sc + γ)X reaction, gated on the incoming ^{54}Ti projectile shown in the lower panel of Figure 5.4. The TOF is corrected for the ion's flight path through the magnetic spectrograph. See Section 4.5.1.

knockout reaction residue ^{53}Sc (see Figure 5.4), events from the ^{9}Be(^{54}Ti, ^{53}Sc + γ)X reaction were selected on an event-by-event basis. Although the momentum acceptance of the S800 is large ($\Delta p/p = \pm 2.5\,\%$), it could not accommodate the full momentum distributions of both ^{53}Sc and ^{52}Ca in the S800 focal plane. As a result, for most runs, ^{53}Sc was not centered in the focal plane, and instead entered at the edge of the S800 acceptance. With a big and uncertain acceptance correction, these runs could not be used for the determination of the inclusive cross section. To extract an accurate inclusive cross section, ^{53}Sc was briefly centered in the S800 focal plane. From the integration of ^{53}Sc in the PID for the ^{53}Sc-centered run, relative to the number of incoming ^{54}Ti and the ^{9}Be target density, the

inclusive cross section was calculated. See Eqn. 4.15 for the full list of required quantities. The final inclusive cross section for the one-proton knockout reaction from ^{54}Ti to ^{53}Sc is $\sigma_{\mathrm{inc}} = 17.6(6)\,\mathrm{mb}$.

Acceptance corrections have a complex dependency on the dispersive and non-dispersive angles and momenta of the reaction residues. These quantaties can be calculated using the position and angles of the residues measured in the focal plane, and then transformed to angles and momenta at the target using an inverse map (see Section 4.5.3). The four reconstructed measurements used in acceptance calculations are labeled: ATA (dispersive angle at the target), DTA (dispersive differential energy at the target), BTA (non-dispersive angle at the target), and YTA (non-dispersive position at the target).

Fortunately, because of the high fragment velocity of $v \sim 0.3\,\mathrm{c}$ and heavy mass of the residue, the reaction products were very forward focused. With the magnetic rigidity of the spectrograph set to center ^{53}Sc in the focal plane, acceptance losses were minimal and only evident in the dispersive direction (see Figure 5.7). To account for these losses, the DTA distribution was fit by several different curves. Examples include a single Gaussian, a double Gaussian (two floating Gaussians), and a skew Gaussian (single Gaussian with different widths σ_- and σ_+). The missing area in the tail was approximated by the area under these curves. The ratio the uncorrected area, to of the total area, including the estimated area under the tail, is the acceptance correction A of Eqn. 4.15. The difference in tail area resulting from the different fits contributed to the systematic error.

The error of 0.6 mb includes both statistical and systematic contributions. The statistical Poisson uncertainties (see Eqn. 4.17) are dominated by the number of detected projectiles (^{54}Ti) and the number of detected residues (^{53}Sc)[2].

[2]Errors are combined through the standard propagation of errors, e.g.

$$\sigma_f^2 = \sum_{i=1}^{a} \sigma_i^2 \left(\frac{\partial f}{\partial x_i}\right)^2 + 2 \sum_{i \neq j}^{a} \sigma_i \sigma_j \left(\frac{\partial f}{\partial x_i}\right)\left(\frac{\partial f}{\partial x_j}\right) + \cdots, \tag{5.1}$$

where f is the full inclusive cross section $\sigma_{\mathrm{inc.}}$ of Eqn. 4.17. Because the different errors

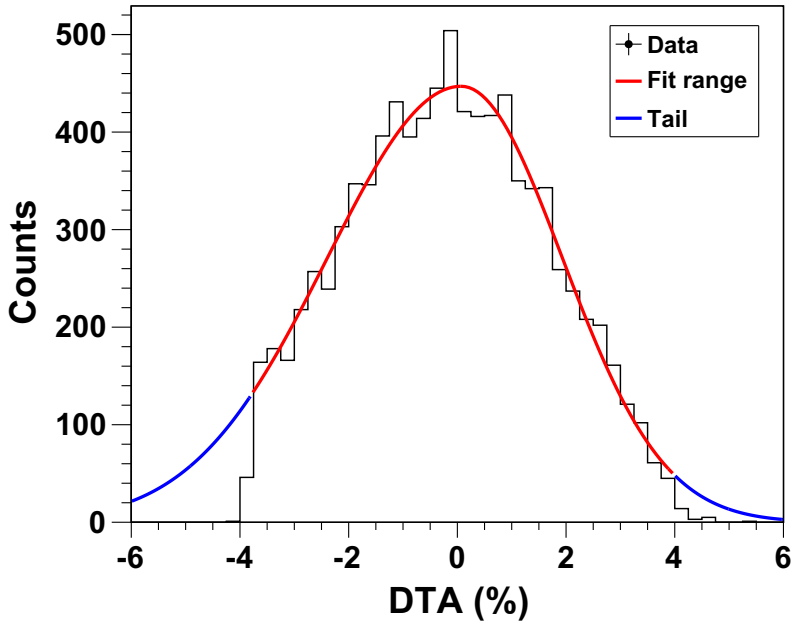

Figure 5.7: Acceptance correction for ^{53}Sc. A skew Gaussian fit is shown. The ^{53}Sc residues lost to acceptance cuts are estimated by the area under the left tail. Several different parametrizations were used. The differences in area due to these different parametrizations contributed to the total uncertainty for the inclusive cross section.

There were several additional sources of systematic error beyond the uncertainty in the acceptance correction: target thickness and stability of the cocktail beam. The uncertainty on the target thickness was provided by the manufacturer. Details on the stability of the cocktail beam follow. By taking both ^{53}Sc and ^{54}Ti of Eqn. 4.17 relative to the integrated beam rate in the OBJ and XFP scalars, we assume that the composition of the cocktail beam does not change. While this approximation is reasonable, the local fluctuation of the beam composition should be folded into the systematic uncertainty. An estimation of the fluctuation came by measuring the proportion of ^{54}Ti relative to the total rate as taken from the OBJ and XFP scalers for several runs on either side of the run used for the determination of the cross section. The fluctuation on the ratio, 3%, provided a reasonable estimate for the stability of the beam composition. The extracted uncertainty was added in quadrature to the other contributions listed above.

---

were uncorrelated, the second term, and other higher order terms were zero.

5.6.2 Observed γ Ray Transitions

The Doppler-reconstructed γ ray spectrum, in coincidence with the ^{53}Sc residues of is shown in Figure 5.8. As outlined in Section 4.4.2 the γ rays were boosted from the lab frame to the residue rest frame using the angle of γ ray emission calculated from the position of the detector Ge crystal segment with the highest energy deposition relative to the position of the target. The fragment velocity $\beta = v/c$ at the moment of γ decay was adjusted to align the Doppler-reconstructed spectra in the forward (37°) and backwards (90°) ring. β values were determined transition-by-transition because of possible differences in lifetime effects. γ rays are emitted in flight by the projectile-like residue, and the velocity of the residue when it decays depends on the amount of target material transversed. For very short lifetimes, e.g. of order $\tau_{1/2} < 1\,\text{ps}$, the average decay position is approximately mid-target (at a incident velocity of $v \sim 0.3\,\text{c}$, the projectiles are traveling at approximately 1 cm per ns). For longer lifetimes of $\tau_{1/2} > 1\,\text{ps}$ the average decay position will be further downstream. Significant lifetimes of a state are noticed in the β value that is near or equal to the end-target value β_{end} and in the shape of the γ ray peak in the spectrum.

The target position z_{tar} effects all angles in the Doppler reconstruction. To fix the target position, a transition of known energy and short half-life, ensuring an average mid-target decay, was used as a reference. For this data, the reference was the $E_\gamma(1494.8\,\text{keV}; 2^+ \rightarrow 0^+)$ 0.9 ps transition in ^{54}Ti.

Both β and z_{tar} were optimized over a grid of possible z_{tar} and β values. z_{tar} was optimized to minimized the absolute difference of the true peak position of 1495 keV and the measured peak position in the Doppler reconstructed spectrum. The optimal β value, as mentioned, was chosen to minimize the absolute difference in energy between the 37° and 90° rings. A target position of $z_{\text{tar}} = 0.15\,\text{cm}$ was extracted, and the uncertainty of transition energies in ^{53}Sc was directly connected to the uncertainty in this choice of z_{tar} through finite difference calculations. z_{tar} was varied at $z_{\text{tar}} \pm \sigma_z$ and the effect on $E_\gamma(\beta, z_{\text{tar}})$ was measured.

Energy (keV)	δE(fit) (keV)	δE(sys.) (keV)	$\delta E(\Delta\beta)$ (keV)	$\delta E(\Delta z)$ (keV)	δE(tot.) (keV)
2110	0.80	0.36	0.42	2.30	3
2459	3.12	0.72	2.13	3.03	5
1111	0.80	0.08	0.17	0.98	2
1273	1.31	0.18	0.39	1.08	2
1539	3.32	1.19	1.30	1.86	4

Table 5.7: Error budget for the measured transition energies in ^{53}Sc.

With the z_{tar} position fixed to the 1495 keV transition in ^{54}Ti, the energy of the first $E_\gamma(3/2^-_1 \rightarrow 7/2^-_{\text{g.s}}) = 2110(3)$ keV transition was in agreement with the previous reported value of 2109 keV by Ref. [138]. In addition to confirming this transition, four new transitions at 1111(2), 1273(2), 1539(4) and 2459(5) keV were reported [42]. The knockout reaction is not expected to populate the $9/2^-$ and $11/2^-$ high-spin states of 2283 keV and 2617 keV reported by Ref. [147] because of the connection between angular momentum j^π of the removed nucleons and the angular momentum of the residue I^π. For single-nucleon knockout from an even-even nuclei like ^{54}Ti, and assuming no coupled-channels effects, these values are identical.

The energy resolution was dominated by the target thickness. See Section 4.4.2 and Figure 4.9. The peak position uncertainties combine the statistical uncertainty from fitting, as done by a fitting code written in the ROOT Data Analysis Framework [149], and the systematic uncertainty that includes both the uncertainty in target position (δz_{tar}) and the uncertainty in velocity ($\delta\beta$) (see Table. 5.7).

5.6.3 Partial Cross Sections

Only the ^{53}Sc-centered run could be used for the extraction of the partial cross section. Both the stripping and diffractive components of the single-particle cross section involve an average over all momentum projections m of the removed nucleon with total angular momentum j (see Eqn. 3.20 and Eqn. 3.22). Each projection m has a different differential

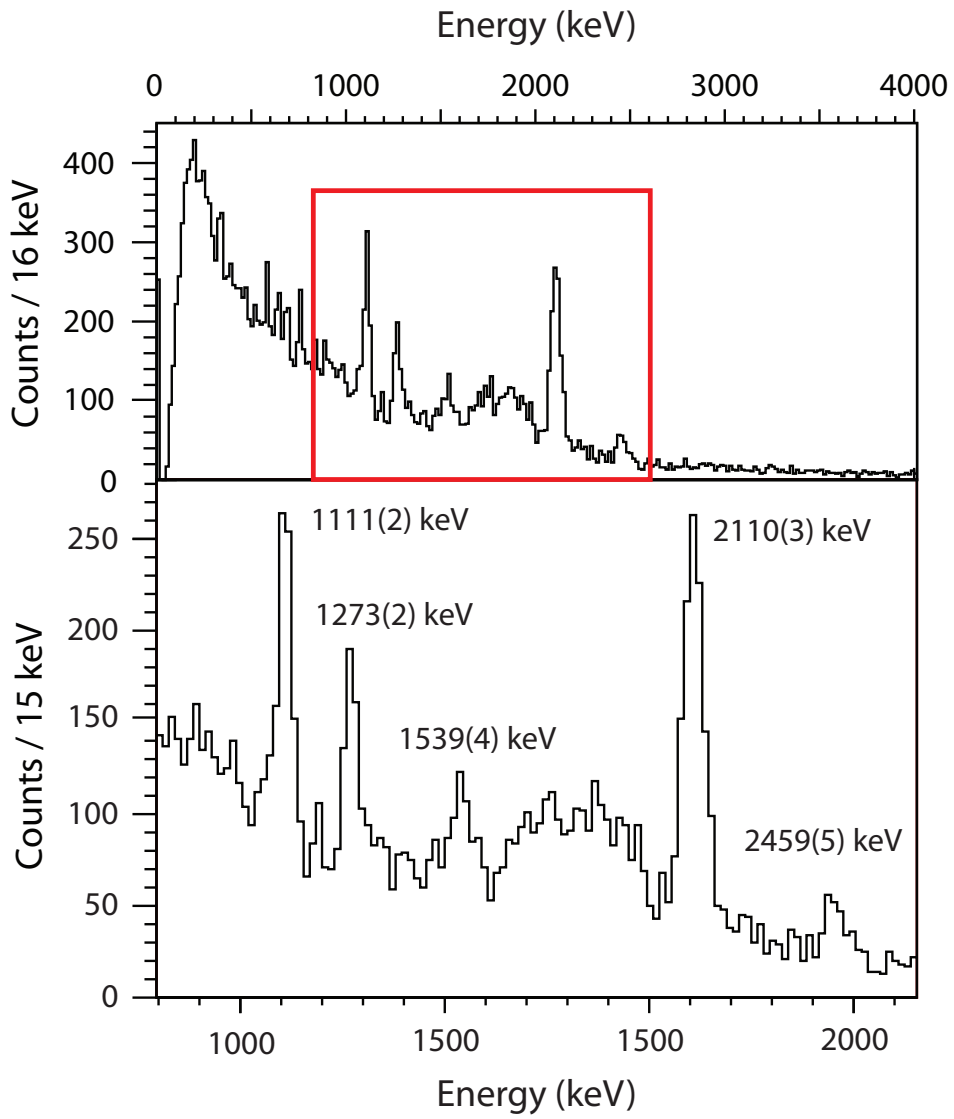

Figure 5.8: Doppler-reconstructed γ ray spectrum of ^{53}Sc. The 2110(3) keV transition, first reported in Ref. [138], was confirmed, and four new transitions at 1111(2), 1273(2), 1539(4), and 2459(5) keV were seen. The lower panel is an expansion of the red rectangle insert of the upper spectrum.

Energy (keV)	δA(stat.) (counts)	$\epsilon_{\mathbf{SeGA}}$(boost.) (%)	$\sum_i \sigma_i$ (mb)	$\delta\left(\sum_i \sigma_i\right)$ (mb)
2110	99	1.760	10.9	1.7
2459	–	1.570	–	–
1111	39	2.814	2.7	0.4
1273	30	2.551	2.3	0.8
1539	–	2.222	–	–

Table 5.8: Measured partial cross sections to final states in ^{53}Sc. The summation over index i indicates the feeding has not been subtracted. Because of the low statistics in the ^{53}Sc-centered run, the areas for two transitions could not be extracted. These are indicated by an en dash (–).

momentum distribution and carries a different fraction of the total, angle-integrated cross section. By selecting a portion of the momentum distribution, the contributions of the different projections to the cross section changes, affecting the final averaged value. Partial cross sections can only be reliably extracted for runs with small acceptance corrections. The large reduction in statistics forced by the use of the single ^{53}Sc-centered run, increased the statistical uncertainty of the partial cross sections and reduced the number of peaks from which a peak area could be confidently extracted.

Partial cross sections must be corrected for feeding, the contribution to the photopeak area from transitions decaying into the state of interest. Unfortunately, because of low statistics associated with the only ^{53}Sc-centered run, the orbital angular momentum assignments associated with the exclusive parallel momentum distributions could not be used to construct a level diagram. Level assignments were only based upon intensity balances and comparisons with shell model.

5.7 Knockout of Deeply Bound Protons

5.7.1 Knockout From the *sd* Shell

With a large overlap between the ground-state wavefunctions of ^{54}Ti and ^{53}Sc ($C^2S = 1.85$), theory, restricted to the proton fp-shell, predicts most (95 %) of the cross section strength will directly populate the ^{53}Sc ground state. From Table 5.3, the summed strength to excited states is only 0.7 mb. In contrast, as inferred from Table 5.8, experiment observes a large percentage, a clear majority, of the total knockout strength feeds excited states in ^{53}Sc. There is an obvious discrepancy between the measured and expected population of excited states. To provide an upper limit on the population of the ^{53}Sc ground state, we can assume the first $3/2^-_1$ state at 2.1 MeV acts like a funnel. The cross section to of all states higher in energy, both observed and unobserved, funnel through this state. Making this approximation, we have

$$\sigma_{\text{g.s.}} = \sigma_{\text{inc}} - \sigma_{2.1\,\text{MeV}} = 6.7(18)\,\text{mb}. \tag{5.2}$$

In this extreme condition, 6.7 mb or 60 % of all cross section goes to excited states (see Table 5.9). The factor of 0.4 between the theoretical partial cross section to the ground state of 16.2 mb and the experimental upper bound of $\sigma_{\text{g.s}} \leq 6.7$ mb is in agreement with the reduction factor systematics reported in Ref. [150].

Experimentally, measured spectroscopic strengths are lower than both the simple IPM predictions (single Slater determinant and full occupancy), and shell model calculations that account for some of the reduction in single-particle strength through configuration mixing. The additional reduction in strength beyond IPM and CI calculations are caused by correlations, for example short-range and long-range. The short-range correlations come from both the extreme repulsion at small distances and the tensor NN interaction. The long-range correlations include coupling of the single-particle strength to low-lying collective excitations (e.g. *2p1h* and *1p2h* excitations and giant resonances). The result

Energy (keV)	$\sigma_{\text{th.}}$ (mb)	$\sigma_{\text{exp.}}$ (mb)
0	16.2	6.7(18)
2110	0.5	–
2331	0.1	–
3383	0.1	–
$\sum_i \sigma_i^{\text{excited}}$	0.7	10.9(17)

Table 5.9: Comparison of theoretical predictions and experimental measurements of the summed strength to states in ^{53}Sc. The measured partial cross sections are divided between the ground and excited states assuming all excited states decay through the 2.1 MeV $3/2^-_1$ state (see Eqn. 5.2). The factor of 0.4 between the theoretical and measured partial cross section to the ground state is commensurate with the reduction factor systematics of Ref. [150]. The large discrepancy between the measured and predicted strength of excited-state population can be resolved if knockout of deeply-bound *sd*-shell protons (outside the *fp*-shell model space) is considered.

of this coupling is a fragmentation of the single-particle strength to high energies, well beyond the limited model space of most shell-model calculations.

The observed experimental strength to excited states must lie outside the model space of the GXPF1 shell-model calculations. That is, we must consider knockout from more deeply bound *sd*-shell protons. In this new picture, the removal of protons from the $\pi(1f_{7/2})$ orbital directly populates the ^{53}Sc ground state, in accordance with the theoretical predictions of Table 5.1, and the strength to excited states is attributed nearly exclusively to *sd*-shell knockout of protons. This strength populates higher-energy states above the first $3/2^-_1$ state, which then feed through the $3/2^-_1$ state to the ground state. The schematic of this model is seen in Figure 5.9.

Although the strength of population to excited states strongly suggests a picture where spectroscopic strength originates from the knockout of deeply-bound *sd*-shell protons, we can look for further support in the population of excited states for the analogous regular-kinematics reaction ^{50}Ti(d, ^{3}He)^{49}Sc and in the inclusive parallel momentum distribution of ^{53}Sc.

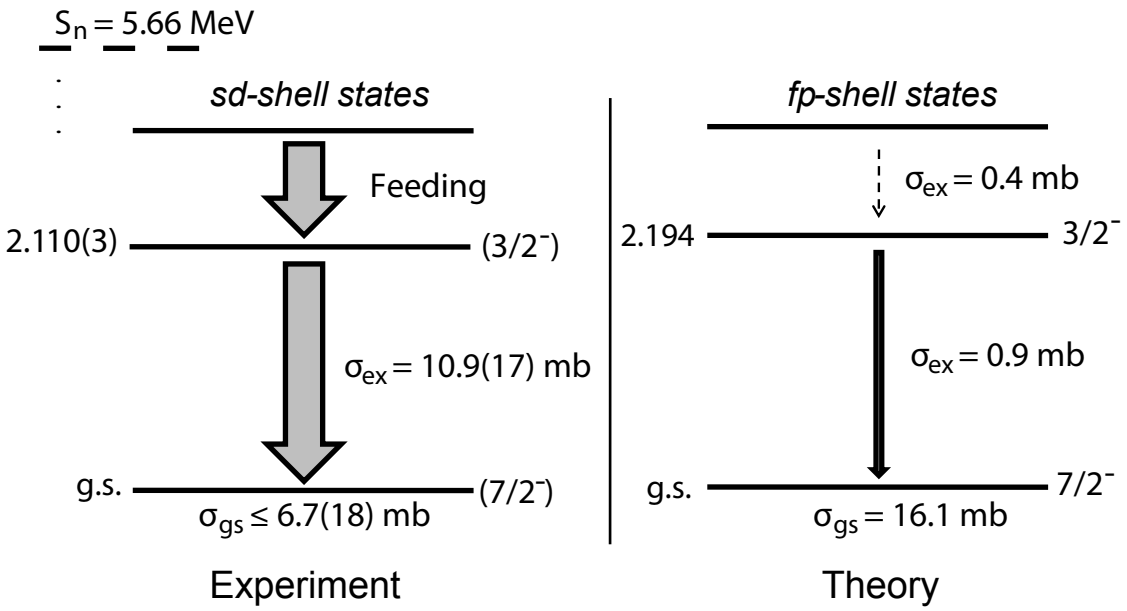

Figure 5.9: Comparison of the theoretical and experimental population of ^{53}Sc in the ^{9}Be(^{54}Ti, ^{53}Sc + γ)X reaction. The energy in MeV, the assumed spin-parity, and summed partial cross sections (sum of feeding and direct population) in mb are displayed. Theory, restricted to the *pf*-shell, predicts most of the knockout strength will directly populate the ground state (95 %); experimentally a large population of excited states (≥ 60 %) is observed.

5.7.2 The ^{50}Ti(d,^{3}He)^{49}Sc and ^{9}Be(^{54}Ti,^{52}Ca + γ)X Reactions

Support for the interpretation of the excited state strength from particle-hole excitations in the *sd*-shell comes from *sd*-shell strength observed in the ^{9}Be(^{54}Ti, ^{52}Ca + γ)X [40] and ^{50}Ti(d, ^{3}He)^{49}Sc reactions [87]. In the two-proton knockout from ^{54}Ti [40], appreciable strength was observed to feed the 3990 keV 3^-_1 state in ^{52}Ca, bypassing the first 2^+ state at 2563 keV. Of the total inclusive strength of $\sigma_{\text{inc.}}$ = 0.32(4) mb, 67(7) % populated the ground state. Given the selectivity of the knockout to the occupancies and orbitals of the removed proton in the initial ^{54}Ti nucleus, the population of the ground state was attributed to the removal of two correlated protons in the $\pi(1f_{7/2})$ orbital and the population of the 3^-_1 state was attributed to the simultaneous removal of two correlated protons from a $\pi(1f_{7/2})$ orbital and an *sd*-shell orbital. This initial conjecture was confirmed by

shell model calculations using the modified WBMB Hamiltonian [151]. Although effective interactions for the excitation of protons into the *fp*-shell are poor—the calculation placed the 3^- state ~ 3 MeV above the experimental value—based on the negative-parity ^{52}Ca spectrum and the theoretical maximum possible cross section to the 3^- state that was several times the experimental value, the shell model calculations provided qualitative support of the strong presence of *sd*-shell particle-hole excitations in the ^{9}Be(^{54}Ti, ^{52}Ca $+\gamma$)X reaction.

^{50}Ti and ^{54}Ti share the same number of protons ($Z = 22$) and are semi-magic in the number of neutrons (the canonical $N = 28$ shell gap for ^{54}Ti; the emergent $N = 32$ shell gap for ^{54}Ti). Thus, we can look to the similar, regular-kinematics transfer reaction ^{50}Ti(d, ^{3}He)^{49}Sc, as performed by Doll et al. [87], to gauge the importance of *sd*-shell excitations. They observed significant spectroscopic strength to excited states, and based on the shape of the angular distributions of the ^{3}He residues for different final state of ^{49}Sc, from which angular momentum assignments of the removed nucleon in ^{50}Ti could be extracted, most of the strength was attributed to the removal of *sd*-shell protons. In particular, this includes the population of the 2.23 MeV and 3.36 MeV states that exhaust nearly the full spectroscopic strength of the $2s_{1/2}$ and $1d_{3/2}$ orbitals [$C^2S(1/2^+, 2s_{1/2}) = 1.40(10)$ and $C^2S(3/2^+, 1d_{3/2}) = 3.62(20)$, respectively].

The results of both reactions, ^{9}Be(^{54}Ti, ^{52}Ca $+\gamma$)X and ^{50}Ti(d, ^{3}He)^{49}Sc strongly support that in the case of the ^{9}Be(^{54}Ti, ^{53}Sc $+\gamma$)X reaction, a sizeable fraction if not all of the strength to excited states in ^{53}Sc can be attributed to the removal of *sd*-shell protons.

5.7.3 Inclusive Parallel Momentum Distribution

As discussed in Section 3.4.4, the parallel momentum distributions of the knockout residues provide information on the orbital momentum distribution of the removed nucleon. Although statistics prevented any meaningful extraction of parallel momentum distributions for individual states, there was enough statistics to extract the experimental

Energy (MeV)	$n\ell j$	C^2S
0.00	$1f_{7/2}$	1.91(20)
2.23	$2s_{1/2}$	1.40(10)
2.36	$1d_{3/2}$	3.62(20)
3.55	$1d_{5/2}$	0.30
3.77	$1d_{5/2}$	0.30
4.01	$2s_{1/2}$	0.22
4.86	$1d_{5/2}$	0.43
5.28	$1d_{5/2}$	0.20
5.60	$1d_{5/2}$	0.20
6.32	$1d_{5/2}$	≤ 0.29
6.32	$1d_{5/2}$	≤ 0.50
6.43	$1d_{5/2}$	≤ 0.50
7.37	$1d_{5/2}$	0.42
7.60	$1d_{5/2}$	0.29
8.59	$1d_{5/2}$	0.29
9.20	$1d_{5/2}$	0.19

Table 5.10: Summary of experimental spectroscopic results for the ^{50}Ti(d, ^{3}He)^{49}Sc reaction as reported by Doll et al. [87]. Strong transfer involving the *sd*-shell protons is seen in the large spectroscopic factors for the positive parity $1/2^+$ and $3/2^+$ 2.3 MeV and 2.36 MeV levels.

inclusive parallel momentum distribution for the ^{53}Sc-centered run. The inclusive momentum distribution includes the summation of all bound final states in the ^{9}Be(^{54}Ti, $^{53}\mathrm{Sc}+\gamma$)X reaction. As per the conjecture of the previous two sections, the dominance of *sd*-shell strength to excited states in ^{53}Sc, the inclusive momentum distribution is likely a superposition of distributions associated with the removal of protons from the $f_{7/2}$ and *sd*-shell orbitals. To check the experimental inclusive cross section for consistency, a theoretical distribution consisting of $f_{7/2}$ and *sd* components with a relative ratio extracted from experiment—6.7(18) mb for $f_{7/2}$ knockout (38 %) and 10.9(17) mb for *sd*-shell knockout (62 %)—was fit to the experimental longitudinal momentum distribution. Additional details will follow.

The experimental parallel momentum distribution was extracted, as explained in Section 4.5.3, from the position and angles of the knockout residues measured by the

position-sensitive CRDC detectors, and then mapped from the focal plane to the target through trajectory reconstruction. This differential energy distribution at the target was then transformed to differential momentum through the use of a relativistic scale factor (see Eqn. 4.18).

The theoretical distributions were calculated according to Section 3.4.4 using the same eikonal Glauber model and S-matrices used in the calculation of the single-particle cross sections. The distribution for *sd*-shell knockout was constructed from an admixture of $\pi(1d_{3/2})$ and $\pi(2d_{1/2})$ orbitals. These contributions were weighted by their full spectroscopic strength: $C^2S(d_{3/2})/C^2S(s_{1/2}) = 2$. After combining the *sd*-distribution and the $f_{7/2}$ distributions, weighted according to their partial cross sections, the final admixture was boosted to the lab frame and then folded with the profile of the incoming beam (see Figure 5.10). With the theoretical and experimental distributions on the same footing, the theoretical distribution was scaled to fit to the experimental distribution.

The resultant fit is seen in Figure 5.10, and the overlay is consistent with the removal of protons from both the $f_{7/2}$ and *sd*-shell ($1d_{5/2}$ and $2s_{1/2}$) orbitals with the fraction proposed before. The shape of the high-momentum component of the distribution places the greatest constraint on the orbital angular momentum assignment of the removed nucleon. The low momentum side is affected by a commonly observed artifact: a low momentum tail formed from a shift of cross section from higher to lower momentum. This effect is likely caused by events where there is significant energy exchange with the target nucleus (stripping component) and it is not described by the simple Glauber model used in the single-particle cross section and parallel momentum distribution calculations. This effect is discussed further in Ref. [152].

5.8 Summary

In the ^{9}Be(^{54}Ti, ^{53}Sc$+\gamma$)X reaction, the 2110(3) keV, $3/2^-_1 \rightarrow 7/2^-_{\text{g.s}}$ ground-state transition was identified and four more, previously unidentified γ rays were measured at 1111(2) keV,

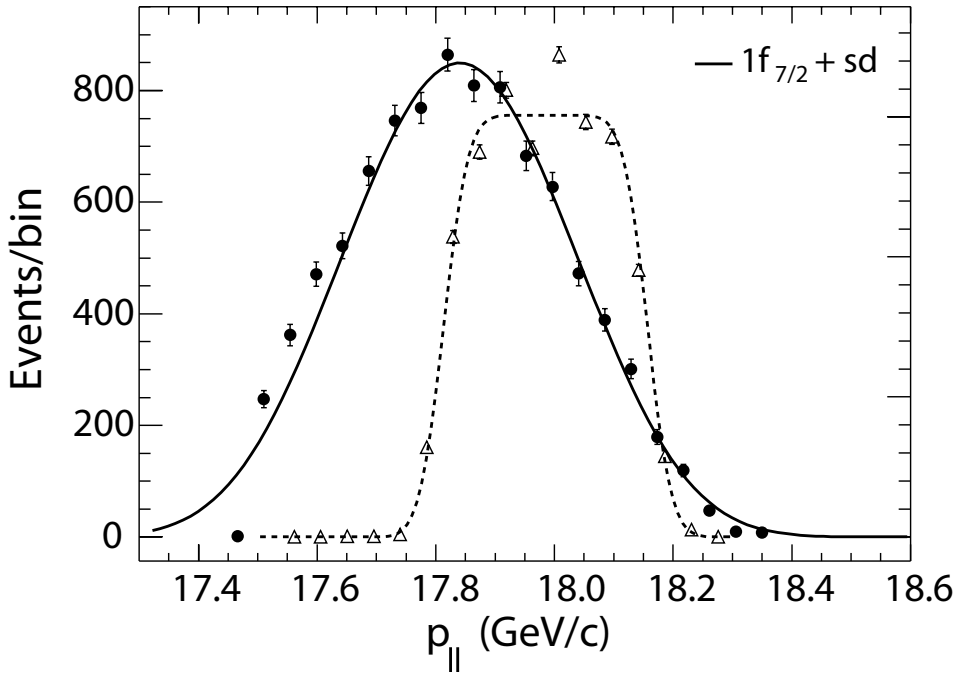

Figure 5.10: Momentum profile of the incoming ^{54}Ti beam (triangles), a fit to the ^{54}Ti momentum profile (used in the creation of the theoretical distribution; see Section 4.5.3) and the measured parallel momentum distribution of ^{53}Sc (circles) compared to theoretical calculations. The theoretical distribution is composed from the addition of $f_{7/2}$ and *sd*-shell contributions, as weighted by their measured partial cross sections: 38% $f_{7/2}$ ($\sigma = 6.7$ mb) and 62% *sd*-shell ($\sigma = 10.9$ mb). The *sd*-shell distribution was created from the addition of $d_{3/2}$ and $s_{1/2}$ contributions as weighted by their full spectroscopic strength, $C^2S(d_{3/2})/C^2S(s_{1/2}) = 2$.

1273(2) keV, 1539(4) keV, and 2459(5) keV. Based on the overwhelming population of excited states ($\approx 60\%$), in comparison to the negligible feeding predicted by shell model calculations within the *fp* model space (see Table 5.3), these excited states were identified as positive-parity states populated through the removal of deeply-bound *sd*-shell protons. This picture is consistent with the results of the two-proton knockout reaction ^{9}Be(^{54}Ti, ^{52}Ca+γ)X and the regular-kinematics transfer reaction ^{50}Ti(d, ^{3}He)^{49}Sc, and with the fit of the experimental inclusive parallel momentum distribution with a calculated distribution that includes an admixture of both $f_{7/2}$ and *sd* shell components mixed according to their extracted partial cross sections.

These results highlight the need for improved cross-shell interactions in the shell

model in this region, and the equivalent experimental need for quantitative spectroscopic information on *sd*-shell configurations at low excitation energy.

Chapter 6

ONE-PROTON PICKUP REACTIONS CENTERED AROUND ^{50}FE

6.1 Motivation

^{9}Be-induced, proton [60, 61, 118, 119] and neutron [153] pickup reactions, with fast beams and inverse kinematics, have recently emerged as a spectroscopic tool for probing *particle*-like states in exotic nuclei whose short half-lives and low production rates make them inaccessible by traditional, low-energy transfer reactions using light beams (e.g. (d,p), $(^{3}\mathrm{He},d)$, etc.) in normal kinematics and conventional, stable targets. Because of momentum matching considerations, the single-nucleon pickup reaction with fast beams in inverse kinematics preferentially populates single-particle states in the projectile with higher orbital angular momentum. As suggested in Refs. [60, 61, 153] and covered in Section 3.5.1, this preferential population might be used to track the descent of higher orbital angular momentum intruder states, for example the $\nu(1f_{7/2})$ orbital whose migration enables the hallmark $2p2h$ configurations in the ground state wavefunction of "island of inversion" nuclei. Lastly, the developments with light, non-cryogenic, non-gaseous, targets (e.g. ^{9}Be) offer experimental advantages over the earlier, more-complex, liquid ^{4}He targets [118, 119] (see Section 3.5.2).

The motivation for this work is two-fold: first, we seek to further develop single-proton pickup reactions as a spectroscopic tool by comparing the magnitude and population pattern of final states following proton-pickup from light targets in three fp shell nuclei. Proton and neutron pickup reactions using a beryllium target and neutron pickup reactions

using both a beryllium and carbon target have been performed along and near the $N = 10$ isotonic chain: ^{9}Be(^{20}Ne, ^{21}Na+γ)X [60], ^{9}Be(^{22}Mg, ^{23}Al+γ)X[61], ^{9}Be(^{22}Mg, ^{23}Mg+γ)X [153], and ^{12}C(^{22}Mg, ^{23}Mg+γ)X [153]. These measurements have shown consistent agreement between the magnitudes and population of excited states as predicted by shell model and reaction theory. In Ref. [60] (see Section 3.5.2) the population patterns observed in the ^{9}Be(^{20}Ne, ^{21}Na + γ)X reaction were consistent with the traditional ^{20}Ne(^{3}He, d)^{21}Na reaction [119]. We seek to perform the first proton pickup reactions on fp shell nuclei: ^{9}Be(^{48}Cr, ^{49}Mn + γ)X, ^{9}Be(^{49}Mn, ^{50}Fe + γ)X, ^{9}Be(^{50}Fe, ^{51}Co + γ)X, ^{12}C(^{48}Cr, ^{49}Mn + γ)X, ^{12}C(^{49}Mn, ^{50}Fe + γ)X, and ^{12}C(^{50}Fe, ^{51}Co + γ)X. See Figure 6.1 for the location of these reactions within the nuclear landscape. Further consistency between measured and predicted yields will show the applicability of single-nucleon pickup reactions across a wide range of the nuclear chart.

Second, we seek to test the reaction theory mechanism through the use of two different targets—a 188 mg/cm^2 ^{9}Be target offering well-bound (S_p = 16.9 MeV) protons, and a 72.8 mg/cm^2, ^{12}C target, offering well-bound (S_p = 16.0 MeV) protons—and through the analysis of the measured, lab-frame momentum distributions of ^{49}Mn, ^{50}Fe, and ^{51}Co, where differences from the expected momentum distributions, created from the convolution of the momentum width of the incoming beam with the differential momentum loss in the target, can reveal higher order, possibly multi-step processes. The target structure enters the calculation of the single-particle cross sections through the overlaps of the form $\phi(\boldsymbol{r}) = \langle ^{A}\mathrm{Z}|\hat{a}^{\dagger}|^{A-1}(\mathrm{Z\text{-}1})(I^{\pi})\rangle$ and the associated spectroscopic factors, e.g. $S = \int d\boldsymbol{r}|\phi(\boldsymbol{r})|^2$. See Section 6.4.2 and Section 6.5.2 for more details. Using two different targets, the effects of the magnitude and inclusiveness over final target residue states can be roughly gauged.

Altogether, six different reactions were analyzed: ^{9}Be(^{48}Cr, ^{49}Mn+γ)X, ^{9}Be(^{49}Mn, ^{50}Fe + γ)X, ^{9}Be(^{50}Fe, ^{51}Co + γ)X, ^{12}C(^{48}Cr, ^{49}Mn + γ)X, ^{12}C(^{49}Mn, ^{50}Fe + γ)X, and ^{12}C(^{50}Fe, ^{51}Co + γ)X. The work contained herein is broken down into two main sections, proton pickup reactions induced by a beryllium target (Section 6.4) and proton pickup reactions

induced by a carbon target (Section 6.5). Within each section, the experimental results are compared with theoretical predictions. The complete work is reviewed in the final summary, Section 6.6.

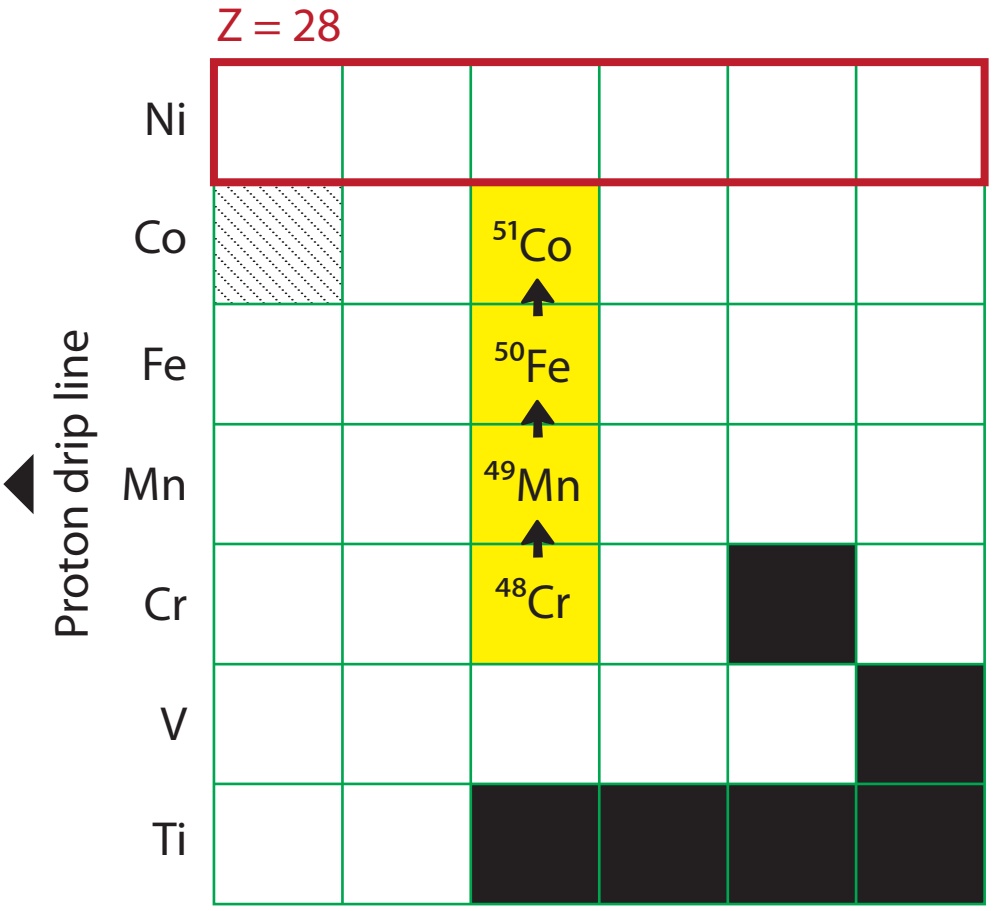

Figure 6.1: Nuclear chart showing the inclusive set of isotopes and reactions studied in this work (yellow squares): T(^{48}Cr, ^{49}Mn + γ)X, T(^{49}Mn, ^{50}Fe + γ)X, and T(^{50}Fe, ^{51}Co + γ)X for target choices $T \equiv {}^{9}$Be and $T \equiv {}^{12}$C. Stable nuclei are indicated by black squares. The unbound nucleus ^{49}Co, revealing the close proximity of the proton drip line, is indicated by a diagonal hash pattern, and the nearby $Z = 28$ magic number, corresponding to the close of the $\pi f_{7/2}$ orbital, is highlighted by a red rectangle. The direction of the pickup reaction from ^{48}Cr to ^{49}Mn, from ^{49}Mn to ^{50}Fe, and from ^{50}Fe to ^{51}Co is indicated by black arrows. Note that the final $A + 1$ pickup residues are more proton-rich than the initial A projectile.

6.2 Background

A limited amount of spectroscopic information is available for the $A+1$ proton-pickup reaction products ^{49}Mn, ^{50}Fe, and ^{51}Co. For ^{49}Mn and ^{50}Fe, the available information includes the location and tentative spins and parities of the low-lying states as probed through a variety of different reactions. A full evaluation for ^{49}Mn is found in Ref. [154] and includes spectroscopy from the β^+-decay of ^{49}Fe (following the β^+-delayed proton emission of ^{50}Co) [155] and γ ray spectroscopy following deep inelastic ^{12}C(^{40}Ca, $2np\gamma$)^{49}Mn [156] and ^{24}Mg(^{28}Si, $p2n\gamma$)^{49}Mn [157] reactions. The full collection of identified states span from the $5/2^-_{\text{g.s}}$ ground state to a high-spin $(31/2^-)$ state at 10.7 MeV.

Full evaluations for ^{50}Fe and ^{51}Co can be found in Ref. [158] and Ref. [159] respectively. ^{50}Fe has been studied through ^{50}Co β^+ decay [155, 160], ^{51}Ni β^+-delayed proton emission [160], and intermediate energy Coulomb excitation [161]. Nine states up to 8.5 MeV have been identified, including the first 2^+_1, 4^+_1, 6^+_1, and 8^+_1 states. No spectroscopic information was available for the most proton-rich of the isotopes ^{51}Co, potentially because of both its low-production cross section and its low proton separation energy of only $S_p = 88$ keV (Ref. [148]; from systematic trends).

6.3 Experimental Setup

6.3.1 Beam Production

The final cocktail beam, optimized for the production of ^{50}Fe, used a primary beam of ^{58}Ni accelerated to 160 MeV/u. The primary beam was fragmented on a 893 mg/cm^2 Be production target and the desired reaction products were selected by rigidity and charge with the A1900 fragment separator, operating at 1 % momentum acceptance for all measurements (reacted and unreacted settings). A 300 mg/cm^2 $^{\text{nat}}$Al wedge, inserted at

Primary beam ^{58}Ni at 160 MeV/u
Wedge 300 mg/cm^2 ^{27}Al (achromatic)
A1900 momentum acceptance 1 % for all measurements.
Cocktail composition and intensity ^{48}Cr at 2.5×10^3 pps; ^{49}Mn at 2.0×10^3 pps; and ^{50}Fe at 0.5×10^3 pps
S800 optics mode Focus mode

Table 6.1: Experimental characteristics of secondary beam production for the proton pickup reactions ^{9}Be(^{48}Cr, ^{49}Mn + γ)X, ^{9}Be(^{49}Mn, ^{50}Fe + γ)X, ^{9}Be(^{50}Fe, ^{51}Co + γ)X, ^{12}C(^{48}Cr, ^{49}Mn + γ)X, ^{12}C(^{49}Mn, ^{50}Fe + γ)X, and ^{12}C(^{50}Fe, ^{51}Co + γ)X.

the Image 2 position of the A1900 (see Figure 4.2) separated nuclei with similar rigidity according to their nuclear charge via energy loss. See Section 4.2 for additional details. A summary of the beam production settings and the final composition and component rates of the cocktail beam used in this analysis is found in Table. 6.1. A two-dimensional PID plot of XFP time-of-flight versus OBJ time-of-flight[1] showing the composition of the incoming cocktail beam is presented in Figure 6.2. The data shown is taken from a subset of data collection runs using the ^{12}C target. The ^{12}C target data was taken later in the experiment, after changes to the TOF electronics. Further details will be covered in later sections.

6.3.2 S800 Setup and Target Selection

The full set of S800 detectors and TOF scintillators were individually calibrated in the standard way. See Chapter 5 for the calibration procedures associated with the analysis of the ^{9}Be(^{54}Ti, ^{53}Sc + γ)X knockout reaction. The CRDC pads, critical for position and momentum measurements, were adjusted for similar gain, bad pads were removed from the center-of-gravity calculations of dispersive position, and position measurements were calibrated using the aid of masks with known hole positions placed in front of each

[1] See Table 6.3 for an overview of the physical TOF measurements corresponding to the labels OBJ and XFP.

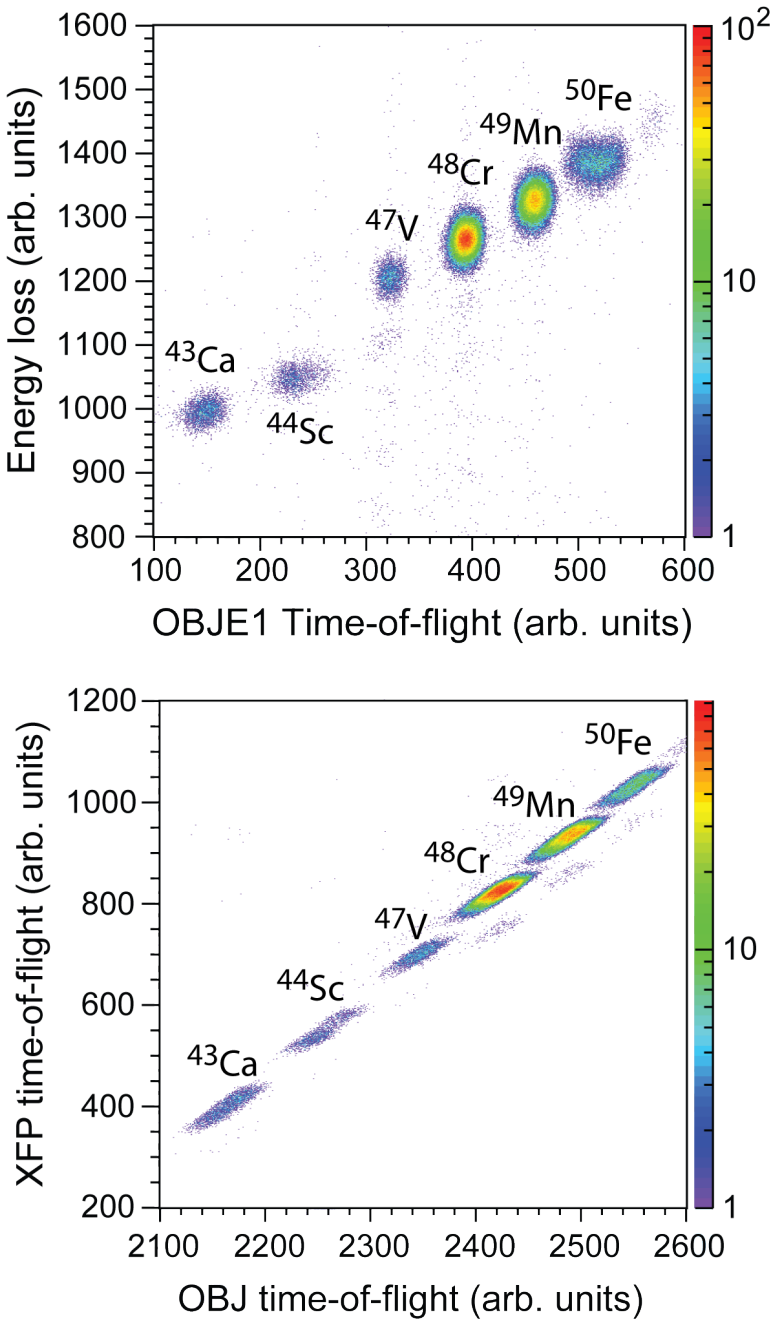

Figure 6.2: Particle identification spectra for an unreacted run (components of the incident cocktail projectile beam are centered in the focal plane) on the ^{12}C target showing the composition of the incoming cocktail beam. The upper pane shows a standard S800 PID plot of the TOF between the object scintillator (OBJ) and the back of the S800 focal plane (E1 scintillator) versus energy loss in the focal plane ion chamber. See Table 6.3 for a description of the OBJ, XFP, and OBJE1 labels given to the different TOF measurements. The lower pane is a two-dimensional TOF spectrum of XFP versus OBJ time-of-flight that can be used, like the one-dimensional difference spectrum shown in the bottom panel of Figure 6.4, to select a single component of the incoming cocktail beam.

CRDC. The TOF of projectiles through the spectrograph were adjusted using the position and angles of the projectiles in the focal plane to account for differing trajectories (see Section 4.5.1).

Run-by-run calibrations were performed for the CRDC non-dispersive position (to account for changes in the drift gas mixture), ion chamber energy loss, and various time-of-flights (OBJ and XFP). With a large number of experimental changes throughout the experiment (see Section 6.3.4), careful run calibrations ensured that the collection of gates and calibrations done for one condition (e.g. XFP-OBJ TOF before the addition of delays) would still apply after changes to the experimental setup (e.g. after the addition of delays).

Three different targets were used in the experiment: ^{9}Be, ^{12}C and ^{93}Nb. Experimental difficulties associated with the heavy ^{93}Nb target, including the increased production of charge states, prevented its inclusion in the present analysis. The ^{9}Be target thickness was 188(4) mg/cm^2 (as provided by the manufacturer). The ^{12}C target thickness of 72.8(13) mg/cm^2 was calculated from the weight, area, and thickness of the carbon foil. The error associated with the thickness of the carbon target was calculated from the associated errors in the geometric parameters as combined according to the standard propagation of errors equation.

6.3.3 SeGA Setup

The standard SeGA "classic" configuration, as used for the ^{9}Be(^{54}Ti, ^{53}Sc + γ)X experimental setup, with two rings of detectors arranged at 37° and 90° with respect to the beam axis (see Figures 4.7 and 4.5), was also used for the present experiment. Although 10 total detectors can be mounted on the 90° ring, only 9 were available for this experiment. The full set of 7 detectors were mounted on the forward ring.

Two different sources were used for the energy and efficiency calibration, ^{226}Ra and ^{152}Eu. The energy and efficiency calibration procedure was covered before (Sections 4.4.3 and 4.4.4) and only details specific to or different in the present analysis will be covered

here. Separate energy calibrations were performed using both the ^{152}Eu and ^{226}Ra sources and the results were tested against each other and absolute literature values. Both sources provided similar energy residuals (SeGA calibrated energies minus true source energies) of ~ 0.5 keV between 121.8 keV and 2447.7 keV, the maximum range covered by either ^{152}Eu or ^{226}Ra sources. The Lorentz-boosted energies seen in the laboratory-frame following the γ-decay from the in-flight ^{49}Mn, ^{50}Fe and ^{51}Co proton-pickup reaction products all lay between this range. Energy calibrations were performed at the beginning, middle, and end of the experiment to check for detector drifts and other changes over time. All consistency checks passed.

The ^{152}Eu source activity was absolutely calibrated at date of issue; the ^{226}Ra sources was not. To get accurate efficiencies across a wide energy range, the uncalibrated ^{226}Ra source had to be included. The minimum to maximum energies emitted by ^{152}Eu that were suitable for efficiency calibration were 121.8 keV to 1408.0 keV. For ^{226}Ra that range was 768.4 keV to 2447.7 keV. Although ^{226}Ra and its decay products emit γ rays down to 186.2 keV, the mounting ring used for the ^{226}Ra source absorbed the lower energy γ rays. This effect was particularly prominent for the 90° ring. Using the individual efficiencies of each observed transition as calculated from the source full-energy peak areas, decay rate, and expected number of emitted γ rays per decay, the efficiency curve of Equation 4.6 was fit. A customized fitter was written for ROOT [149] that kept the parameters that described the curve shape identical for the ^{152}Eu and ^{226}Ra sources (parameters b and c of Equation 4.6), but allowed for two separate amplitude parameters, one for each source ($a_{226\mathrm{Ra}}$ and $a_{152\mathrm{Eu}}$).

The ^{226}Ra amplitude $a_{226\mathrm{Ra}}$ was allowed to vary in relation to the absolutely determined ^{152}Eu amplitude $a_{152\mathrm{Eu}}$. The ^{226}Ra fit was then rescaled according to the difference in amplitude $a_{152\mathrm{Eu}}/a_{226\mathrm{Ra}}$. The final efficiency curves for both the 37° and 90° rings are shown in Figure 6.3. Both the laboratory-frame and projectile-rest frame efficiency curves (Lorentz-boosted efficiency for a sample velocity of $\beta = 0.327$) are displayed. The

Lorentz-boosted efficiency, as detailed in Section 4.4.4, includes the effects of the boost of energy from the residue rest-frame to the laboratory frame and the forward bias of angular emission as observed in the laboratory-frame. The angular contraction accounts for the increased efficiency of the 37° ring in relation to the 90° ring. The final residuals and function errors are small, showing the magnitude of the efficiency calibration across a wide energy range.

6.3.4 Experimental Changes

This experiment was designed to probe the pickup reaction mechanism under the use of different reaction targets, and the experimental differences associated with this change, including the change of spectrograph rigidity to center the reaction products using the different thickness targets, were expected. Additional unexpected changes, however, complicated analysis. A chronographic list of the different experimental changes, with the duration of data collection for each setting, the spectrograph rigidity, reaction setting, and description of the change is shown in Table 6.2. The neutron pickup reactions lie outside the scope of the original intent of the experiment and this thesis. The reaction channel may form the basis of future work, but the smaller difference in rigidity between the unreacted beam and the pickup reaction products for the neutron pickup reaction ($\Delta Z = 0$) in comparison to the proton pickup reaction ($\Delta Z = 1$) will complicate the analysis for heavier nuclei. The smaller difference of rigidity permits a greater proportion of the unreacted beam to enter the focal plane.

Problems with timing drove many of the changes made during the course of the experiment. There were two major problems. The first is shown in Figure 6.4. As shown, the faster TOF components of the cocktail beam were not detected, resulting in the reduction in intensity and even non-observation of several cocktail-beam components. The initial delay on the signal generated by the OBJ and XFP scintillators—see Table 6.3 for the physical time-of-flights corresponding to the labels XFP, OBJ, and XFP-OBJ—was too short,

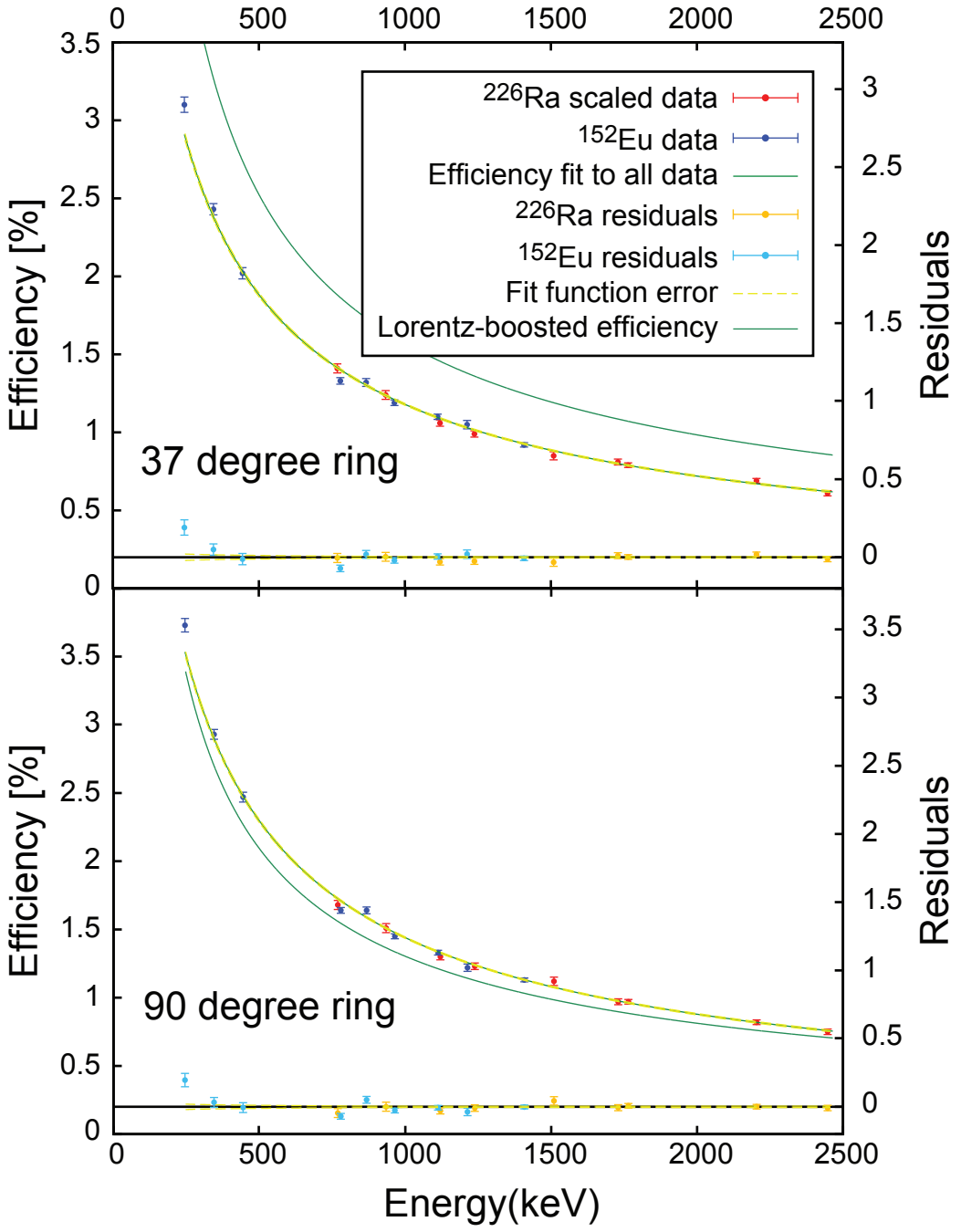

Figure 6.3: SeGA efficiencies for the 37° and 90° rings, as calculated from measured full-energy peak yields extracted from a calibrated ^{152}Eu source and an uncalibrated ^{226}Ra source. Both the lab efficiency curve and the Lorentz-boosted efficiency curve, for a γ ray emitted by a projectile moving at $\beta = 0.324$, are shown. The assumed isotropic angular distribution of γ rays emitted in the residue rest frame is biased to forward angles in the lab frame because of the Lorentz boost, resulting in the perceived increase of efficiency for the 37° ring.

	Time (hr)	$B\rho$ (Tm)	Setting	Change
1.	12.3	1.745	^{9}Be, +1p	Initial setup. This data was not used in the current analysis.
2.	16.7	1.746	^{9}Be, +1p	Insertion of parallel-plate avalanche counters (PPACs) at the intermediate image of the S800 analysis line.
3.	2.0	1.886	^{9}Be, +1n	Changed to the rigidity of the S800 spectrograph to center the neutron pickup products.
4.	2.9	1.745	^{9}Be, +1p	Returned the rigidity of the spectrograph to the +1p reaction setting.
5.	14.5	1.745	^{9}Be, +1p	Increased the delay on the OBJ scintillator by 200 ns and the XFP scintillator by 50 ns.
6.	13.9	1.886	^{9}Be, +1n	Added TACs in parallel with the existing TDC branch to processes the OBJ and XFP time-of-flights. Changed the rigidity of the S800 to center +1n reaction products.
7.	14.4	1.834	^{93}Nb, +1p	Change of target to ^{93}Nb. Corresponding change of spectrograph rigidity.
8.	24.4	2.050	^{12}C, +1p	Change of target to ^{12}C. Corresponding change of spectrograph rigidity.
9.	2.4	2.050	^{12}C, +1n	Change of spectrograph rigidity to center 1n pickup reaction products.

Table 6.2: Major experimental changes during the course of the experiment including changes of spectrograph rigidity to center the new reaction channels and electronics modifications. Only the one-proton pickup data on the ^{9}Be and ^{12}C targets are presented in this thesis. The analysis of other reaction channels may form the basis of future work but are outside the scope of this thesis. See Table 6.3 for a description of the TOF labels.

Label	Description
XFP	Elapsed time between the master trigger (start) and a thin plastic scintillator (XFP scintillator) located at the end of the A1900 fragment separator (stop).
OBJ	Elapsed time between the master trigger (start) and a thin plastic scintillator (OBJ scintillator) physically located at the start of the S800 analysis line (stop).
OBJE1	Identical to the OBJ time-of-flight with addition corrections for the flight path of nuclei through the spectrograph. These corrections depend on the measured angle and momentum of fragments detected in the focal plane.
XFP-OBJ	TOF difference between the OBJ and XFP scintillators. Calculated in the analysis software.
DIA1	Elapsed time between the OBJ scintillator and the master trigger (stop). The TOF difference is measured by the TAC branch and reverses the regular trigger start and stop conditions.
DIA2	Elapsed time between the master trigger (start) and the XFP scintillator (stop). This TAC time-of-flight uses the TAC branch to measure the TOF but is otherwise identical to the XFP TOF.

Table 6.3: Overview of the various timing measurements used in the pickup reaction analysis. Time-to-amplitude converters (TACs), added in parallel to the existing TDC branch, mapped in the data acquisition software to the DIA1 and DIA2 channels, were added in mid-experiment, before the pickup reactions on the ^{12}C target. See Figure 6.4 for sample XFP, OBJ, and XFP-OBJ spectra.

and the signal generated by the scintillator photomultiplier tubes (PMTs) lay outside the 400 ns coincidence gate opened by the master trigger. To present the entire cocktail beam to the electronics, delays were added, 50 ns to the XFP signal and 200 ns to the OBJ signal, pushing the full spread of TOFs of the incoming beam within the coincidence window. The juxtaposition of the TOFs before and after the addition of the delays is shown in Figure 6.4. Black lines show the TOF before delays (summation of settings 2 and 4 of Table 6.3); red lines show the TOF after the delays (setting 5 of Table 6.3). The spectrograph was set to observe the $1p$ pickup reaction products.

A splitting of the TOF into two components was observed in most TOF spectra (OBJ,

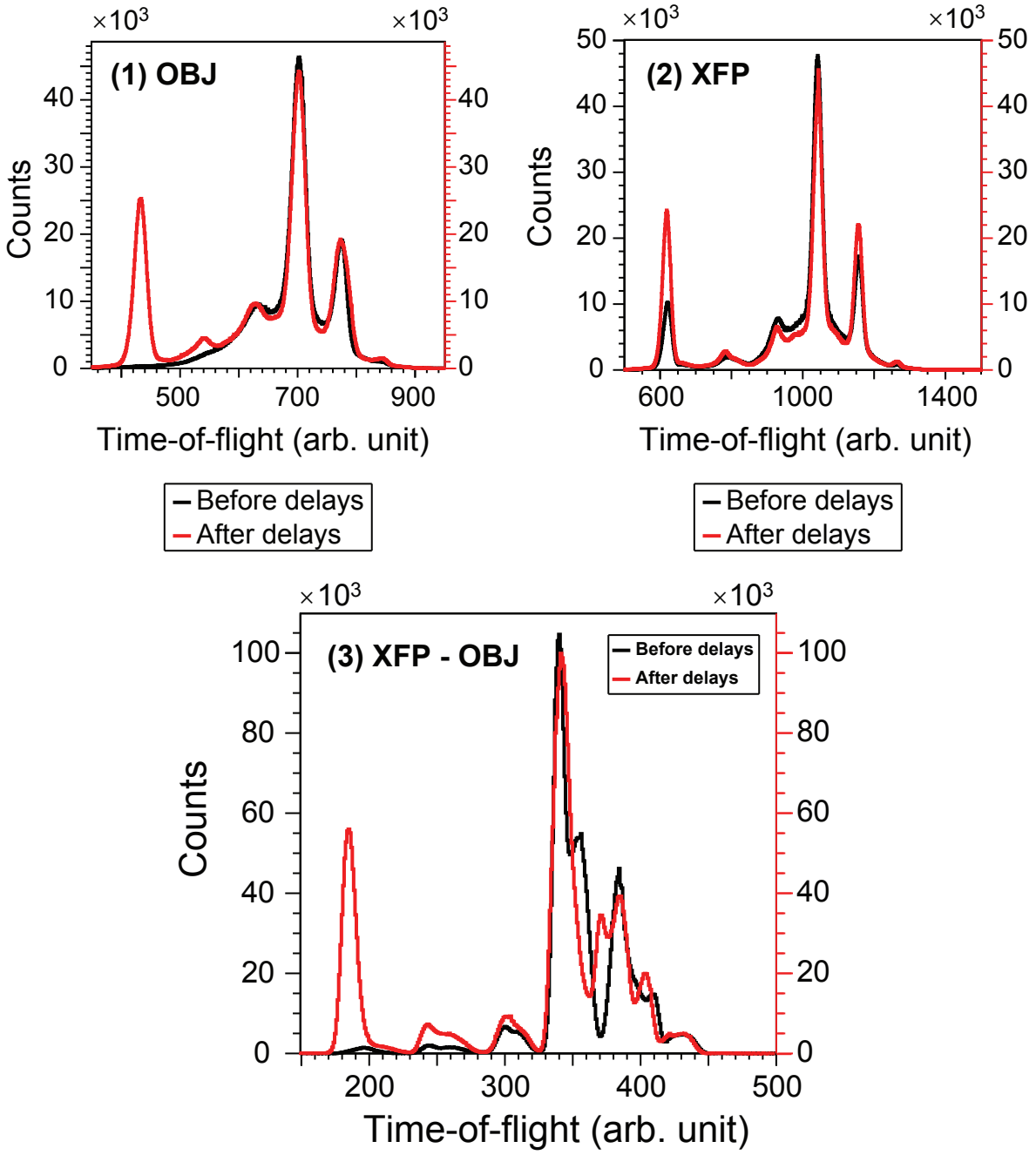

Figure 6.4: Effect of the addition of delays to the XFP and OBJ scintillators. The new delays shifted the measured time of cocktail beam components that previously lay outside the time coincidence window opened by the master trigger within the coincidence window permitting their detection. All three panes reflect the full sum of data taken on the ^{9}Be target with the spectrograph set to measure the pickup reaction products. See Table 6.2 for the location of this experimental setting within the complete experiment timeline. The XFP-OBJ spectrum was used for identification of the cocktail components for the proton pickup reactions using the ^{9}Be target.

XFP, and XFP-OBJ) associated with the ^{9}Be target runs and was attributed to problems in the Time-to-Digital Converter (TDC) branch receiving the signal from the OBJ and XFP scintillators. This splitting widened the time resolution of each cocktail component and led to significant overlap of similar A/Q nuclei in the one-dimensional XFP-OBJ and two-dimensional XFP versus OBJ time spectra used to identify the incoming projectiles. The TACs were added in parallel to the existing TDC branch, and the signals generated by the OBJ and XFP scintillators were split and simultaneously processed by both branches. The TAC channels were mapped in software to the labels DIA1 and DIA2 (see Table 6.3). As seen in Figure 6.5, the TACs significantly eliminated the broadening of the TOF signal.

6.4 Proton Pickup Reactions: ^{9}Be target

6.4.1 Particle Identification

There are two separate particle identifications necessary to label the entire direct, proton-pickup reaction channel: the identification of the incoming ^{A}Z projectile and the identification of the outgoing $^{A+1}$(Z+1) residue. The experimental difficulties outlined in Section 6.3.4 complicated both identifications.

For the ^{9}Be pickup data, before the addition of the TACs, wide incoming time gates were used to compensate for the effects of the TOF broadening. See for example Figure 6.6 for the two-dimensional histograms of XFP time-of-flight versus OBJ time-of-flight (upper panel) and the one-dimensional histogram of XFP-OBJ time-of-flight. The data shown was taken from setting 5 of Table 6.2, i.e. after the addition of the delays to the OBJ and XFP scintillators but before the addition of the TACs. These plots show unavoidable overlap in the TOF of the different cocktail components and therefore the difficulty of placing gates that minimize contamination but that do not restrict the observed rate of the desired reaction channel.

The width of the time gates was set by checking the gate placement against two-

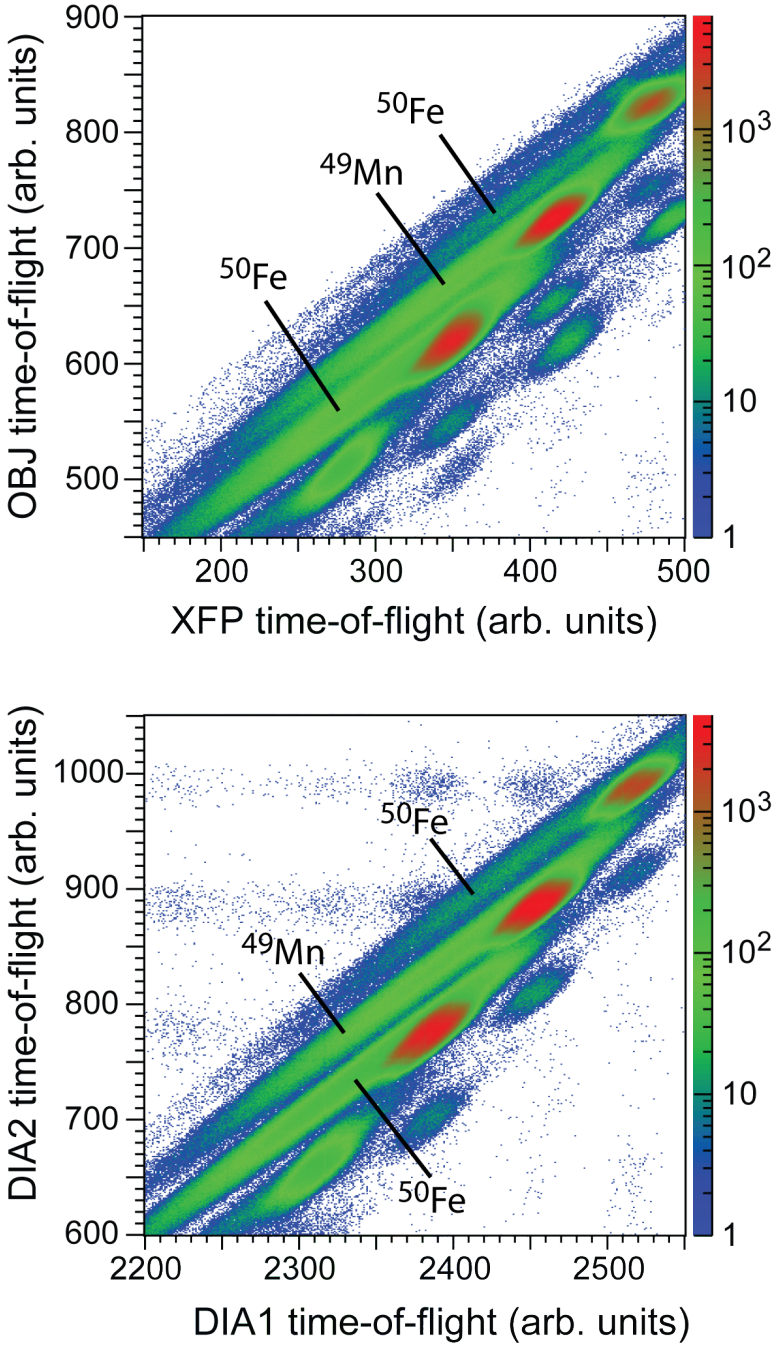

Figure 6.5: Effect the time-to-amplitude (TAC) converters on the TOF and PID for components of the incoming cocktail beam. The upper panel shows a two-dimensional TOF using the TDCs installed before the start of the experiment. The lower panel shows the effect of the TAC branch added in parallel. The physical time-of-flight measured in both panes are identical. Notice the cleaner separation of isotopes in the lower pane. The more diffuse loci in the upper pane is caused by the TOF broadening covered in Section 6.3.4.

component Gaussian fits to the XFP-OBJ spectra, and by looking for any positive correlation between the width of the time gate and the accuracy of the inclusive cross section. The final gate choice allowed cocktail beam components adjacent in TOF to contaminate the identification of the final heavy residue, see the top pane of Figure 6.8, but it ensured that the final inclusive cross section would not have to be adjusted for artificial software cuts to the observed rate of the incoming projectile. The addition of the TACs repaired these problems, and clean TOF gates could be used for identification of the cocktail components impinging on the ^{12}C target.

There were several sources of contamination in the final PID of OBJE1 versus energy loss in the ion chamber: contamination from one or more components of the unreacted beam (e.g. for the ^{9}Be(^{48}Cr,^{49}Mn + γ)X reaction, the ^{49}Mn PID is affected by contamination from both the unreacted ^{48}Cr and ^{49}Mn isotopes), possible scattering of beam off the beam blocker located immediately in front of the S800 focal plane (see the lower panel of Figure 6.7), and tails of one-neutron knockout residues. These issues are shown in the standard PID plot of Figure 6.6. The upper panel shows the plain PID before cleanup. The lower panel shows the PID after cleanup. Following cleanup, unambiguous software gating contours, free of most contamination, could be easily placed around the pickup reaction product. Note that the same gating scheme was used for the data analysis on both the ^{9}Be and ^{12}C targets (details follow).

To eliminate the contamination, all combinations of identifying spectra were tested. These spectra included dispersive and non-dispersive position and angle in the focal plane, TOF (see Table 6.3 for a full list), and energy loss. The combination of XFP time-of-flight and dispersive position (CRDC1 x-position), shown in the upper panel of Figure 6.7 eliminated all sources of contamination. The PID before and after the application of this gate is seen in the upper and lower panels of Figure 6.8. Any artificial cuts to the momentum distribution caused by software cuts to the CRDC1 spectrum were handled during the acceptance corrections covered in Section 6.4.3.

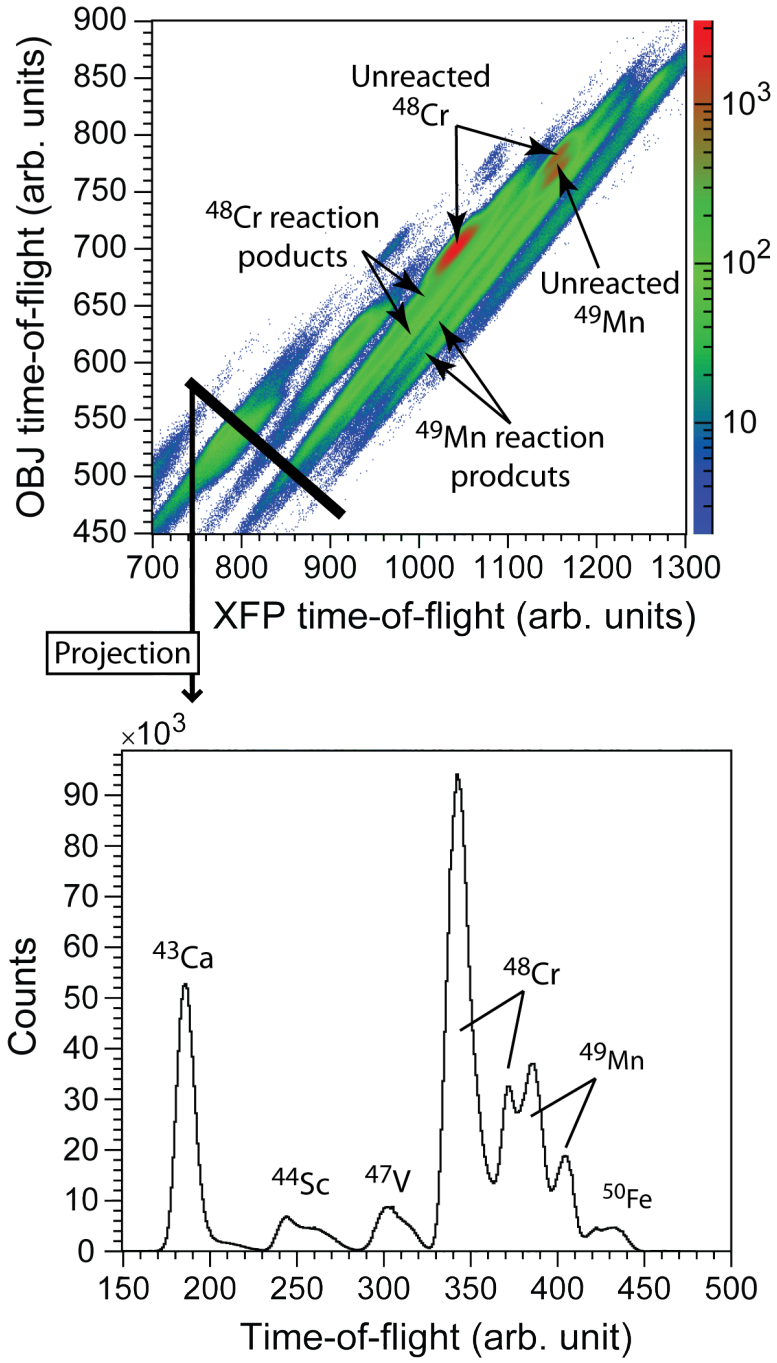

Figure 6.6: Time-of-flight broadening observed in in the ^{9}Be pickup data. The runs summed above occurred after the addition of the delays but before the addition of the TACs. The top pane shows the two-dimensional histogram of XFP versus OBJ time-of-flight; the bottom plane is their difference. See Table 6.2 for the list of TOF definitions. The addition of the new electronics resolved the TOF broadening. See Figure 6.5.

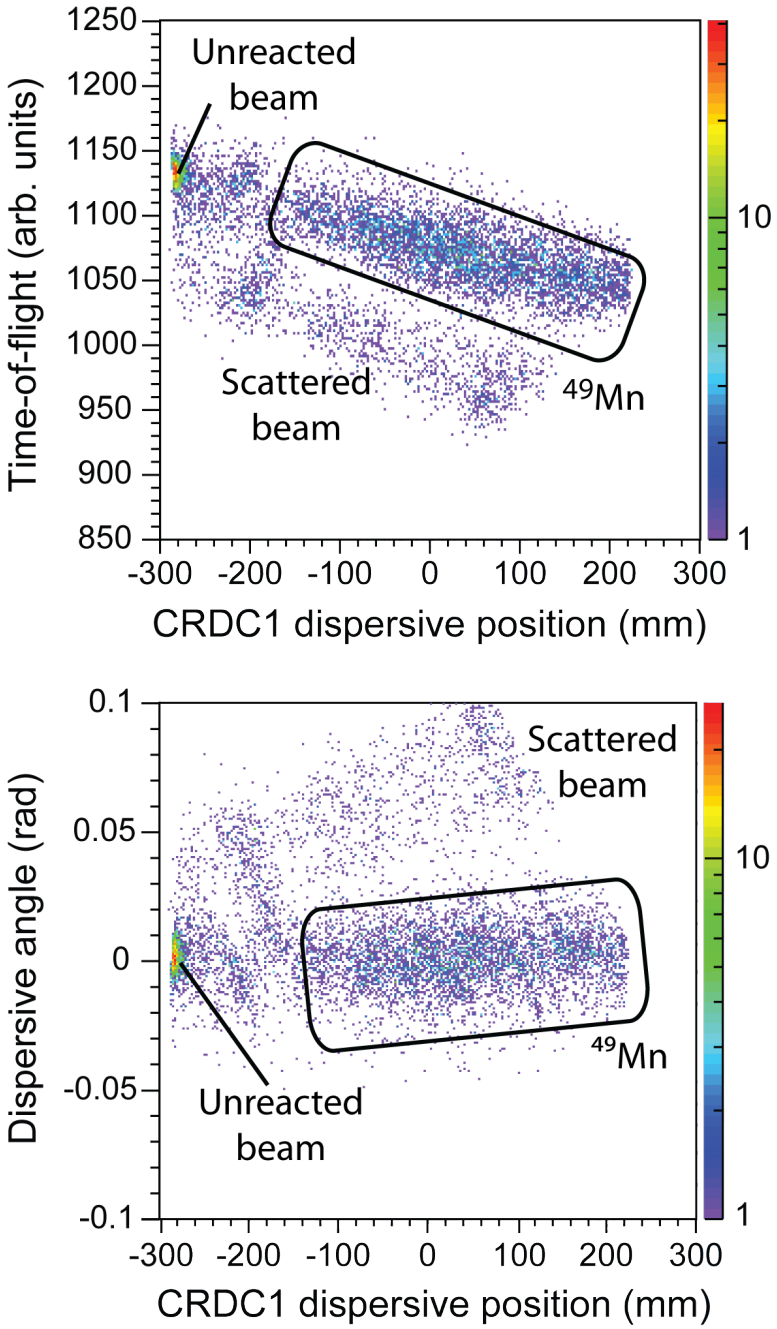

Figure 6.7: Contamination and cleanup of various components present in the PID histogram used to identify the pickup reaction products. The upper histogram of dispersive position in the focal plane (CRDC1 x-position) versus XFP time-of-flight provided the best method of discriminating between true $A+1$ pickup events and contamination. The lower panel of CRDC1 x-position versus dispersive angle shows contamination consistent with scattering of beam in the focal plane. Assumed sources of contamination are labeled.

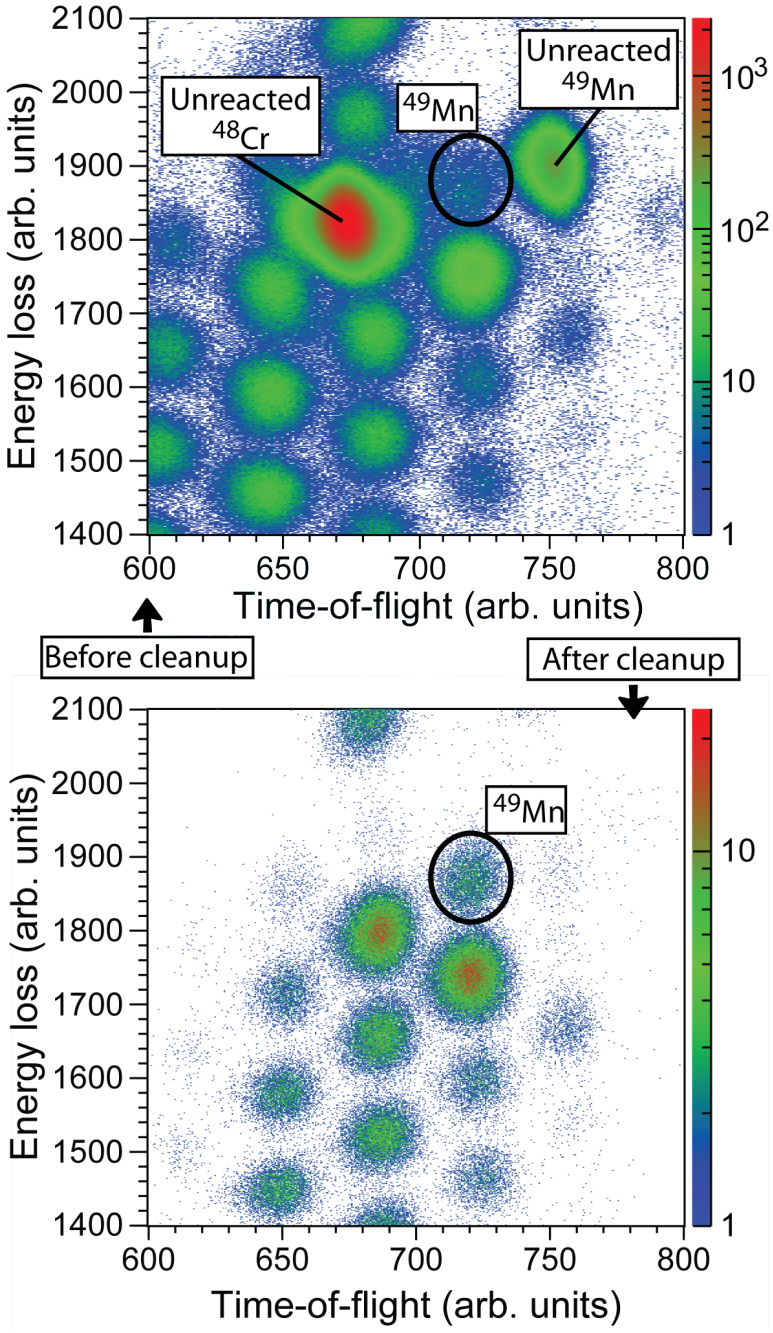

Figure 6.8: Particle identification plot for the ^{9}Be(^{48}Cr,^{49}Mn + γ)X reaction before and after the application of the cleanup gating procedure shown in Figure 6.7. In the upper pane, the PID is only gated upon the incoming TOF and particle singles events. The ^{49}Mn residues are overwhelmed by contamination from components of the cocktail beam (unreacted ^{48}Cr and ^{49}Mn isotopes that enter the focal plane at the edge of the acceptance) and possible scattering off the beam blocker (see Figure 4.3). The lower pane shows the PID after the application of the contour cleanup gate shown in Figure 6.7.

6.4.2 Theoretical Predictions

Theoretical predictions for the strength and pattern of population of states in the pickup residues were taken from the multiplicative combination of single-particle cross sections [162], spectroscopic factors [163], and a center-of-mass correction[2]. The same approach was used for the calculation of the ^{9}Be(^{54}Ti, ^{53}Sc + γ)X partial and inclusive cross sections (see Equation 3.18). There are several assumptions guiding the pickup reaction calculation. First, the pickup reaction was assumed to be direct. The direct nature is reflected in the longitudinal momentum distribution whose broadening from the reaction processes, because of the two-body the initial and final states (see Section 3.5.3), is assumed to be a delta function. A increased width of the measured distribution relative to the calculated distribution outlined above indicates possible deviations from the direct reaction process.

Second, it is assumed that the proton is transfered in a single step, from an initial bound state in the ^{9}Be target, to a bound, single-particle state in the incident projectile (^{48}Cr, ^{49}Mn and ^{50}Fe), creating a $^{A+1}(Z+1)$ pickup residue (^{49}Mn, ^{50}Fe, and ^{51}Co respectively). The ^{9}Be target, now missing a proton, is assumed to be left in one of three states of ^{8}Li, the $2^{+}_{\text{g.s.}}$ ground state, the 1^{+}_{1} excited state at 981 keV, and the 3^{+}_{1} state at 2255(3) keV. With $S_n(^{8}\text{Li}) = 2024$ keV, the 3^{+} ^{8}Li state is unbound. These three states exhaust most of the overlap between the ^{9}Be ground state and all final ^{8}Li states (spectroscopic factor sum rule). Using ^{9}Be(^{48}Cr, ^{49}Mn + γ)X as an example to illustrate the reaction processes for all three pickup reactions using the ^{9}Be target, we have the final CCBA form: ^{48}Cr(^{9}Be, ^{8}Li$(J^{\pi})^{*}$)^{49}Mn$(I^{\pi})^{*}$.

The spectroscopic factors were calculated by B.A. Brown [163] using the NuShellX

[2]The COM correction for a single-nucleon pickup reaction, which arises from shell model calculations that use harmonic oscillator wave functions relative to the A rather than $A+1$ COM are of the form

$$\left(\frac{A}{A+1}\right)^{N},$$

where $N = n + \ell$ (n is defined to start at 0, rather than the convention of defining n to start at 1 as adopted in this thesis). For further details, see Section 3.2.6 and Equation 3.13.

code [66] with the GXPF1A [58] effective interaction. The fp shell calculations assume a ^{40}Ca core and a proton/neutron $1f_{7/2}$, $2p_{3/2}$, $1f_{5/2}$, and $2p_{1/2}$ valence space. The result of these calculations are shown in Figures 6.9, 6.10, and 6.11. These figures show the spectroscopic strength, energies, and quantum numbers associated with final states in ^{49}Mn, ^{50}Fe, and ^{51}Co (respectively). The data was drawn from Tables A.1, A.2, and A.3. In all three cases, the spectroscopic strength is spread thinly over a multitude of states above and below the proton separation energy. For the ^{9}Be(^{48}Cr, ^{49}Mn + γ)X reaction, most of the overlap, with a spectroscopic factor of $C^2S[^{48}\mathrm{Cr}(0^+) \otimes 1f_{7/2}]_{7/2^-} = 0.425$ occurs with the $7/2^-_1$ state calculated to lie at 0.219 MeV and experimentally observed at 261 keV[3]. Negligible overlap occurs with the ground state (shown in bold in the aforementioned tables) and therefore the expected yield (partial cross section) to this state is also expected to be near zero. Most of the summed overlap proceeds to states above the ^{49}Mn proton separation energy of $S_p = 2.1$ MeV (the neutron separation energy is much higher, i.e. $S_n = 16.3$ MeV).

For the ^{9}Be(^{49}Mn, ^{50}Fe + γ)X reaction, because of the higher proton separation energy ($S_p = 4.2$ MeV) of the even-even nucleus, most of the $\langle ^{49}\mathrm{Mn}|\hat{a}_{j\pi}|^{50}\mathrm{Fe}(I^\pi)\rangle$ overlap[4] occurs with bound states in ^{50}Fe. The largest overlaps occurs with the first 2^+_1 state, $C^2S[^{49}\mathrm{Mn}(5/2^-) \otimes 1f_{7/2}]_{2^+_1} = 1.145$ and the 1^+_1 $C^2S[5/2^- \otimes 1f_{7/2}]_{1^+_1} = 0.530$, calculated to lie at 3.349 MeV (the state was not observed experimentally; for additional details, see Section 6.4.4). The spectroscopic strength slowly declines thereafter at higher energies.

---

[3] Pickup and knockout spectroscopic factors are related through the sum rule of Equation 3.12. The number of hole-like states for orbital $n\ell j$ in the initial A nucleus includes a multiplication by $2j + 1$, e.g. 8 for proton transfer to the $1f_{7/2}$ orbital in the ^{9}Be(^{48}Cr, ^{49}Mn + γ)X and ^{12}C(^{48}Cr, ^{49}Mn + γ)X reactions. The multiplication of 8 and 0.425 gives a value of 3.40, close to the naive expectation of 4 hole-like states in the $1f_{7/2}$ orbital for ^{48}Cr.

[4] The overlaps $\langle ^{49}\mathrm{Mn}|\hat{a}_{j\pi}|^{50}\mathrm{Fe}(I^\pi)\rangle$ or $\langle ^{50}\mathrm{Fe}(I^\pi)|\hat{a}^\dagger_{j\pi}|^{49}\mathrm{Mn}\,^{49}\mathrm{Mn}\rangle$ are identical within a multiplicative phase (in general $\langle \phi_a|A|\phi_b\rangle^* \equiv \langle \phi_b|A^\dagger|\phi_a\rangle$ where $*$ indicates complex conjugation). This phase disappears in the square of the matrix element. The definition does not affect the calculation of the spectroscopic factor.

Note, there are several different ways to couple the angular momentum of the initial ^{49}Mn ground state spin of $5/2^-_{\text{g.s}}$ and the total angular momentum of the added nucleon (proton $1f_{7/2}$, $2p_{3/2}$, $1f_{5/2}$, and $2p_{1/2}$ orbitals) to the final ^{50}Fe(I^π) angular momentum. Each of these different couplings has a separate associated spectroscopic factor. For the lowest states included in the reaction calculations the total spectroscopic factor is dominated by one configuration. This configuration is listed (nlj column; Tables A.1, A.2, and A.3). For example, the first 2^+_1 state, predicted to be at 0.788 MeV (experimentally observed to lie at 0.765 MeV) is dominated by the $[5/2^-_{\text{g.s}} \otimes 1f_{7/2}]_{2^+_1}$ configuration with a spectroscopic factor of $C^2S = 1.145$. The other configurations, involving the $2p_{3/2}$, $1f_{5/2}$, and $2p_{1/2}$ orbitals have associated spectroscopic factors of 0.005, 0.000, and 0.007.

Lastly, for ^{51}Co, only one state is known to be proton-bound, with $C^2S[^{50}\text{Fe}(0^+) \otimes 1f_{7/2}]_{7/2^-} = 0.246$. The proton separation energy for this very proton-rich nucleus is estimated from mass systematics to be $S_p = 88$ keV.

The single-particle cross sections were calculated by Tostevin [162], as detailed in Section 3.5.3 in the Coupled Channels Born Approximation (CCBA) framework using the reaction code FRESCO. The calculations were post-form and fully finite range, and were evaluated at the expected ^{9}Be 188 mg/cm^2 mid-target energies of 50.7 MeV/u (^{9}Be(^{48}Cr, ^{49}Mn + γ)X), 52.8 MeV/u (^{9}Be(^{49}Mn, ^{50}Fe + γ)X), and 54.8 MeV/u (^{9}Be(^{50}Fe, ^{51}Co + γ)X). As mentioned, it is assumed that the projectile and target are bound systems and the transfer occurs from one bound state to another.

The calculation of the single-particle cross sections requires the overlaps and spectroscopic factors of the target and projectile, the proton-core, relative motion wave functions of the target and projectile, and the absorptive optical nuclear interactions (calculations details follow).

The target overlaps $\phi(\boldsymbol{r}) = \langle ^9\text{Be}|\hat{a}^\dagger|^8\text{Li}(I^\pi)\rangle$ and spectroscopic factors $S = \int d\boldsymbol{r}|\phi(\boldsymbol{r})|^2$, for the three included ^{8}Li final states, the 2^+_1 ground state, the 1^+_1 state at 980.80(10 keV) (literature value), and the 3^+_1 state at 2255(3) keV, were calculated using Variational

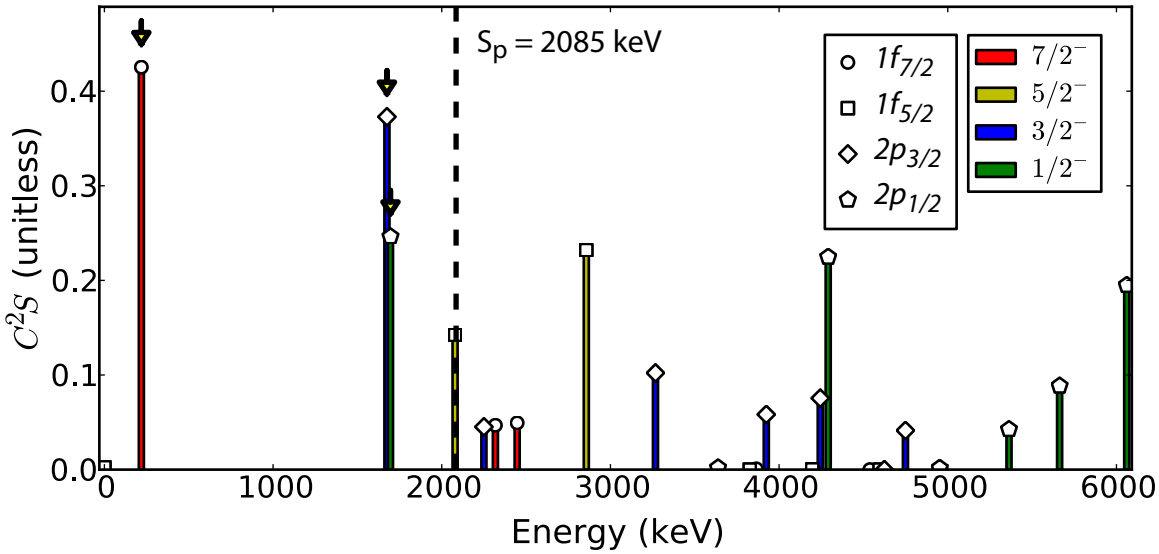

Figure 6.9: Shell-model spectroscopic factors ($C^2S_{\text{S.M.}}$) for the ^{9}Be(^{48}Cr, ^{49}Mn + γ)X reaction. All values, i.e. energies, spectroscopic factors, spins, and parities, are taken from the shell model calculations of Brown [163]. Only levels with spectroscopic strength of $C^2S \geq 0.04$ are displayed. The spin and parity of the final state ^{49}Mn(I^π) is indicated by the color of the bars. See the figure label. The orbital $n\ell_j$ of the transfered proton (in ^{49}Mn) is illustrated through the shapes of the bar caps: circle ($1f_{7/2}$), square ($1f_{5/2}$), diamond ($2p_{3/2}$), and pentagon ($2p_{1/2}$). The proton separation energy of $S_p = 2085(5)$ keV is indicated by a dotted line. The states used in the calculation of the theoretical partial and inclusive cross sections (see Table 6.7) are noted by yellow-filled arrows. The cross section to the ground state is nearly zero. The figure data is taken from Table A.1.

Monte Carlo (VMC) wave functions, as provided by Wiringa [164]. These calculations used a combination of the two-body Argonne v18 Hamiltonian [3] and the three-body Urbana IX [165] Hamiltonian. The final VMC overlaps were then fit by $\pi(1p_{3/2})$ and $\pi(1p_{1/2})$ single-particle wave wave functions calculated in a Woods-Saxon potential. The final spectroscopic factors, involving the integrated norm of the overlap functions are listed in Table 6.7. The summed spectroscopic strength for the $1p_{3/2}$ and $1p_{1/2}$ orbital is 0.97 and 0.36. The total sum of 1.33 is smaller than the inclusive value of 2. The remaining overlap of 0.67 is spread to higher unbound states that were not included in the reaction calculations. Contrast the ^{9}Be target with the ^{12}C target, where nearly all of the spectroscopic overlap of 4 (see Section 6.5.2) is accounted for by the ground state and

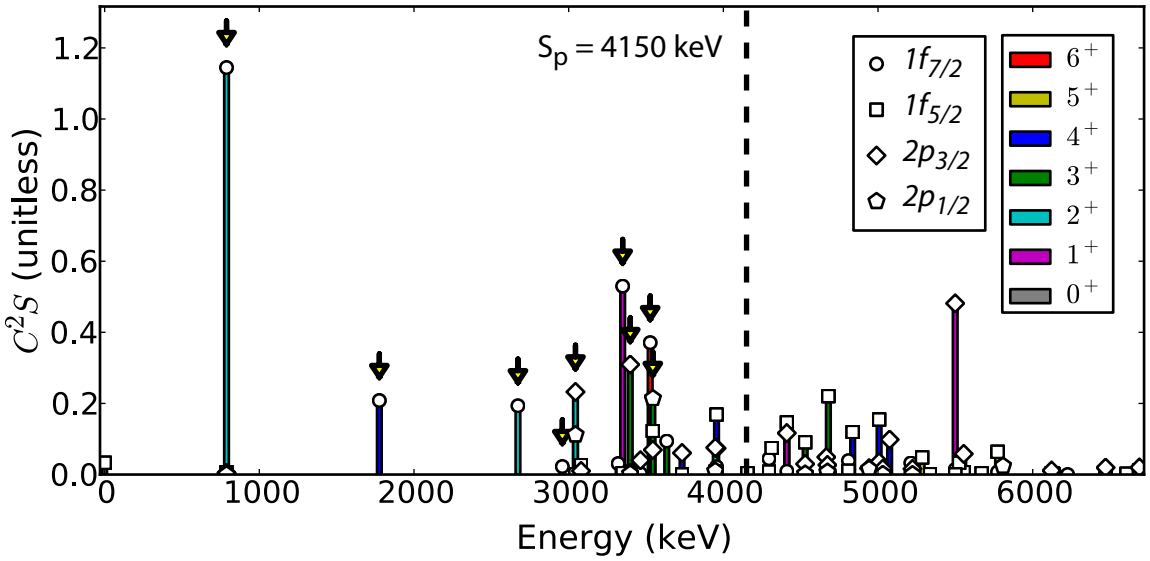

Figure 6.10: Shell-model spectroscopic factors ($C^2S_{\text{S.M.}}$) for the ^{9}Be(^{49}Mn, ^{50}Fe + γ)X reaction. All values, i.e. energies, spectroscopic factors, spins, and parities, are taken from the shell model calculations of Brown [163]. Only levels with spectroscopic strength of $C^2S \geq 0.04$ are listed. The spin and parity of the final state ^{50}Fe(I^π) is indicated by the color of the bars. See the figure label. The orbital $n\ell_j$ of the transfered proton (in ^{50}Fe) is illustrated through the shapes of the bar caps: circle ($1f_{7/2}$), square ($1f_{5/2}$), diamond ($2p_{3/2}$), and pentagon ($2p_{1/2}$). The proton separation energy of $S_p = 4150(60)$ keV is denoted by a dotted line. The states used in the calculation of the theoretical partial and inclusive cross sections (see Table 6.8) are noted by yellow-filled arrows. Two possible fragmented 6^+ states are considered based upon the proximity of their energies of 3.257 MeV and 2.959 MeV to the literature value of 3.159 MeV. Note the high degree of fragmentation to states above and below the proton separation energy (compare this figure to Figures 6.9 and 6.11). The figure data is taken from Table A.2.

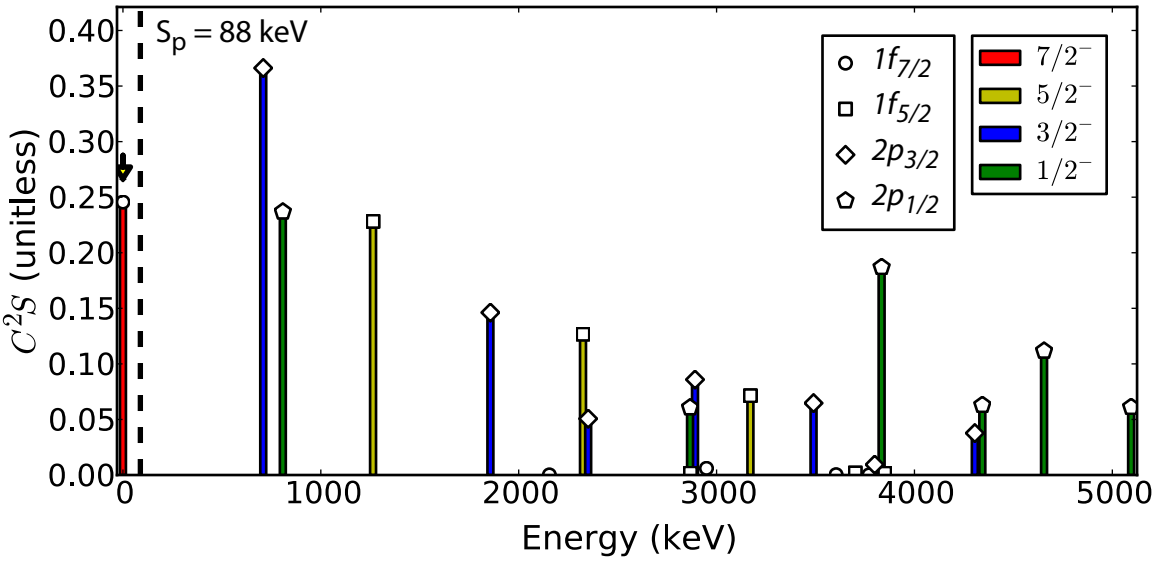

Figure 6.11: Shell-model spectroscopic factors ($C^2S_{\text{S.M.}}$) for the ^{9}Be(^{50}Fe, ^{51}Co + γ)X. All values, i.e. energies, spectroscopic factors, spins, and parities, are taken from the shell model calculations of Brown [163]. Only levels with spectroscopic strength of $C^2S \geq 0.04$ are listed. The spin and parity of the final state ^{51}Co(I^π) is indicated by color. See the figure label. The orbital $n\ell_j$ of the transfered proton (in ^{51}Co) is illustrated through the shapes of the bar caps: circle ($1f_{7/2}$), square ($1f_{5/2}$), diamond ($2p_{3/2}$), and pentagon ($2p_{1/2}$). The low proton separation energy of S_p = 88 keV is denoted by a dotted line. The proton separation energy of S_p = 2085(5) keV is indicated by a dotted line. Only the ground state, as indicated by a yellow-filled arrow, was used in the calculation of the theoretical partial and inclusive cross sections (see Table 6.9). The figure data is taken from Table A.3.

two excited states of ^{11}B.

Projectile overlaps, e.g. $\phi(\boldsymbol{r}) = \langle {}^{48}\text{Cr}|\hat{a}|{}^{49}\text{Mn}(I^\pi)\rangle$ and spectroscopic factors for the ^{9}Be(^{48}Cr, ^{49}Mn + γ)X reaction, were calculated within the shell model using the NuShellX code and GXPF1A effective interaction. The proton-core $p + {}^{A}\text{Z}$ relative-motion wave functions were calculated in the same manner as the $p + {}^{8}$Li* relative-motion wave functions: in a Woods-Saxon potential with a spin-orbit term. The depth of the Woods-Saxon potential was adjusted to the physical separation energy, e.g. $S_p(^{9}\text{Be}) + E_x(^{49}\text{Mn}^*)$. Standard values of r_0 = 1.25 fm, a = 0.7 fm, $V_0^{\text{S.O.}}$ = 6.0 MeV, $r_0^{\text{S.O.}}$ = 1.25 fm, and $a^{\text{S.O.}}$ = 0.7 fm were used for all three ^{9}Be cases.

The final component, the absorptive optical nuclear interactions, were calculated,

^{49}Mn				Target (^{9}Be → ^{8}Li*)			$\sigma_{\text{s.p}}$	
I^π	E_x (MeV)	$\pi\ell_j$	$S_p^{\text{res.}}$(eff.) (MeV)	J_π (^{8}Li)	$S_p^{\text{tar.}}$(eff.) (MeV)	Q (MeV)	$\sigma^{\text{s.p.}}$ (mb)	$\sum_i \sigma_i^{\text{s.p.}}$ (mb)
$7/2^-$	0.262	$1f_{7/2}$	1.813	2^+	16.888	-14.803	2.212	3.904
				1^+	17.870	-15.785	0.882	
				3^+	19.143	-17.058	0.811	
$1/2^-$	*1.703*	$1f_{7/2}$	*0.382*	2^+	16.888	-14.803	0.021	0.039
				1^+	17.870	-15.785	0.014	
				3^+	19.143	-17.058	0.004	
$3/2^-$	*1.741*	$1f_{7/2}$	*0.344*	2^+	16.888	-14.803	0.049	0.082
				1^+_1	17.870	-15.785	0.020	
				3^+_1	19.143	-17.058	0.014	

Table 6.4: Additional details on the calculation of the single-particle cross sections for the ^{9}Be(^{48}Cr, ^{49}Mn + γ)X reaction evaluated at a mid-target energy of 50.7 MeV/u. The complete single-particle cross section for the transfer of a proton from the target to the orbital $n\ell_j$ in ^{48}Cr, forming the pickup residue ^{49}Mn, includes a summation over target final states. The pickup residue ^{49}Mn is labeled by its quantum numbers I^π, excitation energy E_x^{final}, and its effective separation energy of $S_p^{res.}(\text{eff}) = S_p^{\text{res.}}(^{49}\text{Mn})_{\text{g.s}} - E_x$. The ground state separation energy for ^{49}Mn is $S_p^{\text{res.}}(^{49}\text{Mn})_{\text{g.s}} = 2.085\,\text{MeV}$. Each target final state—for the target residual ^{8}Li this includes the $2^+_{\text{g.s.}}$, 1^+_1, and 2^+_2 states—is labeled by its quantum numbers J^π, effective separation energy $S_p^{\text{tar.}}(\text{eff}) = S_p(^{9}\text{Be})_{\text{g.s.}} + E_x(^{8}\text{Li})$, and reaction Q value $Q = S_p^{\text{res.}}(^{49}\text{Mn})_{\text{g.s.}} - S_p^{\text{tar.}}(\text{eff})$. The single-particle cross section to the ground state of ^{49}Mn was not calculated because of the extremely small spectroscopic factor $C^2S = 0.002$ seen in Figure 6.9 and Table A.1. The $7/2^-_1$ energy of 262 keV was taken from experiment. The $1/2^-_1$ and $3/2^-_1$ energies were not observed in this experiment and literature values do not exist. Their energies were taken from shell-model calculations, see Table A.2, and are italicized to note this origin.

as done for the analysis of the ^{9}Be(^{54}Ti, ^{53}Sc + γ)X reactions (see Section 3.4.2.3), using eikonal S-matrices that include the double folding of the proton and neutron densities of the projectile (taken from Hartree-Fock calculations using the SkX Skyrme Hamiltonian) and the target (estimated by a Gaussian) with an effective NN interaction. Folding all these components up within the CCBA calculations gives the single-particle cross sections shown in Tables 6.4, 6.5, and 6.6.

Combining the spectroscopic factors of Figures 6.9, 6.10, and 6.11 with the single-

^{50}Fe				Target (^{9}Be → ^{8}Li*)			$\sigma_{\mathrm{s.p}}$	
I^{π}	E_x^{final} (MeV)	$\pi\ell_j$	$S_p^{\mathrm{res.}}$(eff.) (MeV)	J_{π} (^{8}Li)	$S_p^{\mathrm{tar.}}$(eff.) (MeV)	Q (MeV)	$\sigma^{\mathrm{s.p.}}$ (mb)	$\sum_i \sigma_i^{\mathrm{s.p.}}$ (mb)
0^+	0	$1f_{7/2}$	4.15	2^+	16.888	-12.738	0.020	0.054
				1^+	17.870	-13.720	0.027	
				3^+	19.143	-14.993	0.007	
2^+	1.703	$1f_{7/2}$	3.385	2^+	16.888	-12.738	0.210	0.371
				1^+	17.870	-13.720	0.083	
				3^+	19.143	-14.993	0.078	
4^+	1.851	$1f_{7/2}$	2.299	2^+	16.888	-12.738	0.370	0.655
				1^+	17.870	-13.720	0.147	
				3^+	19.143	-14.993	0.138	
6^+	3.159	$1f_{7/2}$	0.991	2^+	16.888	-12.738	0.516	0.909
				1^+	17.870	-13.720	0.204	
				3^+	19.143	-14.993	0.189	
2^+	*2.672*	$1f_{7/2}$	*1.478*	2^+	16.888	-12.738	0.201	0.355
				1^+	17.870	-13.720	0.080	
				3^+	19.143	-14.993	0.074	
2^+	*3.044*	$2p_{3/2}$	*1.106*	2^+	16.888	-12.738	0.011	0.018
				1^+	17.870	-13.720	0.004	
				3^+	19.143	-14.993	0.003	
1^+	*3.349*	$1f_{7/2}$	0.801	2^+	16.888	-12.738	0.118	0.208
				1^+	17.870	-13.720	0.047	
				3^+	19.143	-14.993	0.043	
3^+	*3.398*	$2p_{3/2}$	0.752	2^+	16.888	-12.738	0.014	0.023
				1^+	17.870	-13.720	0.006	
				1^+	19.143	-14.993	0.004	
3^+	*3.544*	$2p_{1/2}$	0.606	2^+	16.888	-12.738	0.011	0.021
				1^+	17.870	-13.720	0.008	
				3^+	19.143	-14.993	0.002	

Table 6.5: Additional details on the calculation of single-particle cross sections for the ^{9}Be(^{49}Mn, ^{50}Fe + γ)X reaction evaluated at a mid-target energy of 52.8 MeV/u. For additional information on the column labels, please refer to the caption of Table 6.4. The ground-state proton separation energy of ^{50}Fe is 4.150 MeV. Listed energies are from literature when available. Exceptions, e.g. the 2_2^+ state at 2.672 MeV, the 2_3^+ state at 3.044 MeV, and the 1^+ and 3^+ states, were taken from shell model calculations and are italicized (see Table A.2). The two fragmented 6^+ states of Table A.2 are calculated at the experimental energy of 3.544 MeV.

^{51}Co				Target (^{9}Be → ^{8}Li*)			$\sigma_{s.p}$	
I^π	E_x (MeV)	$\pi\ell_j$	$S_p^{res.}$(eff.) (MeV)	J_π (^{8}Li)	$S_p^{tar.}$(eff.) (MeV)	Q (MeV)	$\sigma^{s.p.}$ (mb)	$\sum_i \sigma_i^{s.p.}$ (mb)
0^+	0	$1f_{7/2}$	0.164	2^+	16.888	-16.724	1.632	2.869
				1^+	17.870	-17.706	0.642	
				3^+	19.143	-18.979	0.595	

Table 6.6: Additional details on the calculation of the single-particle cross sections for the ^{9}Be(^{50}Fe, ^{51}Co + γ)X reaction evaluated at a mid-target energy of 54.8 MeV/u. For additional information on the column labels, please refer to the caption of Table 6.4. The ground-state separation energy of ^{51}Co is 88 keV. No excited states were observed and therefore only the partial cross section to the ground state was calculated.

J^π	E_{final} (MeV)	Shell model configuration	COM corr.	$C^2S_{S.M.}$	$\sigma_{s.p.}$ (mb)	σ_{theory} (mb)
$7/2^-$	0.272	$[0^+ \otimes 1f_{7/2}]$	0.940	0.425	3.904	1.56
$1/2^-$	*1.703*	$[0^+ \otimes 2p_{1/2}]$	0.940	0.039	0.245	0.01
$3/2^-$	*1.741*	$[0^+ \otimes 2p_{3/2}]$	0.940	0.373	0.082	0.03
					Inclusive sum:	1.60

Table 6.7: Theoretical predictions of the partial and inclusive cross sections for the ^{9}Be(^{48}Cr, ^{49}Mn + γ)X reaction. Transitions corresponding to the decays of the $1/2^-_1$ and $3/2^-_1$ states were not observed in the current experiment and literature values values do not exist. Italics indicate that shell model energies were used. A statistically insignificant population of the ^{49}Mn ground state is predicted because of the calculated, near zero $C^2S(^{48}\text{Cr} \rightarrow {}^{49}\text{Mn}_{g.s.}) = 0.002$ spectroscopic factor of Table A.1.

particle cross sections of Tables 6.4, 6.5, and 6.6 yields the theoretical predictions for the partial and inclusive cross sections for the ^{9}Be(^{48}Cr, ^{49}Mn + γ)X, ^{9}Be(^{49}Mn, ^{50}Fe + γ)X, and ^{9}Be(^{50}Fe, ^{51}Co + γ)X reactions. The detailed comparison of the theoretical and experimental results are shown in the analysis of the inclusive (Section 6.4.3) and partial cross sections (Section 6.4.5).

6.4.3 Measured Inclusive Cross Sections

Following the cleanup procedure of Section 6.4.1, the number of pickup reaction products could be accurately counted. From the number of pickup residues with respect to the

J^π	E_{final} (MeV)	**Shell model configuration**	**COM corr.**	$C^2S_{\text{S.M.}}$	$\sigma_{\text{s.p.}}$ (mb)	σ_{theory} (mb)
0^+	0	$[5/2^- \otimes 1f_{5/2}]$	0.941	0.033	0.054	0.00
2^+	0.765	$[5/2^- \otimes 1f_{7/2}]$	0.941	1.145	0.371	0.40
4^+	1.851	$[5/2^- \otimes 1f_{7/2}]$	0.941	0.208	0.655	0.13
6^+	3.159	$[5/2^- \otimes 1f_{7/2}]$	0.941	0.023	0.909	0.02
6^+	3.159	$[5/2^- \otimes 1f_{7/2}]$	0.941	0.371	0.909	0.32
2^+	*2.672*	$[5/2^- \otimes 1f_{7/2}]$	0.941	0.194	0.355	0.06
2^+	*3.044*	$[5/2^- \otimes 2p_{3/2}]$	0.941	0.232	0.018	0.00
1^+	*3.349*	$[5/2^- \otimes 1f_{7/2}]$	0.941	0.529	0.208	0.10
3^+	*3.398*	$[5/2^- \otimes 2p_{3/2}]$	0.941	0.309	0.023	0.01
3^+	*3.544*	$[5/2^- \otimes 2p_{1/2}]$	0.941	0.214	0.021	0.00
					Inclusive sum:	1.05

Table 6.8: Theoretical predictions of the partial and inclusive cross sections for the ^{9}Be(^{49}Mn, ^{50}Fe+γ)X reaction. The $0^+_{\text{g.s.}}$ ground state, 2^+_1, and 4^+_1 states were observed in the experiment. See the ^{50}Fe residue rest-frame γ-ray spectrum of Figure 6.16. For the higher spin states, i.e. $J^\pi = 2^+, 4^+, 6^+$, several different couplings of the form $[5/2^-(^{49}\text{Mn}_{\text{g.s.}}) \otimes j_p^\pi]$ are possible depending on the spin and parity of the orbital in ^{49}Mn accepting the transfered proton (the fp model space allows for $1f_{7/2}$, $2p_{3/2}$, $1f_{5/2}$, and $2p_{1/2}$; see text for further details). For all cases, however, one configuration dominates the spectroscopic strength. This configuration is listed. There are two 6^+ fragments predicted by shell model about 500 keV apart. The reaction calculation was done for each at the experimental energy.

J^π	E_{final} (MeV)	**Shell model configuration**	**COM corr.**	$C^2S_{\text{S.M.}}$	$\sigma_{\text{s.p.}}$ (mb)	σ_{theory} (mb)
$7/2^-$	0	$[0^+ \otimes 1f_{7/2}]$	0.942	0.246	2.869	0.66
					Inclusive sum:	0.66

Table 6.9: Theoretical predictions of the partial and inclusive cross sections for the ^{9}Be(^{50}Fe, ^{51}Co + γ)X reaction.

Reaction	σ_{theory} (mb)	$\sigma_{\text{exp.}}$ (mb)
^{9}Be(^{48}Cr, ^{49}Mn + γ)X	1.60	1.63(8)
^{9}Be(^{49}Mn, ^{50}Fe + γ)X	1.05	1.38(7)
^{9}Be(^{50}Fe, ^{51}Co + γ)X	0.66	0.57(8)

Table 6.10: Inclusive cross sections for the ^{9}Be(^{48}Cr, ^{49}Mn + γ)X, ^{9}Be(^{49}Mn, ^{50}Fe + γ)X, and ^{9}Be(^{50}Fe, ^{51}Co + γ)X reactions. The predictions for the ^{9}Be(^{48}Cr, ^{49}Mn + γ)X and ^{9}Be(^{50}Fe, ^{51}Co + γ)X reactions agree with calculated values. The ^{9}Be(^{49}Mn, ^{50}Fe + γ)X theoretical result under-predicts the measured value. This discrepancy may be associated with the difficulty of including the wide spread of spectroscopic strength observed below S_p(^{50}Fe) in the calculations.

number of incoming projectiles, as measured in one of four unreacted runs[5] on the ^{9}Be target, and with respect to the target number density (see Equation 4.17), inclusive cross sections were calculated for the ^{9}Be(^{48}Cr, ^{49}Mn + γ)X, ^{9}Be(^{49}Mn, ^{50}Fe + γ)X, and ^{9}Be(^{50}Fe, ^{51}Co + γ)X reactions. The results are summarized in Table 6.10 which also include the theoretical results of Section 6.4.2. The magnitude of the inclusive cross sections for the ^{9}Be(^{48}Cr, ^{49}Mn + γ)X, ^{9}Be(^{49}Mn, ^{50}Fe + γ)X, and ^{9}Be(^{50}Fe, ^{51}Co + γ)X reactions, of order $\sigma_{\text{inc}} \sim 1$ mb, and the manner in which the inclusive cross sections decrease with respect to increasing proton asymmetry along the $N = 24$ isotonic chain, are similar in behavior to the proton pickup reactions measured by Gade, *et al.* across the $N = 10$ isotonic chain: ^{9}Be(^{20}Ne, ^{21}Na + γ)X [60] with $\sigma_{\text{inc}} = 1.85(12)$ mb and ^{9}Be(^{22}Mg, ^{23}Al + γ)X [61] with $\sigma_{\text{inc}} = 0.54(5)$ mb.

To ensure the consistency of experimental conditions between the reacted and unreacted measurements, only data runs immediately adjacent in time were used. The only exception was for the ^{9}Be(^{50}Fe, ^{51}Co + γ)X reaction. Because of the low production rate of ^{51}Co, two, rather than one, neighboring reacted runs were summed. Acceptance losses were only seen in the dispersive direction and were estimated by fits to the DTA

[5]Recall that for an *unreacted* run the spectrograph's field is set to center the incoming beam passing through the target in the focal plane. For a *reacted* run, the spectrograph is set to center the pickup reaction product.

distribution. See Section 5.6.1 for similar analysis for the ^{9}Be(^{54}Ti,^{53}Sc + γ)X reaction. The contributions to the final, weighted runs are shown in Figures 6.12, 6.13, and 6.14. The consistency of the separate cross section measurements, whose weighted sums form the final reported values, with each other show that the differences associated with the different experimental settings have been accurately accounted for.

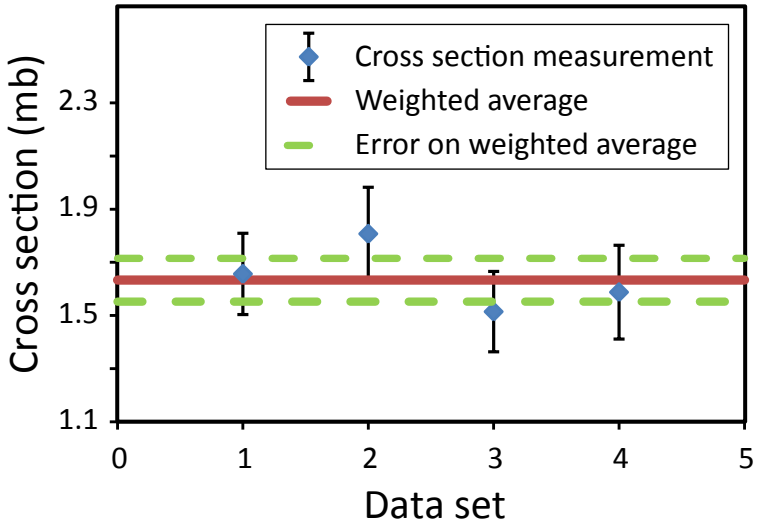

Figure 6.12: Cross section measurements for the ^{9}Be(^{48}Cr,^{49}Mn + γ)X reaction. Each cross section measurement is associated with a separate unreacted run. The consistency of the measurements with each other show the consistency of the separate calibrations applied to each different experimental setting.

The comparison of experiment and theory, contrasted in Table 6.10, shows good agreement between the theoretical predictions and experimental measurements of the inclusive cross section for the even-even pickup reactions, i.e. ^{9}Be(^{48}Cr,^{49}Mn + γ)X and ^{9}Be(^{50}Fe,^{51}Co+γ)X. The theoretical result for the ^{9}Be(^{49}Mn,^{50}Fe+γ)X reaction, although similar in magnitude, under predicts the observed inclusive cross section. This difference is likely caused by the limited number of fragmented states with significant spectroscopic strength included in the final theoretical calculations.

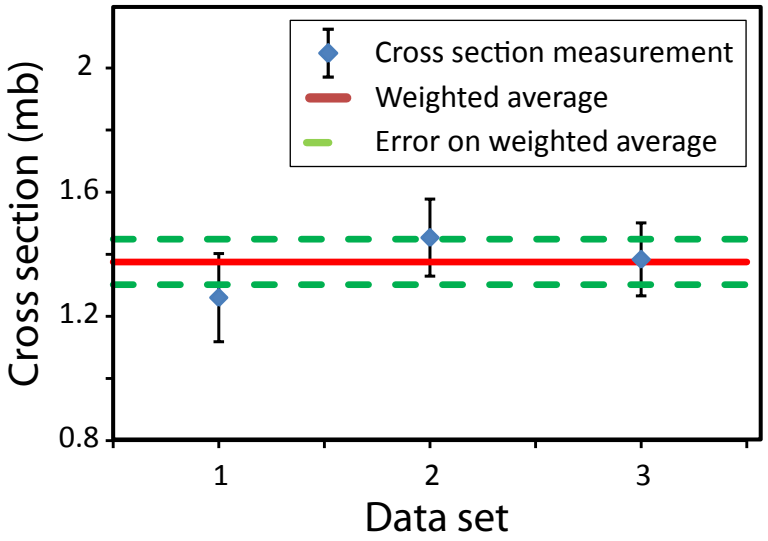

Figure 6.13: Cross section measurements for the ^{9}Be(^{49}Mn, ^{50}Fe$+\gamma$)X reaction. Each cross section measurement is associated with a separate unreacted run. The consistency of the measurements with each other show the consistency of the separate calibrations applied to each different experimental setting. Only three runs were summed, in comparison to the ^{9}Be(^{48}Cr, ^{49}Mn$+\gamma$)X and ^{9}Be(^{50}Fe, ^{51}Co$+\gamma$)X reactions, because of PID problems associated with Setting 5 of Table 6.2.

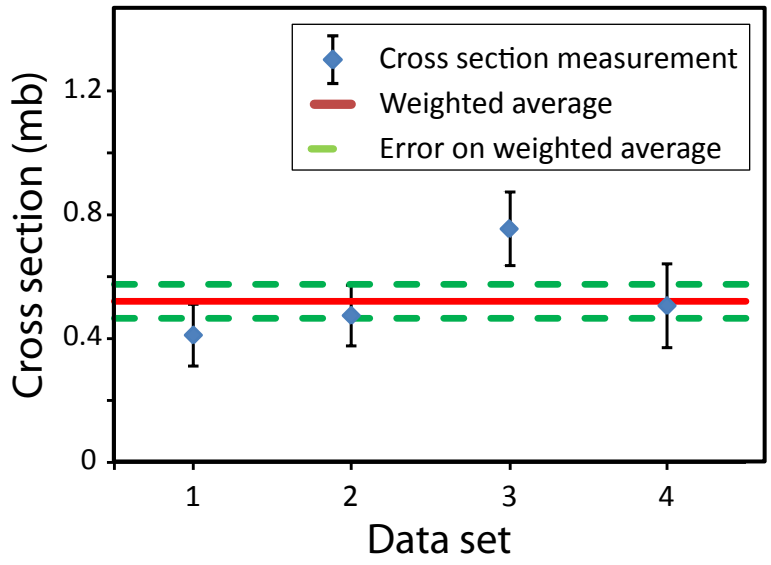

Figure 6.14: Cross section measurements for the ^{9}Be(^{50}Fe, ^{51}Co$+\gamma$)X reaction. Each cross section measurement is associated with a separate unreacted run. The consistency of the measurements with each other show the consistency of the separate calibrations applied to each different experimental setting.

6.4.4 Observed Transitions

The residue rest-frame and laboratory spectra for ^{49}Mn and ^{50}Fe are shown in Figures 6.15 and 6.16. No transitions were observed for ^{51}Co and its spectrum is not shown. The Doppler-reconstructed (residue rest-frame) spectra, shown in the upper frames of these figures, are used, as in the case of the ^{9}Be(^{54}Ti, ^{53}Sc + γ)X reaction, to extract the transition energies and partial cross sections of the projectile-like reaction products. The laboratory frame spectra, shown in the bottom panes, are used to extract the partial cross sections to the final states of the target, stripped of a proton by the heavy projectile. For the ^{9}Be target, the proton pickup reaction leads to one of several ^{8}Li(J^{π}) states. The target final states are included in the DWBA analysis outlined in Section 3.5. Only three excited states are considered in the sum: the $2^{+}_{\text{g.s}}$ ground state, the first 1^{+}_{1} state at 980.80(10) keV (leading to a E_{γ} = 980.80(10) keV transition), and the first 3^{+}_{1} state at 2255(3) keV (leading to a E_{γ} = 2255(3) keV transition) [166]. The 1^{+}_{1} state was observed by Ref. [60] in the laboratory-frame spectra coincident with the ^{21}Na pickup residue. These transitions were not observed in the current, lower-statistics experiment.

Because the Lorentz boost (see Equation 4.3) depends upon the angle of emission, rest-frame energies are boosted to different energies in the SeGA 37° and 90° rings. The differences in the Lorentz boost accounts for the split of the Doppler-reconstructed 260.8(11) keV transition, shown in the upper pane of Figure 6.15 into the two peaks in the lower pane. The measured transition energies, which agree with literature (see Table 6.11), were extracted from spectra with optimized target position z_{tar} and beam velocity β parameters. See Section 5.6.2 for an overview of the method. ^{48}Cr, with a fast $4^{+}_{1} \rightarrow 2^{+}_{1}$ transition of 1106.30(13) keV and 1.23(12) ps [167] provided the best reference to fix the target position for both the ^{9}Be(^{48}Cr, ^{49}Mn + γ)X and ^{9}Be(^{49}Mn, ^{50}Fe + γ)X reactions. For a beam velocity of $\beta \sim 0.3$ or 0.1 mm/ps, a 1.23 ps lifetime corresponds to an average path length of an excited nucleus before decay of 0.12 mm. Thus, for the 188 mg/cm^2, 1.1 mm target, ^{48}Cr decays, on average, roughly in the middle of the target.

The spectra of each of the pickup reaction products—^{49}Mn, ^{50}Fe, and ^{51}Co—will be addressed individually.

In the ^{49}Mn rest-frame spectrum, shown in the upper panel of Figure 6.15, only one transition is seen, the $7/2^{(-)}_1 \rightarrow 5/2^-_{\text{g.s}}$ decay. The measured energy of 260.8(11) keV agrees with the compiled literature value of 261.38(13) keV [154]. Other higher-energy and higher-spin states, like the $9/2^{(-)}_1$ state at 1059.18(24) keV (E_γ = 798.28 keV) and 1541.31(25) keV (E_γ = 482.19, 1278.8 keV) [154] were not observed. The strong population of the $7/2^{(-)}_1$ state is quantified with a measured partial cross section in Section 6.4.5. No ^{8}Li transitions were observed in the laboratory-frame spectrum (lower pane) suggesting a low cross section for the population (statistics were to low to assert a conclusion). Both displayed spectra were created using a tight contour gate on the PID spectrum (with additional gates selecting particle-singles, selecting incoming ^{48}Cr, and eliminating contamination). The tight gate decreases contamination from neighboring ^{48}Cr (the 752.19(11) keV $2^+_1 \rightarrow 0^+_{\text{G.S.}}$ is barely visible in the upper pane of Figure 6.15) and ^{47}Cr but decreases the total peak area in the 260.8(11) keV transition.

Two transitions were seen for ^{50}Fe at 765.6(20) keV and 1086.1(51) keV. Both transitions agree with the literature values of 764.9(3) keV and 1086.6(3) keV [158] (see Table 6.11). These transitions correspond to the $2^+_1 \rightarrow 0^+_{\text{g.s.}}$ and $4^+_1 \rightarrow 2^+_1$ decays respectively. Similarly to the ^{9}Be(^{48}Cr, ^{49}Mn + γ)X reaction, a tight contour gate was used. For ^{50}Fe this was used to eliminate contamination from ^{49}Mn and ^{48}Mn. No ^{8}Li transitions were observable in the rest frame spectrum.

No γ rays were observed for ^{51}Co. The statistics for ^{51}Co are much lower than either ^{50}Fe or ^{49}Mn because of both the smaller incident rate of incoming parent ^{50}Fe (as compared to the rates of ^{48}Cr and ^{49}Mn; see Table 6.1), because of the comparatively lower inclusive cross section for the production of this proton-rich nucleus—carrying through with the simple arithmetic shows that the total production of ^{51}Co in pps is 14 times less than the production of ^{49}Mn and 10 times less than the production of ^{50}Fe—and because

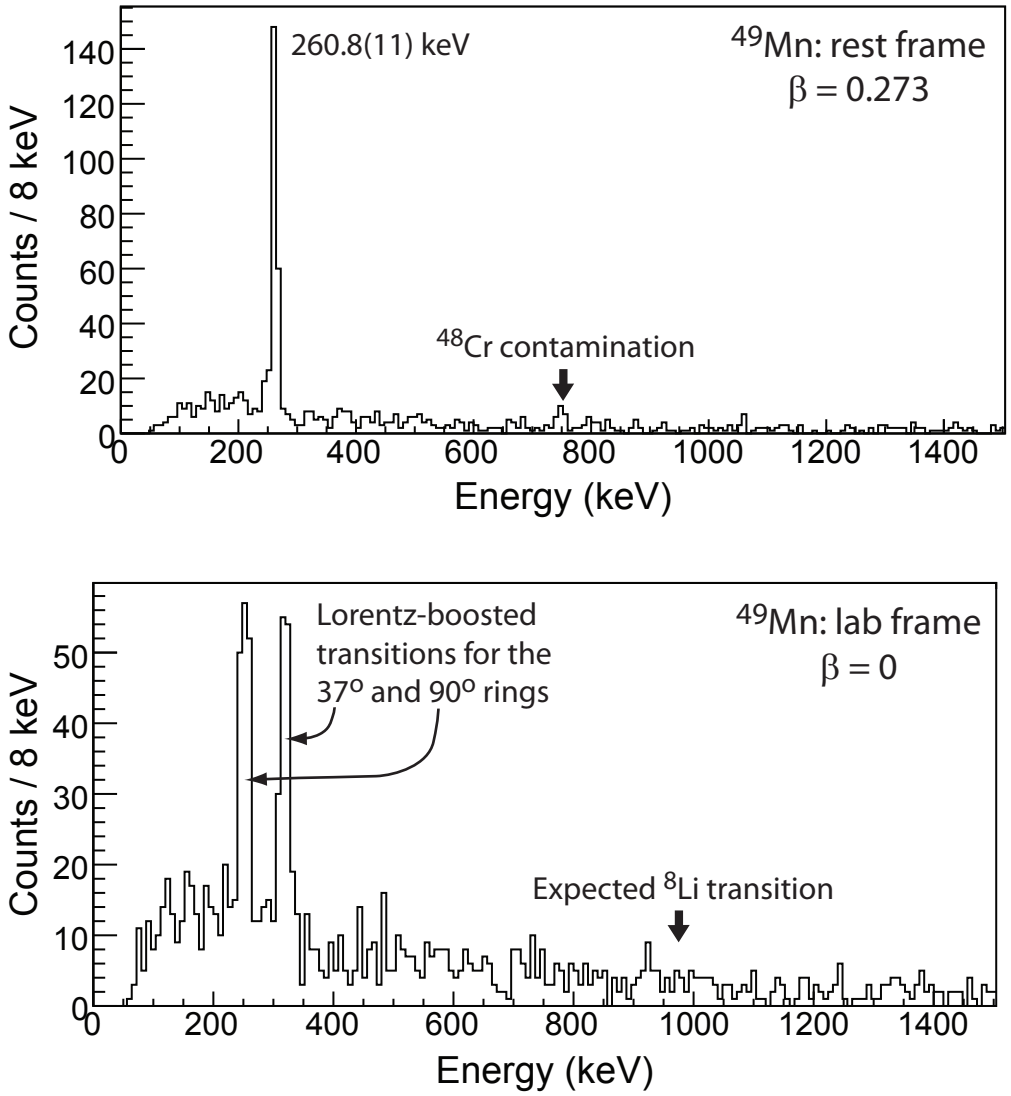

Figure 6.15: Rest-frame and laboratory frame spectra for ^{49}Mn for the ^{9}Be(^{48}Cr, ^{49}Mn + γ)X reaction. The observed 260.8(11) keV transition, corresponding to the decay of the first $7/2^{(-)}_1$ state to the ground state is shown. The energy of the 260.8(11) keV γ rays emitted is boosted from the residue rest frame to the laboratory frame according to Equation 4.3. Because the Lorentz-boost depends upon the emission angle, the transition is observed as two different energies in the laboratory frame. This effect is seen in the bottom panel. Of additional note, the excited states of the ^{9}Be target after proton removal, e.g. $E_\gamma(^{9}\text{Be} \rightarrow {}^{8}\text{Li}^{*}) = 981$ keV (indicated by a black arrow), are not observed. Contamination from ^{48}Cr is observed in the ^{49}Mn rest-frame spectrum (at $E_\gamma \approx 750$ keV).

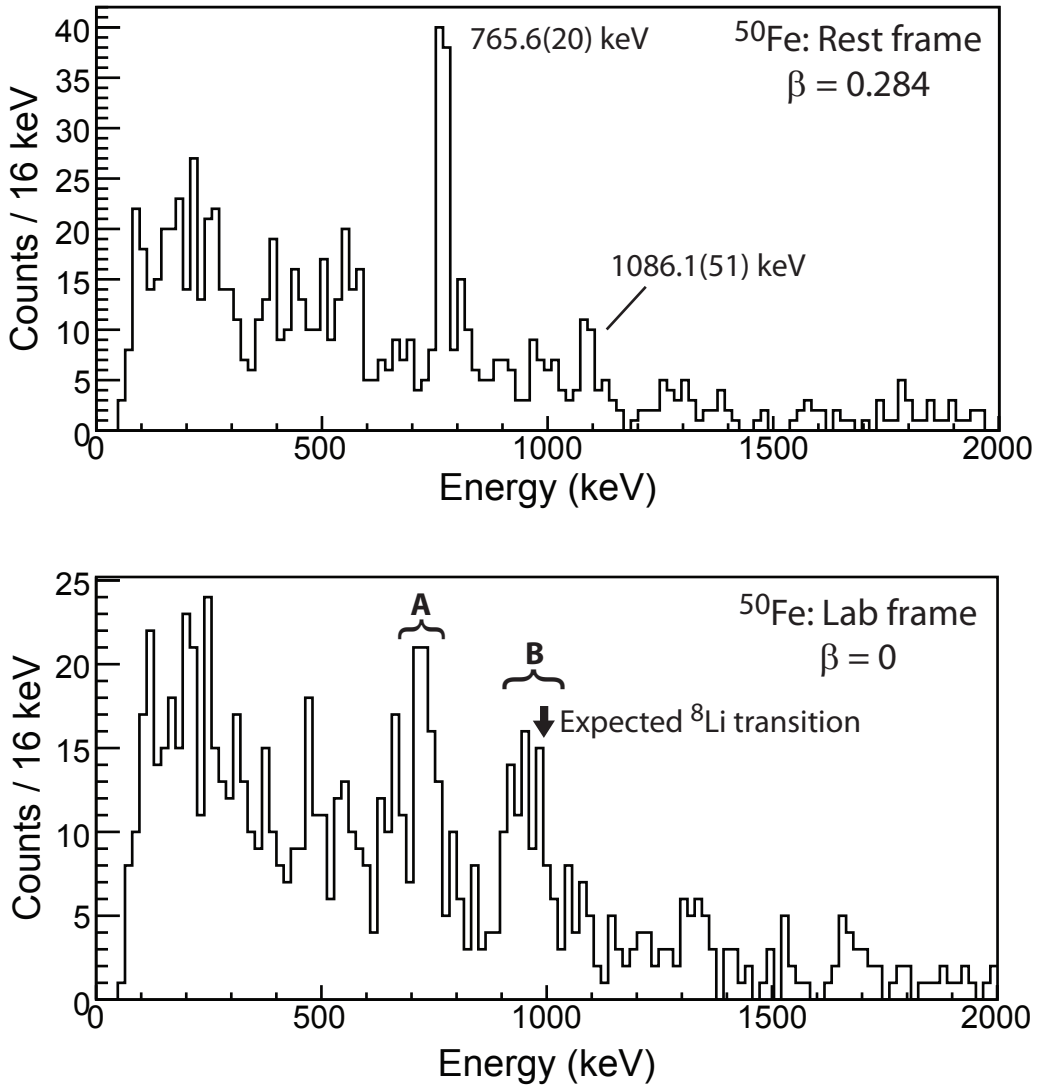

Figure 6.16: Rest-frame and laboratory frame spectra for ^{50}Fe for the ^{9}Be(^{49}Mn, ^{50}Fe $+\gamma$)X reaction. The observed 765.6(20) keV and 1087.1(51) keV transitions (upper panel), corresponding to the $2_1^+ \rightarrow 0^+_{\text{g.s.}}$ and $4_1^+ \rightarrow 2_1^+$ decays are indicated. The 765.6(20) keV residue rest-frame transition is Doppler-boosted to energies indicated by the labels **A** (90° ring) and **B** (37° ring) in the laboratory spectrum (lower panel). The 37° ring, Doppler-boosted transition (**B**) overlaps the expected ^{8}Li 981 keV transition. As in the ^{9}Be(^{48}Cr, ^{49}Mn $+\gamma$)X case (see Figure 6.15), the decays of the ^{8}Li 1_1^+ and 3_1^+ states at E_γ = 981 keV and 2255 keV are not observed.

Isotope	Transition	Measured Energy (keV)	Literature Energy (keV)
^{49}Mn	$7/2^{(-)}_1 \rightarrow 5/2^-_{\text{g.s.}}$	260.8(11)	261.38(13)
^{50}Fe	$2^+_1 \rightarrow 0^+_{\text{g.s}}$	765.6(20)	764.9(3)
	$4^+_1 \rightarrow 2^+_1$	1086.1(51)	1086.6(3)
^{51}Co	–	–	–

Table 6.11: Measured energies for ^{49}Mn and ^{50}Fe from the ^{9}Be(^{48}Cr, ^{49}Mn + γ)X and ^{9}Be(^{49}Mn, ^{50}Fe + γ)X reactions with comparison to theory. No γ rays were observed for ^{51}Co, populated in the ^{9}Be(^{50}Fe, ^{51}Co + γ)X reaction.

^{51}Co is barely bound (S_p = 88 keV as evaluated by Ref. [148]). Although the presence of a high Coulomb barrier at the proton drip line can dramatically increase the lifetimes of unbound states, it is possible that the population of ^{51}Co leads to unbound states with lifetimes smaller than the time necessary to detect ^{51}Co in the S800 focal plane.

For all spectra, energy errors were calculated, as in the analysis of the ^{9}Be(^{54}Ti, ^{53}Sc + γ)X reaction (see Section 5.6.2) from the uncertainty on the energy calibration, the velocity of projectile (β), the target position, and the fitting procedure. These errors were considered to be independent and were added in quadrature. Separate β values were chosen for each transition because of possible differences in lifetimes of the states.

6.4.5 Partial Cross Sections

Partial cross sections were calculated from the full-energy peak yield relative to the number of detected heavy residues. Experimental details are similar to the ^{9}Be(^{54}Ti, ^{53}Sc + γ)X reaction detailed in Section 5.6.3. See Section 4.5.4 for an introduction to the method. The tight gates used to produce the γ spectra of Section 6.4.4 were enlarged. The larger gates included contamination from the inelastic excitation and neutron knockout reaction products, but ensured all γ rays from the pickup reaction products were included. The uncertainty on the size of this gate was included as a systematic contribution to the final uncertainty. The partial cross section to the excited states in the pickup residue accounted

for any feeding, e.g. the $4_1^+ \rightarrow 2_1^+$ transition in ^{49}Mn. The inclusive cross section was subtracted from the yield to excited states to extract the partial cross section to the ground state: $\sigma_{\text{g.s.}} = \sigma_{\text{inc.}} - \sigma_{\text{ex.}}$. For ^{49}Mn, the $1/2_1^-$ and $3/2_1^-$ states, with calculated energies of 1.703 MeV and 1.741 MeV, if they are populated in the reaction (they were not observed in the γ ray spectrum; see Figure 6.15), should decay to the ground state. Therefore the measured cross section to the ground state can only be considered an upper bound. For ^{50}Fe, it is expected that the 4^+ and 6^+ states will funnel through the first 2^+

Special care had to be taken for the ^{9}Be(^{49}Mn, ^{50}Fe + γ)X reaction. The PID for the reaction runs after the addition of the delays (setting 5 of Table 6.2) was very diffuse and smeared, possibly because of non-linearities in the TDC associated with the new ^{9}Be(^{49}Mn, ^{50}Fe + γ)X time-of-flight. The partial cross sections extracted from the good and poor PIDs were statistically inconsistent with each other. The poor quality PID had much lower yield relative to the number of incoming ^{49}Mn nuclei. A decision was made to exclude the data associated with setting 5 and the uncertainties associated with the drop in statistics, see Table A.5, are reflected in the larger uncertainties for the ^{9}Be(^{49}Mn, ^{50}Fe + γ)X partial cross sections.

The comparison of theoretical and experimental partial cross sections are found in Figures 6.17, 6.18, and 6.19. The data for these figures was taken from Tables A.4, A.5, and A.6. The highest statistics case, the ^{9}Be(^{48}Cr, ^{49}Mn + γ)X reaction, whose results are shown in Figure 6.17, shows good agreement between the theoretical and experimental yields to the ground and excited states. Theory predicts and experiment observes a zero cross section to the ground state and a high (nearly the full inclusive strength) partial cross section to the $7/2_1^-$ state at 260.8(11) keV.

The predictions associated with the ^{9}Be(^{49}Mn, ^{50}Fe + γ)X reaction are shown in Figure 6.18 (the figure data was taken from Table A.5). The experimental partial cross sections to the ground state and first 2_1^+ state match the prediction. The experimental partial cross section to the 4_1^+ state should be considered an upper limit. It includes

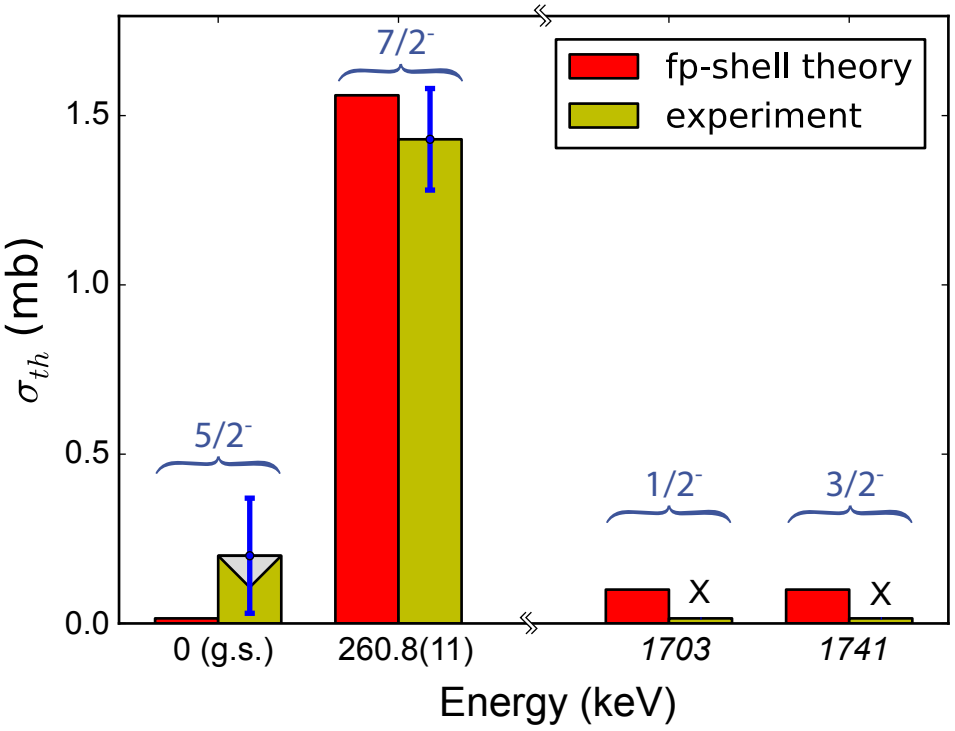

Figure 6.17: Measured and predicted partial cross sections for the ^{9}Be(^{48}Cr, ^{49}Mn + γ)X reaction. The $1/2^-_1$ and $3/2^-_1$ states were not observed (indicated by an **X**) in the current experiment or previous spectroscopic studies and their assigned energies (in italics) were taken from shell model calculations (see Figure 6.9). If the $1/2^-_1$ and $3/2^-_1$ states are fed experimentally, they should directly decay to the ground state and bypass the $7/2^-_1$ state at 0.272 MeV. Because the feeding to the ground state could not be quantified, an upper bound for the population of the ground state, i.e. $\sigma_{\text{g.s.}} \leq 0.20(17)$ mb, is given (the upper limit is indicated by a grey triangle). The population pattern observed, with a population of the ground state consistent with 0 mb ($\leq 0.20(17)$ mb) and a partial cross section to the $7/2^-_1$ state of 1.43(15) mb (nearly all of the inclusive strength), is consistent with theoretical predictions of 0 mb and 1.56 mb. See Table A.4 for the data plotted in this figure.

the effects of feeding from the 6_1^+ and other higher spin states that were not observed because of statistics. The high statistical uncertainty associated with the 4_1^+ state—only 27 counts were observed—impacts the partial cross section to the 2_1^+ state because of feeding subtraction. Although Figure 6.18 includes the 4_1^+ state, the results in Table A.5 are presented with and without the inclusion of the state. In both cases, the partial cross section to the highest reported state, the 4_1^+ state of column 4 and the 6_1^+ state of column 6, should be considered an upper limit because of the inclusion of observed and unobserved feeding from higher-lying states predicted by shell-model calculations and the partial cross section predictions of Figure 6.18.

No transitions were observed in the ^{51}Co spectrum. The theoretical inclusive cross section is equal to the partial cross section to the $7/2^-$ ground state (Figure 6.19). All other states are above the proton separation energy. The theoretical prediction of 0.71 mb is close to the observed value of 0.57(8) mb.

In all three reactions, ^{9}Be(^{48}Cr, ^{49}Mn + γ)X, ^{9}Be(^{49}Mn, ^{50}Fe + γ)X, and ^{9}Be(^{50}Fe, ^{51}Co + γ)X, the pattern and magnitude of population to states in the pickup reaction residues are well-matched by theory, with the exception of the higher lying 4_1^+ state of ^{50}Fe which is likely fed by higher-lying states whose individual partial cross sections are too low to be experimentally observed.

6.4.6 Momentum Distributions

The longitudinal momentum distributions, unlike the distributions associated with the knockout reactions, do not provide direct spectroscopic information. This critical difference is a result of the two-body final state of the pickup reaction (target residue and pickup reaction product) in comparison to the three-body final state of the knockout reaction (target residue, knockout reaction product, and removed nucleon). Further details are shown in Section 3.5.1. The momentum broadening due to the reaction processes is negligible (delta function) and the final distribution widths include the simple convolution

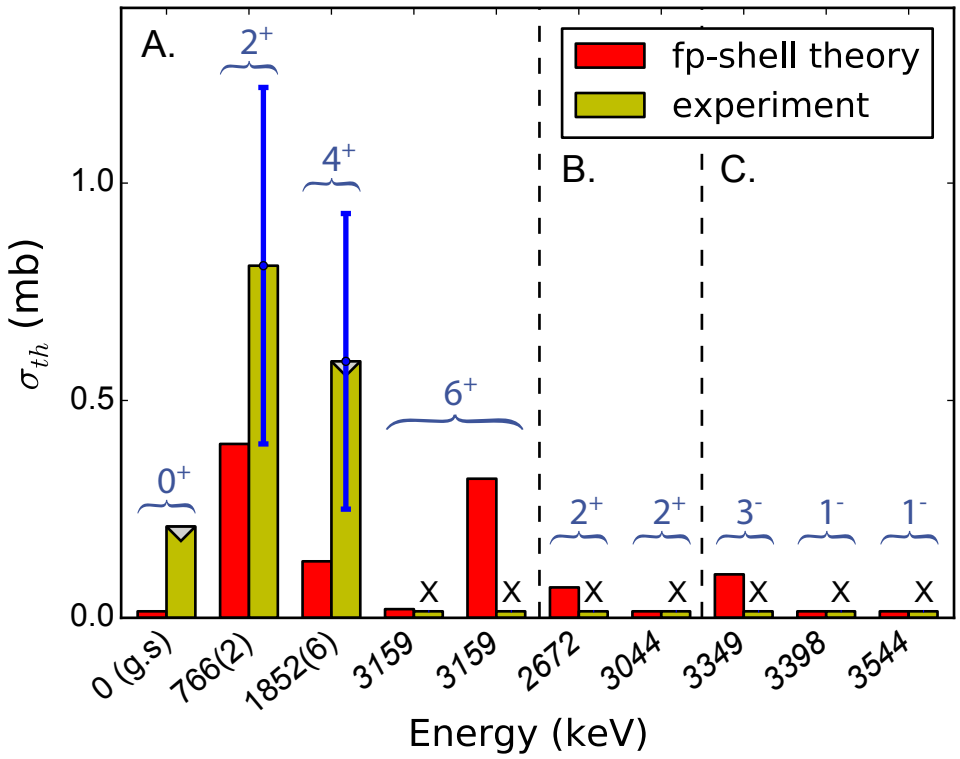

Figure 6.18: Measured and predicted partial cross sections for the ^{9}Be(^{49}Mn, ^{50}Fe + γ)X reaction. States whose energy labels include uncertainties ($0^+_{\text{g.s}}$, 2^+_1, and 4^+_1 states) were observed in the experiment. Experimental states labeled with an **X** were not observed: the 6^+_1 state (partition **A**), the 2^+_2 and 2^+_3 states (partition **B**), and the odd spin 3^+_1, and 1^+ states (partition **C**). Their energies were taken from the shell model calculations of Figure 6.10 and are italicized to note their origin (also, Table A.2). The feeding to both the 4^+_1 state and the ground state could not be accurately estimated, and therefore the values reported are upper bounds (indicated by grey rectangles). The two 6^+_1 states represent two fragments predicted by shell model calculations with different spectroscopic factors. See Table A.5 for the data plotted in this figure.

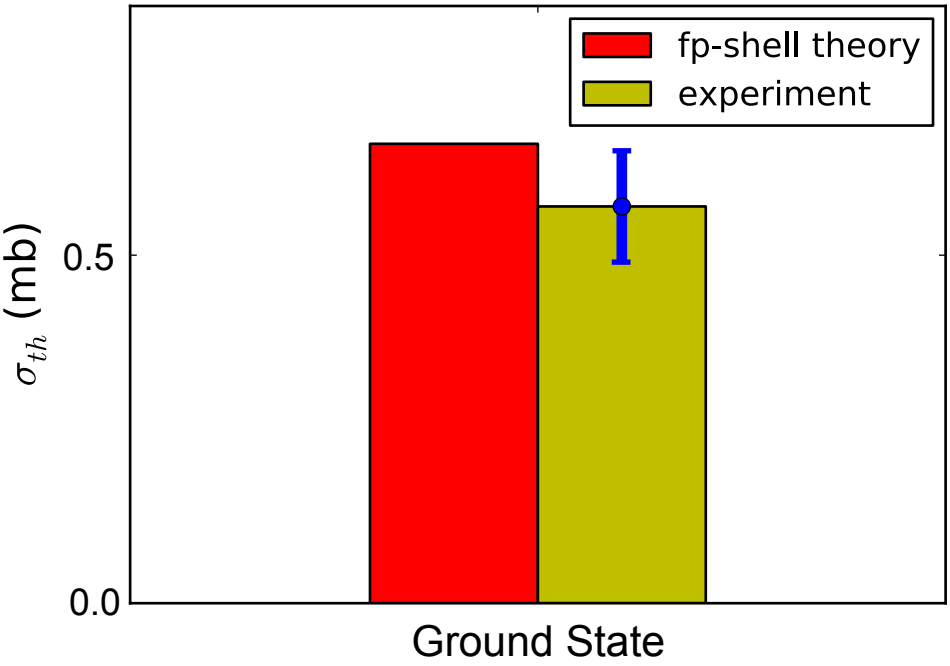

Figure 6.19: Measured and predicted partial cross sections for the ^{9}Be(^{50}Fe, ^{51}Co + γ)X reaction. Because no transitions were observed, the cross section to the ground state is equal to the inclusive cross section. CCBA and shell model calculations (theory) reproduce the magnitude of the observed strength. See Table A.6 for the data plotted in this figure.

of the momentum profile of the beam with the differential momentum loss in the target. Any deviation from this simple model, e.g. an increase in measured width, suggests reaction processes beyond the simple, direct transfer of a proton from a target bound state to a projectile ground state. The increase in differential momentum width is especially significant for reactions that add or remove a proton because of the high Z-dependence of the energy (momentum) loss of a charged particle through matter.

The final, lab-frame momentum distributions for the ^{9}Be(^{48}Cr, ^{49}Mn + γ)X, ^{9}Be(^{49}Mn, ^{50}Fe + γ)X, and ^{9}Be(^{50}Fe, ^{51}Co + γ)X reactions are presented in Figures 6.20, 6.21, and 6.22. These figures include the measured longitudinal momentum distribution of the pickup reaction product, the longitudinal momentum distribution of the incoming beam as measured during a separate run with the unreacted incoming cocktail beam centered in the focal plane, and the theoretical distribution composed from the convolution of the unreacted beam with the differential momentum loss in the target. The central

momentum for the observed reacted (unreacted) parallel momentum distributions are 13.1 GeV/c (13.0 GeV/c) for the ^{9}Be(^{48}Cr, ^{49}Mn + γ)X reaction, 13.7 GeV/c (13.6 GeV/c) for the ^{9}Be(^{49}Mn, ^{50}Fe + γ)X reaction, and 14.3 GeV/c (14.2 GeV/c) for the ^{9}Be(^{50}Fe, ^{51}Co + γ)X reaction.

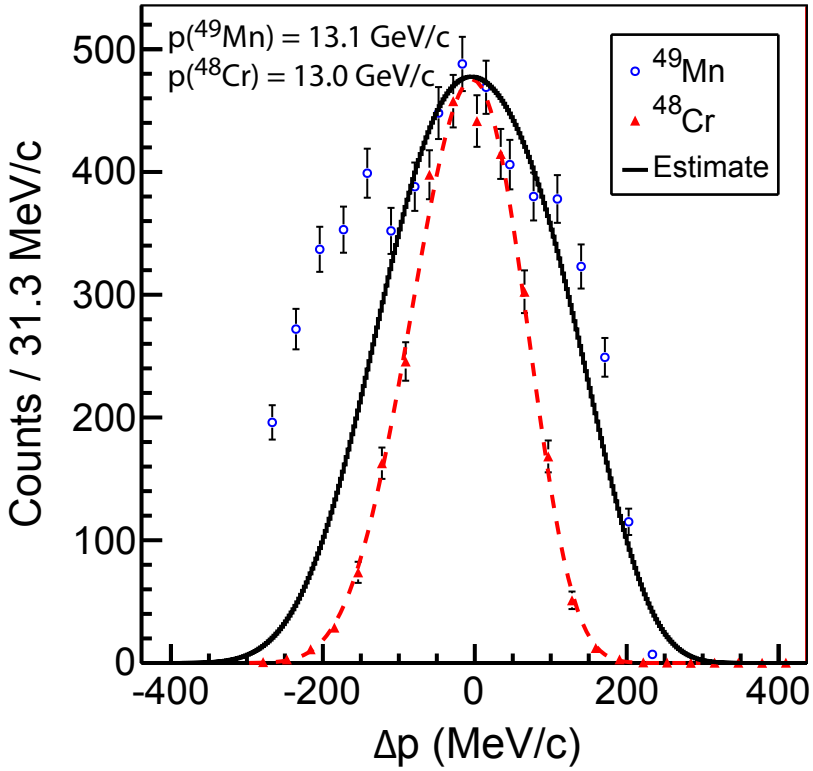

Figure 6.20: Measured lab-frame parallel momentum distribution of ^{49}Mn (^{9}Be(^{48}Cr, ^{49}Mn+γ)X reaction). The unreacted momentum distribution of ^{48}Cr (shown; red triangles) and its fit by Equation 6.1 (red dotted line) are used, along with the differential momentum width associated with the position of the reaction process within the target, to create the theoretical distribution (solid black curve). The observed width of the ^{49}Mn distribution is broadened, as hypothesized in the text, by scattering off the beam blocker. This scattering moves cross section from higher to lower momentum and creates the prominent low-momentum hump observed at about $\Delta p \approx -200$ MeV in the spectrum.

Two artifacts of Figures 6.20, 6.21, and 6.22 must be addressed: the shape of the unreacted beam and the significant difference in width between the measured lab-frame distribution and the theoretical prediction.

Because the profile of the unreacted beam is folded into the final theoretical distribu-

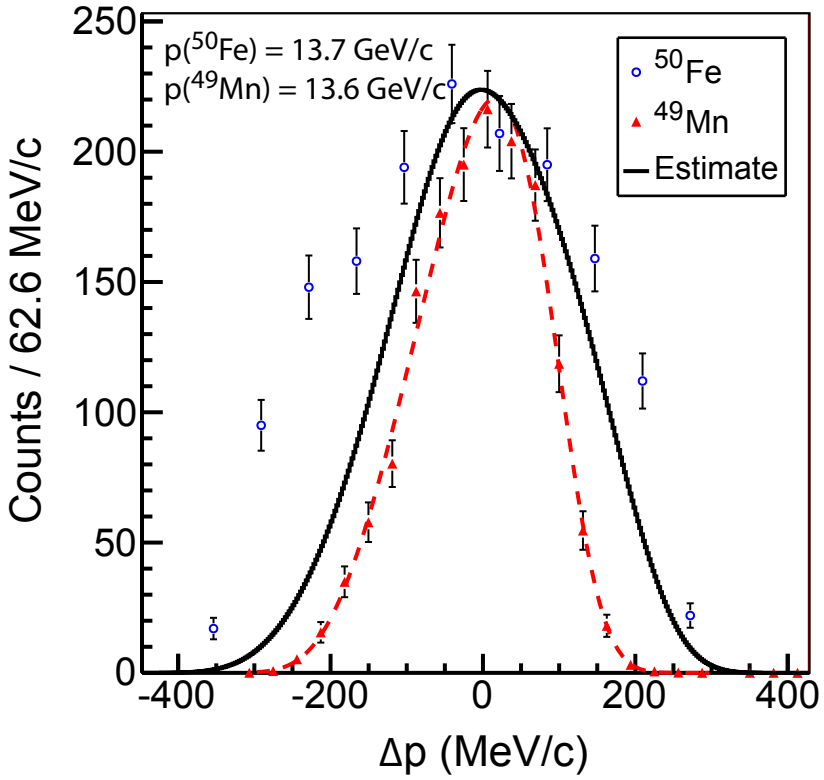

Figure 6.21: Measured, lab-frame, inclusive, parallel momentum distribution of ^{50}Fe (^{9}Be(^{49}Mn, ^{50}Fe + γ)X reaction; blue circles). As detailed in Figure 6.20, the unreacted beam (solid, red triangles), its fit (dashed, red line), showing more skew than the ^{9}Be(^{48}Cr, ^{49}Mn + γ)X reaction, and the theoretical distribution (solid, black line) created from the convolution of the fit to the unreacted ^{49}Mn momentum distribution with the differential momentum loss in the target, are displayed. The broadening of the momentum distribution and the low momentum hump are hypothesized to occur as artifacts from scattering off the beam blocker located in front of the focal plane.

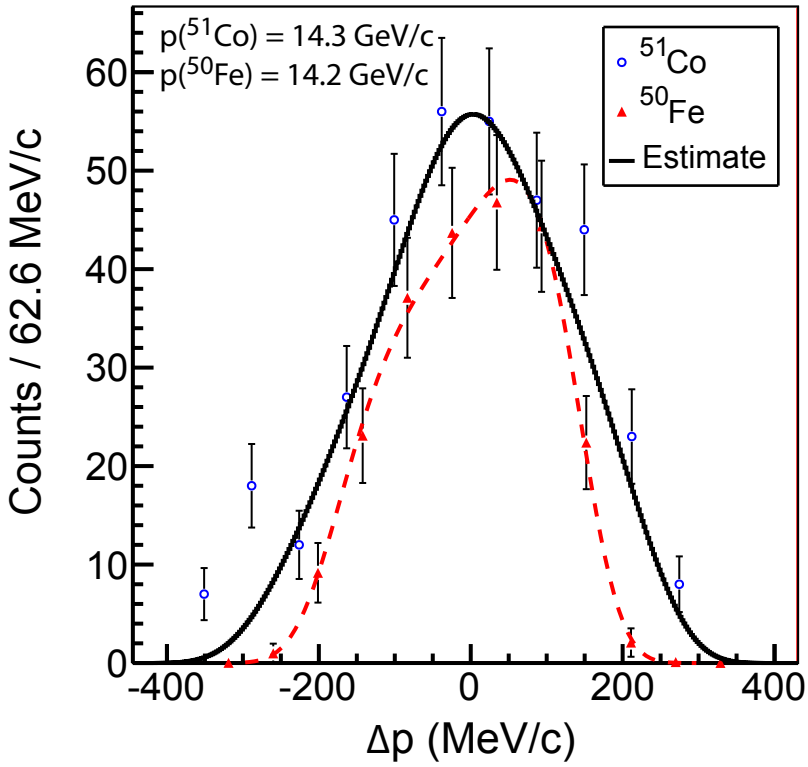

Figure 6.22: Measured, lab-frame, inclusive parallel momentum distribution of ^{51}Co (^{9}Be(^{50}Fe, ^{51}Co + γ)X reaction; blue circles). The unreacted ^{50}Fe and theoretical momentum distributions are also shown. The unreacted beam shows significant skew and asymmetry caused by the A1900 slits. The low-momentum broadening, observed in Figures 6.20 and 6.21, was significantly reduced in the ^{9}Be(^{50}Fe, ^{51}Co + γ)X reaction because of decreased scattering by the beam blocker (see text for additional details). The final overlay of the measured distribution and the theoretical prediction is consistent with the direct reaction assumption of the CCBA calculations.

tion, is important to correctly parametrize the shape. The beam profile depends upon the beam tune through the A1900 fragment separator and analysis line. Typically, the settings of the A1900 are optimized for one fragment and other components of the cocktail beam may be at the edge of the acceptance and have asymmetric beam profiles. For the current experiment, deviations are minor for the ^{9}Be(^{48}Cr, ^{49}Mn + γ)X reaction, stronger for the ^{9}Be(^{49}Mn, ^{50}Fe + γ)X reaction, and strongest for the ^{9}Be(^{50}Fe, ^{51}Co + γ)X reaction where clear asymmetry of the unreacted beam is observed.

The beam profile was successfully parametrized by an equation of the form [168]

$$D(\xi,\ell) = A\exp\left[\frac{1}{8}k - \frac{1}{2}s\delta - \frac{1}{4}(2+k)\delta^2 + \frac{1}{6}s\delta^3 + \frac{1}{24}k\delta^4\right] \text{ where } \delta = \frac{\xi-\ell}{\sigma} \qquad (6.1)$$

A is the amplitude, ℓ is the centroid, σ is the Gaussian width, k is the shape parameter (from Gaussian to top-hat), and s is the skew-parameter. The shape is completely determined by five parameters and achieves an excellent fit. See especially Figure 6.22.

The shape of the low-momentum side of the momentum distribution, particularly Figure 6.20 with the low momentum hump, suggests that the increase in width is caused by an experimental rather than reaction artifact. One possibility is the scattering of the reaction residues off the beam blockers. The beam blockers are plates, located before the focal plane detectors, that can be inserted in the path of the beam. Usually this is done to protect the detectors against the unreacted beam or high-intensity reaction products that enter the focal plane at the edge of the acceptance. Scattering would move the differential cross section in a manner characteristic of the shapes observed. The effect appears to disappear for ^{51}Co and is smaller for ^{50}Fe than ^{49}Mn.

Because of the artificial broadening of the ^{9}Be(^{48}Cr, ^{49}Mn + γ)X and ^{9}Be(^{49}Mn, ^{50}Fe + γ)X parallel momentum distributions, the behavior of the reaction—are there processes beyond the single-step transfer?—cannot be unambiguously determined. For ^{51}Co, because of the smaller affect of the beam blocker on the final lab-frame momentum distribution, the estimated and experimental distributions are consistent with each other and

therefore consistent with ^{9}Be(^{50}Fe, ^{51}Co + γ)X proceeding as a direct reaction, a critical assumption of the CCBA calculations.

6.5 Proton Pickup Reactions: ^{12}C target

6.5.1 Particle Identification

The identification of the incoming projectiles and outgoing pickup residues was easier for the ^{12}C(^{48}Cr, ^{49}Mn + γ)X, ^{12}C(^{49}Mn, ^{50}Fe + γ)X, and ^{12}C(^{50}Fe, ^{51}Co + γ)X reactions in comparison to the equivalent pickup reaction using the ^{9}Be target because of the addition of the TACs, added in parallel to the existing electronics, that removed the time-of-flight splitting. The new TACs finally permitted clean identification of components of the cocktail beam using the two-dimensional spectrum of DIA1 time-of-flight versus DIA2 time-of-flight[6]. There was minimal contamination from neighboring TOF components in the cocktail beam.

A nearly identical suite of gates was taken from Section 6.4.1 and used for the cleanup and identification of pickup reaction residues off the ^{12}C target: the two-dimensional histogram of XFP time-of-flight versus dispersive position in the focal plane (see Figure 6.7 for an example), and the standard PID of OBJE1 time-of-flight versus energy loss in the ion chamber. As with the ^{9}Be analysis, the full set of gates eliminated contamination from the final PID used to count the reaction residues.

6.5.2 Theoretical Predictions

Calculation of the single-partial cross sections follow the earlier ^{9}Be pickup analysis presented in Section 6.4.2 with a few critical differences associated with the treatment of the target. The same assumptions used in the CCBA calculations of the ^{9}Be(^{48}Cr,

[6]DIA1 and DIA2 time-of-flights are physically identical to the OBJ and XFP time-of-fights. The only difference lies in the electronics used to processes the signal See Table 6.3.

^{49}Mn + γ)X, ^{9}Be(^{49}Mn, ^{50}Fe + γ)X, and ^{9}Be(^{50}Fe, ^{51}Co + γ)X reactions apply: a proton is transfered in a single-step from a bound state of a ^{12}C target to a bound state of the projectile. The ^{12}C target is left in one of three bound states of ^{11}B, the $3/2^{-}_{\text{g.s.}}$ ground state, the $1/2^{-}_{1}$ excited state at 2125 keV, and the $3/2^{-}_{1}$ excited state at 5020 keV. Because a proton is removed from the carbon p-shell ($1p_{1/2}$ and $1p_{3/2}$ orbitals), the $5/2^{-}_{1}$ state, located at 4445 keV and below the energy of the $3/2^{-}$ state, is not expected to be populated. All three ^{11}B states included in the analysis are bound. The proton threshold is $S_p(^{11}\text{B}) = 11.2$ MeV.

The p-shell proton overlaps $\langle ^{11}\text{B}|\hat{a}|^{12}\text{C}\rangle$ are taken directly from a Woods-Saxon potential and the parameters of Ref. [85]: the radius parameter of $r_0 = 1.310$ fm and the diffuseness parameter of $a = 0.55$ fm were fixed to the second and fourth moments of the ^{12}C charge radius and the depth of the Woods-Saxon well was adjusted to the separation energy of the proton relative to the ^{48}Cr core. The spectroscopic factors for target initial and final state overlaps, e.g. $S = \int |\langle ^{11}\text{B}(j^{\pi})^{*}|\hat{a}|^{12}\text{C}\rangle|^2$, were calculated in the shell model using the WBP interaction [169]. The inclusion of the three ^{11}B final states nearly exhausted the spectroscopic strength with values of 3.16, 0.58, and 0.19 for overlaps of the ^{12}C ground state with the $3/2^{-}_{\text{g.s.}}$, $1/2^{-}_{1}$ and $3/2^{-}_{2}$ states of ^{11}B respectively. The remaining strength of 0.07 is thinly spread up to the proton separation energy of $S_p = 11.2$ MeV.

The remaining details associated with the calculation of the ^{12}C(^{48}Cr, ^{49}Mn + γ)X, ^{12}C(^{49}Mn, ^{50}Fe + γ)X, and ^{12}C(^{50}Fe, ^{51}Co + γ)X single-particle cross sections follow the earlier ^{9}Be analysis of Section 6.4.2. The final results are listed in Tables 6.12, 6.13, 6.14 as provided by Tostevin [162].

The single-particle cross sections, combined with the reaction-independent spectroscopic factors listed in Section 6.4.2, yield the theoretical estimates for the inclusive and partial cross sections. See Tables 6.15, 6.16, and 6.17. The calculated population pattern and magnitudes are very similar to the ^{9}Be results of Tables 6.7, 6.8, and 6.9. The partial and inclusive cross sections are slightly higher which may be attributed to the nearly complete inclusion of all target spectroscopic strength by the $3/2^{-}_{\text{g.s.}}$, $1/2^{-}_{1}$, and $3/2^{-}_{2}$ states.

^{49}Mn				Target (^{12}C → ^{11}B*)			$\sigma_{s.p}$	
I^π	E_x (MeV)	$\pi\ell_j$	$S_p^{res.}$(eff.) (MeV)	J_π (^{11}B)	$S_p^{tar.}$(eff.) (MeV)	Q (MeV)	$\sigma^{s.p.}$ (mb)	$\sum_i \sigma_i^{s.p.}$ (mb)
$7/2^-$	0.272	$1f_{7/2}$	1.813	$3/2^-$	15.957	-13.872	3.723	4.139
				$1/2^-$	18.082	-15.997	0.237	
				$3/2^-$	20.977	-18.892	0.179	
$1/2^-$	*1.703*	$1f_{7/2}$	*0.382*	$3/2^-$	15.957	-13.872	0.029	0.040
				$1/2^-$	18.082	-15.997	0.008	
				$3/2^-$	20.977	-18.892	0.003	
$3/2^-$	*1.741*	$1f_{7/2}$	*0.344*	$3/2^-$	15.957	-13.872	0.103	0.114
				$1/2^-$	18.082	-15.997	0.008	
				$3/2^-$	20.977	-18.892	0.003	

Table 6.12: Additional details on the calculation of the single-particle cross sections for the ^{12}C(^{48}Cr, ^{49}Mn + γ)X reaction evaluated at a mid-target energy of 56.7 MeV/u [162]. For additional information on the column labels, please refer to the caption of Table 6.4. The ground-state separation energy of ^{49}Mn is 2.085 MeV. The single-particle cross section to the ground state of ^{49}Mn was not calculated because of the extremely small spectroscopic factor $C^2S = 0.002$ listed in Table A.1. The $7/2^-$ energy of 272 keV was taken from experiment; see the caption of Table 6.5 for additional details. The $1/2^-_1$ and $3/2^-_1$ energies were not observed in this experiment and literature values do not exist. These energies were taken from shell-model calculations, see Figure 6.10, and are italicized to note this origin.

Comparison with experimental data is found in the experimental analysis of the inclusive and partial cross sections, Sections 6.5.3 and 6.5.5.

6.5.3 Inclusive Cross Section

Details on the calculation of the inclusive cross sections from experiment can be found in Section 6.5.3. The inclusive cross sections for the ^{12}C(^{48}Cr, ^{49}Mn + γ)X, ^{12}C(^{49}Mn, ^{50}Fe + γ)X, and ^{12}C(^{50}Fe, ^{51}Co+γ)X reactions combined two separate cross section measurements using unreacted and reacted runs located at the beginning and end of the reaction setting. The two results for all three reactions were consistent (within 1σ) of each other. Unlike the ^{9}Be analysis, the ^{12}C pickup data was all taken in one experimental setting; the problems associated with the faulty electronics were eliminated. The cross sections extracted from

^{50}Fe				Target (^{12}C → ^{11}B*)			$\sigma_{s.p}$	
I^π	E_x (MeV)	$\pi\ell_j$	$S_p^{res.}$(eff.) (MeV)	J_π (^{11}B)	$S_p^{tar.}$(eff.) (MeV)	Q (MeV)	$\sigma^{s.p.}$ (mb)	$\sum_i \sigma_i^{s.p.}$ (mb)
0^+	0	$1f_{7/2}$	4.15	$3/2^-$	15.957	-11.807	0.031	0.054
				$1/2^-$	18.082	-13.932	0.011	
				$3/2^-$	20.977	-16.827	0.011	
2^+	1.703	$1f_{7/2}$	3.385	$3/2^-$	15.957	-11.807	0.360	0.400
				$1/2^-$	18.082	-13.932	0.022	
				$3/2^-$	20.977	-16.827	0.018	
4^+	1.851	$1f_{7/2}$	2.299	$3/2^-$	15.957	-11.807	0.628	0.698
				$1/2^-$	18.082	-13.932	0.039	
				$3/2^-$	20.977	-16.827	0.031	
6^+	3.159	$1f_{7/2}$	0.991	$3/2^-$	15.957	-11.807	0.863	0.959
				$1/2^-$	18.082	-13.932	0.054	
				$3/2^-$	20.977	-16.827	0.041	
2^+	*2.672*	$1f_{7/2}$	*1.478*	$3/2^-$	15.957	-11.807	0.339	0.376
				$1/2^-$	18.082	-13.932	0.021	
				$3/2^-$	20.977	-16.827	0.016	
2^+	*3.044*	$2p_{3/2}$	*1.106*	$3/2^-$	15.957	-11.807	0.023	0.025
				$1/2^-$	18.082	-13.932	0.002	
				$3/2^-$	20.977	-16.827	0.001	
1^+	*3.349*	$1f_{7/2}$	*0.801*	$3/2^-$	15.957	-11.807	0.198	0.219
				$3/2^-$	18.082	-13.932	0.012	
				$1/2^-$	20.977	-16.827	0.009	
3^+	*3.398*	$2p_{3/2}$	*0.752*	$3/2^-$	15.957	-11.807	0.029	0.032
				$3/2^-$	18.082	-13.932	0.002	
				$1/2^-$	20.977	-16.827	0.001	
3^+	*3.544*	$2p_{1/2}$	*0.606*	$3/2^-$	15.957	-11.807	0.015	0.021
				$3/2^-$	18.082	-13.932	0.005	
				$1/2^-$	20.977	-16.827	0.001	

Table 6.13: Additional details on the calculation of single-particle cross sections (SPCSs) for the ^{12}C(^{49}Mn, ^{50}Fe + γ)X reaction evaluated at a mid-target energy of 59.0 MeV/u [162]. For additional information on the column labels, please refer to the caption of Table 6.4. The ground-state separation energy of ^{50}Fe is 4.150 MeV. Listed energies are from literature when available. Exceptions, e.g. the 2_2^+ state at 2.672 MeV, the 2_3^+ state at 3.044 MeV, and the 1^+ and 3^+ states, were taken from shell model calculations and are italicized (see Figure 6.10, Table A.2). The two fragmented 6^+ states of Table A.2 are calculated at the experimental energy of 3.544 MeV.

^{51}Co				Target (^{12}C → ^{11}B*)			$\sigma_{s.p}$	
I^π	E_x (MeV)	$\pi\ell_j$	$S_p^{res.}$(eff.) (MeV)	J_π (^{11}B)	$S_p^{tar.}$(eff.) (MeV)	Q (MeV)	$\sigma^{s.p.}$ (mb)	$\sum_i \sigma_i^{s.p.}$ (mb)
0^+	0	$1f_{7/2}$	0.164	$3/2^-$	15.957	-15.793	2.718	3.013
				$1/2^-$	18.082	-17.918	0.166	
				$3/2^-$	20.977	-20.813	0.129	

Table 6.14: Additional details on the calculation of the single-particle cross sections for the ^{12}C(^{50}Fe, ^{51}Co + γ)X reaction evaluated at a mid-target energy of 61.2 MeV/u [162]. For additional information on the column labels, please refer to the caption of Table 6.4. The ground-state separation energy of ^{51}Co is 88 keV [148]. No excited states were observed and therefore only the partial cross section to the ground state was calculated.

J^π	E_{final} (MeV)	Shell model configuration	COM corr.	$C^2S_{S.M.}$	$\sigma_{s.p.}$ (mb)	σ_{theory} (mb)
$7/2^-_{g.s.}$	0.272	$[0^+ \otimes 1f_{7/2}]$	0.940	4.139	0.425	1.65
$1/2^-_1$	1.703	$[0^+ \otimes 2p_{1/2}]$	0.940	0.040	0.245	0.01
$3/2^-_1$	1.741	$[0^+ \otimes 2p_{3/2}]$	0.940	0.114	0.373	0.04
					Inclusive sum:	1.70

Table 6.15: Theoretical predictions of the partial and inclusive cross sections for the ^{12}C(^{48}Cr, ^{49}Mn + γ)X reaction.

J^π	E_{final} (MeV)	Shell model configuration	COM corr.	$C^2S_{S.M.}$	$\sigma_{s.p.}$ (mb)	σ_{theory} (mb)
$0^+_{g.s.}$	0	$[5/2^- \otimes 1f_{5/2}]$	0.941	0.054	0.033	0.00
2^+_1	0.765	$[5/2^- \otimes 1f_{7/2}]$	0.941	0.400	1.145	0.43
4^+_1	1.851	$[5/2^- \otimes 1f_{7/2}]$	0.941	0.698	0.208	0.14
2^+_2	*2.672*	$[5/2^- \otimes 1f_{7/2}]$	0.941	0.376	0.194	0.07
2^+_3	*3.044*	$[5/2^- \otimes 2p_{3/2}]$	0.941	0.025	0.232	0.01
6^+_1	3.159	$[5/2^- \otimes 1f_{7/2}]$	0.941	0.959	0.023	0.02
6^+_1	3.159	$[5/2^- \otimes 1f_{7/2}]$	0.941	0.959	0.371	0.34
1^+_1	*3.349*	$[5/2^- \otimes 1f_{7/2}]$	0.941	0.530	0.219	0.11
3^+_1	*3.398*	$[5/2^- \otimes 2p_{3/2}$	0.941	0.309	0.032	0.01
3^+_2	*3.544*	$[5/2^- \otimes 2p_{1/2}]$	0.941	0.213	0.021	0.00
					Inclusive sum:	1.12

Table 6.16: Theoretical predictions of the partial and inclusive cross sections for the ^{12}C(^{49}Mn, ^{50}Fe + γ)X reaction. The 0^+ ground state, 2^+_1, and 4^+_1 states were observed in the experiment. Further details are found in the caption of Figure 6.8.

J^π	E_{final} (MeV)	**Shell model configuration**	**COM corr.**	$C^2S_{\text{S.M.}}$	$\sigma_{\text{s.p.}}$ (mb)	σ_{theory} (mb)
$7/2^-_{\text{g.s}}$	0	$[0^+ \otimes 1f_{7/2}]$	0.942	3.013	0.246	0.70
					Inclusive sum:	0.70

Table 6.17: Theoretical predictions of the partial and inclusive cross sections for the ^{9}Be(^{50}Fe, ^{51}Co + γ)X reaction.

Reaction	σ_{theory} (mb)	$\sigma_{\text{exp.}}$ (mb)
^{12}C(^{48}Cr, ^{49}Mn + γ)X	1.70	2.00(13)
^{12}C(^{49}Mn, ^{50}Fe + γ)X	1.12	1.72(24)
^{12}C(^{50}Fe, ^{51}Co + γ)X	0.70	0.53(13)

Table 6.18: Measure and predicted inclusive cross sections for the ^{12}C(^{48}Cr, ^{49}Mn + γ)X, ^{12}C(^{49}Mn, ^{50}Fe+γ)X, and ^{12}C(^{50}Fe, ^{51}Co+γ)X reactions. The predictions for the ^{12}C(^{48}Cr, ^{49}Mn+γ)X and ^{12}C(^{50}Fe, ^{51}Co+γ)X reactions agree with calculated values. The ^{12}C(^{49}Mn, ^{50}Fe + γ)X theoretical results under predict the measured value. This discrepancy may be associated with the difficulty of including the wide spread of spectroscopic strength observed below $S_p(^{50}\text{Fe}) = 4150(60)\,\text{keV}$.

the yields of ^{49}Mn, ^{50}Fe, and ^{51}Co are found in Table. 6.18. There is good agreement between experiment and theory for the ^{12}C(^{48}Cr, ^{49}Mn + γ)X and ^{12}C(^{50}Fe, ^{51}Co + γ)X reactions, but not for the ^{12}C(^{49}Mn, ^{50}Fe + γ)X reaction, which theory under-predicts. This behavior, also seen in the analysis of ^{9}Be(^{50}Fe, ^{51}Co + γ)X, was attributed to the high fragmentation of strength to states under the proton separation in ^{50}Fe, for example the 2^+ and 6^+ states, and the difficulty of including the multitude of states in the theoretical calculations of the single-particle cross sections.

6.5.4 Observed Transitions

The analysis of ^{12}C(^{48}Cr, ^{49}Mn + γ)X, ^{12}C(^{49}Mn, ^{50}Fe + γ)X, and ^{12}C(^{50}Fe, ^{51}Co + γ)X follows the earlier analysis of Section 6.4.4. The effective target position (common for all reactions on the ^{12}C target) and effective β values (uniquely determined for each

transition) were chosen in an identical way, with the exception of the ^{50}Fe $4_1^+ \rightarrow 2_1^+$ transition. Additional details will follow. The γ-ray spectra observed in coincidence with ^{49}Mn and ^{50}Fe for the ^{12}C(^{48}Cr, ^{49}Mn + γ)X and ^{12}C(^{49}Mn, ^{50}Fe + γ)X reactions are shown in Figures 6.23 and 6.24. The same transitions are observed in both the ^{9}Be proton pickup analysis and the ^{12}C proton pickup analysis with the exception of the ^{50}Fe $6_1^+ \rightarrow 4_1^+$ transition, which was likely observed because of the additional statistics on the ^{12}C target. Thus, for ^{49}Mn, following the ^{12}C(^{48}Cr, ^{49}Mn+γ)X reaction, the $7/2_1^- \rightarrow 5/2^-_{\text{g.s.}}$ at 260.7(12) keV was observed; for ^{50}Fe, following the ^{12}C(^{49}Mn, ^{50}Fe + γ)X reaction, the $6_1^+ \rightarrow 4_1^+$ transition at $\sim$ 1300 keV, the $4_1^+ \rightarrow 2_1^+$ transition at 1088(7) keV, and the $2_1^+ \rightarrow 0^+_{\text{g.s}}$ transition at 764.2(28) keV were observed; and as for the ^{9}Be target, for ^{51}Co, following the ^{12}C(^{50}Fe, ^{51}Co + γ)X reaction, no residue rest-frame or laboratory-frame γ rays were observed.

The expected cross section for the population of target excited states, following the removal of a proton from ^{12}C leading to one of three considered states in ^{11}B, is low—see the calculated single-particle cross sections of Tables 6.12 6.13, and 6.14—and the three possible decays of ^{11}Be*, 2125 keV ($1/2_1^- \rightarrow 3/2^-_{\text{g.s.}}$), 2895 keV ($3/2_1^- \rightarrow 1/2^-_{\text{g.s.}}$), and 5019 keV ($3/2_1^- \rightarrow 3/2^-_{\text{g.s.}}$) were not observed.

Special care was taken for the ^{50}Fe $4_1^+ \rightarrow 2_1^+$ decay. There were insufficient statistics to align both rings. The transition was assumed to occur in the target. Although a half-life for the 4_1^+ state is not available for ^{50}Fe, the mid-target decay assumption was based on the short half-life of the 2_1^+ state of 1.5(3) ps and the larger $4_1^+ \rightarrow 2_1^+$ transition energy of 1087 keV (lifetimes scale as $\tau_{1/2} \propto 1/E_\gamma^{2\lambda+1}$ where λ is the multipolarity; $\lambda = 2$ here). The energy uncertainty of the 4_1^+ state was dominated by the choice of β which was assumed to lie between the β_{mid} and β_{end} values of $\beta = 0.340$ and $\beta = 0.327$.

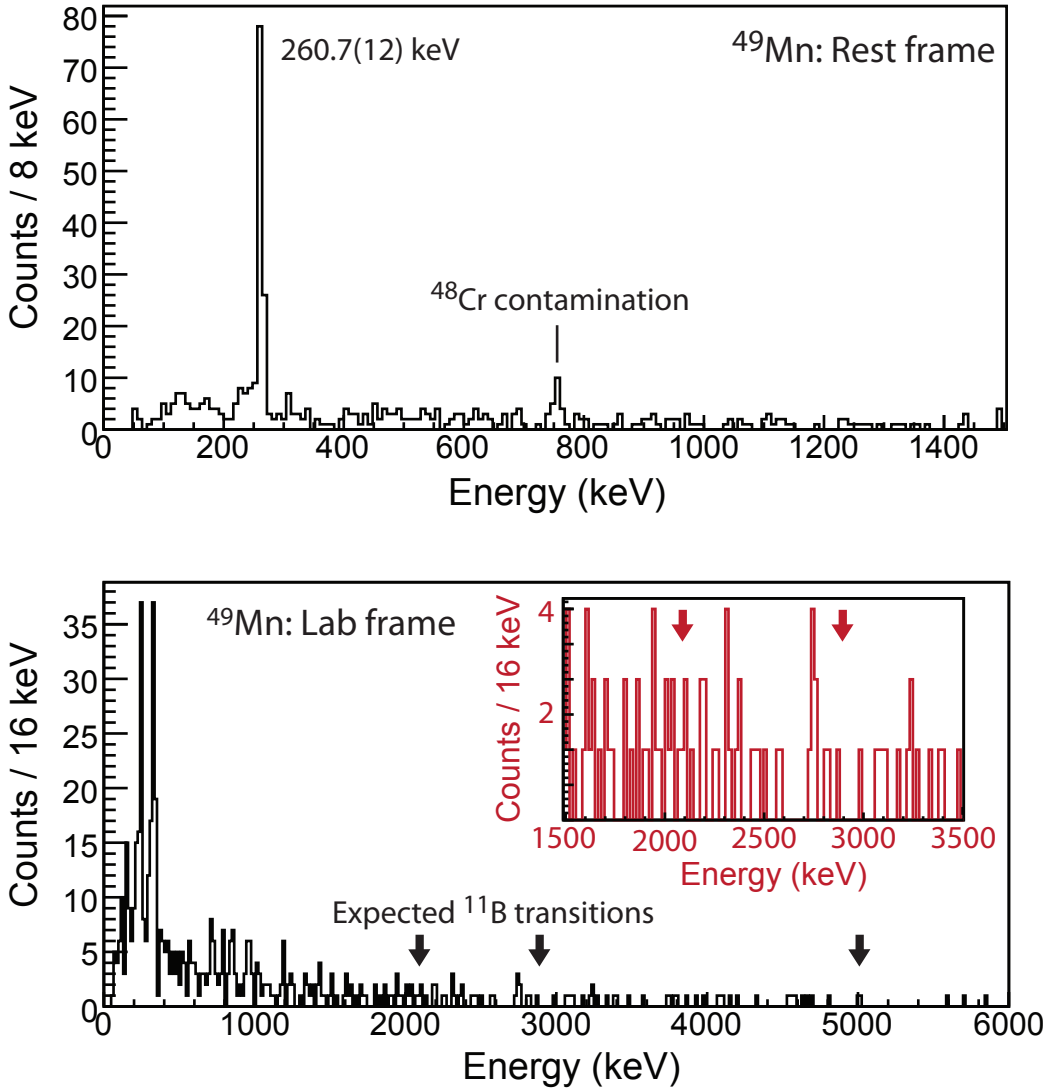

Figure 6.23: Residue rest frame (upper panel) and laboratory frame (lower panel) γ-ray spectra following the ^{12}C(^{48}Cr, ^{49}Mn+γ)X reaction. Only the $7/2^-_1 \rightarrow 5/2^-_{\text{g.s.}}$ 260.7(12) keV transition is observed. The 752 keV transition observed in the rest-frame spectra comes from unwanted ^{48}Cr contamination. The cross sections for the population of the ^{11}B* $1/2^-_1$ and $3/2^-$ states were too low to be experimentally observed. See Table 6.12. Transitions associated with the decay of the excited ^{11}B target occur at 2125 keV, 2895 keV, and 5019 keV.

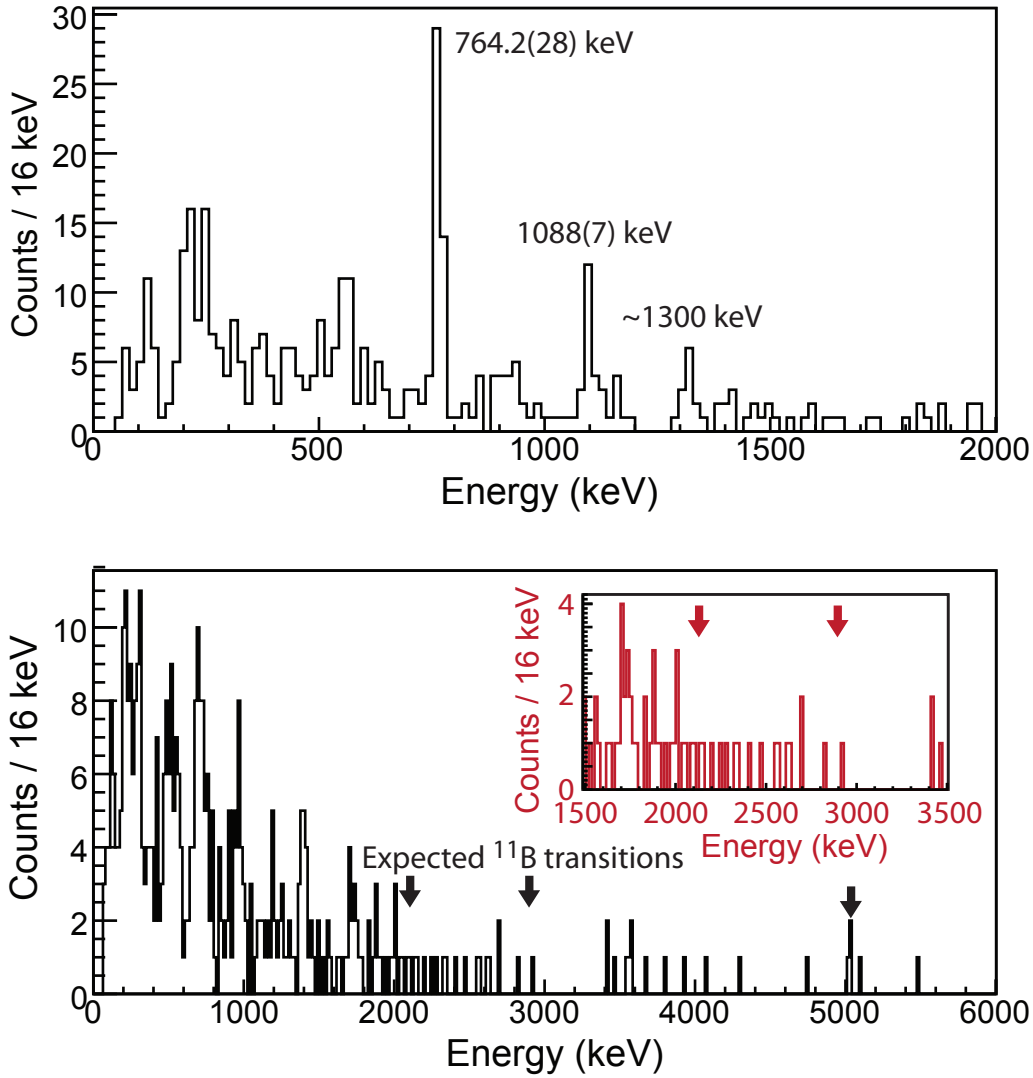

Figure 6.24: Residue rest frame and laboratory frame γ-ray spectra for ^{50}Mn following the ^{12}C(^{49}Mn, ^{50}Fe$+\gamma$)X reaction. Both the $4_1^+ \rightarrow 2_1^+$ transition at 764.2(28) keV, the $2_1^+ \rightarrow 0_{\text{g.s}}^+$ transition at 1088(7) keV, and the $6_1^+ \rightarrow 4_1^+$ transition at $\sim$ 1300 keV were observed. The cross sections for the population of the ^{11}B* $1/2_1^-$ and $3/2^-$ states were too low to be experimentally observed based on the lack of observed transitions in the rest-frame γ-ray spectrum at the expected energies of 2125 keV, 2895 keV and 5019 keV. The suggested peak at 5019 keV is consistent with background.

6.5.5 Partial Cross Sections

The comparison of experimental and theoretical partial cross sections for the ^{12}C(^{48}Cr, ^{49}Mn+γ)X, ^{12}C(^{49}Mn, ^{50}Fe+γ)X, and ^{12}C(^{50}Fe, ^{51}Co+γ)X reactions are shown in Figures 6.25, 6.26, and 6.27. The plotted data was taken from Tables A.7, A.8, and A.9. A similar pattern of excited-state population is experimentally observed for both ^{9}Be and ^{12}C targets and the same conclusions reached in Section 6.4.5 with respect to the ^{9}Be target also apply to the ^{12}C target pickup results: the experimentally observed magnitude and population pattern of states tracks theoretical predictions, with an understood deviation for the ^{12}C(^{49}Mn, ^{50}Fe + γ)X reaction.

There is one difference that should be pointed out, although its investigation is beyond the current scope of this thesis (current theory is only aimed at qualitative agreement). Theory under predicts the increase of cross section observed when moving from the ^{9}Be to ^{12}C target. Taking the two highest statistics cases, the proton pickup reactions from ^{48}Cr to ^{49}C, i.e. ^{9}Be(^{48}Cr, ^{49}Mn + γ)X and ^{9}Be(^{49}Mn, ^{50}Fe + γ)X, and the proton pickup reactions from ^{49}Mn to ^{50}Fe, i.e. ^{9}Be(^{49}Mn, ^{50}Fe + γ)X and ^{12}C(^{49}Mn, ^{50}Fe + γ)X, we find that theory predicts an increase of 6 % and 7 % respectively, while experimental increases of 23(2) % and 25(4) % were observed. This difference could come from the nearly complete treatment of the ^{12}C and ^{11}Be* target overlaps through the inclusion of just three states in ^{11}B ($3/2^-$, $1/2^-$, and $3/2^-$ states) in comparison to the ^{9}Be case where much the spectroscopic overlap goes to unbound states in ^{8}Li which are difficult to include in the calculation of the single-particle cross sections. The decreased complexity in calculations for both proton and neutron (see Ref. [153]) pickup reactions using a carbon target may make ^{12}C a better choice for future spectroscopic studies using pickup reactions.

6.5.6 Momentum Distributions

The expected shapes of the parallel momentum distributions are close in width to the measured distributions. See Figures 6.28, 6.29, and 6.30. The similarity in width between

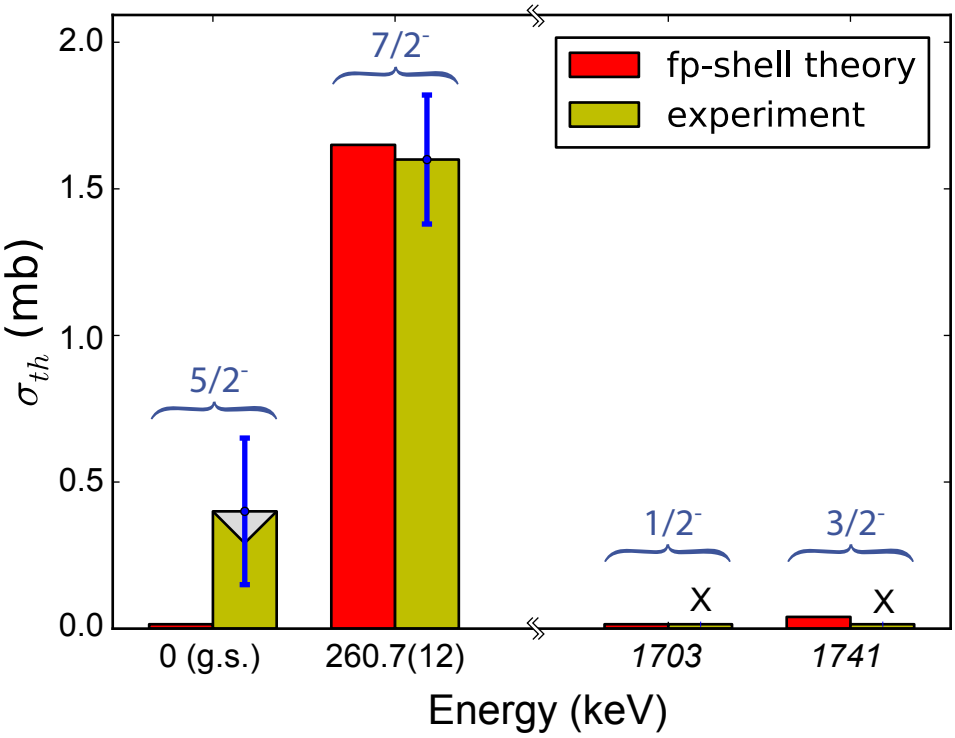

Figure 6.25: Measured and predicted partial cross sections for the ^{12}C(^{48}Cr, ^{49}Mn + γ)X reaction. The $1/2^-$ and $3/2^-$ states were not observed experimentally, which is indicated by an **X** above the experimental state. The energies assigned to these two states are taken from shell-model calculations (see Figure 6.9). This is indicated by an italic font and the absence of experimental error. The experimental population of the ground state is considered an upper bound, as indicated by a grey triangle, because the feeding to the ground state could not be quantified; see also Figure 6.17 for the ^{9}Be(^{48}Cr, ^{49}Mn + γ)X reaction. The population pattern observed, with a low (consistent with zero) partial cross section to the ground state and a high cross section of 1.60(22) mb (nearly all of the inclusive strength) to the $7/2^-_1$ state is consistent with theoretical predictions. See Table A.7 for the data plotted in this figure.

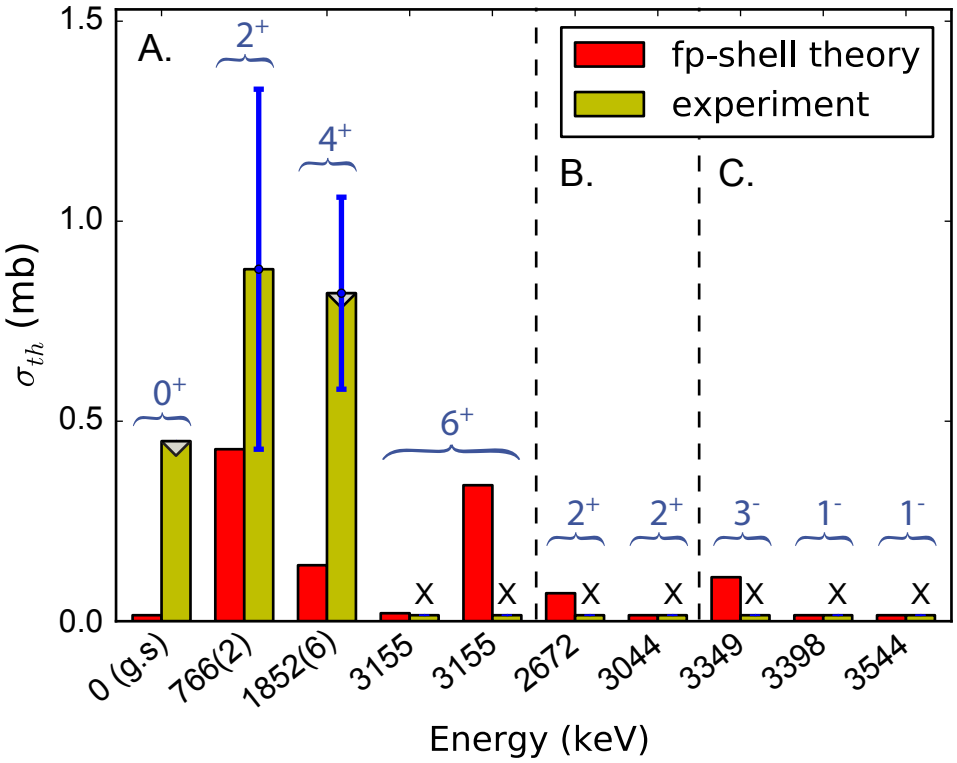

Figure 6.26: Measured and predicted partial cross sections for the ^{12}C(^{49}Mn, ^{50}Fe + γ)X reaction as taken from Table A.8. Results are presented with inclusion of the 4_1^+ state. See the caption of Table A.8 and Figure 6.18 (from the similar ^{9}Be(^{49}Mn, ^{50}Fe + γ)X reaction) for further details. The transitions marked by an **X** (all levels above the 4_1^+) were not observed experimentally and the energies listed (in italics) are taken from the shell model calculations of Figure 6.10. The partial cross section to the 4_1^+ state should be considered upper bound because of unobserved feeding (indicated by a grey triangle). The two 6^+ states represent two shell-model fragments with different spectroscopic factors. The experimental partial cross section to the 6_1^+ state, observed in the γ-ray spectrum of Fig. 6.24 was not extracted and plotted because of the very low statistics and the high resultant uncertainty. The data plotted in this figure was taken from Table A.8.

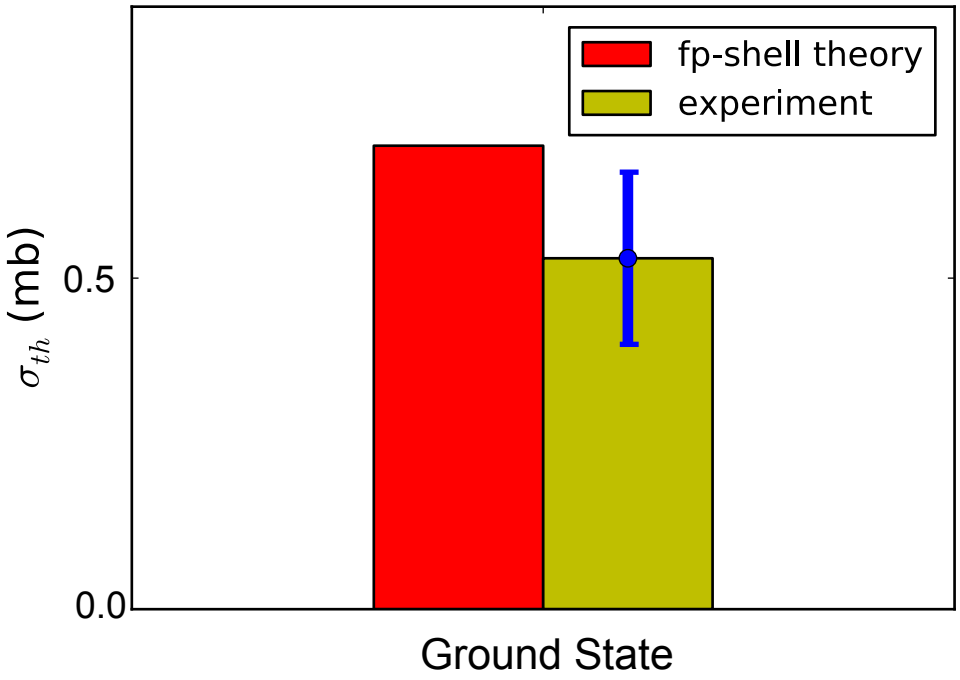

Figure 6.27: Measured and predicted partial cross sections for the ^{12}C(^{50}Fe, ^{51}Co + γ)X reaction . Because no transitions were observed, the cross section to the ground state is identically equal to the inclusive cross section. The data plotted in this figure was taken from Table A.9.

the predicted and measured distributions, as mentioned earlier in the analysis of proton pickup of the ^{9}Be target (see Section 6.5.6), is consistent with a direct reaction. Unlike the momentum distributions measured after the interaction of the projectiles with the ^{9}Be target, the ^{12}C(^{48}Cr, ^{49}Mn + γ)X, ^{12}C(^{49}Mn, ^{50}Fe + γ)X, and ^{12}C(^{50}Fe, ^{51}Co + γ)X parallel momentum distributions are not strongly distorted by the presence of the beam blocker, possibly because the decreased target thickness of the 72.8 mg/cm^2 ^{12}C target, relative to the 188 mg/cm^2 ^{9}Be target, narrowed the observed momentum distributions of the ^{12}C pickup reaction products (less differential momentum broadening) and increased the separation from the beam. A possible affect, however, may be seen in the low-momentum tails. See especially Figure 6.29. Low-momentum tails are indication of dissipative mechanisms beyond the one-step, direct, two-body reaction mechanism.

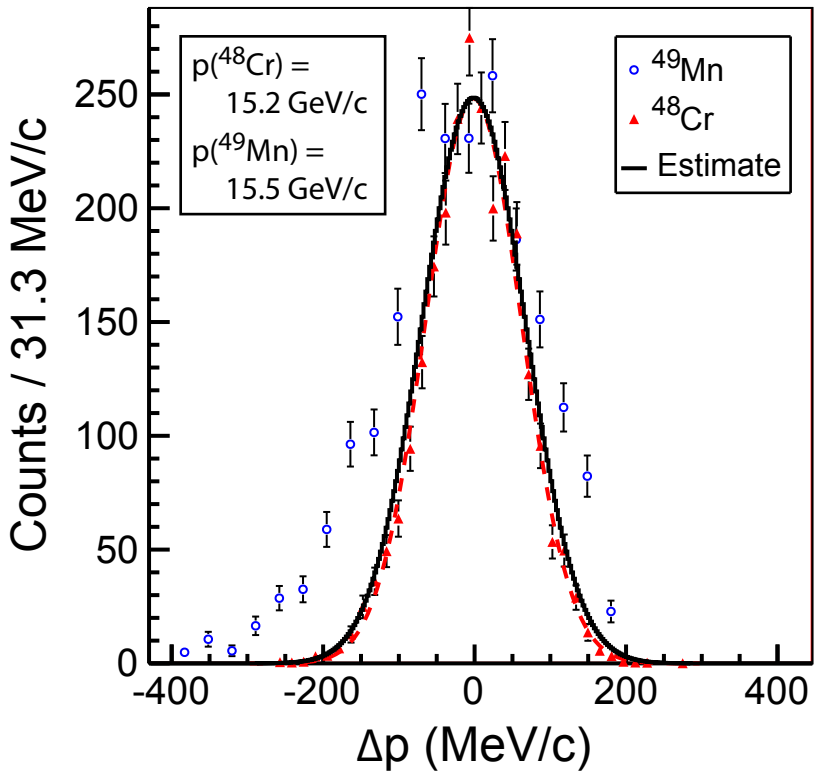

Figure 6.28: Measured and estimated parallel momentum distributions for the ^{12}C(^{48}Cr, ^{49}Mn + γ)X reaction. The width of the estimated distribution is close to the width of the measured parallel momentum distribution showing the direct nature of the reaction. A low momentum tail is observed suggesting the presence of a more complicated, dissipative reaction channels that were not included in the theoretical calculations. A similar tail was observed in the one-proton pickup reaction ^{9}Be(^{22}Mg, ^{23}Al + γ)X [61].

6.6 Summary

The general intent of the current research was to show the general applicability of the proton pickup reaction as a qualitative spectroscopic tool by comparing experimental results and theoretical predictions for the magnitude and pattern of population to states in the excited states yields under different experimental conditions, specifically through the used of two different targets, a 188 mg/cm^2 beryllium target and a 72.8 mg/cm^2 carbon target. The results, taken from the comparison between measured and predicted partial and inclusive cross section shown in Figures 6.17, 6.18, 6.19, 6.25, 6.26, and 6.27 show a general broad agreement between the magnitude of values and the population

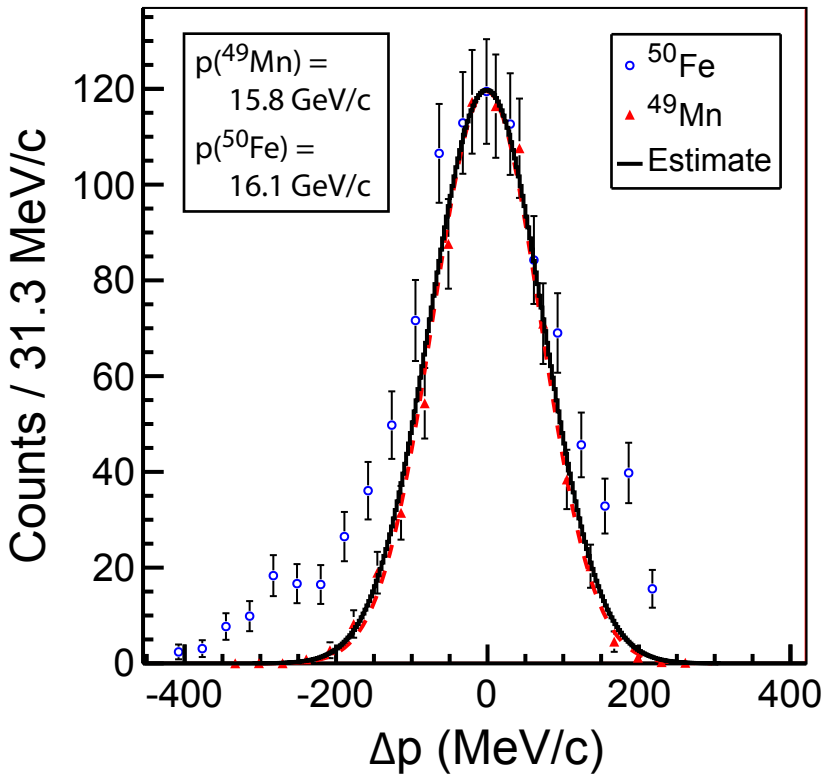

Figure 6.29: Measured and predicted parallel momentum distributions for the ^{12}C(^{49}Mn, ^{50}Fe + γ)X reaction. The width of the measured distribution is close to the width of the measured parallel momentum distribution showing the direct nature of the reaction. A low momentum tail is observed, indicating the presence of additional channels beyond the direct processes included in the CCBA framework.

pattern. Furthermore, the measured parallel momentum distributions for the ^{9}Be(^{50}Fe, ^{51}Co+γ)X, ^{12}C(^{48}Cr, ^{49}Mn+γ)X, ^{12}C(^{49}Mn, ^{50}Fe+γ)X, and ^{12}C(^{50}Fe, ^{51}Co+γ)X reactions, are consistent with a direction reaction processes (a similar deduction for the ^{9}Be(^{48}Cr, ^{49}Mn+γ)X, and ^{9}Be(^{49}Mn, ^{50}Fe+γ)X reactions could not be made because of experimental complications; see Section 6.4.6), a critical assumption of the CCBA calculations.

This new body of work, the first ^{9}Be, fast-beam, inverse-kinematics proton pickup reaction study of fp-shell nuclei, and the first proton pickup from a ^{12}C target, will provide future experimentalists additional confidence in fast-beam proton pickup reactions, which enables experimentalists, in comparison to the well-established single-nucleon knockout reactions, to populate single-proton states in the heavy residue and offer an increased

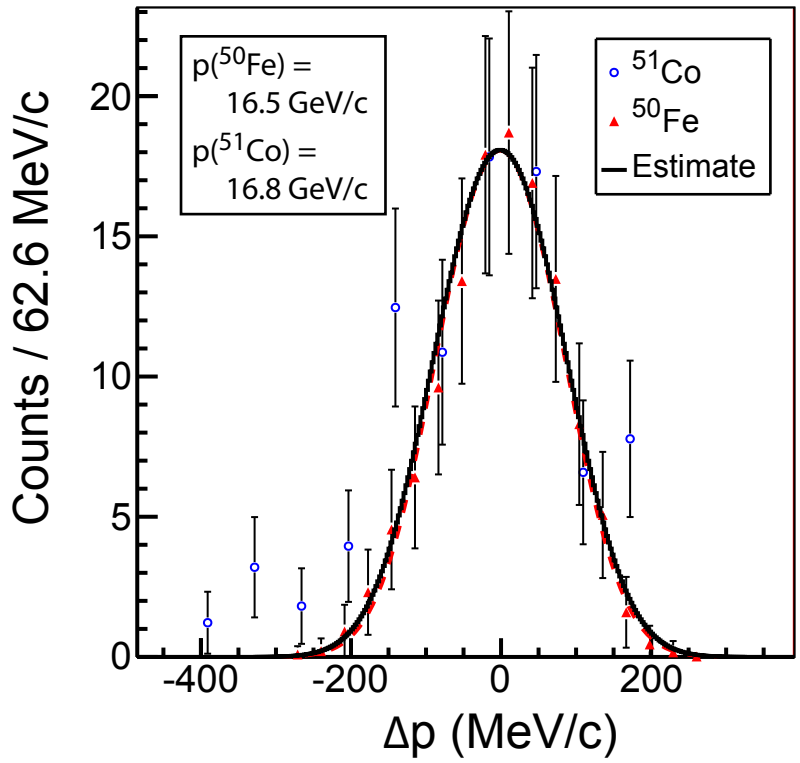

Figure 6.30: Measured and predicted parallel momentum distributions for the ^{12}C(^{50}Fe, ^{51}Co + γ)X reaction. The low momentum bump observed around -300 MeV/c can be attributed to the presence of the beam blocker. For a similar affect see Figures 6.20 and 6.21

sensitivity to states with higher orbital angular momentum.

Chapter 7

SUMMARY AND FUTURE WORK

Chapters 5 and 6 present the analysis and summary of the single-proton knockout and pickup reactions. Detailed conclusions for the two experiments are found in Sections 5.8 and 6.6. In brief, for the ^{9}Be(^{54}Ti, ^{53}Sc + γ)X knockout reaction, the observation of strong strength to excited states in ^{53}Sc was incompatible with shell-model predictions using the *fp* valance space. The discrepancy was attributed to the knockout of *sd*-shell protons outside the valance space and suggested the need for improved cross-shell proton interactions. For the ^{9}Be(^{48}Cr, ^{49}Mn + γ)X, ^{9}Be(^{49}Mn, ^{50}Fe + γ)X, ^{9}Be(^{50}Fe, ^{51}Co + γ)X, ^{12}C(^{48}Cr, ^{49}Mn + γ)X, ^{12}C(^{49}Mn, ^{50}Fe + γ)X, and ^{12}C(^{50}Fe, ^{51}Co + γ)X pickup reactions, the measured magnitude and distribution of strength to final states in the pickup residues qualitatively matched theoretical predictions, the momentum distributions were consistent with a direct reaction processes assumed in the CCBA reaction calculations, and the qualitative conclusions were consistent under the choice either the ^{9}Be or ^{12}C targets. These results provided further confidence in inverse-kinematics, fast-beam single-nucleon pickup reactions as a spectroscopic tool.

Experimental constraints prevented a more detailed conclusion for the ^{9}Be(^{54}Ti, ^{53}Sc + γ)X knockout reaction. As addressed in Section 5.6.1, the spectrograph was set to center to the two-proton knockout residue ^{52}Ca for most reacted runs. These runs, with an unknown acceptance correction, could not be used for the measurement of partial cross sections or longitudinal momentum distributions. A re-designed experiment, with a specific focus on the ^{9}Be(^{54}Ti, ^{53}Sc + γ)X reaction and perhaps a thinner target to reduce the momentum broadening caused by the differential energy loss in the target, would permit the extraction of partial cross sections to final states in ^{53}Sc and, through the

measurement of the longitudinal momentum distributions, the corresponding assignment of quantum numbers associated with the orbital of the removed proton. This additional information can be used to constrain the TBME of proton cross-shell interactions for developed *sdpf* valance-space effective interactions. The new germanium γ-ray tracking array GRETINA [170], with high segmentation and γ-ray tracking and available for use at the NSCL and other labs on a rotating basis starting in 2012, can be used, in addition to its high resolving power and efficiency, through the measurement of γ-γ angular correlation and polarization measurements, to directly measure the spin and parities of γ rays associated with a given transition. In general, knockout reactions could be used to probe other proton (neutron) cross-shell interactions, e.g. *sd-fp* or *fp*-$g_{9/2}$, for nuclei with one or two protons (neutrons) above a closed shell.

Reaction theory is confirmed through agreement with experiment. The successes of CCBA reaction theory and shell-model results at qualitatively describing experimentally observed partial cross sections for fast-beam pickup reactions are still confined to the transfer of a proton or neutron to a limited selection of orbitals in the pickup residue: the proton and neutron *sd*-shell and the proton *fp* shell. Due to momentum-matching considerations, neutron pickup reactions in regions of shell evolution, where high-ℓ intruder orbitals descend and change the nuclear structure significantly, would selectively populate these intruder states and allow quantification of their strength.

Additional target tests are necessary from both an experimental and theoretical viewpoint. Experimentally, for very exotic isotopes produced at rates of a few particles per second, choosing a target to maximize the pickup reaction cross section is critical. The choice is not always obvious. In the neutron pickup reactions of Ref. [153], the surprisingly-large measured inclusive cross section for the ^{9}Be(^{22}Mg, ^{23}Mg + γ)X reaction suggested that the weakly-bound ^{9}Be valance neutron ($\alpha + \alpha + n$) was not sufficiently matched in momentum, and the cross section was likely dominated by pickup from deeply-bound ^{9}Be neutrons. The neutron pickup cross sections were slightly higher for the ^{9}Be target

than the ^{12}C target. In the results of Chapter 6, for proton pickup from the fp-shell, the situation is reversed. Higher cross sections were observed for the ^{12}C target.

A higher statistics experiment would enable a more accurate probe of target final states, a critical test of reaction theory. There were insufficient statistics in the pickup reactions of Chapter 6 to accurately probe target final states in the current experiment. Laboratory-frame γ-ray spectra for any of the six studied pickup reactions did not reveal transitions associated with the decay of excited ^{8}Li or ^{11}B target residuals.

The spectroscopic information obtained through single-nucleon pickup reactions, as addressed in this thesis, are still qualitative rather than quantitative. Additional work is needed to place pickup reactions on a similar quantitative basis as knockout reactions. A series of complementary reactions, for example ^{9}Be(^{54}Ti, ^{53}Sc+γ)X and ^{9}Be(^{54}Ti, ^{55}V+γ)X, related through spectroscopic factor shell-model sum rules (see Equation 3.12), could use the improved model accuracy of the knockout Eikonal single-particle cross sections to constrain current pickup single-particle cross sections.

There are many open questions that require the fertile collaboration of theorists and experimentalists, and whose answers will take us forward into an exciting future offered by next generation experimental facilities, improved models, powerful computers, and new insights into the atomic nucleus.

APPENDICES

Appendix A

DATA TABLES FOR SINGLE-PROTON PICKUP REACTIONS

A.1 Shell-model Spectroscopic Factors

Shell-model spectroscopic factors for the (^{48}Cr,^{49}Mn), (^{49}Mn,^{50}Fe), and (^{50}Fe,^{51}Co) overlaps, as calculated by Brown [163] and plotted in Figures 6.9, 6.10, and 6.11, are listed in Tables A.1, A.2, and A.3.

A.2 Measured and Predicted Partial Cross Sections

The comparison of measured and predicted partial cross sections for ^{9}Be(^{48}Cr, ^{49}Mn + γ)X, ^{9}Be(^{49}Mn, ^{50}Fe + γ)X, ^{9}Be(^{50}Fe, ^{51}Co + γ)X, ^{12}C(^{48}Cr, ^{49}Mn + γ)X, ^{12}C(^{49}Mn, ^{50}Fe + γ)X, and ^{12}C(^{50}Fe, ^{51}Co + γ)X reactions are given in Tables A.4, A.5, A.6, A.7, A.8, and A.9. This data is plotted visually in Figures 6.17, 6.18, 6.19, 6.25, 6.26, and 6.27 (respectively).

I^π (^{49}Mn)	$n\ell_j$	E_x (MeV)	$C^2S_{\text{S.M.}}$
Below $S_p = 2085(25)$ keV			
$7/2^-$	$1f_{7/2}$	0.219	0.425
$3/2^-$	$2p_{3/2}$	1.675	0.373
$1/2^-$	$2p_{1/2}$	1.696	0.246
$5/2^-$	**$1f_{5/2}$**	**0**	**0.002**
Above $S_p = 2085(25)$ keV			
$5/2^-$	$1f_{5/2}$	2.857	0.232
$1/2^-$	$2p_{1/2}$	4.291	0.225
$1/2^-$	$2p_{1/2}$	6.061	0.195
$5/2^-$	$1f_{5/2}$	2.079	0.142
$3/2^-$	$2p_{3/2}$	3.267	0.102
$1/2^-$	$2p_{1/2}$	5.663	0.089
$3/2^-$	$2p_{3/2}$	4.244	0.076
$3/2^-$	$2p_{3/2}$	3.924	0.058
$7/2^-$	$1f_{7/2}$	2.447	0.049
$7/2^-$	$1f_{7/2}$	2.318	0.047
$3/2^-$	$2p_{3/2}$	2.250	0.045
$1/2^-$	$2p_{1/2}$	5.363	0.043
$3/2^-$	$2p_{3/2}$	4.749	0.041

Table A.1: Shell-model spectroscopic factors ($C^2S_{\text{S.M.}}$) for the ^{9}Be(^{48}Cr, ^{49}Mn + γ)X reaction arranged in order of decreasing spectroscopic strength and separated into states located above and below the proton separation energy of $S_p = 2085(5)$ keV [163]. The final-state, ^{49}Mn energies (E_x) are taken from the shell model predictions. Only levels with spectroscopic strength of $C^2S \geq 0.04$ are listed. The spectroscopic factor to the ground state is nearly zero and is included separately (bold text). All states listed below S_p, i.e. $E_x < S_p$, are used in the theoretical calculation of the inclusive and partial cross sections (see Table 6.4). The quantum numbers $n\ell_j$ refer to the ^{50}Fe orbital of the transfered proton. The table data is plotted in Figure 6.9.

I^π (^{50}Fe)	$n\ell_j$	E_x (MeV)	$C^2S_{\text{S.M.}}$
Below $S_p = 4150(60)$ keV			
2^+	$1f_{7/2}$	0.788	1.145
1^+	$1f_{7/2}$	3.349	0.530
6^+	$1f_{7/2}$	3.527	0.371
3^+	$2p_{3/2}$	3.398	0.309
2^+	$2p_{3/2}$	3.044	0.232
3^+	$2p_{1/2}$	3.544	0.214
4^+	$1f_{7/2}$	1.776	0.208
2^+	$1f_{7/2}$	2.672	0.194
4^+	$2p_{5/2}$	3.956	0.169
3^+	$1f_{5/2}$	3.544	0.123
2^+	$2p_{1/2}$	3.044	0.112
3^+	$1f_{7/2}$	3.634	0.094
2^+	$2p_{3/2}$	3.948	0.076
4^+	$2p_{3/2}$	3.956	0.074
3^+	$2p_{3/2}$	3.544	0.069
4^+	$2p_{3/2}$	3.733	0.061
2^+	$2p_{3/2}$	3.464	0.040
0^+	**$1f_{5/2}$**	**0**	**0.033**
4^+	$1f_{7/2}$	3.320	0.031
4^+	$2p_{5/2}$	3.080	0.027
4^+	$1f_{7/2}$	3.733	0.023
Continued on right column...			

I^π (^{50}Fe)	$n\ell_j$	E_x (MeV)	$C^2S_{\text{S.M.}}$
From left column...			
2^+	$2p_{3/2}$	2.672	0.023
6^+	$1f_{7/2}$	2.959	0.023
4^+	$1f_{7/2}$	3.956	0.022
5^+	$1f_{5/2}$	3.577	0.026
Above $S_p = 4150(60)$ keV			
1^+	$2p_{3/2}$	5.499	0.481
3^+	$1f_{5/2}$	4.679	0.221
4^+	$2p_{5/2}$	5.007	0.155
2^+	$1f_{5/2}$	4.411	0.147
4^+	$2p_{5/2}$	4.836	0.120
1^+	$2p_{3/2}$	4.410	0.117
4^+	$2p_{3/2}$	5.075	0.098
3^+	$1f_{5/2}$	4.529	0.091
5^+	$1f_{5/2}$	4.313	0.075
5^+	$1f_{5/2}$	5.773	0.064
3^+	$2p_{3/2}$	5.554	0.058
4^+	$2p_{3/2}$	4.666	0.049
5^+	$1f_{5/2}$	5.285	0.048
5^+	$1f_{7/2}$	4.295	0.045
2^+	$2p_{1/2}$	4.411	0.040
4^+	$2p_{3/2}$	4.836	0.040

Table A.2: Shell-model spectroscopic factors ($C^2S_{\text{S.M.}}$) for the ^{9}Be(^{49}Mn, ^{50}Fe + γ)X reaction arranged by descending spectroscopic strength and separated into states below and above the proton separation energy of $S_p = 4150(60)$ keV [163]. Only values for which $C^2S \geq 0.04$ are reported. The final-state, ^{50}Fe energies (E_x) are taken from the shell-model predictions. The ground state is highlighted and the data continues from the bottom of the second column to the top of the first. The states used in the calculation of the theoretical partial and inclusive cross sections (see Table 6.8) are noted by blue text. Two possible fragmented 6^+ states are considered based upon the proximity of their energies of 3.257 MeV and 2.959 MeV to the literature value of 3.159 MeV. Note the high degree of fragmentation to states above and below the proton separation energy. The quantum numbers $n\ell_j$ refer to the ^{50}Fe orbital of the transfered proton. The table data is plotted in Figure 6.10.

I^π (^{51}Co)	$n\ell_j$	E_x (MeV)	$C^2S_{\text{S.M.}}$
Below S_p = 2085(25) keV			
7/2$^-$	**1f$_{7/2}$**	**0**	**0.246**
Above S_p = 2085(25) keV			
3/2$^-$	2p$_{3/2}$	0.709	0.366
1/2$^-$	2p$_{1/2}$	0.808	0.237
5/2$^-$	1f$_{5/2}$	1.264	0.228
1/2$^-$	2p$_{1/2}$	3.834	0.187
3/2$^-$	2p$_{3/2}$	1.857	0.146
5/2$^-$	1f$_{5/2}$	2.325	0.127
1/2$^-$	2p$_{1/2}$	4.655	0.112
3/2$^-$	2p$_{3/2}$	2.891	0.086
5/2$^-$	1f$_{5/2}$	3.171	0.071
3/2$^-$	2p$_{3/2}$	3.490	0.065
1/2$^-$	2p$_{1/2}$	4.343	0.063
1/2$^-$	2p$_{1/2}$	5.095	0.061
1/2$^-$	2p$_{1/2}$	2.866	0.061
3/2$^-$	2p$_{3/2}$	2.351	0.051

Table A.3: Shell-model spectroscopic factors ($C^2S_{\text{S.M.}}$) for the ^{9}Be(^{50}Fe,^{51}Co+γ)X reaction arranged in order of decreasing spectroscopic strength and separated by states above and below the calculated separation energy of S_p = 88 keV [163]. Only levels with a spectroscopic strength of $C^2S \geq 0.04$ are included. The final-state, ^{51}Co energies (E_x) are taken from the shell model predictions. Only the ground state was used in the calculation of the theoretical partial and inclusive cross sections (see Table 6.9). The quantum numbers $n\ell_j$ refer to the ^{50}Fe orbital of the transfered proton. The table data is plotted in Figure 6.11.

I^π (^{49}Mn)	E_x (keV)	σ_{theory} (mb)	$\sigma_{\text{exp.}}$ (mb)
5/2$^-_{\text{g.s.}}$	0	0	$\leq$ 0.20(17)
7/2$^-_1$	260.8(11)	1.56	1.43(15)
1/2$^-_1$	*1703*	0.01	–
3/2$^-_1$	*1741*	0.03	–
	Inclusive sum:	1.60	1.63(8)

Table A.4: Measured and predicted partial cross sections for the ^{9}Be(^{48}Cr,^{49}Mn + γ)X reaction as plotted in Figure 6.17. See the figure caption for additional details. Energies taken from shell model calculations, the 1/2$^-$ and 3/2$^-$ states, are indicated by an italic font.

		4^+ state included		4^+ state excluded	
I^π (^{50}Fe)	E_x (keV)	σ_{theory} (mb)	$\sigma_{\text{exp.}}$ (mb)	σ_{theory} (mb)	$\sigma_{\text{exp.}}$ (mb)
0_1^+	0	0.00	≤ 0.21	0.0	≤ 0.21
2_1^+	765.6(20)	0.40	0.81(41)	0.87	1.41(22)
4_1^+	1851.7(55)	0.13	0.59(34)	–	–
6^+	3159	0.02	–	–	–
6^+	3159	0.32	–	–	–
2_2^+	*2672*	0.07	–	–	–
2_3^+	*3044*	0.00	–	–	–
1_1^+	*3349*	0.10	–	–	–
3_1^+	*3398*	0.01	–	–	–
3_2^+	*3544*	0.00	–	–	–
	Inclusive sum:	1.05	1.38(7)	0.87	1.38(7)

Table A.5: Measured and predicted partial cross sections for the ^{9}Be(^{49}Mn, ^{50}Fe + γ)X reaction as plotted in Figure 6.18. The high uncertainty on the yield of the 4_1^+ state affects the uncertainty on the yield of the 2_1^+ state because of feeding subtraction. Thus the results are presented with and without the 4_1^+ (and higher lying) states included. The 6^+, 1^+ and 3^+ states were not observed experimentally. The energies were taken from shell model calculations and are italicized to note their origin. The highest energy experimental cross sections listed in column 4 (4^+ state included) and column 6 (4^+ state excluded) should be considered upper bounds because of unobserved feeding. The theoretical prediction of column five includes feeding contributions from the 4_1^+ and 6_1^+ states. The two 6_1^+ states represent two fragments predicted by shell model calculations with different spectroscopic factors.

J^π (^{51}Co)	E_x (keV)	σ_{theory} (mb)	$\sigma_{\text{exp.}}$ (mb)
$7/2^-$	0	0.66	0.57(8)
	Sum:	0.66	0.57(8)

Table A.6: Measured and predicted partial cross sections for the ^{9}Be(^{50}Fe, ^{51}Co + γ)X reaction as plotted in Figure 6.19. No excited states were observed, and therefore the the cross section to the ground state was taken from the inclusive cross section.

J^π (^{49}Mn)	E_x (keV)	σ_{theory} (mb)	$\sigma_{\text{exp.}}$ (mb)
$5/2^-$	0	0	$\leq 0.40(25)$
$7/2^-$	260.8(11)	1.65	1.60(22)
$1/2^-$	*1703*	0.01	–
$3/2^-$	*1741*	0.04	–
	Sum:	1.70	2.00(13)

Table A.7: Measured and predicted partial cross sections for the ^{12}C(^{48}Cr, ^{49}Mn + γ)X reaction as plotted in Figure 6.25. See the figure caption and the caption of Table A.7 for additional details. Energies taken from shell model calculations, i.e. the $1/2^-$ and $3/2^-$ states, are indicated by an italic font.

		4^+ state included		4^+ state excluded	
J^π (^{50}Fe)	E_x (keV)	σ_{theory} (mb)	$\sigma_{\text{exp.}}$ (mb)	σ_{theory} (mb)	$\sigma_{\text{exp.}}$ (mb)
$0^+_{\text{g.s.}}$	0	0.00	≤ 0.45	0.02	≤ 0.45
2^+_1	765.6(20)	0.43	0.88(45)	1.04	1.70(38)
4^+_1	1851.7(55)	0.14	0.82(24)	–	–
6^+_1	3159	0.02	–	–	–
6^+_2	3159	0.34	–	–	–
2^+_2	*2672*	0.07	–	–	–
2^+_3	*3044*	0.01	–	–	–
1^+_1	*3349*	0.11	–	–	–
3^+_1	*3398*	0.01	–	–	–
3^+_2	*3544*	0.00	–	–	–
	Inclusive sum:	1.12	1.72(24)	1.12	1.72(24)

Table A.8: Measured and predicted partial cross sections for the ^{12}C(^{49}Mn, ^{50}Fe + γ)X reaction as plotted in Figure 6.26. Results are presented with and without the inclusion of the 4^+_1 state. The transitions in italics (all levels higher in energy than the 4^+_1 state) were not observed experimentally and the energies listed are taken from shell model calculations. The highest energy experimental cross sections listed in column 4 (4^+ state included) and column 6 (4^+ state excluded) should be considered upper bounds because of unobserved feeding. The theoretical prediction of column five includes feeding contributions from the 4^+_1 and 6^+_1 states. The two 6^+ states represent two shell-model fragments with different spectroscopic factors. The experimental partial cross section to the 6^+_1 state was not extracted because of the very low statistics and the high resultant uncertainty.

J^π (^{51}Co)	E_x (keV)	σ_{theory} (mb)	$\sigma_{\text{exp.}}$ (mb)
$7/2^-_{\text{g.s.}}$	0	0.70	0.53(13)
Inclusive sum:		0.70	0.53(13)

Table A.9: Measured and predicted partial cross sections for the ^{12}C(^{50}Fe, ^{51}Co + γ)X reaction as plotted in Figure 6.27. Because no transitions were observed, the cross section to the ground state is identically equal to the inclusive cross section.

Appendix B

THE BIRTH OF NUCLEAR PHYSICS

B.1 A Symphony of Effort

The grand mall of nuclear physics, like all science, was built through the effort of thousands of people. Most of the people who laid down their bricks are forgotten, but their contribution was essential in creating the path that other intrepid explorers used and lengthened. When creating any history, people only mention the exceptionals, the intellectual forces that alter the landscape. In sake of brevity, this must be done and we do the same below. But one should always keep in mind that these brilliant men and women do not work in isolation.

Only topics that are important to the central themes of nuclear experimentation and shell structure are covered below. This viewpoint is biased and gives artificial gravity to certain topics, but in pursuit of relevance and conciseness, these concessions were made.

B.2 History

The modern concept of the nucleus, as the tiny but extremely dense aggregate of protons and neutrons occupying the center of all atoms, emerged within the last one hundred years. At the turn of the 19th century there were still open questions about the existence of the nucleus. Certainly there was a growing body of evidence. The chemists Robert Boyle and John Dalton (considered the father of modern atomic theory), showed atoms were a convenient concept that explained such phenomena as pressure, why chemicals combined in integer ratios, and why elements could not be further broken down. But atoms as isolated entities could not be studied. This lack of a direct experimental probe allowed

legitimate objections to exist. Max Planck, invoking entropy and the irreversibility of physical processes, stated "the consistent implementation of the second law is incompatible with the assumption of finite atoms. One may anticipate then in the course of further development of the theory a battle will develop between the two hypothesis which will cost one of them its life" [171].

It was Joseph John "J.J." Thompson who defined the atom as a composite object through the discovery of the electron in 1897 [172]. The great connection was made: given a particle that is lighter than any known matter, and given that it comes from matter, it must be a component of matter. And if a component of an atom exists, an atom must exist as well. J.J. Thompson was an experimentalist, and he discovered the electron from his studies of cathode ray tubes. Thompson found that the glowing beam in a cathode-ray tube was not made of light waves or atoms as previous experimenters had thought, but was instead composed of charged negatively charged particles. Through clever application of magnetic and electric fields, he discovered that these particles had a mass far smaller than a hydrogen atom. Thompson would later embed these electrons in a sea of charged mass. This "plum pudding" model (1904) [173], named because electrons were distributed throughout the atom like raisins in plum pudding, was the first theoretical model of nuclear physics.

Radioactivity was discovered by Henri Becquerel, an expert in fluorescence and phosphorescence, in 1896, as he sought to continue Wilhelm Conrad Röntgen's work on x-rays. In 1895, Röntgen (English spelling William Roentgen) found x-rays emanating from the fluorescing glass wall of a covered cathode-ray tube as inferred from the nearby fluorescence of barium platinocyanide [174]. Röntgen would earn the first Nobel prize in Physics for this work. Becquerel, recalling a public lecture by Röntgen, knew that the x-rays were emanating from the fluorescent material in the cathode-ray tube, and decided to try uranic salts (potassium uranium sulfate) to see if they fluoresced x-rays. Becquerel sprinkled the salts on a photographic plate covered by black paper with the intent of exposing

the crystals to direct sunlight. Cloudy weather postponed his experiment for two days. Bequerel decided to develop his plates without exposure to the sun expecting only a faint image. Instead, the photographic plate showed dramatic blackening. Subsequent probes of this effect led Becquerel to conclude that the crystals themselves emitting radiation [175, 176]. Radioactivity had been discovered, and we mark this point as the beginning of nuclear physics.

These initial sparks beget a torrent of discoveries. Marie Curie, née Skołodowska, using an electrometer invented by Pierre and Jacques Curie (brother of Pierre), examined the radiation emitted by Uranium. This radiation was constant despite different methods of preparing the samples (solid, powder, etc.). The intensity of the radiation was only affected by the amount of Uranium in the sample. M. Curie had a critical insight: this radiation must be an intrinsic property of Uranium and not an effect of chemistry. She continued her work, now with her husband P. Currie. Together they discovered and isolated the new radioactive elements Polonium and Radium [177–179]. M. Curie provided the name for this new material property: radioactivity.

Max Planck, in 1900, introduced the quantization of photons to explain the spectrum of black-body radiation: how do the intensity and frequency of radiation relate in a cavity that perfectly absorbs and emits incident radiation [180, 181]. His solution contained the fuel for a revolution, but Planck at that time did not grasp the full importance of his work. The fire was largely provided by Albert Einstein 1905 during his miracle year (*Annus Mirabilis*) in his paper describing the photoelectric effect, and later in 1907 and 1909 in papers on the quantum theory of the specific heats of solids and on energy fluctuations [182–184].

Starting his work in the Cavendish Laboratory, and later at McGill Laboratory and Manchester University, Ernest Rutherford began systematically dissecting the atom. Rutherford's work would span several decades, and the stream of discoveries that emerged from his labs were so critical in the early development of nuclear physics, Rutherford

today is called the father of nuclear physics. Based on the absorption or stopping power of radiation in matter, Rutherford defines α-rays (a ^{4}He nucleus[1]) and β-rays (electrons) as distinct types of radiation. In 1900, at McGill Laboratory, he discovers, along with his current partner the radio chemist Fredrick Soddy, that radiation is emitted by the transmutation of atoms. The original discovery came from the observation of the decay from Thorium into Radium ($^{228}\text{Th} \longrightarrow {}^{228}\text{Ra} + \alpha$) [185–188]. Later they discover that Thorium and Radium decays into the noble gas ^{220}Ra (Radon)[2]. Rutherford and Soddy note that these different radioactive materials have different characteristic times it takes them to decay to half their previous value. A half-life is defined as a unique property of these radioactive materials [189]. They start categorizing these values. Rutherford would name γ radiation (photons) as a distinct type in 1903, based upon Paul Ulrich Villard's discovery in 1900 of a new highly penetrating type of radiation.

The Geiger-Marsden experiment ran in 1909. Hans Geiger and Ernest Marsden, a young undergraduate, directed a collimated beam of α particles emitted by Radium decay upon a thin foil gold target. The target was surrounded by a sheet of fluorescing zinc sulfide. Earlier Rutherford had noticed that α particles when projected through a small slit of mica produce an image blurred near the edges. The electrical forces necessary to produce the deviation in flight path of the alpha particles was enormous. Rutherford hoped that the gold scattering experiments would solve the puzzle of the mica slit experiment and provide insight into the structure of the atom.

Rutherford suggested that Geiger and Marsden check for backscattering for alpha particles off the gold foil. To their great surprise they found scattering greater than 90 degrees. Rutherford was astonished. In his words, "It was quite the most incredible event

[1]Rutherford, continuing work in Manchester with Hans Geiger on alpha radiation, notes that alpha particles have a mass to charge ratio of two. With Thomas Roylds, in 1907, he lets alpha particles penetrate through a thin glass wall of an evacuated discharge tube. The spectrum of the gas inside the tube was identified as Helium and the connection was made: alpha particles are the nuclei of Helium atoms.

[2]The endpoint of the ^{228}Th decay chain is stable ^{208}Pb

that has ever happened to me in my life. It was almost as incredible as if you fired a 15-inch shell at a piece of tissue paper and it came back and hit you" [190]. Rutherford realized that the only way to get large deflections was to concentrated most of the positive mass into the center of the atom. It took Rutherford two years to publish [191, 192]. Rutherford had found the nucleus.

Although core concept of Rutherford's model, that every atom has a tiny nucleus where all of its positive charge is concentrated, is true, there were major flaws with Rutherford's theory, even despite the experimental evidence. First, despite each electron's attraction to the positively charged core, the repulsive force betwen electrons leads to instabilities which rip the atom apart. A stable solution does not exist. Second, an accelerating charged electron should radiate energy. The gradual loss of electron energy would lead the electrons to spiral into the core of the atom. For these reasons, Rutherford's theory of the atomic nucleus was not taken seriously by leading contemporaries. It would take further effort by a unique mind to resolve these difficulties and further connect the internal majesty of the atom to experiment. This person was the great theoretical physicist Niels Bohr.

Bohr, in 1912, provided several great insights into the nature of the atom. First, the radioactive properties come from the atomic nucleus; the chemical properties come from the electron stucture. Second, it is the nuclear charge that determines a nuclei's placement in the period table. And third, during radioactive decay, the position of an element on the periodic chart shifts two places to the left if the atom emits an α particle and one space to the right if the atom emits a β particle (nuclear displacement law).

Bohr hoped to resolve the instabilities associated with Rutherford's model and he did so by bringing quantization to the atom, and in a similar way this radical concept had resolved the problems with black-box radiation (Planck) and the energy of photoelectrons (Einstein), quantization solved the problems associated with the instability of the atom. Bohr's atom placed electrons in orbits around the atom, like planets around the sun. The

quantized energies of photons emitted by atoms were caused by the transition between these different levels. Bohr's revelation came from a last minute connection atomic physics and transitional spectroscopy. A contemporary, J.W. Nicholoson, had published a paper proposing a Saturian system to explain the unusual properties of the Sun's corona. It was immediately clear to Bohr that spectral lines were caused by the different transitions between the different orbitals of the atom [193].

Bohr's paper, "On the constitution of atoms and molecules", was sent in three parts to Rutherford in 1913 [194–196]. He proposed his new model of the atom and calculated Ryberg's constant to great precision with the formula $R = \frac{2\pi^2 me^4}{h^3}$. This work would win Bohr the 1922 Nobel Prize in Physics. The young experimentalist Henry "Harry" Gwyn Jefferys Moseley began his tireless work looking for shifts in the x-ray spectra of different elements (the spectra were generated by passing x-rays through different crystals of material). Moseley's experimental work [197, 198], which in 1914 firmly established the connection between nuclear charge and atomic number, convinced contemporaries that the Bohr-Rutherford model of the atom was correct. Moseley, one of the most talented experimentalists of his time, would die at age 27 in World War I.

Scientific progress stalled during World War I (1914 - 1918), but the small resumption of normalcy that the end of the war provided further advances. Francis William Aston invented the modern mass spectrograph in 1919 [199] based on work by J.J. Thompson. His work was motivated by the separate discovery of isotopes in 1913 by Soddy and Thompson [200–203]. Isotopes (from the Greek "at the same place", as named by a distant relative of Soddy, the Scottish Physician Margret Todd) are atoms with the same number of protons but a different number of neutrons. Soddy noticed from his work on radioactive decay that positions on the periodic table appear to be occupied by multiple entities, different elements with the same chemical properties. J.J. Thompson, on his work on anode rays, put a beam of neon atoms through an electric and magnetic field and noticed that there were two separate marks for neon on his photographic plate. This original

basic setup of Thompson and others was refined into the precision instrument of Aston's. Aston would go on to identify 212 naturally occurring isotopes. Aston's basic design has evolved into a variety of different devices. The modern S800 magnetic spectrograph at the National Superconducting Cyclotron Laboratory (NSCL) allows experimenters to easily identify different isotopes that enter the focal plane of the detector [124, 204]. The S800 spectrograph is covered in greater detail in Sec. 4.3, page 61.

Ernest Rutherford created the first artificial nuclear reaction $\alpha(^{14}\mathrm{N}, ^{17}\mathrm{N} + p)$ by bombarding nitrogen gas with α particles [205]. In 1921, Bohr connects the periodic table with the Bohr-Rutherford model of the atom [206]. Bohr's insight: as electrons are added to an nucleus they fill up the orbitals in order of lowest to highest energy; the lower energy shells must be full before electrons are placed in higher energy orbitals[3]. Each orbital, also called a sub-shell, are arranged in collections that share the same principle quantum number n. The number of allowed electrons per shell depends only on the principle quantum number n as $2n^2$ and the number of allowed electrons per sub-shell (orbital) depends only upon the azimuthal quantum number ℓ as $2(2\ell + 1)$. Each shell can have several subshells whose ℓ value must be less than n (see Sec. 1.2.4 for the relationship between spectroscopic notation ℓ and the associated integer value of angular momentum). The occupancy of an orbital n and ℓ are used to describe the configuration of an atom. For example, consider Argon and its shell configuration labeled $1s^2 2s^2 2p^6$. Here the subscript is used to indicate the filled occupancy of the orbital. With Argon, we make one final note. Each shell is completely full. This leads to an especially stable, nonreactive atom. Other atoms have similar shell closure and the collection of these elements forms the noble gasses. In Sec. 1.2.4, we will see how a similar concepts applies to the configuration of nucleons in an atom.

Wolfgang Pauli, in 1924, explained the behavior of why electrons built up to certain

[3]This maxim works well with lower mass elements. An increasing number of exceptions occur with increasing electron number

closed shells by noting that each electron had to have a unique set of labeling attributes [207]. For Pauli's formulation to work, he had to introduce a new fourth quantum number, of degeneracy two, that was indescribable classically. George Uhlenbeck and Samuel Goudsmit proposed that this quantum number was associated with intrinsic angular momentum of the electron, a unique, inherent property just like mass and charge, and was not caused by an electrons movement though the atom [208]. Pauli would provide the complete mathematical description of intrinsic spin in 1927 [209] and a year later the full relativistic treatment was done by Paul Dirac [210].

Beginning with Louis de Broglie, in 1924, the old system of quantum mechanics where action is quantized but physics is elsewhere classical, was overturned. de Broglie, in his doctoral dissertation [211], postulated that all moving matter, not just light, could be described as a wave where $\lambda = p/h$. From this kernel grew the wave formulation and matrix formulation of quantum mechanics, ascribed to Erwin Schrödinger and Werner Heisenberg respectively. Heisenberg's work was published first [212], and showed how quantum jumps could occur between the stationary orbits of an atom. To do so, Heisenberg's paper made a bold claim: certain quantities, like position, could not be exactly known. Two years later, Heisenberg would publish the generalized version of this principle, Heisenberg's uncertainty relationship [213]. Together with the mathematical physicsts Pascual Jordan, Max Born, and the mathematician David Hilbert, Heisenberg would put this framework within the context of matrix algebra [214–216].

Erwin Schröndinger published his work after Heisenberg [217]. Schrödinger's wave equation begins with de Broglie's breakthrough, that particles can be described as waves, and provides the full description of how the particle wavefunction evolves in both time and space total energy associated with the wavefunction. Schrödinger paper did allowed for certain classical concepts to persist, and so his paper was more widely accepted than Heisenberg's work, but today both the matrix and wave formulations are considered equivalent and responsible for ushering in the modern era of quantum mechanics.

In 1929, Ernest Orlando Lawrence invented the cyclotron [218], a compact method of accelerating charged ions. Experimentalists faced their own barrier when trying to untangle nucleus: the long-range Coulomb repulsion between the incoming projectile and the nucleus of interest. The Coulomb force prevents nuclei from getting close enough for the projectile and target to interact through the very short-range strong force[4]. The kinetic energies of the projectiles should be significantly above that barrier, and this kinetic energy is greater than the decay Q value (kinetic energy of a particle emitted during radioactive decay) for the commonly available radioisotopes. The maximum energy of α particles produced during decay of common radioisotopes is at most 5 MeV (e.g. the Q-values for the alpha particles emitted during ^{238}U and ^{226}Ra decay are 4.2 MeV and 4.8 MeV). The calculated barriers for α particles on ^{56}Fe is 4.5 MeV, and for α particles on ^{197}Au, the barrier is 15.7 MeV. To study the full range of nuclei, the problem lay with the experimentalists to accelerate a stream of highly energetic particles that could probe the very center of the atom. Lawrence, provided the best and most efficient method of his time. Today, the core of this technology is found in the Coupled Cyclotron Facility (CCF) at the NSCL [88, 89].

Other less efficient methods of acceleration had also been developed and were producing good science. John Cockcroft and Ernest Walton used a complicated transformer and voltage multiplying system to accelerate a beam of protons (Cockcroft-Walton accelerator) [219]. This work would lead to the first nuclear reaction using an accelerator (1932) [220], the disintegration of ^{7}Li through the reaction p(^{7}Li,^{8}Be), where the unbound ^{8}Be disintegrates into two α particles. Other accelerating machines were introduced at a similar time: The linear accelerator, also overseen Lawrence and constructed by Ernest Sloan, was constructed simultaneously as the cyclotron at Berkeley, and the new Robert Van de Graaff generator was used to create high accelerating voltages for Merle Tuele's work at Princeton

[4]The processes of tunneling, as described by George Gamov, means the probability of a charged particle at sub-Coulomb kinetic energies reaching the core is extremely small but not zero.

(Van de Graff accelerators).

James Chadwick found the neutron in 1932 [221]. The existence of the neutron had been theorized by Rutherford twelve years earlier in 1920 [222]. Chadwick built upon the work Walter Bothe and Herbert Becker who noticed a highly penetrating type of radiation of was emitted by alpha particles incident upon ^{9}Be and other light metals, and upon the work of Irène Joliot-Curie and Frédéric Joliot-Curie who noticed that this new type of radiation, incident upon paraffin wax, knocked out energetic protons. James Chadwick realized in his experiments that these protons could not come from γ radiation. Such a conclusion would violate energy and momentum conservation. The particle that interacted with the proton had to be massive: the neutron.

Heisenberg quickly incorporated the neutron into a model of the atom (proton-neutron model) later that year and quickly published the new model of the atom [223–225]. The addition finished the major modern constituents of the atom: electron, proton, and neutron. Much later (in 1964) it was proposed that protons and neutrons were themselves not elementary particles, and were composed of quarks, but modern nuclear physics still treats protons and neutrons as the fundamental building blocks of the atom. Neutrons and protons are bound together in the nucleus, and whatever force that bound them had to be much stronger than the Coulomb force (to overcome the Coulomb repulsion between the protons) and be short range (to explain nuclear saturation, i.e. the proportionality of binding energy to atomic mass A).

Hideki Yukawa published his theory of meson exchange in 1935 [1]. The meson (from the Greek word for intermediate, "mesos") had a heavy mass postulated by Yukawa to be between that of an electron and proton. The mass would explain the short range force between nucleons. The pi meson, or pion π, was discovered in 1947 by Occhialini and Powell [6] and Lattes et al. [7] and was found to participate in the nuclear force (then called the strong force). Today, although meson exchange is still an applicable and useful concept in nuclear physics, the strong force is understood as the force between quarks as

mediated by gluons. Only a small amount of that force sneaks out beyond the confines of a nucleon. It is this small, fluctuating residuum, much stronger than the electromagnetic force, that binds protons and neutrons together.

Slowly models were proposed that helped explain how the nucleus as a unified whole behaved. George Gamov proposed the liquid drop model, the first theory of nuclear energy and mass [226, 227], in 1928, the same year he published his theory on α decay [228] and before the discovery of the neutron. With the discovery of the neutron by Chadwick, Gamov's theory was further developed by Niels Bohr, John Archibald Wheeler, and Carl Friedrich von Weizsäcker and this revised model was used by Lise Meitner and Otto Robert Frisch to explain the spontaneous splitting of a heavy atom, a process which they called "fission" [229]. These experimental work communicated to Meitner and Frisch was performed by Fredrich Wilhelm "Fritz" Straßmann and Otto Hahn, who first observed fission by detecting Barium after bombarding Uranium with neutrons.

Two papers appeared in 1949 that finally completed the major ideas behind the nuclear shell model, the theory of how protons and neutrons are arranged in orbitals in the atomic nucleus. The concept is similar to the early model of the electron orbits N. Bohr proposed in 1913. Protons and neutrons independently fill orbitals of specific maximum occupancy, starting with the lowest energy orbitals first (see Fig. 1.4, page 14. Both Maria Goeppert Mayer at Argonne National Laboratory and the team of Johannes Hans Daniel Jensen (Hans Jensen), Otto Haxel, and Hans Eduard Suess realized the importance of the spin-orbit interaction, the interaction between a nucleons orbital angular momentum and intrinsic spin, in the mean potential that each nucleon feels. They published nearly simultaneously [24, 25] and both Mayer and Jensen won Nobel Prizes for their work. The addition of the spin-orbit potential to the potential of a three-dimensional harmonic oscillator finally described the level structure of a nucleus, in particular the large stability of nuclei with specific number of protons or neutrons: 2, 8, 20, 28, 50, 82, and 126. This final configuration, explained many of the current nuclear phenomena including spins

and magnetic moments.

The shell model, also called the independent shell model (IPM), worked well for certain properties of the atom, as enumerated above, but not others, e.g. the existence of rotational bands and large quadrupole moments and quadrupole transition probabilities, properties that could be described well by rotational or vibrational models. Aage Bohr (son of Niels Bohr), Ben Mottelson, and James Rainwater combined the single-particle and collective behaviors into a comprehensive collective mode, the deformed shell model and the particle plus rotor model.

The shell model assumes as spherical potential (isotropic harmonic potential), but for many nuclei, it is experimentally apparent that the nucleus has a stable and static deformation. Rainwater introduced the concept of deformed shell model where the individual nucleons move in a deformed mean potential [230, 231]. The deformations to the harmonic oscillator potential necessary to shift the spherical shell model results to the experimental observations was given to Sven Gösta Nilsson. Both the model and the diagrams showing the shift of single-particle energies with respect to nuclear deformation are named after Nilsson in appreciation of his original paper, published in 1955 [62]. Bohr and Mottelson tried similar methods of combining collective and single-particle behavior. The particle plus rotor model took the valence particles and coupled these valence particles to a collective rotor, where the collective rotor accounts for the behavior of the core [232]. The work of Bohr, Mottelson and Rainwater was rewarded with the Nobel prize in 1975.

Nuclear physics has evolved far beyond these beginnings. Current vanguard, experimental nuclear facilities, like the NSCL, involve over a hundred people and use complicated and powerful machinery to accelerate radioactive beams. And current theoretical calculations involve computers that can perform calculations, like the multiplication of massive matrices, in a few seconds, calculations that would take the whole assortment of the early brilliant physicists years to do. The scope and size of the field has increased

dramatically. Still the basics remain the same. The three original models, although embellished, remain as important as ever. Calculations using the single-particle shell model are cruicial to this work, and work testing the validity of "magic numbers" remains a contemporary topic.

BIBLIOGRAPHY

BIBLIOGRAPHY

[1] H. Yukawa. On the interaction of elementary particle. *Proc. Phys.-Math. Soc. Jpn.*, **17**:48, 1935.

[2] V.G.J. Stoks, R.A.M. Klomp, C.P.F. Terheggen, and J.J. de Swart. Construction of high-quality NN potential models. *Phys. Rev. C*, **49**:2950, 1994.

[3] R.B. Wiringa, V.G.J. Stoks, and R. Schiavilla. Accurate nucleon-nucleon potential with charge-independence breaking. *Phys. Rev. C*, **51**:38, 1995.

[4] R. Machleidt. High-precision, charge-dependent bonn nucleon-nucleon potential. *Phys. Rev. C*, **63**:024001, 2001.

[5] O. Sorlin and M.-G. Porquet. Nuclear magic numbers: New features far from stability. *Prog. Part. Nucl. Phys.*, **61**:602, 2008.

[6] G.P.S. Occhialini and C.F. Powell. Nuclear disintegrations produced by slow charged particles of small mass. *Nature*, **159**:186, 1947.

[7] C.M.G. Lattes, G.P.S. Occhialini, and C.F. Powell. Observations of the tracks of slow mesons in photographic emulsions. *Nature*, **160**:453, 1947.

[8] N. Ishii, S. Aoki, and T. Hatsuda. Nuclear force from lattice QCD. *Phys. Rev. Lett.*, **99**:022001, 2007.

[9] Isotope Science Facility at Michigan State University: Upgrade of the NSCL rare isotope research capabilities, 2006. MSU preprint MSUCL-1345.

[10] P. Ring and P. Schuck. *The Nuclear Many-body Problem*. Spring-Verlang Berlin Heidelberg, 1994.

[11] C.F. von Weizsäcker. Zur theorie der kernmassen. *Z. Phys. A*, **96**:431, 1935.

[12] H.A. Bethe and R.F. Bacher. Nuclear physics A., stationary states of nuclei. *Rev. Mod. Phys.*, **8**:82, 1936.

[13] W.D. Myers and W.J. Swiatecki. Nuclear masses and deformations. *Nucl. Phys.*, **81**:1, 1966.

[14] William D. Myers and W. J. Swiatecki. Average nuclear properties. *Ann. Phys.*, **55**: 395, 1969.

[15] W. D. Myers and W. J. Swiatecki. The nuclear droplet model for arbitrary shapes. *Ann. Phys.*, **84**:186, 1974.

[16] K. Krane. *Introductory Nuclear Physics*. John Wiley and Sons, Inc., 1988.

[17] S.S.M. Wong. *Introductory Nuclear Physics*. Wiley-VCH Verlang GmbH & Co. KGaA, Weinheim, 2004.

[18] Takahiro Tachibana, Masahiro Uno, Masami Yamada, and So Yamada. Empirical mass formula with proton-neutron interaction. *At. Data Nucl. Data Tables*, **39**:251, 1988.

[19] R.N. Boyd. Explosive processes in nucleosynthesis. *Eur. Phys. J. A*, **13**:203, 2002.

[20] E.M. Burbidge, G.R. Burbidge, W.A. Fowler, and F. Hoyle. Synthesis of elements in the stars. *Rev. Mod. Phys.*, **29**:547, 1957.

[21] A. Bohr and B.R. Mottelson. *Nuclear Structure, Vol. I*. Benjiman, 1969.

[22] K.A. Brueckner. Nuclear saturation and two-body forces. II. tensor forces. *Phys. Rev.*, **96**:508, 1954.

[23] K.A. Brueckner, C.A. Levinston, and H.M. Mahmoud. Two-body forces and nuclear saturation. I. Central forces. *Phys. Rev.*, **95**:217, 1954.

[24] M.G. Mayer. On closed shells in nuclei. II. *Phys. Rev.*, **75**:1969, 1949.

[25] O. Haxel, H.J.D. Jensen, and H.E. Suess. On the "magic numbers" in nuclear structure. *Phys. Rev.*, **75**:1766, 1949.

[26] C. Détraz, D. Guillemaud, G. Huber, R. Klapisch, M. Langevin, F. Naulin, C. Thibault, L.C. Carraz, and F. Touchard. Beta decay of $^{27-32}$Na and their descendants. *Phys. Rev. C*, **19**:164, 1979.

[27] G. Huber, F. Touchard, S. Büttgenbach, C. Thibault, R. Klapisch, H. T. Duong, S. Liberman, J. Pinard, J. L. Vialle, P. Juncar, and P. Jacquinot. Spins, magnetic moments, and isotope shifts of $^{21-31}$Na by high resolution laser spectroscopy of the atomic D_1 line. *Phys. Rev. C*, **18**:2342, 1978.

[28] C. Thibault, R. Klapisch, C. Rigaud, A.M. Poskanzer, R. Prieels, L. Lessard, and W. Reisdorf. Direct measurement of the masses of ^{11}Li and $^{26-32}$Na with an on-line mass spectrometer. *Phys. Rev. C*, **12**:644, 1975.

[29] R. Tribble, D. Bryman, D. Dean, C. Elster, R. Ent, T. Glasmacher, U. Heinz, X. Ji, R. Lacey, I.Y. Lee, N. Makins, R. Milner, M. Ramsey-Musolf, H. Nitsche, G. Savard, S. Seestrom, T. Ulrich, U. van Kolck, J. Wilkerson, and W. Zajc (The Nuclear Science Advisory Committee). The frontiers of nuclear science: A long range plan. Technical report, Nuclear Science Advisorary Committee (NSAC), 2007.

[30] H. Simon, D. Aleksandrov, T. Aumann, L. Axelsson, T. Baumann, M. J. G. Borge, L. V. Chulkov, R. Collatz, J. Cub, W. Dostal, B. Eberlein, Th. W. Elze, H. Emling, H. Geissel, A. Grünschloss, M. Hellström, J. Holeczek, R. Holzmann, B. Jonson, J. V. Kratz, G. Kraus, R. Kulessa, Y. Leifels, A. Leistenschneider, T. Leth, I. Mukha, G. Münzenberg, F. Nickel, T. Nilsson, G. Nyman, B. Petersen, M. Pfützner, A. Richter,

K. Riisager, C. Scheidenberger, G. Schrieder, W. Schwab, M. H. Smedberg, J. Stroth, A. Surowiec, O. Tengblad, and M. V. Zhukov. Direct experimental evidence for strong admixture of different parity states in ^{11}Li. *Phys. Rev. Lett.*, **83**:496, 1999.

[31] H. Iwasaki, T. Motobayashi, H. Akiyoshi, Y. Ando, N. Fukuda, H. Fujiwara, Zs. Fülöp, K. I. Hahn, Y. Higurashi, M. Hirai, I. Hisanaga, N. Iwasa, T. Kijima, A. Mengoni, T. Minemura, T. Nakamura, M. Notani, S. Ozawa, H. Sagawa, H. Sakurai, S. Shimoura, S. Takeuchi, T. Teranishi, Y. Yanagisawa, and M. Ishihara. Low-lying intruder 1^- state in ^{12}Be and the melting of the $N = 8$ shell closure. *Phys. Lett. B*, **491**:8, 2000.

[32] J. Fridmann, I. Wiedenhöver, A. Gade, L. T. Baby, D. Bazin, B. A. Brown, C. M. Campbell, J. M. Cook, P. D. Cottle, E. Diffenderfer, D.-C. Dinca, T. Glasmacher, P. G. Hansen, K. W. Kemper, J. L. Lecouey, W. F. Mueller, E. Rodriguez-Vieitez, J. R. Terry, J. A. Tostevin, K. Yoneda, and H. Zwahlen. Shell structure at $N = 28$ near the dripline: Spectroscopy of ^{42}Si, ^{43}P, and ^{44}S. *Phys. Rev. C*, **74**:034313, 2006.

[33] J. Fridmann, I. Wiedenhover, A. Gade, L. T. Baby, D. Bazin, B. A. Brown, C. M. Campbell, J. M. Cook, P. D. Cottle, E. Diffenderfer, D.-C. Dinca, T. Glasmacher, P. G. Hansen, K. W. Kemper, J. L. Lecouey, W. F. Mueller, H. Olliver, E. Rodriguez-Vieitez, J. R. Terry, J. A. Tostevin, and K. Yoneda. 'Magic' nucleus ^{42}Si. *Nature*, **435**:922, 2005.

[34] B. Bastin, S. Grévy, D. Sohler, O. Sorlin, Zs. Dombrádi, N. L. Achouri, J. C. Angélique, F. Azaiez, D. Baiborodin, R. Borcea, C. Bourgeois, A. Buta, A. Bürger, R. Chapman, J. C. Dalouzy, Z. Dlouhy, A. Drouard, Z. Elekes, S. Franchoo, S. Iacob, B. Laurent, M. Lazar, X. Liang, E. Liénard, J. Mrazek, L. Nalpas, F. Negoita, N. A. Orr, Y. Penionzhkevich, Zs. Podolyák, F. Pougheon, P. Roussel-Chomaz, M. G. Saint-Laurent, M. Stanoiu, I. Stefan, F. Nowacki, and A. Poves. Collapse of the $N = 28$ shell closure in ^{42}Si. *Eur. Phys. J. A*, **99**:022503, 2007.

[35] C. M. Campbell, N. Aoi, D. Bazin, M. D. Bowen, B. A. Brown, J. M. Cook, D.-C. Dinca, A. Gade, T. Glasmacher, M. Horoi, S. Kanno, T. Motobayashi, W. F. Mueller, H. Sakurai, K. Starosta, H. Suzuki, S. Takeuchi, J. R. Terry, K. Yoneda, and H. Zwahlen. Measurement of excited states in ^{40}Si and evidence for weakening of the $N = 28$ shell gap. *Phys. Rev. Lett.*, **97**:112501, 2006.

[36] T. Glasmacher, B. A. Brown, M. J. Chromik, P. D. Cottle, M. Fauerbach, R. W. Ibbotson, K. W. Kemper, D. J. Morrissey, H. Scheit, D. W. Sklenicka, and M. Steiner. Collectivity in ^{44}S. *Phys. Lett. B*, **395**:163, 1997.

[37] A. Ozawa, T. Kobayashi, T. Suzuki, K. Yoshida, and I. Tanihata. New magic number, $N = 16$, near the neutron drip line. *Phys. Rev. Lett.*, **84**:5493, 2000.

[38] M. Stanoiu, F. Azaiez, Zs. Dombrádi, O. Sorlin, B. A. Brown, M. Belleguic, D. Sohler, M. G. Saint Laurent, M. J. Lopez-Jimenez, Y. E. Penionzhkevich, G. Sletten, N. L. Achouri, J. C. Angélique, F. Becker, C. Borcea, C. Bourgeois, A. Bracco, J. M. Daugas, Z. Dlouhýe;, C. Donzaud, J. Duprat, Zs. Füöp, D. Guillemaud-Mueller, S. Grévy,

F. Ibrahim, A. Kerek, A. Krasznahorkay, M. Lewitowicz, S. Leenhardt, S. Lukyanov, P. Mayet, S. Mandal, H. van der Marel, W. Mittig, J. Mrázek, F. Negoita, F. De Oliveira-Santos, Zs. Podolyák, F. Pougheon, M. G. Porquet, P. Roussel-Chomaz, H. Savajols, Y. Sobolev, C. Stodel, J. Timár, and A. Yamamoto. $N = 14$ and 16 shell gaps in neutron-rich oxygen isotopes. *Phys. Rev. C*, **69**:034312, 2004.

[39] A. Huck, G. Klotz, A. Knipper, C. Miehé, C. Richard-Serre, G. Walter, A. Poves, H. L. Ravn, and G. Marguier. Beta decay of the new isotopes ^{52}K, ^{52}Ca, and ^{52}Sc: A test of the shell model far from stability. *Phys. Rev. C*, **31**:2226, 1985.

[40] A. Gade, R. V. F. Janssens, D. Bazin, R. Broda, B. A. Brown, C. M. Campbell, M. P. Carpenter, J. M. Cook, A. N. Deacon, D.-C. Dinca, B. Fornal, S. J. Freeman, T. Glasmacher, P. G. Hansen, B. P. Kay, P. F. Mantica, W. F. Mueller, J. R. Terry, J. A. Tostevin, and S. Zhu. Cross-shell excitation in two-proton knockout: Structure of ^{52}Ca. *Phys. Rev. C*, **74**:021302, 2006.

[41] H. L. Crawford, R. V. F. Janssens, P. F. Mantica, J. S. Berryman, R. Broda, M. P. Carpenter, N. Cieplicka, B. Fornal, G. F. Grinyer, N. Hoteling, B. P. Kay, T. Lauritsen, K. Minamisono, I. Stefanescu, J. B. Stoker, W. B. Walters, and S. Zhu. Beta decay and isomeric properties of neutron-rich Ca and Sc isotopes. *Phys. Rev. C*, **2010**:014311, 2010.

[42] S. McDaniel, A. Gade, R. V. F. Janssens, D. Bazin, B. A. Brown, C. M. Campbell, M. P. Carpenter, J. M. Cook, A. N. Deacon, D. C. Dinca, S. J. Freeman, T. Glasmacher, P. G. Hansen, B. P. Kay, P. F. Mantica, W. F. Mueller, J. R. Terry, J. A. Tostevin, and S. Zhu. Population of positive-parity states in ^{53}Sc through one-proton knockout. *Phys. Rev. C*, **81**:024301, 2010.

[43] D.-C. Dinca, R. V. F. Janssens, A. Gade, D. Bazin, R. Broda, B. A. Brown, C. M. Campbell, M. P. Carpenter, P. Chowdhury, J. M. Cook, A. N. Deacon, B. Fornal, S. J. Freeman, T. Glasmacher, M. Honma, F. G. Kondev, J.-L. Lecouey, S. N. Liddick, P. F. Mantica, W. F. Mueller, H. Olliver, T. Otsuka, J. R. Terry, B. A. Tomlin, and K. Yoneda. Reduced transition probabilities to the first 2^+ state in ^{52,54,56}Ti and development of shell closures at $N = 32, 34$. *Phys. Rev. C*, **71**:041302, 2005.

[44] B. Fornal, S. Zhu, R. V. F. Janssens, M. Honma, R. Broda, P. F. Mantica, B. A. Brown, M. P. Carpenter, P. J. Daly, S. J. Freeman, Z. W. Grabowski, N. J. Hammond, F. G. Kondev, W. Królas, T. Lauritsen, S. N. Liddick, C. J. Lister, E. F. Moore, T. Otsuka, T. Pawłat, D. Seweryniak, B. E. Tomlin, and J. Wrzesiński. Development of shell closures at $N = 32, 34$. II. Lowest yrast excitations in even-even ti isotopes from deep-inelastic heavy-ion collisions. *Phys. Rev. C*, **70**:064304, 2004.

[45] P. F. Mantica, B. A. Brown, A. D. Davies, T. Glasmacher, D. E. Groh, M. Horoi, S. N. Liddick, D. J. Morrissey, A. C. Morton, W. F. Mueller, H. Schatz, A. Stolz, and S. L. Tabor. β-decay properties of ^{55,56}Ti. *Phys. Rev. C*, **68**:044311, 2004.

[46] D. E. Appelbe, C. J. Barton, M. H. Muikku, J. Simpson, D. D. Warner, C. W. Beausang, M. A. Caprio, J. R. Cooper, J. R. Novak, N. V. Zamfir, R. A. E. Austin, J. A. Cameron,

C. Malcolmson, J. C. Waddington, and F. R. Xu. Detailed γ-ray spectroscopy of ^{55}Cr and ^{56}Cr: Confirmation of the subshell closure at $N = 32$. *Phys. Rev. C*, **67**:034309, 2003.

[47] A. Gade and T. Glasmacher. In-beam nuclear spectroscopy of bound states with fast exotic ion beams. *Prog. Part. Nucl. Phys.*, **60**:161, 2008.

[48] P. Doll, G. J. Wagner, K. T. Köpfle, and G. Mairle. The quasihole aspect of hole strength distributions in odd potassium and calcium isotopes. *Nucl. Phys. A*, **263**: 210, 1976.

[49] S.M. Banks, B.M. Spicer, G.G. Shute, V.C. Officer, G.J. Wagner, W.E. Dollhopf, L.I. Qingli, C.W. Glover, D.W. Devins, and D.L. Friesel. The ^{48}Ca(d, ^{3}He)^{47}K reaction at 80 MeV. *Nucl. Phys. A*, **437**:381, 1985.

[50] G. J. Kramer, H. P. Blok, and L. Lapikás. A consistent analysis of $(e,e'p)$ and $(d,^{3}\mathrm{He})$ experiments. *Nucl. Phys. A*, **679**:267, 2001.

[51] A. Gade, B. A. Brown, D. Bazin, C. M. Campbell, J. A. Church, D. C. Dinca, J. Enders, T. Glasmacher, M. Horoi, Z. Hu, K. W. Kemper, W. F. Mueller, T. Otsuka, L. A. Riley, B. T. Roeder, T. Suzuki, J. R. Terry, K. L. Yurkewicz, and H. Zwahlen. Evolution of the $E(1/2^+_1) - E(3/2^+_1)$ energy spacing in odd-mass K, Cl, and P isotopes for $N = 20-28$. *Phys. Rev. C*, **74**:034322, 2006.

[52] E.K. Warburton, J.A. Becker, and B.A. Brown. Mass systematics for $A = 29-44$ nuclei: The deformed $A \sim 32$ region. *Phys. Rev. C*, **41**:1147, 1990.

[53] B.H. Wildenthal. Empirical strengths of spin operators in nuclei. *Prog. Part. Nucl. Phys.*, **11**:5, 1984.

[54] Yutaka Utsuno, Takaharu Otsuka, Thomas Glasmacher, Takahiro Mizusaki, and Michio Honma. Onset of intruder ground state in exotic Na isotopes and evolution of the $N = 20$ shell gap. *Phys. Rev. C*, **70**:044307, 2004.

[55] J.R. Terry, B.A. Brown, C.M. Campbell, J.M. Cook, A.D. Davies, D.C. Dinca, A. Gade, T. Glasmacher, P.G. Hansen, B.M. Sherrill, H. Zwahlen, D. Bazin, K. Yoneda, J.A. Tostevin, T. Otsuka, Y. Utsuno, and B. Pritychenko. Single-neutron knockout from intermediate energy beams of $^{30-32}$Mg: Mapping the transition into the "island of inversion". *Phys. Rev. C*, **77**:014316, 2008.

[56] M. Honma, T. Otsuka, B.A. Brown, and T. Mizusaki. Effective interaction for pf-shell nuclei. *Phys. Rev. C*, **65**:061301, 2002.

[57] S. N. Liddick, P. F. Mantica, R. V. F. Janssens, R. Broda, B. A. Brown, M. P. Carpenter, B. Fornal, M. Honma, T. Mizusaki, A. C. Morton, W. F. Mueller, T. Otsuka, J. Pavan, A. Stolz, S. L. Tabor, B. E. Tomlin, and M. Wiedeking. Lowest excitations in ^{56}Ti and the predicted $N = 34$ shell closure. *Phys. Rev. Lett.*, **92**:072502, 2004.

[58] M. Honma, T. Otsuka, B.A. Brown, and T. Mizusaki. Shell-model description of neutron-rich pf-shell nuclei with a new effective interaction GXPF1. *Eur. Phys. J. A*, **25**:399, 2005.

[59] P.G. Hansen and J.A. Tostevin. Direct reactions with exotic nuclei. *Annu. Rev. Nucl. Part. Sci.*, **53**:219, 2003.

[60] A. Gade, P. Adrich, D. Bazin, M.D. Bowen, B.A. Brown, C.M. Campbell, J.M. Cook, T. Glasmacher, K. Hosier, S. McDaniel, D. McGlinchery, A. Obertelli, L.A. Riley, K. Siwek, J.A. Tostevin, and D. Weisshaar. Inverse-kinematics one-proton pickup with intermediate-energy beams: The ^{9}Be(^{20}Ne, ^{21}Na + γ)X reaction. *Phys. Rev. C*, **76**:061302, 2007.

[61] A. Gade, P. Adrich, D. Bazin, M.D. Bowen, B.A. Brown, C.M. Campbell, J.M. Cook, T. Glasmacher, K. Hosier, S. McDaniel, D. McGlinchery, A. Obertelli, L.A. Riley, K. Siwek, J.A. Tostevin, and D. Weisshaar. In-beam γ-ray spectroscopy at the proton dripline: ^{23}Al. *Phys. Lett. B*, **666**:218, 2008.

[62] G. Nilsson. Binding states of individual nucleons in strongly deformed nuclei. *K. Dan. Vidensk. Selsk. Mat. Fys. Medd.*, **29**:16, 1955.

[63] J.P. Elliot. Collective motion in the nuclear shell model. I. Classification schemes for states of mixed configurations. *Proc. R. Soc.*, **A245**:128, 1958.

[64] J.P. Elliot. Collective motion in the nuclear shell model. II. The introduction of intrinsic wave-functions. *Proc. R. Soc.*, **A245**:562, 1958.

[65] E. Caurier, G. Martínez-Pinedo, F. Nowacki, A. Poves, and A.P. Zuker. The shell model as a unified view of nuclear structure. *Rev. Mod. Phys.*, **77**:427, 2005.

[66] W. Rae. NuShell and NuShellX shell model code, 2008. Available at `http://knollhouse.edu/NuShellX.aspx`.

[67] E. Caurier and F. Nowacki. Present status of shell model techniques. *Acta. Phys. Pol. B*, 30:705, 1999.

[68] MShell code. MShell code. *RIKEN Accel. Prog. Rep.*, **13**:14, 2000.

[69] E.W. Ormand and C.W. Johnson. REDSTICK code, 2002.

[70] B.A. Brown, A. Etchegoyen, and W.D.M. Rae. The computer code OXBASH, MSU-NSCL Report No. 524. Technical report, Michigan State University, 1998.

[71] B.A. Brown. The nuclear shell model towards the drip lines. *Prog. Part. Nucl. Phys.*, **47**:517, 2001.

[72] E. Caurier, F. Nowacki, and A. Poves. Large-scale shell model calculations for exotic nuclei. *Eur. Phys. J. A*, **15**:145, 2002.

[73] A. Poves and N. Frederic. The nuclear shell model. *Lect. Notes Phys.*, **581**:70, 2001.

[74] I. Talmi. Fifty years of the shell model: The quest for the effective interaction. *Adv. Nucl. Phys*, **27**:1, 2003.

[75] J. Carlson. Green's function Monte Carlo study of light nuclei. *Phys. Rev. C*, **87**:2026, 1987.

[76] S.C. Pieper and R.B. Wiringa. Quantum Monte Carlo calculations of light nuclei. *Annu. Rev. Nucl. Part. Sci.*, **51**:53, 2001.

[77] B.S. Pudliner, V.R. Pandharipande, J. Carlson, S.C Pieper, and R.B. Wiringa. Quantum monte carlo calculations of nuclei with $A \leq 7$. *Phys. Rev. C*, **56**:1720, 1997.

[78] P. Navràtil, J.P. Vary, and B.R. Barrett. Properties of ^{12}C in the ab initio nuclear shell model. *Phys. Rev. Lett.*, **84**:5728, 2000.

[79] P. Navràtil, J.P. Vary, and B.R. Barrett. Large-basis ab initio no-core shell model and its application to ^{12}C. *Phys. Rev. C*, **62**:054311, 2000.

[80] B.A. Brown. Lecture notes in nuclear physics. Available from `http://www.nscl.msu.edu/~brown/Jina-workshop/BAB-lecture-notes.pdf`, 2005.

[81] B.A. Brown. New skyrme interaction for normal and exotic nuclei. *Phys. Rev. C*, **1958**:220, 1998.

[82] M. Horoi. High performance shell model calculations. JINA Workshop "Nuclear Shell Model Applications," Feb 13-17, 2006, 2006. Available at `http://www.nscl.msu.edu/~brown/Jina-workshop/mhoroi-msufeb06.pdf`.

[83] X. Campi, H. Flocard, A.K. Kerman, and S. Koonin. Shape transition in the neutron rich sodium isotopes. *Nucl. Phys. A*, **251**:193, 1975.

[84] A.E.L. Dieperink and F. de Forest. Center-of-mass effects in single-nucleon knock-out reactions. *Phys. Rev. C*, **10**:543, 1974.

[85] B.A. Brown, P.G. Hansen, B.M. Sherrill, and J.A. Tostevin. Absolute spectroscopic factors from nuclear knockout reactions. *Phys. Rev. C*, **65**:061601, 2002.

[86] J. Enders, T. Baumann, B.A. Brown, N.H Frank, P.G Hansen, P.R. Heckman, B.M. Sherrill, A. Stolz, M. Thoennessen, J.A. Tostevin, E.J. Tryggestad, S. Typel, and M.S. Wallace. Spectroscopic factors measured in inclusive proton-knockout reactions on ^{8}B and ^{9}C at intermediate energies. *Phys. Rev. C*, **67**:064301, 2003.

[87] P. Doll, G. Mairle, H. Breuer, K.T. Knopfle, T. Tohei, and G.J. Wagner. On positive-parity states of ^{45}Sc, ^{47}Sc and ^{49}Sc. *J. Phys. G*, **5**:1421, 1979.

[88] D. J. Morrissey. The coupled cyclotron project at the NSCL. *Nucl. Phys. A*, **616**:45, 1997.

[89] P. Miller, F. Marti, D. Poe, M. Steiner, J. Stetson, and X.Y. Wu. Commissioning of the coupled cyclotron facility at the NSCL. In *Proceedings of the 2001 Particle Accelerator Conference, Chicago*, 2001.

[90] J.A. Tostevin. Single-nucleon knockout reactions at fragmentation beam energies. *Nucl. Phys. A*, **682**:320, 2001.

[91] P.G. Hansen, A.S. Jensen, and B. Jonson. Nuclear halos. *Annu. Rev. Nucl. Part. Sci.*, **45**:591, 1995.

[92] I. Tanihata. Neutron halo nuclei. *J. Phys. G*, **22**:157, 1996.

[93] J. H. Kelley, Sam M. Austin, R. A. Kryger, D. J. Morrissey, N. A. Orr, B. M. Sherrill, M. Thoennessen, J. S. Winfield, J. A. Winger, and B. M. Young. Parallel momentum distributions as a probe of halo wave functions. *Phys. Rev. Lett.*, **1995**:30, 1995.

[94] T. Aumann, A. Navin, D.P. Balamuth, D. Bazin, B. Blank, B.A. Brown, J.E. Bush, J.A. Caggiano, B. Davids, T. Glasmacher, V. Guimaráes, P.G. Hansen, R.W. Ibbotson, D. Karnes, J.J. Kolata, V. Maddalena, B. Pritychenko, H. Scheit, B.M. Sherrill, and J.A. Tostevin. One-neutron knockout from individual single-particle states of ^{11}Be. *Phys. Rev. Lett.*, **84**:35, 2000.

[95] J.R. Terry, D. Bazin, B.A. Brown, C.M. Campbell, J.A. Church, J.M. Cook, A.D. Davies, D.-C. Dinca, J. Enders, A. Gade, T. Glasmacher, P.G. Hansen, J.L. Lecouey, T. Otsuka, B. Pritychenko, B.M. Sherrill, J.A. Tostevin, Y. Utsuno, K. Yoneda, and H. Zwahlen. Direct evidence for the onset of intruder configurations in neutron-rich Ne isotopes. *Phys. Lett. B*, **640**:86, 2006.

[96] A. Gade, D. Bazin, B.A. Brown, C.M. Campbell, J.A. Church, D.C. Dinca, J. Enders, T. Glasmacher, P.G. Hansen, Z. Hu, K.W. Kemper, W.F. Mueller, H. Olliver, B.C. Perry, L.A. Riley, B.T. Roeder, B.M. Sherrill, J.R. Terry, J.A. Tostevin, and K.L. Yurkewicz. One-neutron knockout reactions on proton-rich nuclei with $N = 16$. *Phys. Rev. C*, **69**:034311, 2004.

[97] P.G. Hansen and B.M. Sherrill. Reactions and single-particle structure of nuclei near the drip lines. *Nucl. Phys. A*, **693**:133, 2001.

[98] J.A. Tostevin. Core excitation in halo nucleus break-up. *J. Phys. G*, **25**:735, 1999.

[99] M.S. Hussein and K.W. McVoy. Inclusive projectile fragmentation in the spectator model. *Nucl. Phys. A*, **445**:124, 1985.

[100] R.J. Glauber. *Lectures in Theoretical Physics*. Interscience, 1959.

[101] G.J. Kramer, H.P. Blok, J.F.A Van Hienen, S. Brandenburg, M.N. Harakeh, Van Der S.Y. Werf, P.W.M. Glaudemans, and A.A. Wolters. Spectroscopic factors from the ^{51}V(d,^{3}He)^{50}Ti reaction. *Nucl. Phys. A*, **477**:55, 1988.

[102] S.K. Charagi and S.K. Gupta. Coulomb-modified Glauber model description of heavy-ion reaction cross sections. *Phys. Rev. C*, **41**:1610, 1990.

[103] L. Ray. Proton-nucleus total cross sections in the intermediate energy range. *Phys. Rev. C*, **20**:1857, 1979.

[104] J. S. Al-Khalili, J. A. Tostevin, and I. J. Thompson. Radii of halo nuclei from cross section measurements. *Phys. Rev. C*, **54**:1843, 1996.

[105] C.A. Bertulani and H. Sagawa. Probing the ground-state and transition densities of halo nuclei. *Nucl. Phys. A*, **588**:667, 1995.

[106] C.A. Bertulani and A Gade. MOMDIS: a Glauber model computer code for knockout reactions. *Comp. Phys. Comm.*, **175**:372, 2006.

[107] A. Gade, D. Bazin, B. A. Brown, C. M. Campbell, J. A. Church, D. C. Dinca, J. Enders, T. Glasmacher, P. G. Hansen, Z. Hu, K. W. Kemper, W. F. Mueller, H. Olliver, B. C. Perry, L. A. Riley, B. T. Roeder, B. M. Sherrill, J. R. Terry, J. A. Tostevin, and K. L. Yurkewicz. Reduced occupancy of the deeply bound $0d_{5/2}$ neutron state in ^{32}Ar. *Phys. Rev. Lett.*, **93**:042501, 2004.

[108] C. A. Bertulani and P. G. Hansen. Momentum distributions in stripping reactions of radioactive projectiles at intermediate energies. *Phys. Rev. C*, **2004**:034609, 2004.

[109] H. Esbensen and G.F. Bertsch. Eikonal approximation in heavy-ion fragmentation reactions. *Phys. Rev. C*, **64**:014608, 2001.

[110] A. Bonaccorso and D.M. Brink. Nucleon transfer to continuum states. *Phys. Rev. C*, **38**:1776, 1998.

[111] N. Austern, Y. Iseri, M. Kamimura, M. Kawai, G. Rawitscher, and M. Yahiro. Continuum-discretized coupled-channels calculations for three-body models of deuteron-nucleus reactions. *Phys. Rep.*, **154**:125, 1987.

[112] J.A. Tostevin, D. Bazin, B.A. Brown, T. Glasmacher, P.G. Hansen, V. Maddalena, A. Navin, and B.M. Sherrill. Single-neutron removal reactions from ^{15}C and ^{11}Be: Deviations from the eikonal approximation. *Phys. Rev. C*, **66**:024607, 2002.

[113] D.M. Brink. Kinematical effects in heavy-ion reactions. *Phys. Lett. B*, **40**:37, 1972.

[114] W.R. Phillips. Heavy-ion transfer reactions. *Rep. Prog. Phys.*, **40**:345, 1977.

[115] G.R. Smith, J.R. Shepard, R.L. Boudrie, R.J. Peterson, G.S. Adams, T.S. Bauer, G.J. Igo, G. Pauletta, C.A. Whitten, A. Wriekat, B. Hoistad, and G.W. Hoffmann. (p,d) reaction at 800 MeV. *Phys. Rev. C*, **30**:593, 1984.

[116] S. Frullani and J. Mougey. Single-particle properties of nuclei through $(e,e'p)$ reactions. *Adv. Nucl. Phys*, **13**:1, 1984.

[117] P. D. Bond, J. Barrette, C. Baktash, C. E. Thorn, and A. J. Kreiner. Selective population of high-j orbitals in Er nuclei by heavy-ion-induced transfer. *Phys. Rev. Lett.*, **46**: 1565, 1981.

[118] S. Shimoura. Single particle states in exotic nuclei via nucleon transfer reactions at 3060 A MeV. *J. Phys. G*, **31**:1759, 2005.

[119] S. Michimasa, S. Shimoura, H. Iwasaki, M. Tamaki, S. Ota, N. Aoi, H. Baba, N. Iwasa, S. Kanno, S. Kubono, K. Kurita, M. Kurokawa, T. Minemura, T. Motobayashi, M. Notani, H.J. Ong, A. Saito, H. Sakurai, E. Takeshita, S. Takeuchi, Y. Yanagisawa, and A. Yoshida. Proton single-particle states in the neutron-rich ^{23}F nucleus. *Phys. Lett. B*, **638**:146, 2006.

[120] A. M. Mukhamedzhanov, P. Bém, V. Burjan, C. A. Gagliardi, B. F. Irgaziev, V. Kroha, J. Novák, Š Piskorcaron, E. Šimečková, R. E. Tribble, F. Veselý, and J. Vincour. Asymptotic normalization coefficients from the ^{20}Ne(^{3}He,d)^{21}Na reaction and astrophysical factor for ^{20}Ne(p,γ)^{21}Na. *Phys. Rev. C*, **2003**:035806, 2006.

[121] J.J. Thompson. Coupled reaction channels calculations in nuclear physics. *Comp. Phys. Rep.*, **7**:167, 1988.

[122] W.F. Mueller., J.A. Church, T. Glasmacher, D. Gutknecht, G. Hackman, P.G. Hansen, Z. Hu, K.L. Miller, and P. Quirin. Thirty-two-fold segmented germanium detectors to identify γ-rays from intermediate-energy exotic beams. *Nucl. Instr. and Meth. A*, **466**:492, 2001.

[123] W.F. Mueller, D. Bazin, C.M. Campbell, J.A. Church, D.C. Dinca, A. Gade, T. Glasmacher, P.G. Hansen, K.L. Yurkewicz, H. Olliver, B.M. Sherrill, and J.R. Terry. In-beam γ-ray spectroscopy of fast beams at the NSCL. *Nucl. Phys. A*, **734**:428, 2004.

[124] D. Bazin. The S800 spectrograph. *Nucl. Instr. and Meth. B*, **204**:629, 2003.

[125] H. Koivisto, D. Cole, A. Fredell, C. Lyneis, P. Miller, J. Moskalik, B. Nurnberger, and J. Ottarson. ARTEMIS - The new ECR ion source for the Coupled Cyclotron Facility at NSCL/MSU. In *Proceedings of the Workshop on the Production of Intense Beams of Highly Charged Ions, Catania, Italy, 2427 September 2000, Italian Phys. Soc. Conf. Proc.*, volume **72**, page 135, 2001.

[126] P.A. Zavodszky, B. Arend, D. Cole, J. DeKamp, G. Machicoane, F. Marti, P. Miller, J. Moskalik, J. Ottarson, J. Vincent, and A. Zeller. Design of SuSI - superconducting source for ions at NSCL/MSU - II. The conventional parts. *Nucl. Instr. and Meth. B*, **241**:959, 2005.

[127] D. J. Morrissey, B. M. Sherrill, M. Steiner, A. Stolz, and I. Wiedenhoever. Commissioning the A1900 projectile fragment separator. *Nucl. Instr. and Meth. B*, **204**:90, 2003.

[128] D. Bazin. S800 spectrograph service level description. Available at `http://www.nscl.msu.edu/files/s800_sld_2007-2.pdf`, 2006.

[129] J. A. Caggiano. *Spectroscopy of exotic nuclei with the S800 spectrograph*. PhD thesis, Michigan State University, 1999.

[130] R. Fox and J. Kusler. Spectcl histogram and data analysis package. Available from `http://sourceforge.net/projects/nsclspectcl/`, 2010.

[131] Z. Hu, T. Glasmacher, W. F. Mueller, and I. Wiedenhöver. An automatic energy-calibration method for segmented germanium detectors. *Nucl. Instr. and Meth. A*, **482**:715, 2002.

[132] G.F. Knoll. *Radiation Detection and Measurement*. John Wiley and Sons, Inc., 2010.

[133] A. Lorenz, H.D. Lemmel, W. Bambynek, T. Barta, P. Christmas, N. Coursol, K. Debertin, R.G. Helmer, R. Jedlovszky, A.L. Nichols, F.J. Schima, and Y. Yoshizawa. X-ray and gamma-ray standards for detector calibration. Technical report, IAEA, 1991.

[134] J. Morel, S. Sepman, M. Rasko, E. Terechtchenko, and J. U. Delgado. Precise determination of photon emission probabilities for the main X- and γ-rays of ^{226}Ra in equilibrium with daughters. *Appl. Radiat. Isot.*, **60**:341, 2004.

[135] M. Berz, K. Joh, J. A. Nolen, B. M. Sherrill, and A. F. Zeller. Reconstructive correction of aberrations in nuclear particle spectrographs. *Phys. Rev. C*, **47**:537, 1993.

[136] O.B. Tarasov and D. Bazin. Lise++: Radioactive beam production with in-flight separators. *Nucl. Instr. and Meth. B*, **266**:4567, 2008.

[137] A. Bürger, T.R. Saito, H. Grawe, H. Hübel, P. Reiter, J. Gerl, M. Górska, H.J. Wollersheim, A. Al-Khatib, A. Banu, T. Beck, F. Becker, P. Bednarczyk, G. Benzoni, A. Bracco, S. Brambilla, P. Bringel, F. Camera, E. Clément, P. Doornenbal, H. Geissel, A. Görgen, J. Grebosz, G. Hammond, M. Hellström, M. Honma, M. Kavatsyuk, O. Kavatsyuk, M. Kmiecik, I. Kojouharov, W. Korten, N. Kurz, R. Lozeva, A. Maj, S. Mandal, B. Million, S. Muralithar, A. Neußer, F. Nowacki, T. Otsuka, Zs. Podolyák, N. Saito, A.K. Singh, H. Weick, C. Wheldon, O. Wieland, and M. (the RISING collaboration) Winkler. Relativistic coulomb excitation of neutron-rich ^{54,56,58}Cr: On the pathway of magicity from $N = 40$ to $N = 32$. *Phys. Lett. B*, **622**:29, 2005.

[138] H.L. Crawford, R.V.F Janssens, P.F. Mantica, J.S. Berryman, R. Broda, M.P. Carpenter, B. Fornal, G.F. Grinyer, N. Hoteling, B. Kay, T. Lauritsen, K. Minamisono, I. Stefanescu, J.B. Stoker, W.B. Walters, and S. Zhu. Beta-decay studies of of neutron rich nuclei near ^{52}Ca. *Acta Phys. Pol. B*, **40**:481, 2009.

[139] C. Guénaut, G. Audi, D. Beck, K. Blaum, G. Bollen, P. Delahaye, F. Herfurth, A. Kellerbauer, H.J. Kluge, D. Lunney, S. Schwarz, L. Schweikhard, and C. Yazidjian. Mass measurements of $^{56-57}$Cr and the question of shell reincarnation at $N = 32$. *J. Phys. G*, **31**:S1765, 2005.

[140] R. V. F. Janssens, B. Fornal, P. F. Mantica, B. A. Brown, R. Broda, P. Bhattacharyya, M. P. Carpenter, M. Cinausero, P. J. Daly, A. D. Davies, T. Glasmacher, Z. W. Grabowski, D. E. Groh, M. Honma, F. G. Kondev, W. Krolas, T. Lauritsen, S. N. Liddick, S. Lunardi, N. Marginean, T. Mizusaki, D. J. Morrissey, A. C. Morton, W. F. Mueller, T. Otsuka, T. Pawlat, D. Seweryniak, H. Schatz, A. Stolz, S. L. Tabor, C. A. Ur, G. Viesti, I. Wiedenhover, and J. Wrzesinski. Structure of ^{52,54}Ti and shell closures in neutron-rich nuclei above ^{48}Ca. *Phys. Lett. B*, **546**:55, 2002.

[141] F. Perrot, F. Maréchal, C. Jollet, Ph. Dessagne, J.-C. Angélique, G. Ban, P. Baumann, F. Benrachi, U. Bergmann, C. Borcea, A. Buţă, J. Cederkall, S. Courtin, J.-M. Daugas, L. M. Fraile, S. Grévy, A. Jokinen, F. R. Lecolley, E. Liénard, G. Le Scornet, V. Méot, Ch. Miehé, F. Negoiţă, N. A. Orr, S. Pietri, E. Poirier, M. Ramdhane, O. Roig, I. Stefan, and W. Wang. β-decay studies of neutron-rich K isotopes. *Phys. Rev. C*, **74**:014313, 2006.

[142] J. I. Prisciandaro, P. F. Mantica, B. A. Brown, D. W. Anthony, M. W. Cooper, A. Garcia, D. E. Groh, A. Komives, W. Kumarasiri, P. A. Lofy, A. M. Oros-Peusquens, S. L. Tabor, and M. Wiedeking. New evidence for a subshell gap at $N = 32$. *Phys. Lett. B*, **510**:17, 2001.

[143] S. Zhu, R.V.F. Janssens, B. Fornal, S.J. Freeman, M. Honma, R. Broda, M.P. Carpenter, A.N. Deacon, B.P. Kay, F.G. Kondev, W. Krolas, J. Kozemczak, A. Larabee, T. Lauritsen, S.N. Liddick, C.J. Lister, P.F. Mantica, T. Otsuka, T. Pawlat, A. Robinson, D. Seweryniak, J.F. Smith, D. Steppenbeck, B.E. Tomlin, J. Wrzesinski, and X. Wang. One-particle excitations outside the ^{54}Ti semi-magic core: The ^{55}V and ^{55}Ti yrast structures. *Phys. Lett. B*, **650**:135, 2007.

[144] F. Tondeur. Self-consistent study of nuclei far from stability with the energy density method. In *4th International Conference on Nuclei Far from Stability*, 1981.

[145] X. L. Tu, X. G. Zhou, D. J. Vieira, J. M. Wouters, Z. Y. Zhou, H. L. Seifert, and V. G Lind. Direct mass measurements of the neutron-rich isotopes of chlorine through iron. *Z. Phys. A*, **337**:361, 1990.

[146] O. Sorlin, V. Borrel, S. Grevy, D. Guillemaud-Mueller, A. C. Mueller, F. Pougheon, W. Bohmer, K. L. Kratz, T. Mehren, P. Moller, B. Pfeiffer, T. Rauscher, M. G. Saint-Laurent, R. Anne, M. Lewitowicz, A. Ostrowski, T. Dorfler, and W. D. Schmidt-Ott. First beta-decay studies of the neutron-rich isotopes $^{53-55}$Sc and $^{56-59}$V. *Nucl. Phys. A*, **632**:205, 1998.

[147] S. Bhattacharyya, M. Rejmund, A. Navin, E. Caurier, F. Nowacki, A. Poves, R. Chapman, D. O'Donnell, M. Gelin, A. Hodsdon, X. Liang, W. Mittig, G. Mukherjee, F. Rejmund, M. Rousseau, P. Roussel-Chomaz, K.-M. Spohr, and Ch. Theisen. Spectroscopy of ^{52,53}Sc. *Phys. Rev. C*, **79**:014313, 2009.

[148] G. Audi, A. H. Wapstra, and C. Thibault. The 2003 atomic mass evaluation: (II). Tables, graphs and references. *Nucl. Phys. A*, **729**:337, 2003.

[149] R. Brun and F. Rademakers. ROOT - An object oriented data analysis framework, Proceedings AIHENP'96 workshop, Lausanne, Sep. 1996. *Nucl. Instr. and Meth. B*, **389**:81, 1997.

[150] A. Gade, P. Adrich, D. Bazin, M. D. Bowen, B. A. Brown, C. M. Campbell, J. M. Cook, T. Glasmacher, P. G. Hansen, K. Hosier, S. McDaniel, D. McGlinchery, A. Obertelli, K. Siwek, L. A. Riley, J. A. Tostevin, and D. Weisshaar. Reduction of spectroscopic strength: Weakly-bound and strongly-bound single-particle states studied using one-nucleon knockout reactions. *Phys. Rev. C*, **77**:044306, 2008.

[151] E.K. Warburton. In-medium and core-polarization effects in $^{50}\mathrm{K}(0^-) \xrightarrow{\beta^-} {}^{50}\mathrm{Ca}(0^+)$. *Phys. Rev. C*, **44**:1024, 1991.

[152] A. Gade, D. Bazin, C.A. Bertulani, B.A. Brown, C.M. Campbell, J.A. Church, D.C. Dinca, J. Enders, T. Glasmacher, P.G. Hansen, Z. Hu, K.W. Kemper, W.F. Mueller, H. Olliver, B.C. Perry, L.A. Riley, B.T. Roeder, B.M. Sherrill, J.R. Terry, J.A. Tostevin, and K.L. Yurkewicz. Knockout from ^{46}Ar: $\ell = 3$ neutron removal and deviations from eikonal theory. *Phys. Rev. C*, **71**:051301, 2005.

[153] A. Gade, J.A. Tostevin, T. Baugher, D. Bazin, B.A. Brown, C. M. Campbell, T. Glasmacher G. F. Grinyer, S. McDaniel, K. Meierbachtol, A. Ratkiewicz, S. R. Stroberg, K. A. Walsh, D. Weisshaar, and R. Winkler. Inverse-kinematics one-neutron pickup with fast rare-isotope beams. To be published, 2011.

[154] T.W. Burrows. Nuclear data sheets for $A = 49$. *Nucl. Data Sheets*, **109**:1879, 2008.

[155] L. Faux, S. Andriamonje, B. Blank, S. Czajkowski, R. Del Moral, J. P. Dufour, A. Fleury, T. Josso, M. S. Pravikoff, A. Piechaczek, E. Roeckl, K. H. Schmidt, K. Sümmerer, W. Trinder, M. Weber, T. Brohm, A. Grewe, E. Hanelt, A. Heinz, A. Junghans, C. Röhl, S. Steinhäuser, B. Voss, Z. Janas, and M. Pfützner. β-delayed proton radioactivity of ^{44}Cr, ^{47}Mn, ^{48,49}Fe and ^{50}Co. *Nucl. Phys. A*, **602**:167, 1996.

[156] J. A. Cameron, M. A. Bentley, A. M. Bruce, R. A. Cunningham, W. Gelletly, H. G. Price, J. Simpson, D. D. Warner, and A. N. James. High-spin states in the mirror nuclei ^{49}Cr and ^{49}Mn. *Phys. Lett. B*, **235**:239, 1990.

[157] C. D. O'Leary, M. A. Bentley, D. E. Appelbe, D. M. Cullen, S. Ertürk, R. A. Bark, A. Maj, and T. Saitoh. Mirror symmetry up to the band termination in ^{49}Mn and ^{49}Cr. *Phys. Rev. Lett.*, **79**:4349, 1997.

[158] Z. Elekes, J. Timar, and B. Singh. Nuclear data sheets for $A = 50$. *Nucl. Data Sheets*, **112**:1, 2011.

[159] H. Xiaolong. Nuclear data sheets for $A = 51$. *Nucl. Data Sheets*, **107**:2131, 2006.

[160] C. Dossat, N. Adimi, F. Aksouh, F. Becker, A. Bey, B. Blank, C. Borcea, R. Borcea, A. Boston, M. Caamano, G. Canchel, M. Chartier, D. Cortina, S. Czajkowski, G. de France, F. de Oliveira Santos, A. Fleury, G. Georgiev, J. Giovinazzo, S. Grévy, R. Grzywacz, M. Hellström, M. Honma, Z. Janas, D. Karamanis, J. Kurcewicz, M. Lewitowicz, M.J. López Jiménez, C. Mazzocchi, I. Matea, V. Maslov, P. Mayet, C. Moore, M. Pfützner, M.S. Pravikoff, M. Stanoiu, I. Stefan, and J.C. Thomas. The decay of proton-rich nuclei in the mass $A = 36 - 56$ region. *Nucl. Phys. A*, **792**:18, 2007.

[161] K. Yamada, T. Motobayashi, N. Aoi, H. Baba, K. Demichi, Z. Elekes, J. Gibelin, T. Gomi, H. Hasegawa, N. Imai, H. Iwasaki, S. Kanno, T. Kubo, K. Kurita, Y. Matsuyama, S. Michimasa, T. Minemura, M. Notani, T. Onishi K., H. Ong, S. Ota, A. Ozawa, A. Saito, H. Sakurai, S. Shimoura, E. Takeshita, S. Takeuchi, M. Tamaki,

Y. Togano, Y. Yanagisawa, K. Yoneda, and I. Tanihata. Reduced transition probabilities for the first 2^+ excited state in ^{46}Cr, ^{50}Fe, and ^{54}Ni. *Eur. Phys. J. A*, **2005**:409, 2005.

[162] J.A. Tostevin. Single-particle cross sections for the proton-pickup reactions. Private communications, 2010.

[163] B.A. Brown. Spectroscopic factors for the proton-pickup reactions. Private communications, 2010.

[164] W.R. Wiringa. Two-cluster distribution functions, 2010. Overlaps available at `http://www.phy.anl.gov/theory/research/overlap/`.

[165] J. Carlson, V. R. Pandharipande, and R. B. Wiringa. Three-nucleon interaction in 3-, 4- and ∞-body systems. *Nucl. Phys. A*, **401**:59, 1983.

[166] D.R. Tilley, J.H. Kelley, J.L. Godwin, D.J. Millener, J.E. Purcell, C.G. Sheu, and H.R. Weller. Energy levels of light nuclei $A = 8, 9, 10$. *Nucl. Phys. A*, 745:155, 2004.

[167] T.W. Burrows. Nuclear data sheets for $A = 48$. *Nucl. Data Sheets*, **107**:1747, 2006.

[168] N. H. Brook and I. O. Skillicorn. A comparison of the momentum spectra in deep inelastic scattering with the modified leading logarithmic approximation. *Phys. Lett. B*, **497**:55, 2001.

[169] E. K. Warburton and B. A. Brown. Effective interactions for the $0p1sd$ nuclear shell-model space. *Phys. Rev. C*, **1992**:923, 1992.

[170] I.Y. Lee, R.M. Clark, M. Cromaz, M.A. Deleplanque, M. Descovich, R.M. Diamond, P. Fallon, A.O. Macchiavelli, F.S. Stephens, and D. Ward. GRETINA: A gamma ray energy tracking array. *Nucl. Phys. A*, **746**:255, 2004.

[171] A. Pais. *Subtle is the Lord: The Science and Life of Albert Einstein*. Oxford University Press, 1982.

[172] J.J. Thompson. Cathode rays. *Phil. Mag.*, **44**:293, 1897.

[173] J.J. Thompson. XXIV. On the structure of the atom: an investigation of the stability and periods of oscillation of a number of corpuscles arranged at equal intervals around the circumference of a circle; with application of the results to the theory of atomic structure. *Phil. Mag.*, **7**:236, 1904.

[174] W. Röntgen. Über eine neue Art von Strahlen. In *Sitzungsberichte der Physikalisch-medicinischen Gesellschaft zu Würzburg*, 1896.

[175] H. Becquerel. Sur les radiations émises par phosporescence. *C.R. Acad. Sci.*, **122**: 420, 1896.

[176] H. Becquerel. Sur les radiations invisibles émises par les corps phosphorescents. *C.R. Acad. Sci.*, **122**:501, 1896.

[177] P. Curie and M. Curie. Rayons émis par les composés de l'uranium et du Thorium. *C.R. Acad. Sci.*, **126**:1101, 1898.

[178] P. Curie and M. Curie. Sur une substance nouvelle radioactive, contenue dans la pechblende. *C.R. Acad. Sci.*, **127**:175, 1898.

[179] P. Curie, M. Curie, and G. Bémont. Sur une nouvelle substance fortement radioactive, contenue dans la pechblende. *C.R. Acad. Sci.*, **127**:1215, 1898.

[180] M. Planck. Entropy and temperature of radiant heat. *Ann. Phys.*, **1**:719, 1900.

[181] M. Planck. On the law of distribution of energy in the normal spectrum. *Ann. Phys.*, **4**:553, 1901.

[182] A. Einstein. Über einen die Erzeugung und Verwandlung des Lichtes betreffenden heuristischen Gesichtspunkt. *Ann. Phys.*, **17**:132, 1905.

[183] A. Einstein. Prinzip von der Erhaltung der Schwerpunktsbewegung und die Trägheit der Energie. *Ann. Phys.*, **20**:199, 1906.

[184] A. Einstein. Planckshe Theorie der Strahlung und die Theorie der Spezifischen Wärme. *Ann. Phys.*, **22**:180, 1907.

[185] E. Rutherford and F. Soddy. The radioactivity of Thorium compounds I. *Trans. Chem. Soc. London*, **81**:321, 1902.

[186] E. Rutherford and F. Soddy. The radioactivity of Thorium compounds II. *Trans. Chem. Soc. London*, **82**:837, 1902.

[187] E. Rutherford and F. Soddy. The cause and nature of radioactivity I. *Phil. Mag.*, **4**: 370, 1902.

[188] E. Rutherford and F. Soddy. The cause and nature of radioactivity II. *Phil. Mag.*, **4**: 596, 1902.

[189] E. Rutherford. A radio-active substance emitted from Thorium compounds. *Phil. Mag.*, **49**:1, 1900.

[190] A. Pais. *Inward Bound: Of Matter and Forces in the Physical World*. Oxford University Press, 1986. p. 186.

[191] E. Rutherford. The scattering of alpha and beta particles by matter and the structure of the atom. *Phil. Mag.*, **21**:669, 1911.

[192] E. Rutherford. The structure of the atom. *Nature*, **92**:423, 1913.

[193] N. Bohr. The spectra of helium and hydrogen. *Nature*, **92**:231, 1914.

[194] N. Bohr. On the constitution of atoms and molecules, part I. *Phil. Mag.*, **26**:1, 1913.

[195] N. Bohr. On the constitution of atoms and molecules, part II: systems containing only a single nucleus. *Phil. Mag.*, **26**:476, 1913.

[196] N. Bohr. On the constitution of atoms and molecules, part III: systems containing several nuclei. *Phil. Mag.*, **26**:857, 1913.

[197] H.G.J Moseley and C.G. Darwin. XIV. The reflexion of the x-rays. *Phil. Mag.*, **26**: 1024, 1913.

[198] H.G.J Moseley. LXXX. The high-frequency spectra of the elements. *Phil. Mag.*, **27**: 703, 1914.

[199] F.W. Aston. The constitution of the elements. *Nature*, **104**:393, 1919.

[200] F. Soddy. The radio-elements and the periodic law. *Chem. News*, **107**:97, 1913.

[201] F. Soddy. Intra-atomic charge. *Nature*, **92**:399, 1913.

[202] F. Soddy. Radioactivity. *Chem. Soc. Ann. Rep.*, **10**:262, 1913.

[203] J.J. Thompson. Rays of positive electricity. *Proc. R. Soc.*, **A89**:1, 1913.

[204] J. Yurkon, D. Bazin, W. Benenson, D.J. Morrissey, B.M. Sherrill, D. Swan, and R. Swanson. Focal plane detector for the S800 high-resolution spectrometer. *Nucl. Instr. and Meth. A*, **422**:291, 1999.

[205] E. Rutherford. Collisions of alpha particles with light atoms. IV. An anomalous effect in nitrogen. *Phil. Mag.*, **37**:518, 1919.

[206] N. Bohr. Atomic structure. *Nature*, **109**:208, 1921.

[207] W. Pauli. Über den Zusammenhang des Abschlusses der Elektronengruppen im Atom mit der Komplexstruktur der Spektren. *Z. Phys. A*, **1925**:765, 1925.

[208] G. E. Uhlenbeck and S. Goudsmit. Ersetzung der Hypothese vom unmechanischen Zwang durch eine Forderung beziglich des inneren Verhaltens jedes einzelnen Elektrons. *Die Naturwissenschaften*, **13**:953, 1925.

[209] W. Pauli. Zur Quantenmechanik des magnetischen Elektrons. *Z. Phys. A*, **43**:601, 1927.

[210] P.A.M. Dirac. The quantum theory of the electron. *Proc. R. Soc.*, **117**:601, 1928.

[211] L. de Broglie. *Recherches sur la Théorie des Quanta*. PhD thesis, Paris University, 1924.

[212] W. Heisenberg. Über quantentheoretische Umdeutung kinematischer und mechanischer Beziehungen. *Z. Phys.*, **33**:879, 1925.

[213] W. Heisenberg. Über den anschaulichen Inhalt der quantentheoretischen Kinematik und Mechanik. *Z. Phys.*, **43**:172, 1927.

[214] M. Born and P. Jordan. Zur Quantenmechanik. *Z. Phys.*, **34**:858, 1925.

[215] M. Born, W. Heisenberg, and P. Jordan. Zur Quantenmechanik II, Zeitschrift für Physik. *Z. Phys.*, **35**:557, 1925.

[216] H.A. Kramers and W. Heisenberg. Über die Streuung von Strahlung durch Atome. *Z. Phys.*, **31**:681, 1925.

[217] E. Schrödinger. Quantisierung als Eigenwertproblem (Erste Mitteilung). *Ann. Phys.*, **79**:361, 1926.

[218] E.O. Lawrence and M.S. Livingston. The production of high speed light ions without the use of high voltages. *Phys. Rep.*, **40**:19, 1932.

[219] J.D. Cockcroft and E.T.S. Walton. Artificial production of fast protons. *Nature*, **129**: 242, 1943.

[220] J.D. Cockcroft and E.T.S. Walton. Disintegration of lithium by swift protons. *Nature*, **129**:649, 1943.

[221] J. Chadwick. Possible existence of a neutron. *Nature*, **129**:312, 1932.

[222] E. Rutherford. Nuclear constitution of atoms. *Proc. Roy. Soc*, **A97**:324, 1920.

[223] W. Heisenberg. Über den Bau der Atomkerne. I. *Z. Phys. A*, **77**:1, 1932.

[224] W. Heisenberg. Über den Bau der Atomkerne. II. *Z. Phys. A*, **78**:156, 1932.

[225] W. Heisenberg. Über den Bau der Atomkerne. III. *Z. Phys. A*, **80**:587, 1932.

[226] G. Gamow. Discussion on the structure of atomic nuclei. *Proc. R. Soc.*, **A136**:386, 1929.

[227] G. Gamow. Mass defect and nuclear constitution. *Proc. R. Soc.*, **A126**:623, 1930.

[228] G. Gamow. Zur Quantentheorie des Atomkernes. *Z. Phys. A*, **51**:210, 1928.

[229] L. Meitner and O.R. Frisch. Disintegration of uranium by neutrons: a new type of nuclear reaction. *Nature*, **143**:239, 1939.

[230] J. Rainwater. Nuclear energy level argument for a spheroidal nuclear model. *Phys. Rev.*, **79**:432, 1950.

[231] A. Bohr. On the quantization of angular momenta in heavy nuclei. *Phys. Rev.*, **81**: 134, 1951.

[232] A. Bohr and B.R. Mottelson. Moments of inertia of rotating nuclei. *K. Dan. Vidensk. Selsk. Mat. Fys. Medd.*, **1955**:131, 1953.